

Paleomonsoon Reconstruction Using Marine Proxies of the Indian Ocean

A THESIS

Submitted for the Award of Ph.D. Degree of
MOHANLAL SUKHADIA UNIVERSITY

In the
Faculty of Science
By
Pullabhatla Kiran Kumar



Under the Supervision of
Dr. M. G. Yadava
Scientist-SG
Geosciences Division
Physical Research Laboratory, Ahmedabad, India

DEPARTMENT OF PHYSICS
MOHANLAL SUKHADIA UNIVERSITY
UDAIPUR, INDIA
2019

Abbreviations

θ	: Potential Temperature
σ_θ	: Water Density
‰	: per mill
$\delta^{13}\text{C}$: Isotopic composition of carbon with respect to VPDB
$\delta^{15}\text{N}$: Isotopic composition of Nitrogen with respect to Air N_2
$\delta^{18}\text{O}$: Isotopic composition of oxygen with respect to (VPDB, VSMOW)
δD	: isotopic composition of hydrogen with respect to VSMOW
AMS	: Accelerator Mass Spectrometer
AS	: Arabian Sea
ASHSW	: Arabian Sea High Saline Water mass
BOB	: Bay of Bengal
BoBW	: Bay of Bengal Water mass
C	: Carbon
CI	: Central India
CTD	: Conductivity Temperature Depth
D	: Deuterium
DIC	: Dissolved Inorganic Carbon
DO	: <i>Dansgaard Oeschger</i>
<i>E</i>	: <i>Evaporation</i>
EA	: Elemental Analyzer
EICC	: East India Coastal Current
ENSO	: El-Niño Southern Oscillation
GC	: Gas Chromatograph
GCM	: General Circulation Model
GMWL	: Global Meteoric Water Line
GNIP	: Global Network of Isotopes in Precipitation
GPCP	: <i>Global Precipitation Climatology Project</i>
H	: Hydrogen
HE	: Heinrich Event
IAEA	: International Atomic Energy Agency
IAPSO	: <i>International Association for the Physical Sciences of the Oceans</i>
IOD	: Indian Ocean Dipole
IRMS	: Isotope Ratio Mass Spectrometer
ISM	: Indian Summer Monsoon
ITCZ	: Inter Tropical Convergence Zone
LGM	: Last Glacial Maxima

LMWL	: Local Meteoric Water Line
MIS	: Marine Isotopic Stage
MJO	: Madden Julian Oscillation
MLD	: Mixed Layer Depth
MMB	: Makrana Marble
N	: Nitrogen
NARM	: Narmada water
NEI	: North East India
O	: Oxygen
OMZ	: Oxygen Minimum Zone
P	: Precipitation
PDO	: Pacific Decadal Oscillation
PRL	: Physical Research Laboratory
PSGW	: Persian Gulf Water mass
R	: Runoff
RSW	: Red Sea Water mass
S	: Salinity
SC	: Somalia Current
SEAS	: South Eastern Arabian Sea
SST	: Sea Surface Temperature
SLAP	: Southern Light Antarctic Precipitation
SWING	: Stable Water Isotope Intercomparison Group
TD	: Thermocline Depth
TRMM	: Tropical Rainfall Measuring Mission
VPDB	: Vienna Pee Dee Belemnite
VSMOW	: Vienna Standard Mean Ocean Water
WICC	: West India Coastal Current
WICO	: Inter-laboratory comparison exercise for $\delta^2\text{H}$ and $\delta^{18}\text{O}$ analysis of water samples
WMC	: Winter Monsoon Current
WMO	: World Meteorological Organization

Abstract

Stable isotopes of oxygen, carbon, and hydrogen are used as a tool to study modern seawater hydrological dynamics (effect of runoff and large-scale ocean mixing) and to reconstruct past climate from ocean sediment cores. Significant variations in the Indian monsoon (IM), at intra-seasonal, annual, centennial to millennial time scales, are observed due to changes in the inter-hemispheric (northern and southern) dynamics, ice sheet extensions (glacial and interglacial) and short term climate processes. This thesis reports results on oceanic changes based on measurements of stable isotopic composition ($\delta^{18}\text{O}$, δD) carried out on modern seawater samples and inferences on IM from three sediment cores ($\delta^{18}\text{O}$, $\delta^{13}\text{C}_{\text{org}}$, $\delta^{15}\text{N}$, over the last ~70 ka) raised from the northern Indian Ocean (NIO).

Isotopic compositions ($\delta^{18}\text{O}$ and δD) of surface seawater samples from NIO show significant spatial and temporal variability. Seasonal variability in the $\delta^{18}\text{O}$ -S relation (slope and intercept) of surface waters of the NIO are observed with stronger $\delta^{18}\text{O}$ -S and δD - $\delta^{18}\text{O}$ relations during the winter than the spring time. During winter time, the dominance of runoff effects on the $\delta^{18}\text{O}$ -S association is found. Substantial changes in the slope and intercept of $\delta^{18}\text{O}$ -S relation for subsurface waters could be a characteristic of water mass dynamics in NIO. Reanalysis of large volume of recently published results on salinity and $\delta^{18}\text{O}$ measurements on surface seawater suggests that variation in the $\delta^{18}\text{O}$ of the Eastern Arabian Sea is mainly controlled by the influx of low salinity water from relatively fresher Bay of Bengal through winter time boundary currents.

Based on the sedimentary records from NIO, significantly strong and weak monsoon periods associated with the global climatic events during the last ~ 70 ka were observed. Record from the Andaman Sea sediment core shows an abrupt decrease in the ISM during the mid-Holocene (7-4.5 ka). During the Last Glacial Maximum, the Andaman Sea salinity was 2 (psu) higher than the early Holocene. $\delta^{18}\text{O}$ analysis of mixed habitat planktonic foraminifera species shows significant variation in the stratification over the NIO during last ~ 70 ka. In contrary to the earlier inferences, the present work based on a compilation of high-resolution $\delta^{18}\text{O}$ foraminifera records from the eastern Arabian

Sea provides evidence that the south Asian summer monsoon steadily declined during the Holocene. Abrupt variation in the $\delta^{18}\text{O}$ values of *G. ruber* in response to short term climatic events were observed: with warm (cold) Dansgaard-Oeschger (Heinrich) events associated with relatively stronger (weaker) monsoon periods. The bulk sediment analysis for $\delta^{15}\text{N}$, $\delta^{13}\text{C}_{\text{org}}$, and N & C_{org} (wt %) infers a substantial variation in the productivity over the western Bay of Bengal, associated with the variability in the upper ocean stratification during the last ~ 16 ka.

El-Niño Southern Oscillation (ENSO) is known to have affected IM: most of the severe droughts in India are associated with active ENSO periods. Given the heterogeneity in rainfall patterns over India, the ENSO influence on Indian summer monsoon has been revisited. During strong El-Niño events, the multiple isotopic (proxy-based) and satellite data set show a weaker summer monsoon over central India (CI) and relatively stronger summer monsoon over northeast India (NEI). The general circulation model derived $\delta^{18}\text{O}_{\text{rain}}$ variation over the CI during ENSO events mimic the weaker rainfall conditions. Since these observations were unprecedented and counterintuitive, further verification from paleo-proxy records (speleothem cave deposits) showed a similar dipole nature of rainfall patterns over CI and NEI during ENSO periods, confirming observed ENSO's role on rainfall. Both instrumental and paleoclimate proxy records showed a decadal variability in the ISM concurred with variation in the El-Niño strengths. Armed with this new “calibration” of $\delta^{18}\text{O}_{\text{rain}}$ and ENSO, we infer that the high-resolution speleothem records from CI an NEI based stronger (weaker) rainfall conditions over CI (NEI) during 1625 – 1715 AD, represents an absence of long term El-Niño or stronger La-Niña like conditions over the central Pacific Ocean.

Keywords: Indian Summer Monsoon, Stable isotopes, ENSO, LGM, Ocean stratification, Foraminifera, Deep-sea sediment, Speleothem, Bay of Bengal, Arabian Sea.

Chapter-1
Introduction

Introduction

Seasonal reversal of the wind system (monsoon) is an essential process that occurs over the Indian subcontinent and is known to play a crucial role in the modern climate. The economic and societal conditions of India depend primarily on the crop yield, which in turn is decided by the variability in monsoon rainfall. The Indian subcontinent is separated by the rest of Asia by the Himalayan ranges from the north and surrounded by the three seawater bodies viz. the Arabian Sea (west), the equatorial Indian Ocean (south) and Bay of Bengal (east; Figure 1.1).

Instrumental based data and historical records show that strength of the monsoon was not constant throughout: severe water deficiency and catastrophic excess rainfall conditions were observed in the subcontinent, several times in the recent past (Gadgil and Gadgil, 2006; Guhathakurta and Rajeevan, 2008; Krishna Kumar et al., 2004; Kumar et al., 2013; Mallya et al., 2016; Prasanna, 2014). These strong fluctuations (stronger and weaker monsoon) severely affected the economic conditions, therefore, it is necessary to understand its significant variability, at spatio-temporal scales, to address the possible future scenario in the era of the global climate change (Ghosh et

al., 2016; Kumar et al., 2013; Patnaik et al., 2012; Wang et al., 2005a, 2012). Proxy data (preserved signatures of the environment that can be directly measured) from natural archives can be used to reconstruct past monsoon variability over the Indian subcontinent (Black et al., 2007; Emiliani, 1955; Sarkar et al., 1990; Shackleton, 1967; Yadava and Ramesh, 2005; Zachos et al., 2001).

Stable isotopic composition of water molecules (i.e., ratio of abundances of ^{18}O to ^{16}O and ^2H to ^1H) in rainwater, atmospheric moisture and seawater can be used to characterise sources of moisture and understand hydrological cycle of the modern climate (Clark and Fritz, 2013; Dansgaard, 1964; Gat, 1996; Rozanski et al., 1993, 1992; Rozanski and Sonntag, 1982; Yang et al., 2016). Various processes affecting isotopic ratios in the natural archives, so far, are very well-identified; protocols for retrieving past climate signatures and analytical methods are also largely established.

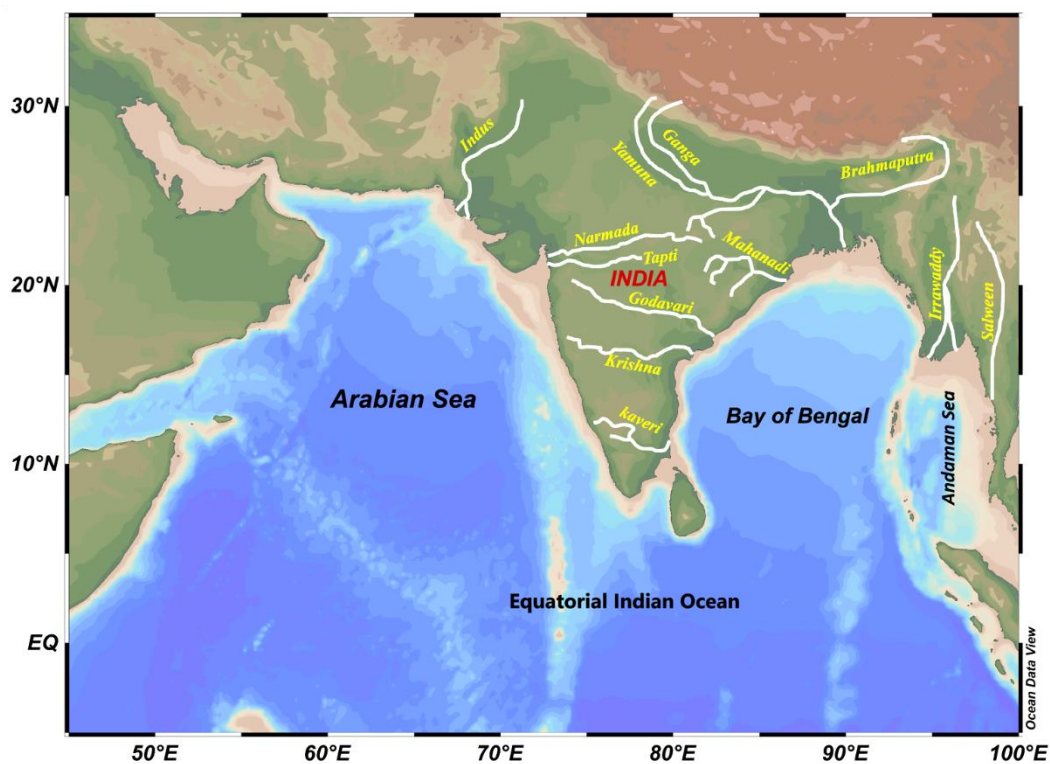


Figure 1.1: The northern Indian Ocean comprises of the Arabian Sea, Bay of Bengal, and the Andaman Sea. Lines (white) over the Indian subcontinent represent the major river systems.

1.1.Indian Summer Monsoon (ISM) and its mechanism

Uneven distribution of landmass and sea in the Indian Ocean region (northward bounded by land and southward open ocean) causes intense differential heating of land and ocean, producing significant temperature gradient compared to the other oceans (Gadgil, 2007; Gadgil and Gadgil, 2006; Rao et al., 2005). This happens due to different specific heat capacities of land and ocean; heating and cooling of the land is faster than the ocean. In summer, the land gets heated quicker and more than the ocean; however, this behavior reverses in winter (O'Hare 1997; Byrne and O'gorman 2013). During summer, this differential heating of land and ocean creates a low-pressure system over the Indian subcontinent and high-pressure condition over the ocean (Gadgil, 2007; Gadgil and Gadgil, 2006; O'HARE, 1997; Sarkar et al., 1990). This pressure gradient causes movement of winds from the high-pressure (ocean) to the low-pressure areas (land). The northward and southward migration of the intertropical convergence zone (ITCZ) is associated with the apparent seasonal position of the Sun over a latitude (Figure 1.2), which is believed to contribute to the varying seasonal rainfall over the Indian subcontinent (Gadgil, 2007; Gadgil and Gadgil, 2006). ITCZ is a low-pressure zone where the surface trade winds from both the hemispheres convergence and are usually associated with the formation of deep convecting clouds and substantial rainfall. This seasonal reversal of wind patterns and transport of massive amounts of moisture from the Indian Ocean causes heavy rainfall over the Indian subcontinent (Krishnamurthy and Ajayamohan, 2010; Krishnan et al., 2003; Mooley and Shukla, 1989; Sikka, 1978). Average rainfall over India for 1901-2013 is 900 ± 90 mm (Dwivedi et al., 2019; Saikranthi et al., 2017). During Indian summer (June, July, August, and September-JJAS), the ITCZ is located north of the equator; the south-easterly trade winds cross the equator; after changing its direction, these are identified as south-westerlies and hence southwest monsoon (SW monsoon or summer monsoon; Figure 1.3a). These winds bring enormous moisture, from the southern Indian Ocean and the Arabian Sea to the Indian subcontinent (Kishtawal et al. 1991; O'Hare 1997; Krishnamurthy and Kinter 2003; Murtugudde and Annamalai 2004;

Gadgil 2007). The onset of monsoon over the Indian subcontinent takes place during late May to early June over Kerala. During the summer monsoon, 80% of the annual rainfall is received over the Indian plains (Maximum over Kerala, Western Ghats and Northeast India including Myanmar, Bangladesh, and adjoining landmasses; Bollasina 2014).

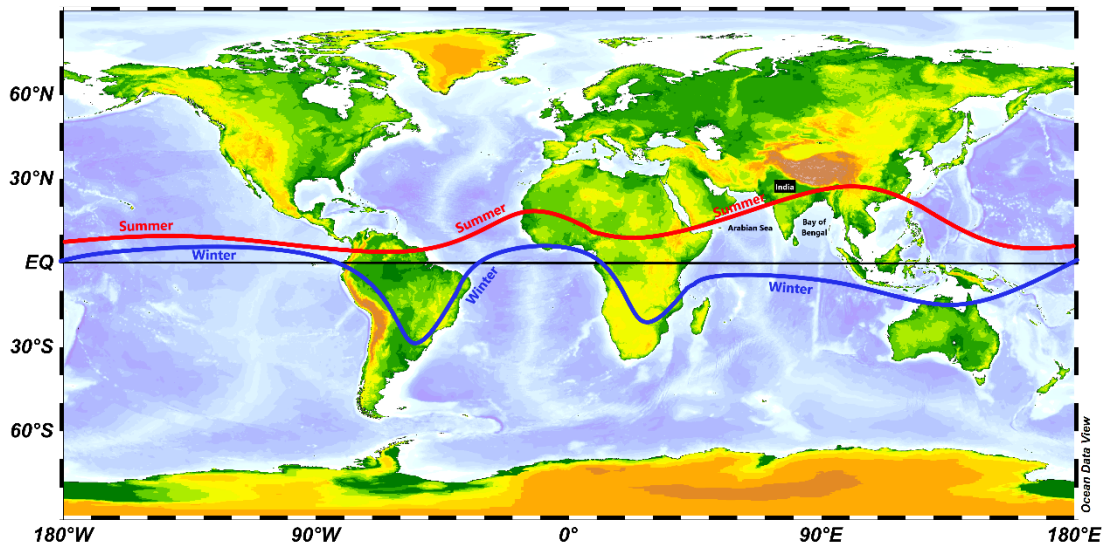


Figure 1.2: Schematic of the mean position of ITCZ during the northern hemisphere summer (July) and winter (January). The red line shows the northernmost location of ITCZ during the northern hemisphere summer, and the blue line indicates the southernmost limit of ITCZ position during the southern hemisphere summer. Source: adapted from Tarbuck and Lutgens (1979).

Once the ITCZ reaches its northern limit (maximum position in the northern hemisphere, Figure 1.2), it starts moving southward; winds change its direction to become north-easterlies and onset of the northeast monsoon (NE monsoon or winter monsoon; December, January, February-DJF) takes place (Figure 1.3b). The cold and dry northeast monsoon winds are mostly confined to the land regions (Galvin, 2008; Prasanna Kumar et al., 2004a; Tiwari et al., 2011). However, some part of the northeast winds carry the moisture from the Bay of Bengal and causes a significant amount of rainfall over the southern India peninsular regions (Tamil Nadu, southern Andhra Pradesh, Pondicherry; Kripalani and Kumar 2004; Rajeevan et al. 2012). The periods of transition of the winds from southwest to northeast and vice-versa are called the pre-

(March April, and May: MAM) and post- (October and November: ON) monsoon, respectively. During this pre- and post-monsoon periods, winds are calm, and almost no rainfall is observed in major parts of the Indian subcontinent. However, during the pre-monsoon (MAM) periods, northwest India experiences a significant amount of rain due to the western disturbance (Chand and Singh, 2015; Pisharoty and Desai, 1956). Similarly, during the post-monsoon (ON) periods, conditions over the Bay of Bengal favors the formation of the Tropical Cyclones (Girishkumar and Ravichandran, 2012a).

The Indian subcontinent has several major river systems (Figure 1.1). The source of water for these is rainfall (summer monsoon) and ice-melt (Himalayan glaciers). An enormous amount of rainfall during the SW monsoon finally debouches into the Indian Ocean through numerous river systems as freshwater (Figure 1.1). This freshwater is transported and distributed in the northern Indian Ocean through the surface ocean boundary current systems. Since freshwater input is modulated by the land-based processes (rainfall variation), this makes the Indian Ocean a vast archive of terrestrial paleo-environment: primarily the rainfall amount. However, it will be sensitive to the average rainfall variation over the Indian subcontinent rather than the regional rainfall conditions.

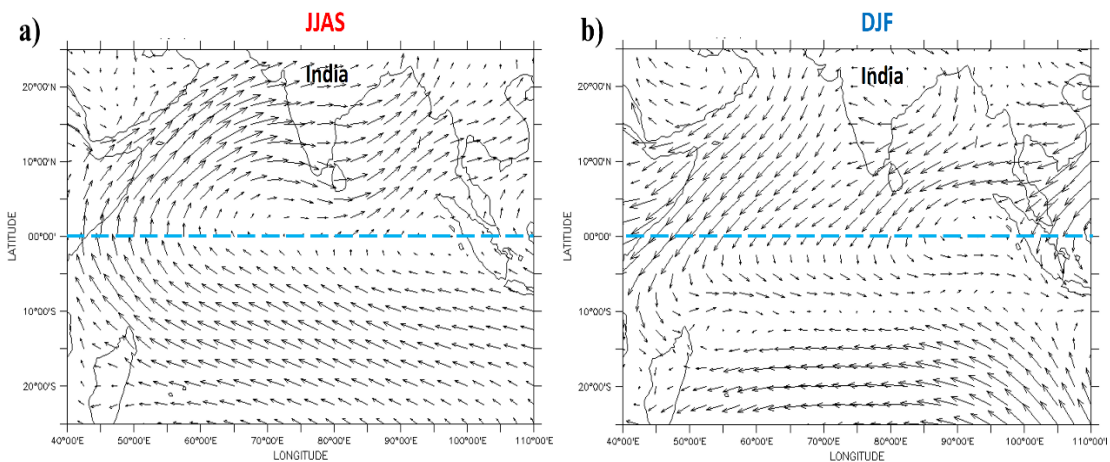


Figure 1.3: Seasonal reversal of surface atmospheric winds (at 925 mbar height) over the Indian subcontinent and adjoining oceans: a) during the summer monsoon winds, i.e., southwest monsoon b) during the winter monsoon winds, i.e., northeast monsoon. The blue

dashed horizontal line (at 0°N) shows the equator. Source: Kalnay et al., 1996. (redrawn using data from <http://apdrc.soest.hawaii.edu/las/v6/dataset?catitem=12819>)

1.2. Indian Ocean Setting

The Indian Ocean is the third largest ocean after the Pacific Ocean and the Atlantic Ocean, with a spatial distribution of 68,556,000 km², an average depth of ~ 4 km, and bounded between 80°S-25°N and 40°E-100°E. It is landlocked from the northern side with the open ocean in the southern front; this allows maximum penetration of the northward moving ITCZ up to 30°N and southward movement up to 20°S (Gadgil 2007; due to differential heating capacity of land-sea). The northern Indian Ocean, i.e., north of the equator, is divided into two parts viz. the Arabian Sea (AS) and the Bay of Bengal (BoB, Figure 1.1). Even though both (AS and BoB) the ocean water bodies are located in the same latitudinal region, they have different characteristics. The seasonal reversal of wind affects oceanic conditions significantly in the northern Indian Ocean than the southern Indian Ocean. These seasonal reversal winds induce the surface ocean boundary currents in the northern Indian Ocean, which change their directions from clockwise during the SW monsoon and anti-clockwise during the NE monsoon (Figure 1.4). During the SW monsoon the Eastern boundary current in the eastern Arabian Sea, i.e., West India Coastal Current (WICC) moves from north to equatorward and joins the western boundary current in BoB, i.e., East Indian Coastal Current (EICC) that runs from equatorward to northward direction, and reverses during NE monsoon (Schott and McCreary Jr, 2001a; Vinayachandran and Kurian, 2008; Wyrтки, 1973). These directional changes in surface boundary currents play a very significant role in the northern Indian Oceanic system by transporting surface seawater (having different characteristics) from the AS to BoB and vice versa (Figure 1.4).

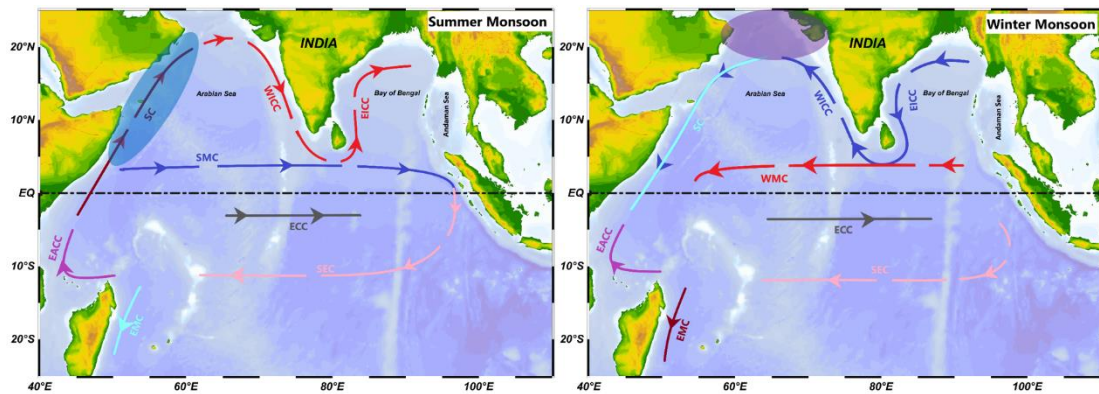


Figure 1.4: Surface ocean current systems (seasonal reversal) over the northern Indian Ocean during summer and winter monsoon. SC: Somalia Current; WICC: West India Coastal Current; EICC: East India Coastal Current; SMC: Summer Monsoon Current; WMC: Winter Monsoon Current; EACC: East African Coastal Current, ECC: Equatorial Counter Current. The arrow shows the direction of the currents during the respective seasons (Source: Wyrтки 1973; Schott and McCreary Jr 2001). Blue patch over Somalia coast represents the intense upwelling region during the summer monsoon, and the purple patch over the northern Arabian Sea represents the convecting mixing region during winter.

The Arabian Sea: The western part of the northern Indian Ocean, is affected by the strong south-westerly winds during the SW monsoon causing an intense wind-induced Ekman pumping, i.e., upwelling over the Somalia coast (blue patch in Figure 1.4; summer monsoon; Smith and Codispoti 1980; Madhupratap et al. 1996; McCreary Jr et al. 1996; Schott and McCreary Jr 2001; Goes et al. 2005). Upwelling is the movement of cold and nutrient-rich water from the subsurface to the surface; it increases the primary production over the Somalia coast. Similarly, during the NE monsoon, as winds are dry and cold when they pass over the northern AS, it enhances evaporative cooling of the surface seawater that increases water density: which leads to vertical mixing; this is known as ‘convecting mixing’ (Figure 1.4: winter monsoon; Madhupratap et al. 1996). This convecting mixing brings nutrient-rich seawater from the subsurface depth to the surface, causing an increase in the primary productivity during the winter monsoon (Madhupratap et al., 1996a; Prasanna Kumar et al., 2004a).

The Salinity budget, which is defined as Precipitation + Runoff - Evaporation ($P + R - E$) is negative in the AS; since evaporation dominates over the contributions from both precipitation and runoff (from the continental region). The net effect is that irrespective

of seasons, the AS has high saline water conditions (Govil and Naidu, 2010; Rao et al., 1981; Shetye et al., 1994; Vinayachandran and Kurian, 2008).

One of the critical processes over the ocean is water mass formation (vast water body having a uniform range of temperature, salinity, and associated density) and its movement. Traditionally, the relation between the potential temperature (θ ; °C) and S, along with density (σ_θ ; kg m⁻³) variation is used to characterize ocean water masses (Emery, 2001; Helland-Hansen, 1916). Potential temperature (θ), is conventionally used for water mass identification (rather than *in situ* temperature), to account for the pressure effects. It is the temperature of water parcel (at any depth) that would be measured if the water parcel were brought to the ocean surface without a change in the heat content of the parcel with the surroundings (adiabatically). The density of seawater (sigma theta: σ_θ) is calculated based on the *in situ* salinity and potential temperature. Water masses are identified based on their characteristic ranges in temperature, salinity, and density. Four different water masses have been identified in the AS; namely Bay of Bengal Water mass: BoBW (lower salinity and low density); Arabian Sea High Saline Water mass: ASHSW (T: 28- 24 °C, S: 36.7-35.3, σ_θ : 22.8-24.5 kg m⁻³); Persian Gulf Water mass: PSGW (T: 19-13 °C, S: 37.9- 35.1, σ_θ : 26.2-26.8 kg m⁻³); and the Red Sea Water mass: RSW (T:11-9 °C, S: 35.6-35.1, σ_θ : 27.0-27.4 kg m⁻³) (Emery, 2001; Jain et al., 2017; Kumar and Prasad, 1999a; Rochford, 1964; Shetye et al., 1994; Varadachari et al., 1968a).

Bay of Bengal: The eastern part of the northern Indian Ocean is influenced by numerous river channels, which are fed by the monsoonal and Himalayan glacier rivers (Karim and Veizer, 2002; Lambs et al., 2005; Ramesh and Sarin, 1992). These riverine inputs to the northern BoB make low salinity water on the northern side with an increase in the salinity towards southern BoB with ~ 2 increase per latitude (moving towards equatorward). In addition, direct precipitation also gives a significant amount of freshwater in the Bay. This enormous amount of freshwater through both the rivers and direct rainfall in the BoB makes a well-stratified ocean (Han et al., 2001; Prasad, 1997; Vinayachandran et al., 1999). Due to its strong stratification, the wind-induced

mixing is not strong enough to bring the subsurface water (nutrient-rich) to the surface (Han et al., 2001; Vinayachandran et al., 1999). This makes the BoB a less productive region than the AS; however, strong small scale eddies, dry and cold winter induced vertical mixing can contribute a significant amount of nutrient to the surface during different seasons.

In addition to these physical ocean dynamics, a high number of tropical cyclones are observed in the BoB from October to December every year, with characteristics of deep depression to severe cyclones. The ocean and atmospheric conditions (SST, moisture content, vertical wind shear) over the BoB are well favorable to the cyclogenesis during post-monsoon.

The Andaman Sea: A marginal sea, which is separated from the BoB on the western side by the Andaman & Nicobar Islands; Myanmar and Bangladesh landmasses are on its north and eastern sides and Indonesia on its southern side. The Andaman & Nicobar Islands are distributed between 6° N and 14° N in the northeast Indian Ocean; a channel is known as the ‘10 Degree Channel’, separates these two islands. The Andaman Sea is connected to the BoB through three primary passages, i.e., southern channel (deepest ~ 1500 m water depth), middle channel (10 degree Channel; moderate ~ 700 m water depth) and northern channel (shallow ~ 300 m water depth; Rodolfo 1969; Sikka 1978; Robinson et al. 2007; Chatterjee et al. 2017; Rashid et al. 2019). The average water depth of the Andaman Sea is ~2000 m. The Irrawaddy, Salween rivers, low saline water from the BoB, and direct precipitation influence the salinity budget and stratification over the Andaman Sea (Chatterjee et al., 2017; Rashid et al., 2019).

1.3. Stable Isotopologues and Isotopic Fractionation

Isotopes are the atoms of an element having the same number of protons but different numbers of neutrons; hence, they have different atomic weights. Stable isotopes are non-radioactive forms of these atoms, and the difference in their atomic weights enables them to be used in a wide variety of applications, including hydrological and environmental studies. Naturally occurring stable isotopes in water

and other substances are used to track the origin, history, sources, sinks, and their interactions in water, carbon, and nitrogen cycles. Since measurement of absolute number or abundance of an isotope is practically impossible, the relative abundance of these isotopes (R) is used to monitor changes in various physical and chemical process:

$$R = \text{Abundance of heavier isotope} / \text{Abundance of lighter isotope};$$

Changes in the R with respect to a known standard can be used as a parameter to understand the different physical and chemical processes. Isotopic ratios are reported as deviation (δ ; delta) from an international standard (worldwide accepted standard). International Atomic Energy Agency, Vienna produces, maintains, and provides international standards with known isotopic ratios for a variety of measurements. Different standards are used based on the type of samples and isotopes of interest (explained in detail in Materials and Methods chapter-2).

Stable isotope ratios are expressed by ' δ ' (Delta) notation, for oxygen and carbon isotopes are defined as:

$$\delta^{18}\text{O} = (R_{\text{sample}}/R_{\text{standard}} - 1) \times 1000, \text{ in per mil (\text{‰}) for oxygen isotopes: } R = {}^{18}\text{O}/{}^{16}\text{O}$$

$$\delta^{13}\text{C} = (R_{\text{sample}}/R_{\text{standard}} - 1) \times 1000, \text{ in per mil (\text{‰}) for carbon isotopes: } R = {}^{13}\text{C}/{}^{12}\text{C}$$

For carbonate samples, standard used is the Vienna Pee Dee Belemnite (VPDB), and for water samples, it is the Vienna Standard Mean Ocean Water (VSMOW). Since the variability or deviation observed in the natural processes is quite small (of the orders 10^{-3}) a multiplication factor '1000' is used to report the values in per mil (‰) (Epstein and Mayeda 1953; Craig 1961). The ' δ ' value of a sample specifies a specific ratio of abundances of stable isotopes; another term 'isotope composition' is often used to refer to it.

Isotope fractionation describes various processes that affect and hence change the relative abundance of stable isotopes or *isotopic composition of a particular sample (in any phase)*. For example, various climatic parameters, such as temperature, humidity, and atmospheric circulation, control the ratio of abundances of heavier to the lighter

isotope of oxygen isotope (i.e., $^{18}\text{O}/^{16}\text{O}$) in the rain. The largest change takes place during a phase transition, which modifies δ in both phases significantly, for instance, condensation of vapor mass and evaporation of liquid water.

Equilibrium Fractionation refers to fractionation occurring in reactions if the reactant and the products are allowed to remain in contact for a sufficiently long time to achieve chemical equilibrium; in such cases, the equilibrium between forward and reverse reactions are established, and ' δ ' of reactant and products have unique values. If reactants and products are in contact for a long time, isotopes in the system are distributed in such a way that the total energy of the system is minimized, heavier isotope preferably goes into the compound with strong binding. A similar type of process can happen during phase change, such as condensation of vapor mass, where equilibrium is established between vapor formation and condensation. Equilibrium fractionation occurs when the thermodynamic equilibrium condition is attained, and it is inversely proportional to the temperature. This type of equilibrium is often observed in nature when the process occurs slowly and in a closed system. For example, globally condensation of cloud vapor follows close to equilibrium type process (Dansgaard 1964).

Kinetic fractionation refers to fractionation occurring in reactions or processes where it is partially or fully unidirectional; forward and reverse movements of reactants or products are not balanced, and hence isotopic equilibrium concept is not applicable. The reactants and products are separated before the isotopic equilibrium is reached. Evaporation at the ocean surface is described by the kinetic fractionation process, which occurs due to different diffusion rates of water isotopologues (Craig and Gordon, 1965a; Merlivat and Jouzel, 1979).

1.4. Isotopic fractionation in precipitation (rainwater)

Stable isotopic composition of rainwater is affected by various canonical effects:

- **Amount effect:** Dansgaard (1964) observed that the amount of precipitation and $\delta^{18}\text{O}$ of rain are inversely correlated. Usually, deep convecting clouds are associated with extreme rainfalls, strong updrafts and downdrafts, characterized by rainwater lower in $\delta^{18}\text{O}$ and δD . At an island station, where temperature fluctuations are minor, $\delta^{18}\text{O}$ variability is found to be dependent on rainfall amount with an observed gradient of $\sim -1.5\text{‰}$ per 100 mm increase in the monthly rainfall (Araguás-Araguás et al., 1998a; Dansgaard, 1964; Gat and Gonfiantini, 1981; Yadava and Ramesh, 2005). However, this effect is observed to deviate as we go towards the higher latitude (mid-latitude and above) where temperature plays a vital role than the amount of rainfall.
- **Temperature effect:** The temperature effect is more prominent in high-latitudes than the tropical regions (almost negligible). A linear relationship between the mean annual surface air temperature and the mean annual $\delta^{18}\text{O}$ of precipitation is observed (Figure 1.5). The relationship is based on the Global Network of Isotopes in Precipitation (GNIP) and the mean annual air temperature at each station (Dansgaard, 1964; Rozanski et al., 1993).

The observed relations are:

$$\delta^{18}\text{O} = 0.69 \times T_{\text{annual}} - 13.6$$

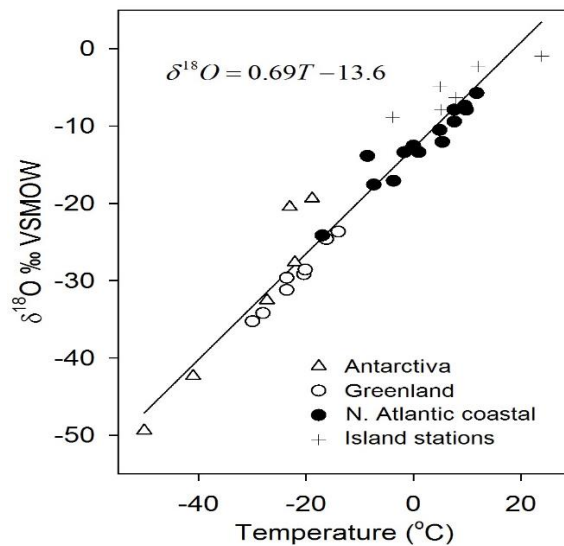


Figure 1.5: $\delta^{18}\text{O}$ of surface water and surface temperature relation (modified from Dansgaard, 1964). Source: Clark and Fritz (2013).

- **Altitude effect:** As temperature drops with elevation, $\delta^{18}\text{O}$ of rainfall is observed to deplete (Figure 1.6) with increasing altitude (Clark and Fritz, 2013). Lowering of temperature favors the conversion of increased fraction of vapor mass into precipitation.

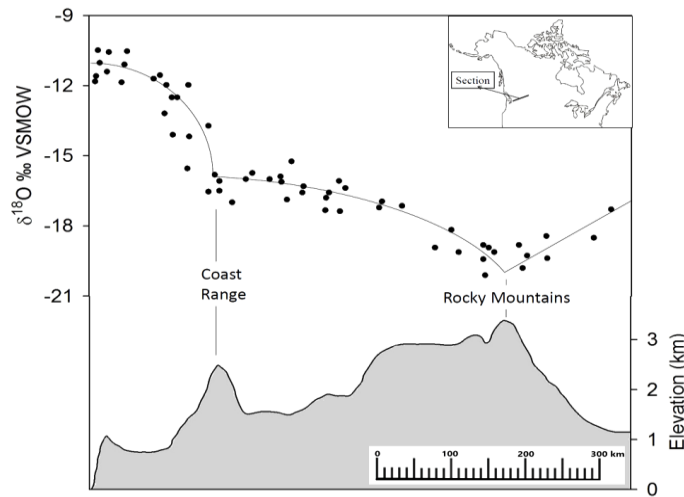


Figure 1.6: $\delta^{18}\text{O}$ of precipitation variability with altitude. Source: Yonge et al., 1989.

Continental effect: As the vapor (moist air) moves away from the source region (ocean) across a continent, its isotopic composition changes more rapidly due to rainout influenced by topography variations and the extreme temperature characterizing the continental climate. The continental temperatures are associated with strong seasonal variation (Clark and Fritz, 2013). Coastal precipitation is associated with enriched rainfall than the central regions, which are associated with depleted rainfall with strong seasonal differences (Rozanski et al., 1993). While moving coast to inland, the rain has successively depleted ' δ ' values. It is called the continental effect.

1.4.1. Rayleigh Fractionation

Rayleigh fractionation model explains the evolution of a system in which multiple phases are associated, and one phase is uninterruptedly removed. It shows that with equilibrium condition attained before removal, the vapor parcel

gets continually depleted in ^{18}O as it rainouts with time (Clark and Fritz, 2013; Rozanski and Sonntag, 1982; Sonntag et al., 1983).

Rayleigh fractional model is expressed mathematically as:

$$R = R_o f^{(\alpha-1)}$$

Where R is the isotopic composition of the changing reservoir, f is the fraction of the remaining in the reservoir, R_o is the initial isotopic composition, and α is the equilibrium isotope fractionation factor ($\alpha_{\text{product-reactant}}$).

For water vapour system, since heavier isotopes (^2H and ^{18}O) always prefer liquid phase, precipitation is enriched in ^2H and ^{18}O , relative to the residual vapor reservoir, the degree of enrichment remains a function of the condensation temperature (Araguás-Araguás et al., 1998a; Gat, 1996; Gat and Gonfiantini, 1981; Rozanski et al., 1993). So, as clouds move across the continent, progressive rain-out results in precipitation successively depleted in ^{18}O .

1.4.2. Global Meteoric Water Line (GMWL)

Global Meteoric Water Line (GMWL) is an average relation between $\delta^{18}\text{O}$ and δD of natural terrestrial surface water, which has not undergone any excessive evaporation (Craig, 1961). The $\delta^{18}\text{O}$ - δD isotopic composition of global precipitation is strongly associated with a slope of 8; this is similar to the ratio of the equilibrium fractionations (at 25°C , Clark and Fritz 2013). However, for a given region this relation is called the Local Meteoric Water Line (LMWL), it includes the effect of local atmospheric circulation, seasonal variation of the moisture sources and variability in the evaporation and precipitation (Araguás-Araguás et al., 1998a; Clark and Fritz, 2013; Rozanski et al., 1993). The kinetic fractionation effect on rainfall over a given region is compared with the known LMWL to decipher precipitation pathways that include the source of moisture, cloud condensation process, and effect of local evaporation. Several kinetic processes can lead to effects that can modify the slope in $\delta\text{D} - \delta^{18}\text{O}$ relation that

may be significantly different from the GMWL and LMWL for a given location.

Since 1961, the Global Network of Isotopes in Precipitation (GNIP; http://www-naweb.iaea.org/napc/ih/IHS_resources_isohis.html) examines and monitors the isotopic composition of precipitation at various sites all over the world. The global precipitation shows a linear relationship:

$$\delta D = 8.17 (\pm 0.07) \times \delta^{18}O + 11.27 (\pm 0.65)$$

For the water which has evaporated or has mixed with the locally evaporated water, the slope of $\delta^{18}O$ - δD plot shifts off the meteoric water line, and intersects the GMWL at the point corresponding to the original un-evaporated composition of the water (Clark and Fritz, 2013; Gat and Gonfiantini, 1981; Merlivat, 1978; Rozanski et al., 1993).

1.5. Stable Isotopes of Hydrogen and Oxygen

1.5.1. Hydrogen Isotopes

Hydrogen has three naturally occurring isotopes; two stable (^1H [99.98%] protium; ^2H [0.02%] deuterium, D) and one radioactive (^3H [trace] tritium, T: half-life of 12.32 years). These isotopes are strongly influenced by kinetic processes that result in a significant fractionation relative to the oxygen isotopes (during precipitation and evaporation) and are highly dependent on relative humidity of the ambient environment (Clark and Fritz, 2013; Craig, 1961; Craig and Gordon, 1965a; Gat and Gonfiantini, 1981; Merlivat and Jouzel, 1979).

Ocean is the largest reservoir of water in the hydrological system. It is the main source of water in vapor, liquid, and solid forms that occur in the atmosphere, on the surface, and below ground level. Well-Mixed ocean water has δD and $\delta^{18}O$ close to 0‰ (the absolute abundance for **VSMOW**: D/H ratio of 0.00015576 (Hagemann et al. 1970); $^{18}\text{O}/^{16}\text{O}$ ratio = 0.0020052 (Baertschi 1976)). However, continuous evaporation, precipitation, and other water mixing processes lead to inhomogeneous mixing and kinetic fractionation processes, and therefore, the isotopic composition of ocean water

and related products change significantly (Gat and Gonfiantini, 1981; Rozanski et al., 1993).

1.5.2. Oxygen Isotopes

Oxygen with an atomic weight very close to 16 is composed of 8 protons, and in its most common form with 8 neutrons (viz. ^{16}O). A small fraction of oxygen atoms (^{18}O) has two extra neutrons hence atomic mass is 18, whereas ^{17}O has one extra neutron having atomic mass 17. The natural abundances of these oxygen isotopes are ^{16}O (98%), ^{17}O (0.02%), and ^{18}O (2%). The ratio of these two oxygen isotopes (heavier to lighter; $^{18}\text{O}/^{16}\text{O}$) in water changes during different physical (evaporation, condensation, mixing of two different composition water bodies) and chemical processes where oxygen is involved, leading to change in the distribution of these isotopes in product and reactant. For example, in the case of evaporation (a physical process), vapor will be concentrated (enriched) more with the lighter isotope (^{16}O) relative to the original water body (Figure 1.7), leaving residual water concentrated more in the heavier isotope (^{18}O). Later, when the vapor parcel starts precipitation, initial condensate (rainwater) will be enriched in ^{18}O with subsequent precipitation depleted in ^{18}O relative to the previous lot (Rayleigh distillation model; Figure 1.7). In precipitation, the spatial pattern of the isotopic ratio arises due to the preferential rainout of isotopically heavier water molecules during condensation (Aggarwal et al., 2012; Noone, 2012; Rozanski et al., 1993).

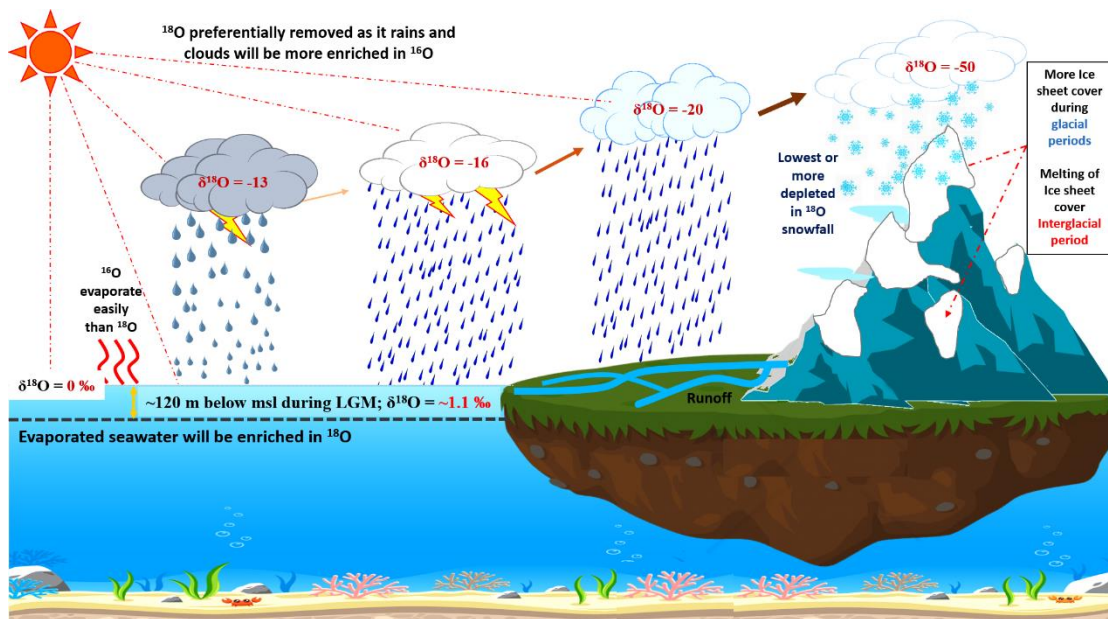


Figure 1.7: Schematic diagram to explain fractionation by Rayleigh distillation model (gradual depletion in ^{18}O) and isotopic effects (local and global). Primary evaporation from the ocean, direct precipitation, and runoff from land to sea refer to the local effects. ^{18}O depleted precipitation (snow; decreased $\delta^{18}\text{O}$) when locked up as ice sheets over the land (polar regions), causes sea-level changes (reduced), and global seawater enrichment in ^{18}O ; this refers to the global effect (occurring on time scales \sim thousands of years or more). Source: adapted from Clark and Fritz (2013).

1.6. Paleoclimate archives and proxies

Paleoclimate proxies are the material properties sensitive to climate change (physical, chemical, or biological) preserved throughout the geological time scales, and hence, these can be used to understand the past climatic condition. These proxy records help us to understand how the Earth's climate system changed over the geological time scales (Smerdon, 2017).

The use of these proxy to reconstruct past climate requires an understanding of how they are related to some aspect of climate systems. For example, some proxies, such as atmospheric gases trapped in glacial ice (e.g., carbon dioxide and methane), provide a relatively direct measurement of atmospheric chemistry at the time the ice formed and was sealed off from the atmosphere. Other proxies are less direct, such as stable isotope measurements (e.g., oxygen and carbon) from shells of marine organisms. These indirect proxies require calibration studies in the modern system to establish the

relationship between climate processes and the proxy. Most of the archives (e.g., speleothem, deep-sea sediment cores, and corals) preserve these isotopic signatures of different climatic conditions during their formations, which can provide valuable information about the past changes in these climate variables (Pearson 2012).

1.6.1. Speleothems

Speleothem is a collective name for various types of deposits found in a cave such as flowstones, soda straw, stalagmites, stalactites; these are formed by drip water (Figure 1.8). Source of the dripping water is the rainwater, surface water, or groundwater that percolates through the soil surface and absorbs carbon dioxide (abundant in the soil, due to respiration and microbial decomposition $p\text{CO}_2$ is high) transforming the water into mild carbonic acid. The weak acid then dissolves small amount of calcium carbonate from the limestone bedrock as it travels through fissures along the pathway until it enters the cave galleries. As the water drips into the cave environment, the dissolved carbon dioxide is released (since it faces low $p\text{CO}_2$), and calcium carbonate is precipitated back as speleothems (Fairchild et al., 2006).

Mineralogy of speleothem is mostly calcite, sometimes aragonite, and rarely mixture of both these. Slight differences in the bedrock composition and dripping patterns result in the creation of speleothems of various shapes and colors and contribute to cave decoration. Another primary method for carbonate deposition is the evaporation of dripping water that may occur when the cave is of small size or has good air circulation.

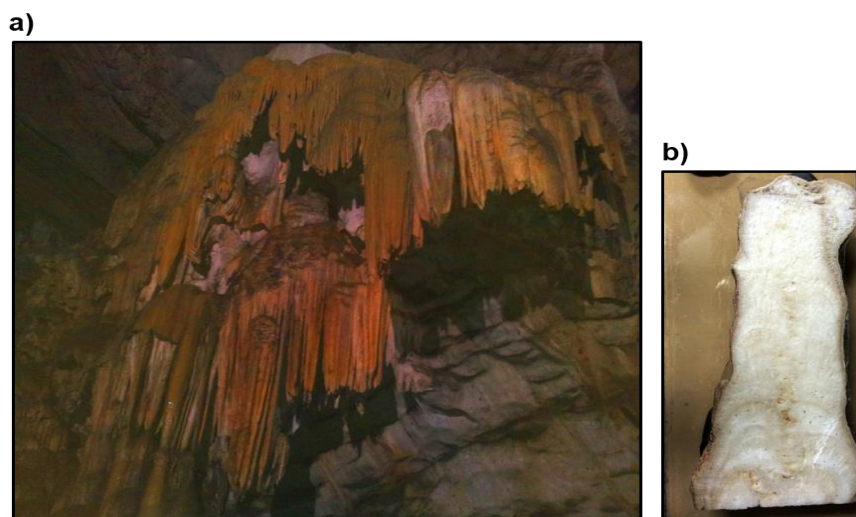


Figure 1.8: A typical speleothem (cave deposits) formation: a) rock bodies hanging on the ceiling (stalactites) of Borra Cave (Andhra Pradesh), b) a cross-sectional view of a stalagmite (that grew the floor towards roof).

1.6.2. Deep-Sea Sediment core & Foraminifera

Deep-sea sediment cores are the best archives for understanding the past oceanographic changes. Sediment cores include organic materials such as pollen grains, diatoms, foraminifera, and inorganic components in the form of various minerals. Based on their limited habitable conditions, geochemical and isotopic signatures of any one of these fractions can serve as a good proxy for paleoenvironmental studies (Emiliani, 1955; Kotthoff et al., 2017; Murray, 2006; Urey, 1947). Significant advantages of studying the deep-sea sediment core are that it will record long-term paleoclimate conditions and remains unaffected by the human disturbances. However, the disadvantage is that the temporal variation recorded have coarse resolution (~ a few hundred years).

Foraminifera is one of the best proxies for the oxygen isotopic analysis to reconstruct paleomonsoon/paleoceanographic conditions (Duplessy et al., 1970; Emiliani, 1955; Pearson, 2012; Urey, 1947). These are unicellular micro-organisms that live in the entire water column, and their shells are made of calcite- CaCO_3 (Anand et al., 2008; Berger and Parker, 1970; Emiliani, 1955; Hemleben et al., 2012; Murray, 2006; Saraswat, 2015; Urey, 1947). Foraminifera is divided into two groups viz., *planktonic* and benthic species. Planktonic foraminifera lives in the surface water column of the

ocean, whereas *benthic* forams live in the bottom water of the ocean (bottom water and sediment interface; Emiliani 1955; Saraswat 2015). Each of the planktonic foraminifera species has different depth habitats, ranging from surface to sub-surface and deep water. During the period of wind-induced upwelling, cold and nutrient-rich water replaces the warm surface water; this is favorable condition for the survival and growth of (sub-polar) planktonic foraminifera species *Globigerina bulloides*; therefore, their abundance increases (Bé and Hutson, 1977; Cullen and Prell, 1984; Curry et al., 1992; Prell, 1981; Zhang, 1985). The planktonic foraminifera *G. bulloides* is a temperate, cold, high nutrient-rich environment favorable condition living species, during upwelling in the tropical, regions, similar conditions persisted and causes their abundances to increase. High abundance of the sub-polar planktonic *G. bulloides* species in low latitudes indicate the monsoon driven upwelling (Curry et al., 1992; Naidu et al., 1992; Prell, 1981). The other important planktonic foraminifera species viz. the *G. ruber*, *G. sacculifer* and *G. menardii* (Figure 1.9) live throughout a year in the surface ocean waters as shown by the studies based on sediment traps (Anand et al., 2008; Guptha et al., 1997).

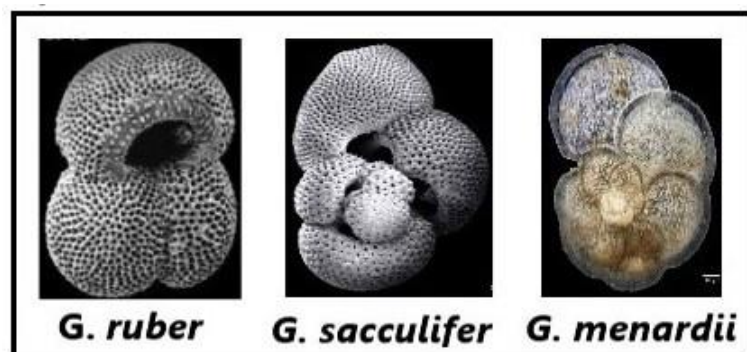


Figure 1.9: Planktonic foraminifera species used for the reconstruction of upper ocean climatic conditions (in this study). Source: <https://www.foraminifera.eu/species>.

Habitat of *G. ruber* species is a warm and oligotrophic condition. It lives near-surface water (at average water depth ~0-25 m) and *G. sacculifer* (water depth 25-50 m), whereas *G. menardii* species live within water depth ~100-200 m, which represents upper thermocline. Both these planktonic species, *G. ruber* and *G. sacculifer*, are

known to live throughout a year (Anand et al., 2008; Guptha et al., 1997). Their characteristic habitat makes these as important species for reconstructing paleoclimate. To infer past climate conditions, in addition to the counting of foraminifera shells for abundance estimation, Urey (1947) used the isotopic composition of foraminifera shells to reconstruct the past temperature.

In seawater, when carbonate precipitates (foraminifera shells, corals, and other forms), calcite is enriched in ^{18}O than the ambient seawater when both compositions are expressed against the same standard reference value (Hillaire-Marcel and Ravelo 2007). However, this fractionation is a function of seawater oxygen isotopic composition and ambient water temperature (Figure 1.10). Oxygen isotopic composition of the seawater can vary with time due to several processes, broadly, (i) global effect and (ii) local effect (Figure 1.7).

Global effect:

During periods of the strong glacial events (cold events), a large amount of ocean water after evaporation (vapor enriched in light isotope: ^{16}O), is precipitated as snow in high latitudinal regions and polar sites; these were locked up as ice sheets over land and cause significant changes in the sea levels and average isotopic composition of the seawater. For example, a reduction of the mean sea level by ~120 m during the Last Glacial Maximum (LGM: ~ 18-24 ka) relative to the present level was observed, and the water that remained in the ocean was enriched in ^{18}O , this is known as ice-volume effect (Shackleton 1967; Fairbanks 1989). The amount of water stored as ice sheets on land influences the average change in the $\delta^{18}\text{O}$ composition of the global ocean on the timescale of the mixing time of the ocean (Shackleton, 1967). During the interglacial periods (warm events), when these ice sheets melted, water with more light isotopes returned back to the ocean and depleted the isotopic composition, close to the present-day level. Due to the ice-volume effect, estimates show that the average change in $\delta^{18}\text{O}$ composition of the ocean water was ~1.1‰ (during LGM, 'δ' value was higher than the present level; Fairbanks 1989; Adkins et al. 2002). This gives a rough estimate as,

0.09 ‰ increase in $\delta^{18}\text{O}$ composition for ~10 m decrease of sea level in the average global ocean, due to glaciation.

Local effect:

The local effect causes frequent and quick changes in the isotopic composition of the seawater, which are due to the ambient temperature variation, river runoff, precipitation, and mixing of water masses having different isotopic composition. During evaporation from the ocean surface, the moisture is depleted in ^{18}O , and hence $\delta^{18}\text{O}$ values of precipitation are depleted in ^{18}O compared with that of seawater (Craig and Gordon, 1965a; Gat and Gouffier, 1981). The evaporation causes salinity of the sea surface water to increase while it decreases with the precipitation or freshwater runoff (Sengupta et al., 2013; Zika et al., 2015).

Salinity (S) and $\delta^{18}\text{O}$ are both influenced by the balance between evaporation and precipitation, they are highly correlated in the surface ocean, and a linear correlation is expected (Bigg and Rohling, 2000; Criss, 1999; Delaygue et al., 2001; Fairbanks, 1989; McConnell et al., 2009). The $\delta^{18}\text{O}$ –S relation derived based on the modern calibration is used for paleo-salinity reconstruction. The relationship between spatial variations in $\delta^{18}\text{O}$ and salinity (gradient in $\delta^{18}\text{O}$ –S relation) for global surface water was observed ~ 0.5‰/1.0 psu (LeGrande and Schmidt, 2006; Schmidt, 1999). However, dominated by the effects of mixing between the local precipitation (freshwater input) and seawater, a significant deviation from this global relationship (gradient) is observed at the regional scale.

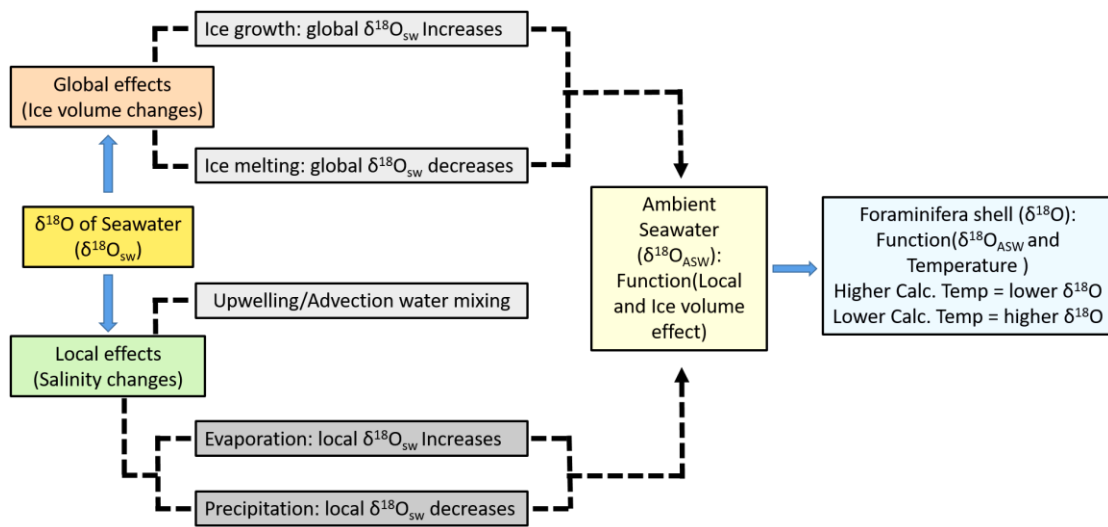


Figure 1.10: Environmental factors that influence the $\delta^{18}\text{O}$ composition of planktonic foraminifera's shells. Source: adapted from Hillaire-Marcel and Ravelo (2007).

During their life cycle, foraminifera- CaCO_3 shells will have the imprints of the ambient water oxygen isotopic composition; while calcifying their shells, they use calcium and bicarbonate ions from the surrounding water (Anand et al., 2008; Emiliani, 1955; Urey, 1947). In many species of foraminifera, calcification process is slow enough, so that condition for equilibrium fractionation is applicable; therefore, oxygen isotopic composition of shell calcite is in isotopic equilibrium with the seawater. In such cases isotopic fractionation between the calcite and the seawater is inversely related to calcification temperature (ambient water temperature). The thermodynamic isotopic fractionation that occurs during calcite precipitation will produce an offset in the $\delta^{18}\text{O}$ of the shell, relative to the seawater $\delta^{18}\text{O}$ values (Delaygue et al., 2001; Duplessy et al., 1970; Emiliani, 1955; Urey, 1947). Based on laboratory experiments for water-carbonate system, temperature dependence is known: $\delta^{18}\text{O}$ of calcite decreases by ~ 0.21 to 0.23 ‰ per unit increase in water temperature (Epstein and Mayeda, 1953; Erez and Luz, 1983; O'Neil et al., 1969). After their life cycle is over, these shells sink to the ocean bottom and get buried in the sediment and remain preserved unless sediments are disturbed later. During their life cycle, changes in the oceanic conditions (such as SST, SSS, river runoff) are reflected in the $\delta^{18}\text{O}$ in the fraction of the carbonate deposited on the growing shells. Therefore, foraminifera- $\delta^{18}\text{O}$ can be used as a proxy

for the reconstruction of ambient water oxygen isotopic composition and water temperature. While interpreting foraminifera- $\delta^{18}\text{O}$ record, apart from the past temperature variability, one must also consider all the other processes which would have modified seawater- $\delta^{18}\text{O}$. Hence, average isotopic composition of foraminifera is a function of the different processes as discussed above.

Several sediment cores, collected from different oceans have been studied so far for $\delta^{18}\text{O}$ in foraminifera. These have shown a consistent pattern in $\delta^{18}\text{O}$ variability, explained to have originated due to large temperature change in the past, and hence, the name is given as glacial and interglacial climate conditions (Emiliani, 1955; Shackleton, 1967). The major variations observed as peaks and troughs, corresponding to the extreme high and low values in $\delta^{18}\text{O}$ values, have ~100 ka periodicity. In the reconstructed data, these are labeled as “Marine Isotope Stages (MIS).” Odd numbers associated with these stages represent interglacial and even number as glacial periods. For example, MIS-1 is the recent interglacial period (15 ka to present), and MIS-2 is the recent glacial period (LGM ~ 24-18 ka).

1.7. Carbon Isotopes

Carbon has three isotopes, two stable (^{12}C and ^{13}C) and one radioactive (^{14}C) with respective abundances: $^{12}\text{C} = 98.89\%$, $^{13}\text{C} = 1.11\%$ and $^{14}\text{C} = 10^{-12}\%$ and this element is the backbone of life on Earth.

The $\delta^{13}\text{C}$ of a foraminifera shell (carbonate) is a function (Figure 1.11) of the carbon isotopic composition of the dissolved inorganic carbon (DIC) in ambient seawater ($\delta^{13}\text{C}_{\text{DIC}}$). However, it is not in isotopic equilibrium with seawater (Broecker and Peng, 1982; Broecker and Maier-Reimer, 1992). The primary reason for its imbalance is due to the fact that because of strong biological (called vital) effects, biogenic calcification is relatively rapid. Furthermore, $\delta^{13}\text{C}_{\text{DIC}}$ in seawater is not uniform throughout the world's ocean, and the average $\delta^{13}\text{C}_{\text{DIC}}$ of the ocean varies with time. Foraminifera specimens having different sizes also show variability in the $\delta^{13}\text{C}$ values. Additionally, $\delta^{13}\text{C}$ is influenced by (i) different vital effects, (ii) fluctuations in the habitat during the

life cycle and/or seasonal variation in marine environmental conditions, (iii) discrepancy in the dissolution of shells depending on the thickness of their walls, (Broecker and Peng, 1982; Broecker and Maier-Reimer, 1992; Ravelo and Fairbanks, 1995). Hence, due to several complex controlling factors that may cause changes in the $\delta^{13}\text{C}$ of foraminifera, interpretation of the $\delta^{13}\text{C}$ variation is not straight forward as it is with the $\delta^{18}\text{O}$ variation.

Besides ocean sediments, corals, tree-rings, and ice-cores are also well-studied important archives, and these are widely used in the paleoclimate reconstructions.

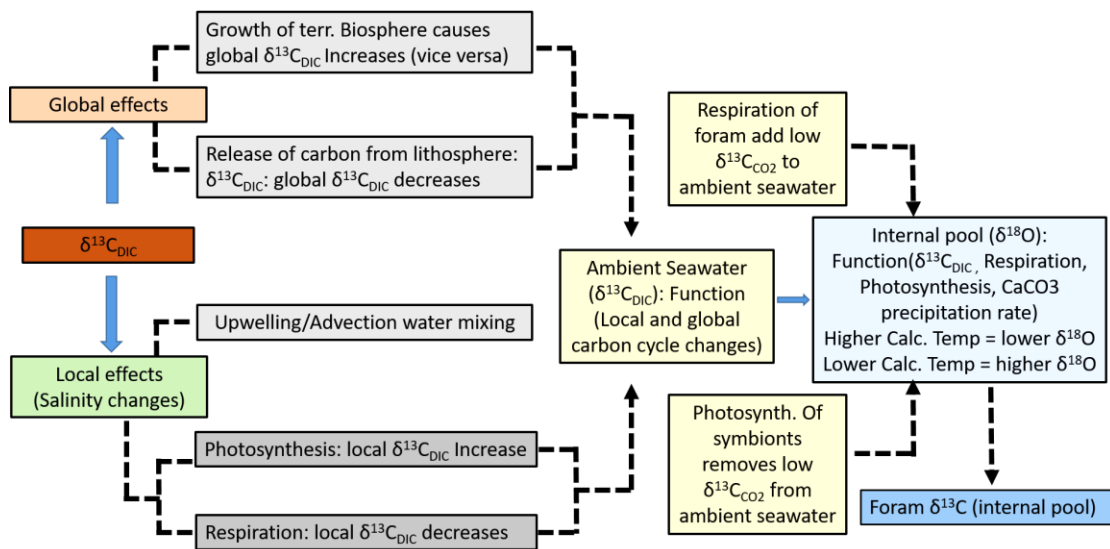


Figure 1.11: The Environmental factors that influence the $\delta^{13}\text{C}$ composition of planktonic foraminifera's shells. Source: adapted from Hillaire-Marcel and Ravelo (2007).

1.8. Bulk sediment $\delta^{15}\text{N}$ and $^{13}\text{C}_{\text{Org}}$

Nitrogen has two stable isotopes ^{14}N and ^{15}N with abundances as 99.64% and 0.36%, respectively. The atmospheric nitrogen (N_2) is very inactive during biological processes. However, it gets into the biological system through photosynthesis by various mediators. Nitrogen is a critical nutrient element in the marine ecosystems, limiting the growth of marine life in most of the oceans (Howarth, 1988; Howarth and Marino, 2006; Vitousek and Howarth, 1991). Atmospheric N_2 gets into the biological system by reduction of N_2 to ammonia through microorganisms (diazotrophs) under

anaerobic conditions. Nitrification is the biological process performed by bacteria where ammonia is converted to nitrate (NO_3^-) or nitrite (NO_2^-). Denitrification is a process where nitrate is reduced to gaseous nitrogen (N_2 or N_2O) species under anaerobic conditions. Oxygen Minimum Zone (OMZ; dissolved oxygen concentration is less than 0.5ml/l) is the permanent anaerobic conditions in the world oceans (Gibson and Atkinson, 2003). The strong OMZ regions in the oceans are associated with surface biological productivity that consumes lot of dissolved oxygen at depths during degradation of the organic material. In OMZ, anaerobic bacteria utilize NO_3^- for the decomposition of organic matter, and this causes significant fractionation in nitrogen isotopic composition of NO_3^- . During denitrification bacteria consumes preferentially lighter isotope ($^{14}\text{NO}_3^-$) and hence enriching the residual NO_3^- in heavier isotope ($^{15}\text{NO}_3^-$). $\delta^{15}\text{N}$ of sediment organic material is a function of isotopic composition of the source of NO_3^- and degree of fractionation during phytoplankton uptake. The higher $\delta^{15}\text{N}$ of bulk sediment suggests stronger denitrification which in turn was controlled by surface productivity (Ganeshram et al., 1995).

Organic carbon (C_{org}) preserved in the sea sediment is originated as particulate organic carbon and is an indicator of the primary productivity at the surface (Schulz et al., 1998). The preservation of C_{org} improves drastically in regions underlying OMZ, with high sedimentation rates and in the regions where reducing conditions prevail at the sediment-water interface (Henrichs, 1992).

1.9. Previous studies from the northern Indian Ocean

A significant amount of work has been done in understanding the northern Indian Ocean dynamics occurring monthly to millennium time scales. Previous studies have identified different water masses over AS observed at the surface to deeper depths (Rochford, 1964; Varadachari et al., 1968; Shetye et al., 1994; Emery, 2001; Prasad et al., 2001; Schott and McCreary Jr, 2001). The density of these water masses increases as depth increases, so shallow water masses are lower in density (mostly have tropical origin), and bottom water mass is higher in density (mostly polar origin). Four different water masses are identified in the AS namely Bay of Bengal Water mass: BoBW;

Arabian Sea High Saline Water mass: ASHSW; Persian Gulf Water mass: PSGW; and the Red Sea Water mass: RSW (Emery, 2001; Jain et al., 2017; Prasad et al., 2001; Rochford, 1964; Shetye et al., 1994; Varadachari et al., 1968a).

Data on seawater isotopic measurements from the northern Indian Ocean are very limited in spatial and temporal scales. Only a few studies have reported oxygen and hydrogen isotopic composition of seawater samples from the Indian Ocean and have contributed to the preliminary understanding of the surface water processes (Achyuthan et al., 2013; Delaygue et al., 2001; Deshpande et al., 2013; Sengupta et al., 2013; Singh et al., 2010; Srivastava et al., 2007; Tiwari et al., 2013). The $\delta^{18}\text{O}$ -S relation is an essential relationship for the paleo-salinity reconstruction. However, these relations vary with seasons and locations (Achyuthan et al., 2013; Delaygue et al., 2001; Deshpande et al., 2013; Sengupta et al., 2013; Singh et al., 2010). $\delta^{18}\text{O}$ value for runoff waters from the Ganga river system (to the BoB) is $\sim -6\text{‰}$ (Achyuthan et al., 2013; Ramesh and Sarin, 1992; Somayajulu et al., 2002). Nonetheless, during strong rainfall, the average $\delta^{18}\text{O}$ value of the runoff may reach as low as $\sim -9\text{‰}$ (Delaygue et al., 2001). During the periods of strong snowmelt from the Himalayan region (source for Himalayan originated rivers), water with much lower isotopic composition is contributed (Karim and Veizer, 2002; Lambs et al., 2005; Ramesh and Sarin, 1992). Rainfall amount over the land and corresponding changes in the slope and intercept of $\delta^{18}\text{O}$ -S relation represent the salinity related amount effect such that ^{18}O -depleted runoff could also result from higher rainfall: (Araguás-Araguás et al., 1998a; Dansgaard, 1964; Singh et al., 2010; Yadava and Ramesh, 2005). Majority of studies on the $\delta^{18}\text{O}$ of seawater variations are mainly restricted to the surface water samples only (Achyuthan et al., 2013; Deshpande et al., 2013; Singh et al., 2010), very few studies have attempted to understand these relations in vertical profile of the northern Indian Ocean (Delaygue et al., 2001; Sengupta et al., 2013; Singh et al., 2010; Srivastava et al., 2007; Tiwari et al., 2015). The $\delta^{18}\text{O}$ variation of natural waters (i.e., precipitation) has been studied since 1960s to infer hydrological processes (Craig, 1961; Craig and Gordon, 1965b; Dansgaard, 1964).

Large amount of work has been done in reconstructing the paleoceanography and paleoclimate from the northern Indian Ocean based on the deep-sea sediment cores: from the AS (Banakar et al., 2010; Gupta et al., 2003; Kessarkar et al., 2013; Saraswat et al., 2016, 2013; Sarkar et al., 2000, 1990; Singh et al., 2006, 2016), from BoB (Ahmad et al., 2005; Kudrass, 2001; Rashid et al., 2011) and the Andaman Sea (Rashid et al. 2007; Sijinkumar et al. 2010, 2016; Raza et al. 2014, 2017; Ali et al. 2015; Gebregiorgis et al. 2016). These studies have addressed monsoon variability over the long time span, from glacial to interglacial periods. Duplessy (1982) showed that monsoon was weaker during the LGM. Sarkar et al. (1990) have shown that during LGM, the winter monsoon was stronger than the summer monsoon. In addition to the long term glacial and inter-glacial global climate variability, a short term intense warm and cold periods were observed within the interglacials (example during MIS-3). Significant strong short term cold and warm events during the MIS-3 and MIS-2 were identified as Heinrich Events and Dansgaard-Oeschger Events, respectively (Dansgaard et al., 1982; Heinrich, 1988; Stocker, 1999). DO events were usually associated with rapid warming of Greenland, by 5 - 10 °C, within a few decades or less than that (most often 1500 years cycle, but not always), followed by gradual cooling over several hundred to thousand years (Bond et al., 1993; Dansgaard et al., 1982). Heinrich events were sporadic and distinct events associated with ice-rafted debris in the North Atlantic, which is associated with cooling events in the Northern Hemisphere (Heinrich, 1988). These global cold (warm) events were associated with weak (strong) monsoon over the Indian subcontinent (Deplazes et al., 2014; Jin et al., 2007; Kudrass, 2001; McGee et al., 2018; Pausata et al., 2011).

Only a few studies have tried to reconstruct the past variation in the thermocline depth (Gebregiorgis et al., 2016; Singh et al., 2016). Some studies based on the abundance of different species of planktonic foraminifera have been carried out over the northern Indian Ocean to reconstruct the paleoceanographic conditions (Gupta et al. 2003; Ishikawa and Oda 2007; Munz et al. 2015; Singh 2016; Singh et al. 2016; Verma et al. 2018).

Instrumental and high-resolution proxy records have shown intra-seasonal to intra-annual scale variability in the Indian monsoon systems. These variations are associated with various ocean-atmospheric coupled processes. Mainly the El-Niño Southern Oscillation (ENSO), Indian Ocean Dipole (IOD), Madden Julian Oscillation (MJO) and Pacific Decadal Oscillation (PDO) are the strong influencing processes on ISM (Ashok and Saji, 2007; Gadgil, 2007; Joseph et al., 2009; Ju and Slingo, 1995; Kumar et al., 1999). ENSO events are associated with a shift in the low-level convergence of surface winds from the western Pacific (normal condition) to the central or towards more eastern Pacific Ocean (abnormal condition). This shifting causes the low-level divergence of surface winds over most parts of the Indian subcontinent and other regions (Indonesia Australia and Southeast Asia), which is further associated with weaker ISM. Previous studies have shown the weakening trends of ISM over the Indian subcontinent in response to El-Niño variability (Ashok et al., 2007; Kumar et al., 2006; Mishra et al., 2012; Sulochana and Francis, 2016), however, some studies have shown the weakened influence of ENSO on ISM (Horii et al., 2012; Kawamura et al., 2005; Krishnamurthy and Kirtman, 2003; Kumar et al., 1999; Sarkar et al., 2004). Indian Ocean Dipole (IOD) is a dipole variability in the sea surface temperature over the eastern and western Indian Ocean, the positive IOD (lower SST anomaly over the eastern Indian Ocean) causes the significantly higher rainfall over the Indian subcontinent, lower rainfall during negative IOD (higher SST over eastern Indian Ocean; Gadgil, 2003). Madden Julian Oscillation (MJO) is 30-60 days cycle associated with eastward-moving deep convecting clouds with average speed of 5 m/s (Madden and Julian, 1972). During the course of these events clouds pass through the Indian Ocean causing significant amount of rain over the subcontinent. Previous studies have shown the active and break monsoon periods are associated with the eastward-moving deep convective clouds of the MJO cycle (Rajeevan et al., 2010; Singh and Bhatla, 2019).

1.10 Scope of the present work

$\delta^{18}\text{O}$ -S relation in modern seawater is one of the best tools for predicting and understanding the past variability in the oceanic conditions over the Indian Ocean. Results available so far on $\delta^{18}\text{O}$ -S relations are mostly based on studies that are limited in sampling and also have poor spatial and temporal coverage (Achyuthan et al., 2013; Deshpande et al., 2013; Duplessy, 1982; Singh et al., 2010; Srivastava et al., 2007; Tiwari et al., 2015). To establish $\delta^{18}\text{O}$ -S relations, it requires new efforts using a large number of seawater samples; it will provide a better understanding of the signatures of the high-resolution variability (in time and space both) of monsoon over the Indian Ocean. Most of the previous studies on $\delta^{18}\text{O}$ -S calibration were based on the limited number of water samples, which were collected during single cruise or a season. Some of the earlier results have shown that monsoon has weakened from the early Holocene to the present (Fleitmann et al., 2003; Gupta et al., 2003), however, contrary to it, few others have reported strengthening of the monsoon for the same time period (Kudrass, 2001; Saraswat et al., 2013; Sarkar et al., 2000). These contradictory inferences on Indian monsoon variability need to be understood at the regional to the subcontinental scale. Except few studies, in most of the earlier work, sampling was confined to the shallow water levels (up to 50 m); however, it may not represent the deepwater $\delta^{18}\text{O}$ and δD signatures which maybe just different (Sengupta et al., 2013; Singh et al., 2010; Srivastava et al., 2007; Tiwari et al., 2015). This prompts a need to understand the present $\delta^{18}\text{O}$ and δD variability with depth, and representative $\delta^{18}\text{O}$ -S relations and regional differences among these relations. If found to vary with depth, then it becomes essential to understand different processes and factors causing those variabilities and its implication for the paleoclimate reconstructions.

Very few studies have reported changes in the surface ocean dynamics in the Indian Ocean based on $\delta^{18}\text{O}$ of planktonic foraminifera (Da Silva et al., 2017; Sijinkumar et al., 2016; Singh et al., 2016). Reconstruction of the upper ocean dynamics and its understanding is essential for prediction of the effects, quantitatively, induced by global climate change in the future. In addition to the long-term (a few thousands of years) variations, it has been well established that the coupled ocean-atmospheric processes

occurring at shorter time scales also affect Indian monsoon significantly (Ashok et al., 2004; As-syakur et al., 2014; Gadgil, 2007; Gadgil and Gadgil, 2006; Joseph et al., 2009; Rajeevan et al., 2012). The ability in monsoon prediction (days to seasons) by the dynamical and complex models remains low, partly due to lack of our complete understanding of the monsoon system and our inability to model the interactive processes that govern it (Wang et al., 2015). Dynamics of the Indian monsoon system over spatial and temporal scales need to be studied in response to different ocean-atmospheric coupled processes, and they are required to be tested against high-resolution paleoclimate reconstruction from terrestrial and ocean-based archives.

Based on the knowledge gaps in the current understanding of the stable isotopic composition of the modern seawater and paleoclimate reconstruction of monsoon and surface ocean dynamics, three broad objectives were aimed.

Broad Objectives:

- ❖ Paleomonsoon reconstruction based on sedimentary records of the Indian Ocean.
- ❖ Understanding $\delta^{18}\text{O}$ and δD variations in the modern water over the Indian Ocean.
- ❖ Spatio-temporal variability of the Indian monsoon with respect to the coupled ocean-atmospheric processes.

Specific Objectives:

- Spatial and temporal variations of $\delta^{18}\text{O}$ and δD in the surface water of the northern Indian Ocean.
- Quantifying effects of surface current, precipitation and river runoff on isotopic variations in the surface seawater of the Indian Ocean.
- Studying sediment core from various locations of the Indian Ocean for a better understanding of the past spatial variability in the upper oceanic conditions.
- Paleomonsoon reconstruction based on oxygen isotopic variations in foraminifera.

- Reconstruction of past upper-ocean water conditions based on the depth habitat of foraminifera.
- Synthesis of already available multiple data sets to get a comprehensive picture of monsoon variability over the Indian subcontinent.

1.11. Outline of the Thesis

- ***Chapter-1: Introduction:***

This chapter gives a brief introduction of the contemporary Indian oceanography conditions, general aspects of stable isotopes, and the concept of isotope fractionation. A summary of previously published work on $\delta^{18}\text{O}$ variation in deep-sea sediment cores and reconstruction of summer monsoon variability is also presented. Broad and specific objectives of the thesis are included.

- ***Chapter-2: Materials and Methods:***

In this chapter, details on study areas and sampling locations are discussed. Analytical techniques and methods for measuring the stable isotopic composition of various materials (seawater, carbonates, and bulk sediment) are presented. Many types of data used in this thesis work are also described. This chapter also briefly addresses the radiocarbon measurement technique.

- ***Chapter-3 Seawater $\delta^{18}\text{O}$ and δD dynamics in the northern Indian Ocean:***

This chapter discusses the current stable isotope systematics ($\delta^{18}\text{O}$ and δD) of the north Indian Ocean and the effect of the monsoon on stable isotopic compositions. Variability on spatial, vertical, and temporal scales in $\delta^{18}\text{O}$ and δD values and their implications on the interpretation of the reconstructed data is also presented.

- ***Chapter-4 Paleoceanography and paleoclimatology of the northern Indian Ocean:***

Monsoon reconstructed based on the analysis of three deep-sea sediment cores, and a new approach to interpreting past upper-ocean conditions are presented in this chapter.

- ***Chapter-5: ISM variability and teleconnection with Global processes: understanding from instrumental and paleoclimate data***

Indian monsoon and its spatial and temporal distribution in the modern context are discussed. Variability in response to the coupled ocean-atmospheric processes and its implications in interpreting reconstructed data is discussed.

- ***Chapter-6: Synthesis and scope for Future work***

This chapter highlights the significant results of this thesis work. Insight into future potential research aspects is presented.

Chapter-2
Materials and Methods

Material and Methods

The core objective of this thesis work is to understand the present and past-monsoon variability using stable isotopes in the modern seawater, and carbonate samples of deep-sea sediment cores from the northern Indian Ocean. Following sections of this chapter will discuss the sampling and measurement techniques:

2.1 Sample collections for this work

2.1.1 Seawater samples

A large number of seawater samples ($n = 453$ samples) from the surface and subsurface layers were collected from the northern Indian Ocean to understand stable isotope

composition and their relation with the monsoon variability in the modern period (Figure 2.1). The sub-surface water samples (up to 1000 m) were collected during two different cruises (SK-355 and SK-359, respectively) over the northern Indian Ocean.

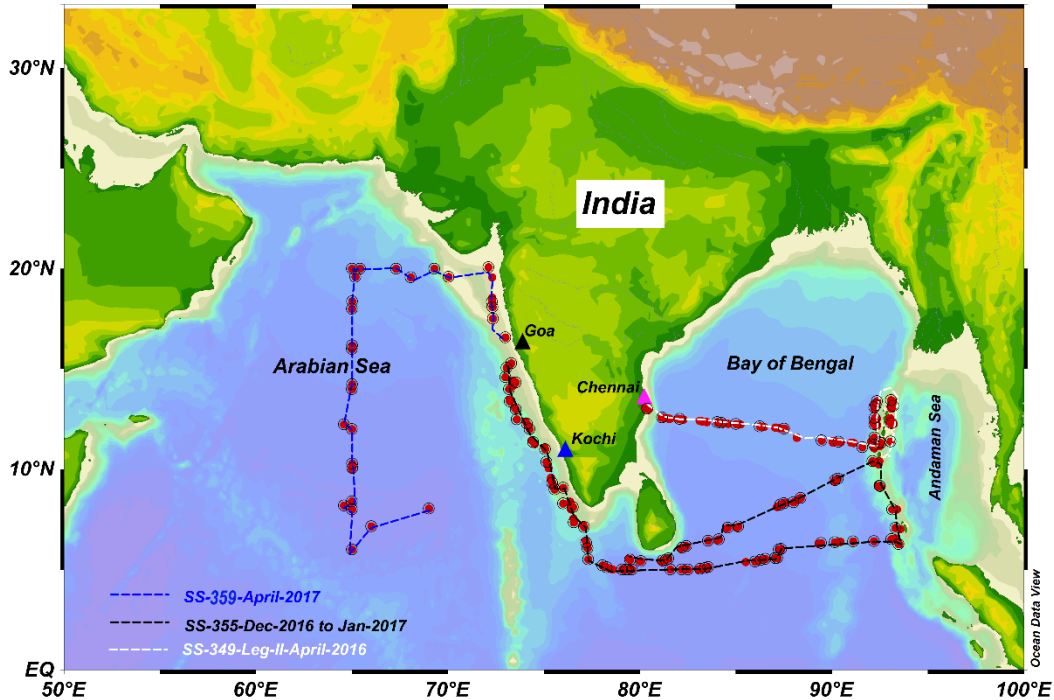


Figure 2.1: Location of surface and subsurface seawater samples collected during three different research cruises. Sagar Sampada: SS-349-Leg-II (April-2016); SS-355 (December-2016 to January-2017) and SS-359 (April-2017).

For understanding a high-resolution spatial variability of different processes, we have divided the northern Indian Ocean into three regions: the Arabian Sea (45° - 78° E/ 5° - 25° N), Bay of Bengal (5° N- 22° N/ 78° - 92° E) and the Andaman Sea (92° E- 100° E/ 5° N- 20° N). A total of 330 surface water samples (depth \leq 1m), and 140 subsurface water samples were collected during April-2016, December-2016 to January-2017 and during April-2017 (Figure 2.1) onboard FORV *Sagar Sampada* (Figure 2.2) cruises SS-349-Leg-II, SS-355, and SS-359, respectively from the northern Indian Ocean.



Figure 2.2: All the water samples were collected onboard FORV *Sagar Sampada*.

Surface water samples were collected using a bucket thermometer sampler (Figure 2.3b). A thermometer is mounted inside it for measuring the water sample temperature. The container to collect seawater samples is made of oil-proof rubber barrel, so occasional collisions against the side of the ship are damped. Subsurface water samples were collected using conductivity-temperature-depth (CTD) rosette (Figure 2.3a) at specific depths (from the surface to about 1000 m water depth) over the Arabian Sea and off the Andaman Islands. Onboard FORV *Sagar Sampada* (SS), a CTD rosette fitted with twelve Niskin bottles (10L capacity each) are available. The rosette is tied with a strong iron cable attached to a winch on board that can be dropped up to ~3000 m. Temperature of the subsurface samples was measured by sensors mounted on rosette sampler (temperature, salinity, depth, fluorescence, dissolved oxygen, and Photosynthetically Active Radiation: PAR).

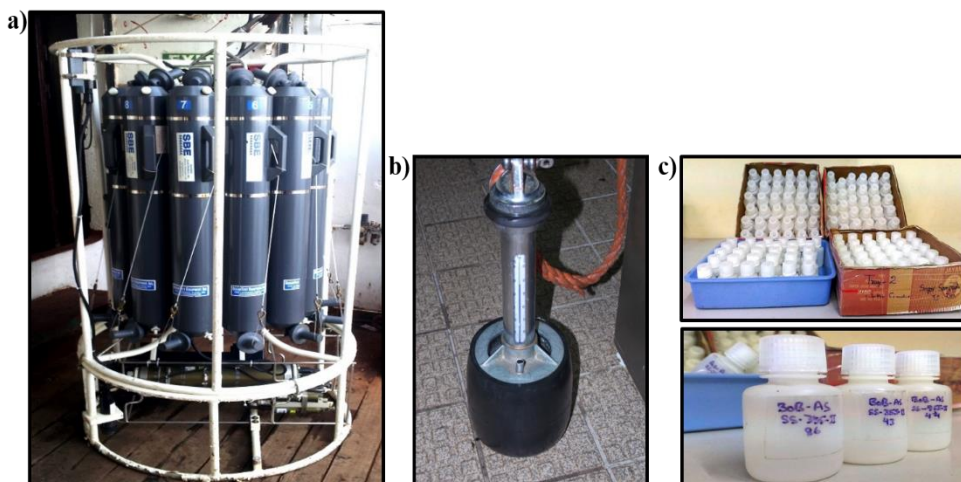


Figure 2.3: a) CTD rosette used for collecting seawater samples at specific water depths b) bucket thermometer instrument was used to collect surface water samples all along the cruise track c) collected seawater samples were preserved in the narrow neck airtight TARSON® bottles (15 ml).

All the surface and subsurface seawater samples collected were divided into two aliquots and then transferred into clean and dry narrow-neck and air-tight bottles (TARSON®, 15 ml volume, Figure 2.3c). These bottles were filled until they started overflowing, to avoid air bubbles in these. One aliquot of each sample was tightly closed and wrapped with the Teflon tape to avoid any loss of water through evaporation and stored in the sample repository maintained at 24 ± 1 °C for isotopic analysis at a later stage. The other aliquots were used for on-board salinity measurements using Auto Salinometer.

The Auto Salinometer (AutoSal®) is an instrument that measures the salinity of seawater based on the conductivity ratios and provides highly reproducible results (± 0.001 , Figure 2.4a). It has a unique continuous flow system where the seawater sample is extracted from the sample bottle at low air pressure. The flow system is maintained at a stable temperature by a heated water bath; the water flow rate and bath temperature can be set manually. Before measuring salinity of the seawater sample, the flow system is rinsed twice with the same seawater sample to avoid the contamination of the previous sample (or memory effect). Each sample takes about less than 1 min for a

single measurement; all samples were measured thrice, and the mean value was taken as the final estimate of the analysis (standard deviation $\sim \pm 0.001$). A very small quantity of sample was required for all the measurements (~ 0.5 - 0.8 ml). The values of the bath temperature, conductivity ratio, and corresponding salinity were displayed on the machine.

International Association for the Physical Sciences of the Ocean (IAPSO) has recognized seawater with salinity 34.995 and conductivity ratio (K_{15}) 0.99987 as an international standard (Figure 2.4b). This standard was used to check the accuracy of the estimated salinity during measurements (Figure 2.4b; Srivastava et al. 2007).

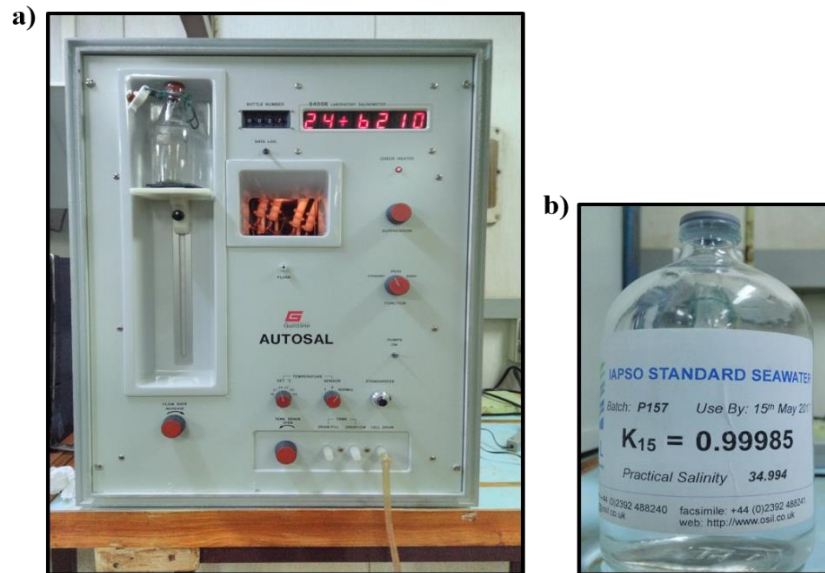


Figure 2.4: a) Salinometer (AutoSal) onboard *Sagar Sampada* used for salinity measurements of the collection surface and subsurface seawater samples. b) IAPSO standard seawater salinity standard used for calibration of Auto-SAL.

2.1.2. Deep-sea sediment cores

Three sediment core samples from the northern Indian Ocean (Table.2.1) were studied in this thesis work: 1) from the Andaman Sea (SK-234-60), 2) from the northern equatorial Indian Ocean off Tuticorin (SK-151-A/3) and 3) from the western BoB off Krishna river basin (SK-336-GC-I).

(i) A ~4 m long sediment core sample SK-234-60 (from the Andaman Sea) was studied for understanding the paleomonsoon and upper oceanic conditions variability based on the $\delta^{18}\text{O}$ of shells of planktonic foraminifera species (Awasthi et al., 2014).

(ii) The ~6 m long sediment core SK-151-A/3 was collected from the equatorial Indian Ocean (off Tuticorin) during *ORV Sagar Kanya* 151 expedition in March-2000. The sediment core was subsampled at 2 cm interval in the upper 100 cm section, after that at 4 cm interval till 6.07 m at the base. Top 15 cm of the core was lost during the time of the core recovery process at the deck of the ship.

(iii) The sediment core SK-336-GC-I was collected from the western Bay of Bengal (off Krishna river basin) during *ORV Sagar Kanya* 336 expedition in December 2016. This 4.85 m long sediment core was subsampled at 5 cm interval along the entire length of the core. The top portion of the core is observed to be dominantly clay /mud, while after 50 cm, it is semi-solid or paste-like in nature. From top towards the bottom, color changes as: for 0-60 cm, greyish brown; for 0-100 cm, light gray; for 100-485cm, blackish gray. Top part in this core was intact, and hence the modern sediment material could be analyzed.

Table 2.1: Details of the three sediment cores studied in this work.

S.No	Sample	Latitude (°N)	Longitude (°E)	Water depth	Core length
1.	SK-234-60 (the Andaman Sea)	12° 05' 46"	94° 05' 18"	2000 m	4.00 m
2.	SK-151-A/3 (equatorial Indian Ocean)	08° 49' 70"	78° 51' 30"	440 m	6.07 m

3.	SK-336-GC-I (the Bay of Bengal)	15° 32'36"	81° 34'93"	2030 m	4.85 m
----	--	------------	------------	--------	--------

2.2. Methods to separate foraminifera species

Separation of planktonic and benthic foraminifera species was done from 5-10 g of sediment sample taken from each slice. Each sample was soaked in a solution for the overnight period (6-7 hrs); prepared using Milli-Q water, sodium hexametaphosphate, sodium hydroxide pellets in which 3-4 drops of hydrogen peroxide (H₂O₂ ~30%) were added for removing the clay particles. The soaked sediment was transferred to a sieve of 63µm size, and wet sieving was done with a continuous flow of Milli-Q water. Sieved samples were then transferred to a clean beaker, and after 10-15min of ultrasonication, these were kept in an oven at 60 °C for drying for an overnight period. The dried samples were further sieved (dry sieving) through a 250 µm size sieve. Later, identification and picking of the planktonic and benthic foraminifera species in the lot (greater than 250 µm sizes) were carried out under *zoom type stereo-microscope*; these were used for the isotopic analysis (Figure 2.5a).

Two species of planktonic foraminifera (*Globigerina ruber* and *Globorotalia menardii*) were separated for oxygen and carbon isotopic analysis (Figure 2.5b; Table. 2.2).

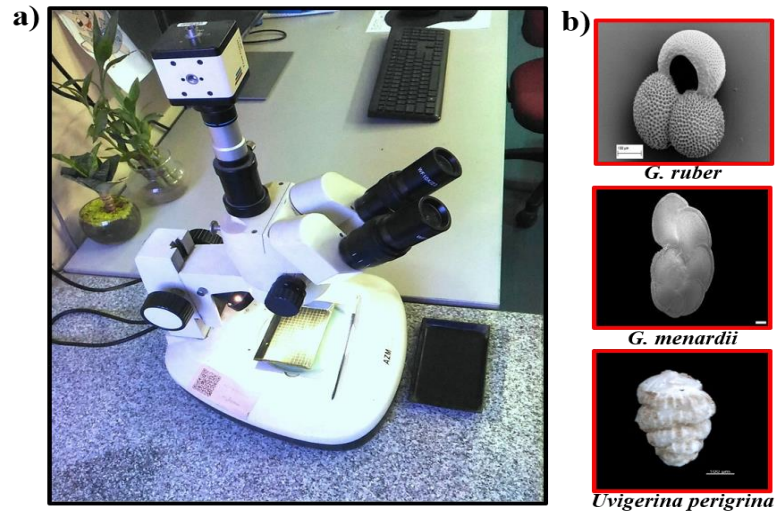


Figure 2.5: a) Stereo-zoom microscope (model no: LABOVISION-AZM 100) used for separating planktonic and benthic foraminifera b) Two different planktonic foraminifera species and one benthic (Source: <https://www.foraminifera.eu/singleca/>) separated from the sediment cores.

Table 2.2: The foraminifera species separated from the two sediment cores and used for the isotopic analysis in this study.

S.No	Sample	Planktonic	Benthic
1.	SK-151-A/3	<i>G. ruber, G. menardii</i>	<i>Uvigerina perigrina</i>
2.	SK-234-60	<i>G. ruber, G. sacculifer, G. menardii</i>	<i>none</i>

Additionally, a benthic foraminifera species (*Uvigerina perigrina*; Figure 2.5b) was also separated; it is an infaunal species that live at the interface of the seawater-sediment surface at the ocean bed. During their life cycle, these secrete calcium carbonate by taking dissolved ions from the ambient seawater and form a shell around their body, the isotopic composition of a shell can be used to infer the seawater temperature conditions during the past (when it was formed).

2.3. Instruments to measure stable isotope ratios

2.3.1. The isotope ratio mass spectrometer (IRMS)

Isotope ratio mass spectrometry (IRMS) is a widely used technique in various disciplines where a change in the composition of stable isotopes has significant application. Ratio of stable isotopes in different samples (seawater, rainwater, bulk sediments, and carbonates) were measured in the IRMS having a gas type source. IRMS instrument works on the principle of detection of mass to charge ratio, as shown in a schematic diagram (Figure 2.6a). A mass spectrometer has three main components: 1) source, where a sample is ionized, 2) analyzer, which separates different isotopologues usually by a strong magnetic field, and 3) detector, where isotope ratios are measured. Faraday cups are the commonly used detectors in most of the modern IRMS. IRMS can accurately and precisely measure ratios of abundances of different isotopologues, and hence isotopic ratios of elements C, O, and H, which are $^{13}\text{C}/^{12}\text{C}$, $^{18}\text{O}/^{16}\text{O}$, and $\text{D}/^1\text{H}$ are routinely measured by such machines. Ratios of these isotopes are reported relative to international standards.

Ion Source:

The sample for which isotope ratio is to be measured is converted into suitable gas first (e.g., in CO_2 form for $^{13}\text{C}/^{12}\text{C}$, $^{18}\text{O}/^{16}\text{O}$ measurements, and in H_2 form for $\text{D}/^1\text{H}$ measurements). Ion source consists of a chamber, where a thorium coated tungsten resistance emits electron as it is heated when about 1.5 A current is passed through it. Emitted electrons collide with the sample gas (CO_2 or H_2) and ionize them with high efficiency. In order to increase ionization efficiency, the magnetic field is applied to make the path of the electrons as a spiral. Positively ionized gas molecules (singly charged) are then accelerated by high voltage (~2.5 kV) potential difference applied between the source and analyzer. Later, the positive ion beam is focused using collimating plates into the analyzer.

A molecule with charge (q) under accelerating voltage (V) gains kinetic energy:

$$qV = \frac{1}{2} mv^2 \text{ ----- (1)}$$

(m= mass of the molecule and v= velocity with which it leaves the source chamber)

Analyser (magnetic Chamber):

When a charged molecules of (CO₂, H₂) in the form of a single charged positive ions enter into the magnetic chamber, it will be separated based on the mass to charge ratio. In the case of CO₂ ions, three dominant beams with masses 44, 45, and 46 amu (atomic mass unit, corresponding to mainly ¹²C¹⁶O₂, ¹³C¹⁶O₂, and ¹²C¹⁶O¹⁸O) are produced. These ions follow curvilinear paths owing to the Lorentz force. This force is balanced by the centripetal force on the ion beam entering perpendicular to the direction of the magnetic field (B):

$$q (v \times B) = mv^2/r \text{ ----- (2)}$$

Using equations 1 & 2:

$$r^2 = [(2Vm) / (B^2q)] \text{ ----- (3)}$$

The radius of curvature (r) of the singly charged ion is directly proportional to the square root of its mass (Eqn-3) when all other (V, B, and q) are constant (Faure, 1977; Potts, 2012). The ions with more mass (¹²C¹⁶O¹⁸O = 46) are detected into a path of a higher radius of curvature compared to that of the lighter mass (¹²C¹⁶O₂ = 44).

Detector:

The currents generated due to ion beams are measured using Faraday cups (detectors), which are connected to very high resistances (~ 10⁹ Ω). Faraday cups are metal cups where ions collide inside and give up their positive charges and kinetic energies, and become neutral. This produces currents that are passed through the external high resistance resistors. In IRMS, the voltage across the resistance produced by ions is measured. This is proportional to the number of ions entering into the Faraday cup (detector) per unit time.

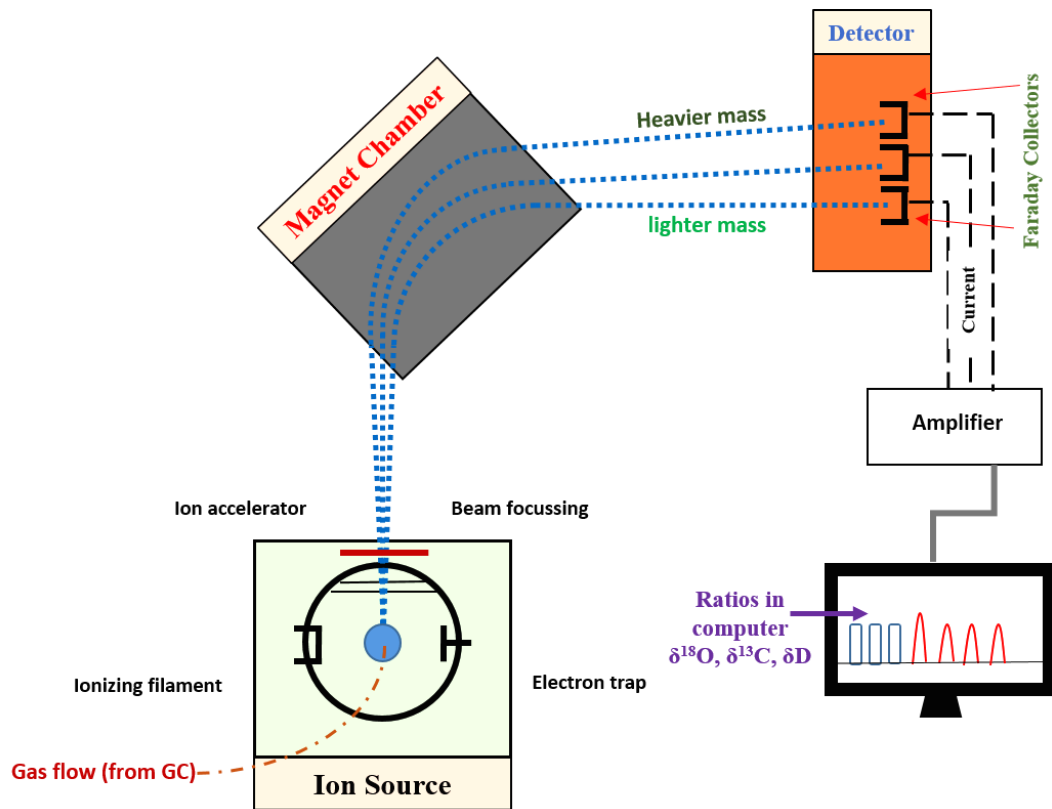


Figure 2.6a: Schematic diagram of the isotope ratio mass spectrometer (IRMS). Source: (Clark and Fritz, 1997).



Figure 2.6b: Delta-V plus IRMS aided with a Gasbench at Physical Research Laboratory, Ahmedabad.

Based on the sample type and the isotopes of interest, different peripherals are connected to the IRMS (Figure 2.6b), for example, *Elemental Analyzer* for organic carbon and nitrogen isotope ratio measurements and *Gasbench* for oxygen, carbon, and hydrogen isotope ratio measurements in carbonate and water samples (Figure 2.7).

2.3.2 External peripherals

(A) *Gas bench*: is an external peripheral connected to the IRMS to inject sample- CO₂ for measuring $\delta^{18}\text{O}$ in water samples and $\delta^{18}\text{O}$ and $\delta^{13}\text{C}$ in carbonate samples, and to inject sample-H₂ to measure δD in water samples (Figure 2.7a). The preparation method for water and carbonate samples is different. There are two main sections in a Gasbench:

(i) *A sample introduction system (sample tray):*

The sample tray is a container where samples for analysis are kept; a total of 88 samples can be mounted, which can be measured in one single batch run. Depending upon the sample type (water or carbonate), temperature of the sample tray is adjusted. For water samples, the tray temperature is fixed at 24 (± 0.5) °C (room temperature) to avoid samples, evaporation during measurements. Similarly, for carbonate samples, tray temperature is fixed at 72 (± 0.5) °C.

(ii) *Gasbench (GC column):*

The gas released or equilibrated with the sample is transferred to the Gasbench (discussed in section 2.4.1). However, the released or equilibrated gas might also contain the water vapor along with the gas. This water is removed by the transfer of sample stream by a gastight but hygroscopic Nafion® tubing. A resulting dry gas (such as CO₂ + He; H + He) flow toward the Valco loop and then is transferred to the Gas-chromatograph (GC) column. GC column separates different gas compounds released from the sample loop, e.g., N₂, H₂,

and CO₂. The compounds eluting from the GC column are transferred through the Nafion® guard trap via open split into IRMS.

(B) Elemental Analyser (EA):

Ratio of stable isotopes of Nitrogen ($\delta^{15}\text{N}$) and carbon ($\delta^{13}\text{C}_{\text{org}}$) in organic material are measured using Elemental analyzer with an interface Conflo VI to Delta V plus IRMS (Figure 2.7b). Sample packed in the ultraclean tin capsule is injected into a high temperature (1020°C) furnace and combusted in pure oxygen under inert conditions. The released gases are passes through specialized reagents (chromium oxide, silver cobaltous oxide) to produce carbon dioxide (CO₂), water (H₂O), and Nitrogen (N₂) and oxides of nitrogen (NO_x). These gases are further passed to the reduction column (contains copper granules) with the help of helium gas (carrier gas), where oxides of nitrogen are reduced to N₂. The final output will be the mixture of N₂, CO₂, and H₂O; later, moisture is trapped by the magnesium perchlorate column. The gas mixture (N₂, CO₂) was then passed through GC column, where each gas was separated based on their properties and retention time. The separated gas was later introduced in the Delta-V plus IRMS through Conflo VI, and finally, the isotopic ratios of nitrogen and carbon in the samples are measured.

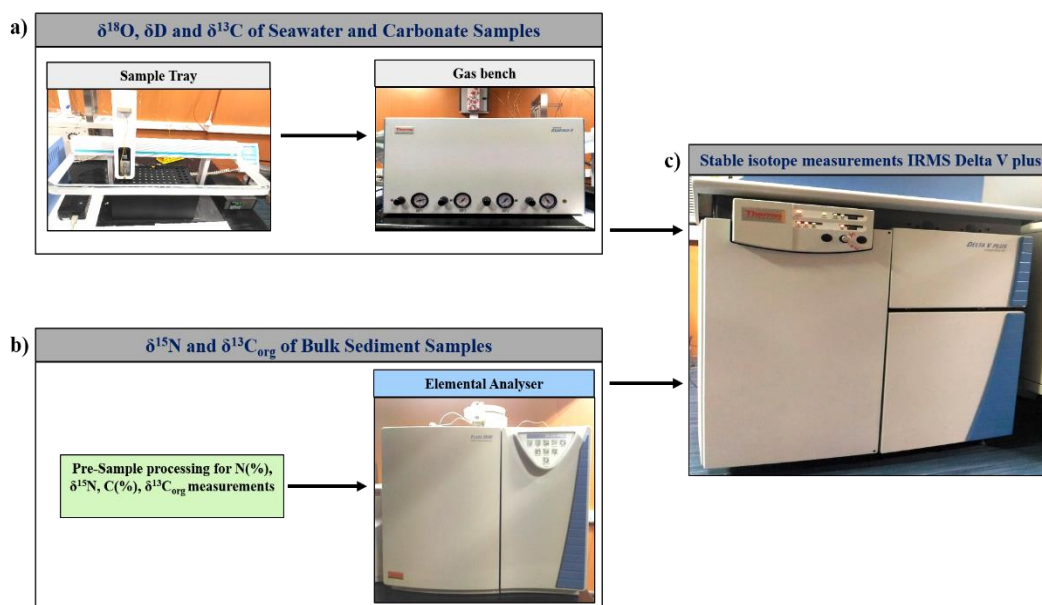


Figure 2.7: External peripherals of IRMS a) sample tray and Gasbench b) Elemental Analyser. c) Delta V plus-IRMS.

2.4. Stable Isotope ratio measurements and techniques

2.4.1. δ¹⁸O and δD measurements for seawater samples: equilibration method

Oxygen (δ¹⁸O) and hydrogen (δD) isotope ratios measurements of water samples collected during different cruises were done at Physical Research Laboratory, Ahmedabad. The measurement method involves equilibration of external reference gas with the sample water (Epstein and Mayeda, 1953). About 0.3ml of the sample water (seawater) were taken in 12 ml quartz vials fitted with vacuum-tight caps (Figure 2.8a). Each vial was flushed for ~10 mins (for δ¹⁸O measurement, flushed with He + CO₂ mixture with composition of 0.2% CO₂ and remaining He; similarly, for δD measurement, flushed with He + H₂ with ~2% H₂ and remaining He). The flushed sample vials (which contain He+CO₂ for δ¹⁸O measurements and He + H₂ for δD measurements) were kept for isotopic exchanges until the equilibrium condition was achieved (Figure 2.8b). During this, exchange of isotopes between the two phases (i.e., gas-water) takes place, and after sufficient time forward and reverse exchange process reaches to equilibrium condition; in which flush gas in the vial is labeled with a definite

‘ δ ’ value. After equilibrium condition is achieved, ‘ δ ’ will not change further, even if the time for exchange is extended. ‘ δ ’ values will have some effect relative to the actual isotopic composition of water sample. However, since the laboratory standard also passes through the same procedure, estimation of the offset value is not required.

Equilibration time is different for both $\delta^{18}\text{O}$ and δD measurements; for $\delta^{18}\text{O}$ it is ~ 18 hrs, and for δD measurement, it is ~ 1 hr when catalyst needles (unique and patented by Thermo) are used. The catalyst used is the platinum-coated needle; these are used to achieve the equilibrium in a short time (1hr). They activate the flushing gas, and quick exchange of hydrogen isotopes take place. The equilibrated gas is then transferred to the IRMS through the GC column for isotope ratio measurements (Figure 2.8a). The final raw values of $\delta^{18}\text{O}$ and δD were then converted to the values with respected to the international standards. Reproducibility of measurements was better than 0.1‰ for $\delta^{18}\text{O}$ and 1‰ for δD .

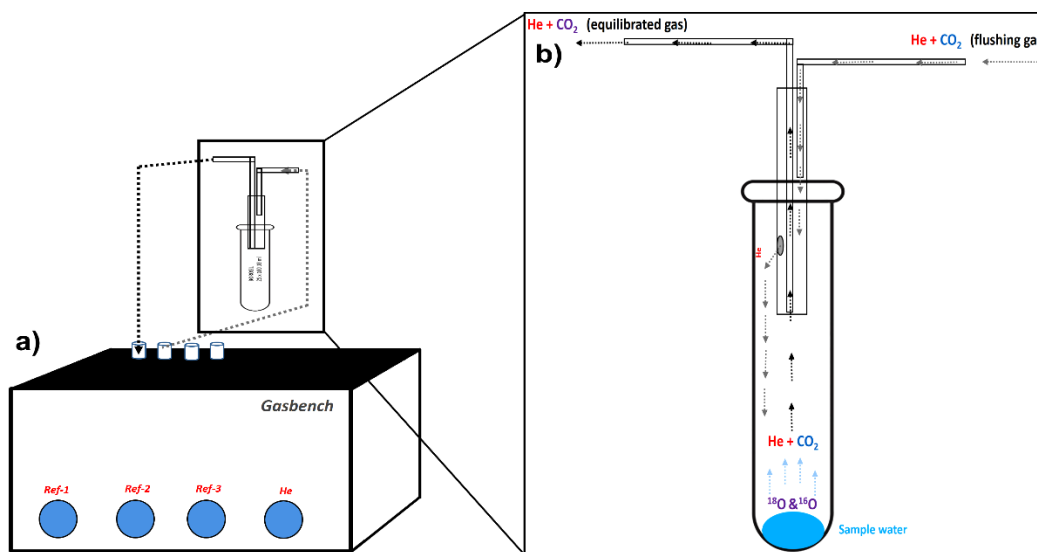


Figure 2.8: Schematic diagram of **a)** external Gasbench and **b)** pathways of flushing gas ($\text{He} + \text{CO}_2$) and the equilibrated gas flow to the Gasbench (for δD measurements the flush gas is $\text{He} + \text{H}_2$). Source: redrawn from ThermoFisher Manual.

Inter-laboratory calibration

Precision and accuracy of the measurements were consistently monitored by using an internal laboratory water standard (called ‘NARM’ with a $\delta^{18}\text{O}$ of -4.1‰ and δD of $-$

32.13‰ relative to Vienna Standard Mean Ocean Water (VSMOW), along with samples in each batch, ('NARM' for Narmada water is frequently calibrated with VSMOW to reconfirm its $\delta^{18}\text{O}$ and δD values). Different international standards are used as a reference based on the sample type and their location (Table. 2.3a).

Table 2.3a: List of the international standards used for stable isotope ratio measurements in water and carbonate samples for calibrating in the present work.

S.No	International Standard	Reported Values	Sample Types (Location)	Reference Standard
1.	VSMOW	$\delta^{18}\text{O} = 0$ $\delta\text{D} = 0$	Water (tropical)	VSMOW
2.	SLAP	$\delta^{18}\text{O} = -55.50$ $\delta\text{D} = -428.0$	Water (high latitude)	VSMOW
3.	GISP	$\delta^{18}\text{O} = -24.8$ $\delta\text{D} = -189.5$	Water (high latitude)	VSMOW
4.	NBS-19	$\delta^{13}\text{C} = 1.95$ $\delta^{18}\text{O} = -2.20$	Carbonates	VPDB

The Narmada river (located in Madhya Pradesh and Gujarat) water was used as a secondary standard (prepared in PRL stable isotope laboratory for $\delta^{18}\text{O}$ and δD measurements) for water samples (rainwater, seawater, and moisture) and calibrated with the international standards procured from International Atomic Energy Agency (IAEA). Every two years, worldwide Inter-laboratory comparison exercise is organized for IRMS labs, by the Isotope Hydrology Laboratory at IAEA, Vienna. In this exercise, some water samples (with unknown isotopic compositions) are provided, and estimated results are communicated back to IAEA. PRL IRMS laboratory participated in the inter-laboratory comparison exercise conducted during 2016, and the values measured by the PRL IRMS lab are in good agreement with the IAEA reported consensus values (WICO-1 to 8; Wassenaar et al. 2018) within $\pm 0.1\text{‰}$ for $\delta^{18}\text{O}$ and 1‰ for δD (Table 2.3b).

Table 2.3b: Measured values in PRL-IRMS and reported values by IAEA during the 2016 international inter-laboratory comparison exercise.

S.No	Sample	Measured $\delta^{18}\text{O}$ (PRL)	Reported $\delta^{18}\text{O}$ (IAEA)	Measured δD (PRL)	Reported δD (IAEA)
1.	WICO-1	-10.9 ± 0.05	-10.80 ± 0.02	-77.2 ± 0.5	-77.4 ± 0.9
2.	WICO-2	-5.2 ± 0.07	-5.11 ± 0.03	-42.2 ± 0.5	-41.7 ± 1.1
3.	WICO-3	-22.0 ± 0.07	-22.01 ± 0.05	-167.1 ± 0.6	-168.3 ± 1.0
4.	WICO-4	-0.7 ± 0.05	-0.50 ± 0.05	-0.7 ± 0.7	0.5 ± 1.1
5.	WICO-5	-15.8 ± 0.07	15.68 ± 0.02	-113.7 ± 0.7	-114.3 ± 1.1
6.	WICO-6	-41.2 ± 0.05	-41.41 ± 0.04	-319.6 ± 0.6	323.7 ± 0.9
7.	WICO-7	5.4 ± 0.04	5.61 ± 0.08	53.2 ± 0.6	55.7 ± 1.6
8.	WICO-8		-3.45 ± 0.10		-17.6 ± 1.2

2.4.2. Isotope analysis for Carbonate Samples (Foraminifera species)

Pre-processing steps (discussed in Section 2.2 and Figure 2.9) are required before $\delta^{18}\text{O}$ and $\delta^{13}\text{C}$ analysis of foraminifera shells. About 200–300 μg of each subsample of planktonic foraminifera *G. ruber* (white), and *G. menardii* were transferred to 12 ml quartz vials fitted with vacuum-tight caps. Later, each tube was flushed with He gas for 10 min (~ 100 ml/min), once all the vials (88 tubes in a run of one batch) were flushed, ~ 0.1 ml of 100% ortho-phosphoric (H_3PO_4) acid was added in all the vials and kept for ~ 1 hour for complete dissolution-reaction of carbonate samples, this produces sample CO_2 . The temperature of the sample tray is maintained at $72 (\pm 0.5) ^\circ\text{C}$. The CO_2 gas is then injected into the Delta-V plus-isotope ratio mass spectrometer (IRMS) via Gasbench. Makrana Marble (MMB), a secondary laboratory standard, was (prepared in PRL stable isotope laboratory) placed in between the samples at regular intervals for monitoring the precision and accuracy of the measurements. MMB is a 99.99% pure CaCO_3 , a large piece of marble collected from Makrana village in Rajasthan. The external precision (1σ) was better than $\pm 0.08\text{‰}$ for both $\delta^{18}\text{O}$ and $\delta^{13}\text{C}$.

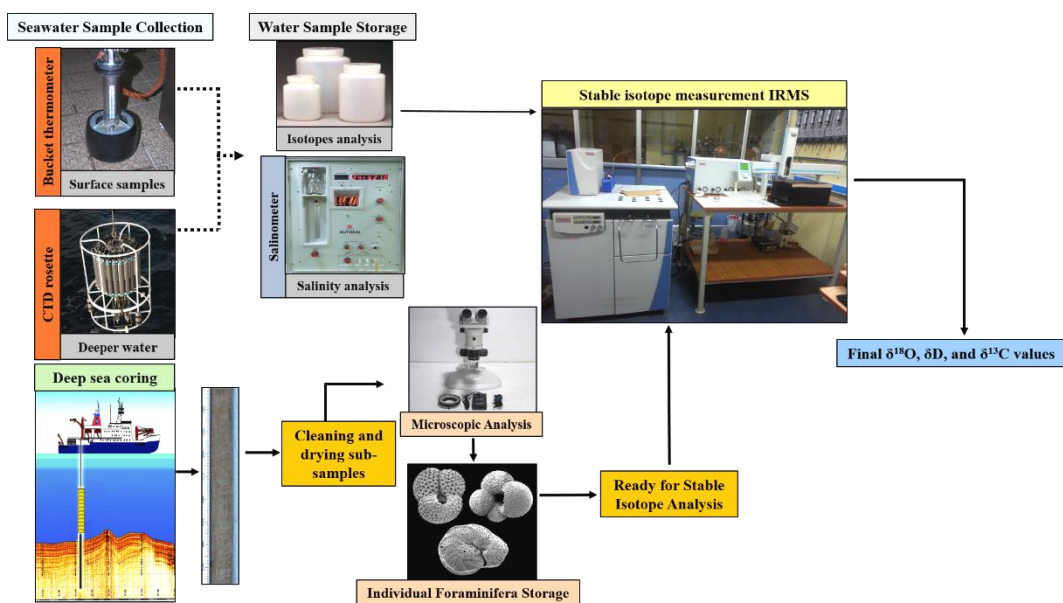


Figure 2.9: Steps involved from sample collection to the final stage of stable isotope measurements.

2.4.3. $\delta^{18}\text{O}$, δD , and $\delta^{13}\text{C}$ calculations for water and carbonate samples

The raw data of $\delta^{18}\text{O}$, δD , and $\delta^{13}\text{C}$ obtained for different samples (seawater, bulk sediment, and carbonates) are estimated relative to the laboratory standards (NARM and MMB). These need to be converted to values relative to the international standards such as Vienna Pee Dee Belemnite (VPDB) for oxygen and carbon in carbonates and Vienna Standard Mean Ocean Water (VSMOW) for oxygen and hydrogen in water. For converting the values relative to the laboratory standards to those relative to the international standards, the following equations were used (Clark and Fritz, 1997):

$$\delta^{18}\text{O}_{(\text{Sample-VPDB})} = \delta^{18}\text{O}_{(\text{MMB-VPDB})} + \delta^{18}\text{O}_{(\text{Sample-MMB})} + [\delta^{18}\text{O}_{(\text{MMB-VPDB})} \times \delta^{18}\text{O}_{(\text{Sample-MMB})} \times 10^{-3}]$$

$$\delta^{13}\text{C}_{(\text{Sample-VPDB})} = \delta^{13}\text{C}_{(\text{MMB-VPDB})} + \delta^{13}\text{C}_{(\text{Sample-MMB})} + [\delta^{13}\text{C}_{(\text{MMB-VPDB})} \times \delta^{13}\text{C}_{(\text{Sample-MMB})} \times 10^{-3}]$$

MMB has been calibrated with respect to the International standard (VPDB), and the values are:

$$\delta^{18}\text{O}_{(\text{MMB-VPDB})} = -10.7\text{‰},$$

$$\delta^{13}\text{C}_{(\text{MMB-VPDB})} = 3.9\text{‰},$$

For $\delta^{18}\text{O}$ and δD of water samples, the conversion equations remain the same; however, instead of ‘VPDB’ it is replaced by VSMOW, and ‘MMB’ is replaced by ‘NARM,’ the estimated values are:

$$\delta^{18}\text{O}_{(\text{NARM-VSMOW})} = -4.1\text{‰}$$

$$\delta\text{D}_{(\text{NARM-VSMOW})} = -32.1\text{‰}$$

In the above discussion, the procedure on the conversion of raw data, reported relative to laboratory standard to the international standard, was given. Some more aspects of the raw data are important and hence presented below:

Corrections are required to account for some of the isobaric contributions from several other isotopologues, which have contributions to the masses detected at Faraday cups, although low but not insignificant during $\delta^{18}\text{O}$ and $\delta^{13}\text{C}$ measurements. Similarly, for analysis of δD , it requires H_3^+ (H_3^+ ion) interference correction.

Craig correction: The masses 45 and 46 of CO_2 has a small contribution from very small abundant isotopes ^{13}C and ^{17}O . During the conversion of molecular ratios into atomic ratios to estimate $\delta^{18}\text{O}$ and $\delta^{13}\text{C}$, a correction is required to remove the effect of $^{13}\text{C}^{16}\text{O}^{17}\text{O}$ from $^{12}\text{C}^{16}\text{O}^{18}\text{O}$ ($\delta^{18}\text{O}$), which is called Craig correction (Craig, 1957):

$$\delta^{13}\text{C} = 1.0676\delta_{45} - 0.0338\delta_{46}$$

$$\delta^{18}\text{O} = 1.0010\delta_{46} - 0.0021\delta_{45}$$

Where δ_{45} , δ_{46} are current ratios expressed as $^{45}\text{CO}_2/^{44}\text{CO}_2$ and $^{46}\text{CO}_2/^{44}\text{CO}_2$, [$^{45}\text{CO}_2$: $^{13}\text{C}^{16}\text{O}_2$, and $^{46}\text{CO}_2$: $^{12}\text{C}^{16}\text{O}^{18}\text{O}$], respectively.

H_3 correction: During ionization, H_3^+ ($\text{H}_2^+ + \text{H}_2 \rightarrow \text{H}_3^+ + \text{H}^*$) ions are also produced and get measured along with HD^+ ions. The formation of H_3^+ ions are directly proportional to the concentration of H_2^+ ions. By calculating $(\text{HD}^+ + \text{H}_3^+)/\text{H}_2^+$ ratio for different H_2^+ ion currents, the effect of the H_3^+ ions can be accounted, and suitable correction can be applied (Sessions et al., 2001).

2.4.4. $\delta^{15}\text{N}$ and $\delta^{13}\text{C}_{\text{org}}$ measurements for the bulk sediment

Analysis of $\delta^{15}\text{N}$ and $\delta^{13}\text{C}_{\text{org}}$ for the bulk sediment and sample preparation steps are different. Each bulk Sediment subsamples were dried at 60°C for 24-36 hrs before measuring for $\delta^{15}\text{N}$ and $\delta^{13}\text{C}_{\text{org}}$ in the elemental analyzer (EA). Completely dried samples were grounded (very fine) for homogenous mixing and then divided into two aliquots, one for $\delta^{15}\text{N}$ and another for $\delta^{13}\text{C}_{\text{org}}$ measurements. Known amount of samples packed in ultraclean tin capsules were dropped inside a heated reactor which contains an oxidant such as copper oxide and chromium oxide and combusted at 1020 °C to produce N_2 , NO_x , H_2O and CO_2 which were trapped and reduced in a stream of helium in the reduction column (oxides of nitrogen were reduced). Both $\delta^{15}\text{N}$ and $\delta^{13}\text{C}_{\text{org}}$ measurements were performed on Delta V plus IRMS attached to EA through Conflow IV.

Elemental concentrations of N (weight %) and C_{org} (weight %) in bulk sediment samples were calculated using a calibration curve (straight line) generated based on international standards of known %C (IAEA-CH-3 cellulose standard, 44.40 %) and %N (such as protein: 13.32 % and IAEA-N-2 ammonium sulphate: 22.20 %) against area under the curve using the same EA. These known international standards isotopic composition IAEA-N-2 (20.3‰) and IAEA-CH-3 (-24.7‰) values are used for the EA stability and precision monitoring for $\delta^{15}\text{N}$ and $\delta^{13}\text{C}_{\text{org}}$ measurements, respectively.

(i) $\delta^{15}\text{N}$ measurement in Sediment samples:

The finely powdered sediment samples were weighed in tin capsules (around ~30-40 mg of sediment). These tin capsules with sediment samples were tightly packed without any atmospheric air inside. Then these capsules were mounted in the auto-sampler tray of EA, which introduced these samples periodically one after another to the combustion chamber of the Elemental Analyser to produce sample N_2 for $\delta^{15}\text{N}$ measurements. The $\delta^{15}\text{N}$ measurements are reported in per mill (‰) with respect to the Air- N_2 (atmospheric nitrogen

isotopic composition as standard), and analytical precisions obtained were better than 0.3‰.

$$\delta^{15}\text{N} = (\text{R}_{\text{sample}}/\text{R}_{\text{standard}} - 1) \times 1000; \text{ for nitrogen isotopes: } \text{R} = {}^{15}\text{N}/{}^{14}\text{N}$$

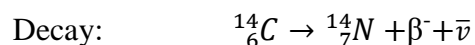
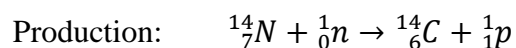
(ii) $\delta^{13}\text{C}_{\text{org}}$ measurement in Sediment samples:

To measuring $\delta^{13}\text{C}_{\text{org}}$ of the samples from sediment cores, firstly, removal of inorganic carbon by the de-carbonation method was performed. Each dried fine-grained sediment sample was acidified with 2M HCl and heated at 80°C for overnight (~14 to 18 hrs). These decarbonized samples were then rinsed with Milli-Q water in the centrifuge machine for two to three times to remove acid traces (Nieuwenhuize et al., 1994). Later samples were dried in the oven at 60°C. The dried specimens were then packed in ultraclean tin capsules (~2- 5 mg) and mounted in the EA-autosampler for estimation of $\delta^{13}\text{C}_{\text{org}}$.

2.5. Radiocarbon (^{14}C) dating

In paleoclimate studies, the most important parameter after the proxy-based data (stable isotopes) is the chronology. The age of a sample can be obtained by various dating methods depending upon the sample type and the maximum age to be determined. Radiocarbon dating is a method of estimating the age of a sample by measuring concentration of the remaining ^{14}C (radioactive isotope) against its known half-life (Arnold and Libby, 1949; Hua, 2009; Libby et al., 1949). ^{14}C radiocarbon dating works on the principle of balance between the continuous production of ^{14}C in the atmosphere, due to the high energy cosmic ray interaction with the ^{14}N , and losses due to radioactive decay. The newly produced ^{14}C in the upper atmosphere is oxidized and forms CO_2 and mixes with the atmospheric CO_2 . It is exchanged continuously in the living entities of carbon reservoirs (e.g., trees, animals, oceans, different organisms in aqueous systems, humans). Once these entities are disconnected from exchange process (when the life span, in case of animals, humans and different living species is over, by natural or artificial reasons), the ^{14}C present in these object at the time of disconnection with

atmosphere starts decaying with a half-life of 5730 years to ^{14}N (Hua, 2009; Petrucci et al., 2017). The production and decay are as follows:



Information of the half-life of ^{14}C , along with the current ratio of ^{14}C to ^{12}C , helps determine the age. The specific activity in pre-industrial times was $13.56 \text{ dpm (gC)}^{-1}$, dpm stands for decay per minute; this is taken as a reference value for modern activity. Accelerator Mass Spectrometry (AMS) is a highly sensitive technique that can be used to estimate ratio $^{14}\text{C}/^{12}\text{C}$ in milligram level carbon samples (Bhushan et al., 2019). By this method age of a sample can be dated up to 50,000-55,000 years (~8-10 half-lives) back in time.

$$({}^{14}\text{C}/^{12}\text{C})_t = ({}^{14}\text{C}/^{12}\text{C})_0 e^{-\lambda t}$$

Where $({}^{14}\text{C}/^{12}\text{C})_t$ is the residual abundance ratio at time ‘t’ and $({}^{14}\text{C}/^{12}\text{C})_0$ is the initial ratio. ‘t’ is the age of the sample and ‘λ’ is the characteristic decay constant ($\lambda = 0.693/5730 \text{ yr}$)

Radiocarbon ^{14}C dating in AMS is carried out in the two-step process:

(i) *Graphitization preparation:*

^{14}C measurements by AMS required the sample transformed into elemental carbon or graphite for producing intense, stable ion beams with a negligible memory effect in the ion source chamber of AMS. The carbonate samples (foraminifera), which need to be dated by AMS for $^{14}\text{C}/^{12}\text{C}$ analysis, have to be converted into graphite form. Graphite is one of the stable forms of carbon. Before graphitization, the sample carbon needs to convert into pure CO_2 form. In this thesis work, mixed planktonic foraminifera species (*G. ruber*, *G. menardii*, *G. sacculifer*, and *Orbulina Univerversa*) were used for radiocarbon dating. The cleaned (chemically treated for clay and mud removal) mixed planktonic foraminifera species were separated from the sediment cores. For conversion of carbonate sample to pure CO_2 , a specially designed glass system

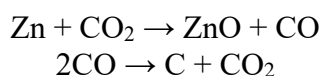
developed at Physical Research Laboratory, Ahmedabad was utilized (Figure 2.10). Each carbonate (foraminifera) sample weighing around ~ 4 mg was transferred to pre-cleared dry sample glass reaction tubes (13 mm diameter). The air inside the glass tube was removed to avoid contamination from the modern atmospheric CO₂; diffusion pumps were used to get a good vacuum, better than 1micron of Hg inside the tube. Once the atmospheric air was removed, and the maximum vacuum was achieved, ortho-phosphoric (H₃PO₄) acid was injected using a 1ml syringe (about 0.5ml). The acid reacts with the carbonate sample and releases CO₂. However, along with CO₂ other unwanted gases may also be released during the reaction (dominantly water vapor) to avoid this, the CO₂ was transferred in purification steps repeatedly.



Figure 2.10: CO₂ preparation system for the carbonate type samples at Physical Research Laboratory, Ahmedabad.

For AMS dating, a pure CO₂ prepared from the sample is first converted into graphite form. A specially designed graphitization reactor at Radiocarbon Lab, PRL, Ahmedabad, uses tubes of 12 cm long, 6 mm outside diameter of quartz tubes. The tubes are sealed at one end and specially designed for small-mass samples graphite preparation. In one batch, five graphite preparation can be performed on this graphite reactor. The pure CO₂ is converted into graphite form in the presence of pure metal Fe (catalyst) and Zn powders. For preparing graphite of ~ 3mg equivalent C of CO₂ gas,

~ 4 mg of Fe and ~ 20 mg of Zn is taken in the ultraclean quartz tubes. The Fe and Zn powder containing each tubes were then heated for ~1 hr at 300 °C for moisture removal. Once this heating was done, the sample's CO₂ is reacted with these catalyst metal Fe and Zn powder at 450 °C and 500 °C, respectively. The activated Zn reacts with the CO₂ and finally precipitated as elemental carbon (or graphite form) on the Fe powder.



In the end, ~85- 95% efficiency of sample pure CO₂ to C conversion was observed in each run. This Fe powder with laminated graphite (of samples CO₂) was used for further AMS dating.

(ii) ¹⁴C measurement by AMS:

By AMS method concentration of ¹⁴C/¹²C (also ¹³C/¹²C) in a sample to be dated can be measured. The greatest advantage of this method is that it requires a small amount of carbon sample (~ 0.3 to 1mg C), and high precision results can be obtained in the reasonable machine running time (~1 hr).

Graphite prepared from the sample was then pressed into a cylindrical cavity of an aluminum holder called target. These targets were mounted in the sample carousel, which is located in the source part of the AMS (Figure 2.11), later evacuated to high vacuum levels (10⁻⁵ to 10⁻⁶ mbar). In a single run during the analysis, about 50 targets can be mounted, including targets prepared from laboratory and international standards. The international standards used for estimating modern values were OXALIC ACID-I (OX-I) and OXALIC ACID-II (OX-II). Similarly, for background, laboratory standards of anthracite and marble materials were used.

It is well known that the radiocarbon dating of marine shell samples (or marine mammal residue) is skewed by the reservoir effect of the oceans. As a result, in most regions, marine samples yield radiocarbon ages substantially older than those yielded by the terrestrial samples. The ¹⁴C ages of marine fossils collected from the surface

waters (up to ~ 200 m depth) measured worldwide result in the average age of 400 years, older than the contemporary terrestrial wood since the reservoir from which these foraminifers consume carbon has lower $^{14}\text{C}/^{12}\text{C}$ ratios compared to the atmosphere. This is due to the mixing of deeper depleted ^{14}C water with surface water (Oeschger et al., 1975; Stuiver and Braziunas, 1993). The reservoir ages vary from basin to basin, so while calibrating AMS radiocarbon ages (raw data), the reservoir age correction is needed for accurate age estimation of the samples.

In the present study, AMS radiocarbon ages (RAW data) were calibrated using the Calib704 software (Stuiver et al., 2017). Dutta et al. (2001) and Southan et al. (2002) dated various mollusks to determine the reservoir ages from several sites in the Arabian Sea and Bay of Bengal. In the present work AMS ^{14}C dates sedimentary records were corrected for 400 year reservoir age following Dutta et al., (2001) and Southan et al., (2002) with reservoir age correction $\Delta R = 60 \pm 52$ years for the southern AS and $\Delta R = 511 \pm 57$ years for the western Bay of Bengal.

Ages for the other depths (beyond the ^{14}C dating limit) were assigned by the extrapolation of calibrated ages, assuming constant sedimentation rates. In the present study, significant changes in the sedimentation rate were observed in the SK-151-A/3 and SK-336-GC-I cores.



Figure 2.11: 1MV-AMS (HV make) installed at Physical Research Laboratory, Ahmedabad. Radiocarbon dating for sediment core samples used in this study was carried out using this instrument.

2.6. Other data used in this work

2.6.1. Satellite Remote Sensing/Reanalysis data

In this thesis work, I used the Hadley Centre Sea Ice and Sea Surface Temperature dataset (HadISST) derived SST data for estimating the SST anomaly over the Niño3.4 region (170°W-120°W/5°S-5°N of the central Pacific Ocean) for El-Niño Southern Oscillation (ENSO) variability (Rayner et al., 2003). Niño3.4 region is a better indicator of changes in the strength of ISM in response to the ENSO than other regions (Niño1+2, Niño3 and Niño4), as the maximum influence of SST anomaly for Niño3.4 on ISM is observed (Kumar et al. 2006; Rajeevan and Pai 2007; Ratnam et al. 2010; Annamalai and Liu 2005). A positive SST anomaly over the Niño3.4 region is considered as El-Niño event, for this study I considered threshold temperature for the El-Niño and La-Niña episodes as the SST anomaly over the Niño3.4 region is $\geq \pm 0.5^{\circ}\text{C}$ (El-Niño $\geq +0.5^{\circ}\text{C}$ and La-Niña $\leq -0.5^{\circ}\text{C}$). The spatial and temporal variation of rainfall was studied over the region bounded by 74.5 – 86.5°E, 16.5 – 26.5°N which is known as the core monsoon (CM) region, i.e., within which the monsoon trough/ Continental

Tropical Convergence Zone (CTCZ) normally fluctuates, and maximum rainfall is observed during summer monsoon (Rajeevan et al., 2006). I have used the Global Precipitation Climatology Project (GPCP) derived monthly mean rainfall data sets for spatial analysis of rainfall over the Indian subcontinent. The GPCP is a merged product of the precipitation information available from several sources of remote sensing, land observation, radar observation, and rain-gauge data into a final combined single product (Adler et al. 2003). GPCP data is available at monthly time scales at $2.5^{\circ} \times 2.5^{\circ}$ resolution for 1979-2013. The GPCP monthly precipitation data is available with coarse resolution; however, most of the important large scale rainfall and deep convection process are able to reproduce and identified in this data in comparison to the high-resolution data from Tropical Rainfall Measuring Mission (Saikranthi et al., 2017). Significance of the correlations was calculated using *Student t-test*. The threshold of the significant correlation is 0.3 (0.35) for 1979-2013 at the monthly (seasonal) scale at 95% confidence level.

2.6.2. Observational data

In addition to the remote sensing data, I have used the Homogeneous Indian Monthly Rainfall Data, a merged product of rainfall data from Indian Meteorological Department and Indian Institute of Tropical Meteorology (Kothawale and Rajeevan, 2017; Parthasarathy et al., 1994, 1993) from the Indian subcontinent over the period 1965 – 2013 (~50 years). This data is available at https://tropmet.res.in/static_pages.php?page_id=53.

2.6.3. General circulation model simulation data

In this thesis work, the isotope enabled general circulation model (GCM) derived $\delta^{18}\text{O}_{\text{rain}}$, and rainfall data were used for spatial pattern analysis. The Stable Water Isotope Intercomparison Group (SWING) phase-2 provides ten different model-simulated data on global $\delta^{18}\text{O}$ of precipitation. Out of all, only few models are able to reproduce the spatial and temporal variation of rainfall over the India subcontinent (Midhun and Ramesh, 2016). I have used the Isotope General Spectral Model

(isoGSM) in this thesis work for understanding the spatial and temporal variation of $\delta^{18}\text{O}_{\text{rain}}$ in response to global climatic processes. IsoGSM model-derived data is available at monthly time scale resolution with a spatial resolution of $1.914^\circ \times 1.875^\circ$.

The isoGSM model simulation data from the SWING2 archive available at https://data.giss.nasa.gov/swing2/swing2_mirror/isoGSMnew/. An International Atomic Energy Agency (IAEA) in collaboration with the World Meteorological Organization (WMO) established the Global Network of Isotopes in Precipitation (GNIP) is a program to assess stable isotopes in worldwide global precipitation. The IsoGSM derived $\delta^{18}\text{O}_{\text{rain}}$ simulation is the most realistic variability in reproducing the monthly variations when compared with the observation of GNIP derived $\delta^{18}\text{O}$ of precipitation over the globe than other models (Yoshimura et al., 2008). The isoGSM model-simulated data is available for the period from 1979-2009; detailed information is available in Midhun and Ramesh (2016) and Yoshimura et al. (2008).

2.6.4. Paleoclimate proxy data

Cave deposits are one of the best continental proxies for the reconstruction of past-rainfall conditions (Yadava and Ramesh, 2005; Sinha et al. 2007; Berkelhammer et al. 2010). In this thesis work, two high resolution (annual growth) cave speleothem records (previously published data) are used to understand the past spatial variability of rainfall over the Indian subcontinent in response to coupled ocean-atmospheric processes (such as ENSO and IOD). One record from Jhumar cave ($18^\circ 52' \text{ N} - 81^\circ 52' \text{ E}$) located near the town of Jagdalpur in central India and one from Wah Shikar Cave ($25^\circ 15' \text{ N} - 91^\circ 52' \text{ E}$) located ~ 30 km from the city of Shillong in northeast India (Sinha et al., 2011a) were studied. Both the cave locations are affected by the high rainfall amount during the JJAS (summer monsoon; Sinha et al., 2011a). The lower (higher) $\delta^{18}\text{O}$ of speleothem infers the stronger (weaker) monsoon conditions.

In addition to the cave deposit records, high resolution, well-dated marine sediment cores from various regions of the northern Indian Ocean were also used to compare and understand the spatial variability of past oceanographic conditions and monsoonal effect.

Chapter-3
Seawater $\delta^{18}\text{O}$, δD dynamics in the Northern
Indian Ocean

Seawater $\delta^{18}\text{O}$, δD dynamics in the northern Indian Ocean

The northern Indian Ocean is comprised of the Arabian Sea (AS) on its western side and Bay of Bengal (BoB) & the Andaman Sea on its eastern side. Studying the dynamics of the northern Indian Ocean is imperative as it plays an important role in the Indian monsoon, which determines the water availability over the Indian subcontinent (about AS, BoB, and the Andaman Sea explained in Chapter-1). One of the best proxies to study modern and past dynamics of the ocean is its oxygen isotopic composition ($\delta^{18}\text{O}$) together with the salinity (S). The $\delta^{18}\text{O}$ composition of sea surface water and its relation with S ($\delta^{18}\text{O}$ –S relation) are controlled by the major hydrological components, i.e., precipitation (P), continental runoff (R), and Evaporation (E), upwelling/advection and diffusion (Rohling, 2007). Mixing of oceanic water with runoff, large-scale ocean mixing, sea ice, and glacier melting can be studied by the $\delta^{18}\text{O}$ –S relation in the surface

ocean water (Bigg and Rohling, 2000; Singh et al., 2014). $\delta^{18}\text{O}$ and S composition of the sea surface water covary linearly: both increase with evaporation and decrease with higher precipitation and/or continental runoff. As these processes differ spatiotemporally, the $\delta^{18}\text{O}$ –S relation provides evidence of effective physical processes (Benway and Mix, 2004). The runoff into BoB and the Andaman Sea from the Indian and Myanmar rivers is seasonal with maximum discharge during the summer monsoon, which also coincides with excess precipitation over evaporation (positive P+R-E) in this region (Prasad, 1997; Subramanian, 1993). Annually BoB is diluted through $\sim 1.6 \times 10^{12} \text{ m}^3 \text{ yr}^{-1}$ freshwater discharge from the Ganges, Brahmaputra, Irrawaddy, Mahanadi, Godavari, and Krishna rivers (Lambs et al., 2005). River water (glacier melt and precipitation) is relatively lower (depleted in ^{18}O) in $\delta^{18}\text{O}$ for the ocean water, which results in making the northern BoB water depleted in ^{18}O compared to the rest of BoB (Breitenbach et al., 2010; Singh et al., 2014).

Application of $\delta^{18}\text{O}$, δD , S and their relations (i.e., $\delta^{18}\text{O}$ –S and δD – $\delta^{18}\text{O}$) for understanding oceanic processes are well documented, however, the available data from BoB were inadequate until now for demarcating these surface processes (evaporation, runoff mixing, precipitation, etc.). The $\delta^{18}\text{O}$ –S relation is consistent with the negative P+R-E (excess of evaporation over precipitation and runoff) in the Arabian Sea and positive P+R-E (excess of precipitation and runoff over evaporation) budget in BoB (Delaygue et al., 2001; Singh et al., 2014, 2010). Boundary currents, which transport low saline water from the northern BoB to the Arabian Sea and vice-versa, influence the $\delta^{18}\text{O}$ –S relation in the surface ocean water. Besides, tropical cyclones can also influence the $\delta^{18}\text{O}$ of the seawater by depleted ^{18}O precipitation over the sea during winter (Chakraborty et al., 2016; Lawrence and Gedzelman, 1996). BoB witnesses frequent cyclones during winter (Sahoo and Bhaskaran, 2016), and hence provides a natural laboratory for studying the cyclone effect on $\delta^{18}\text{O}$. The $\delta^{18}\text{O}$ of precipitation and its influence on $\delta^{18}\text{O}$ –S relation during cyclonic events in BoB has not been studied. *d-excess* is used to understand kinetic fractionation during a phase change (Dansgaard, 1964). The degree of kinetic fractionation during evaporation is influenced

by numerous factors such as relative humidity gradient, air, and water temperature, and the evaporative cooling of the water surface (Cappa et al., 2003; Merlivat and Jouzel, 1979).

In addition to the above-explained processes, formation of ocean water mass is one of the important processes that play a major role in ocean dynamics. Water mass is an identifiable body of water with a common formation history that has physical properties (temperature, salinity, chemical, and isotopic composition) distinct from surrounding waters. Different water masses have been characterized to have a different $\delta^{18}\text{O}$ –S relation in the central BoB (Sengupta et al., 2013). Traditionally, relation between the potential temperature (θ) and S, along with density (σ_θ) variation is used to characterize ocean water masses (Emery, 2001; Helland-Hansen, 1916). Movement of these water masses along a specific density layer plays a vital role in transporting water bodies with different characteristics (nutrients, trace metals, and heat, etc.; Emery, 2001). Each water mass has its characteristic temperature, salinity, and corresponding density ranges (Rochford, 1964; Varadachari et al., 1968; Emery, 2001). Depending upon various dynamical processes (such as local advection, upwelling, and mixing of different water masses), surface, subsurface, and deeper ocean water may show distinct values of slopes and intercepts in $\delta^{18}\text{O}$ –S relation (Sengupta et al., 2013). Only a few studies have attempted and used the $\delta^{18}\text{O}$ and salinity of the sea surface water to apprehend the mixing of different surface water masses in the Indian Ocean (Srivastava et al., 2007; Tiwari et al., 2013). Paleo-salinity estimates in the northern Indian Ocean derived from a constant $\delta^{18}\text{O}$ –S relation might have been hampered because of the observed variation in this relation, in different water masses of the northern Indian Ocean.

3.1. Seawater Sampling and Methodology

This section is divided into two parts first discusses the results from water samples analyzed from BoB and the Andaman Sea, and the second section presents the results from seawater samples collected from AS. A total of ~325 surface water samples (depth

≤ 2 m), and 140 subsurface water samples were collected during April 2016; December 2016–January 2017 and during April-2017 onboard FORV *Sagar Sampada* cruises (SS-349; SS-355 and SS-359) in the northern Indian Ocean. The surface water samples were collected using a bucket thermometer sampler. Subsurface water samples were collected using CTD rosette sampler from Specific depths from seven stations (~2 m, up to 1000 m depth) off Andaman Island and from the Arabian Sea. Each sample was made into two aliquots, one used for on-board salinity and temperature measurement and the other aliquot used for stable oxygen ($\delta^{18}\text{O}$) and hydrogen (δD) isotopic measurements, on Delta-V plus isotope ratio mass spectrometer (IRMS) connected with gas bench. The method for salinity and stable isotope measurements are explained in detail in Chapter-2.

3.2. Bay of Bengal and the Andaman Sea

308 surface and 44 subsurface water samples were collected during SS-349 and SS-355 over the post and pre-monsoon periods (Figure 3.1a). Subsurface samples were collected at specific depths (~2 m, ~5 m, ~10 m, ~20 m, ~50 m, ~100 m, and ~200 m).

3.2.1. Spatial Variation in $\delta^{18}\text{O}$, δD and salinity over the northern Indian Ocean

Significant spatial variation in $\delta^{18}\text{O}$ and S of surface water were observed in the northern Indian Ocean, with higher values in the southeastern Arabian Sea (SEAS) and lower values in the central and eastern BoB, for both pre- and post-monsoon water samples (Figure 3.1b, 3.1d). The observed mean $\delta^{18}\text{O}$, S, and sea surface temperature (SST) were $0.02 (\pm 0.26) \text{‰}$, $33.02 (\pm 0.92)$ and $28.57 (\pm 1.16) \text{°C}$, respectively. Low S and low $\delta^{18}\text{O}$ values ($S < 32.5$ and $\delta^{18}\text{O} < -0.25 \text{‰}$) were observed in the central BoB and the Andaman Sea. SST showed less variation in the central to northern BoB (Figure 3.1c). Similar spatial variation of S, SST, and $\delta^{18}\text{O}$ over the northern Indian Ocean was also observed in the previous studies (Achyuthan et al., 2013; Sengupta et al., 2013; Singh et al., 2010).

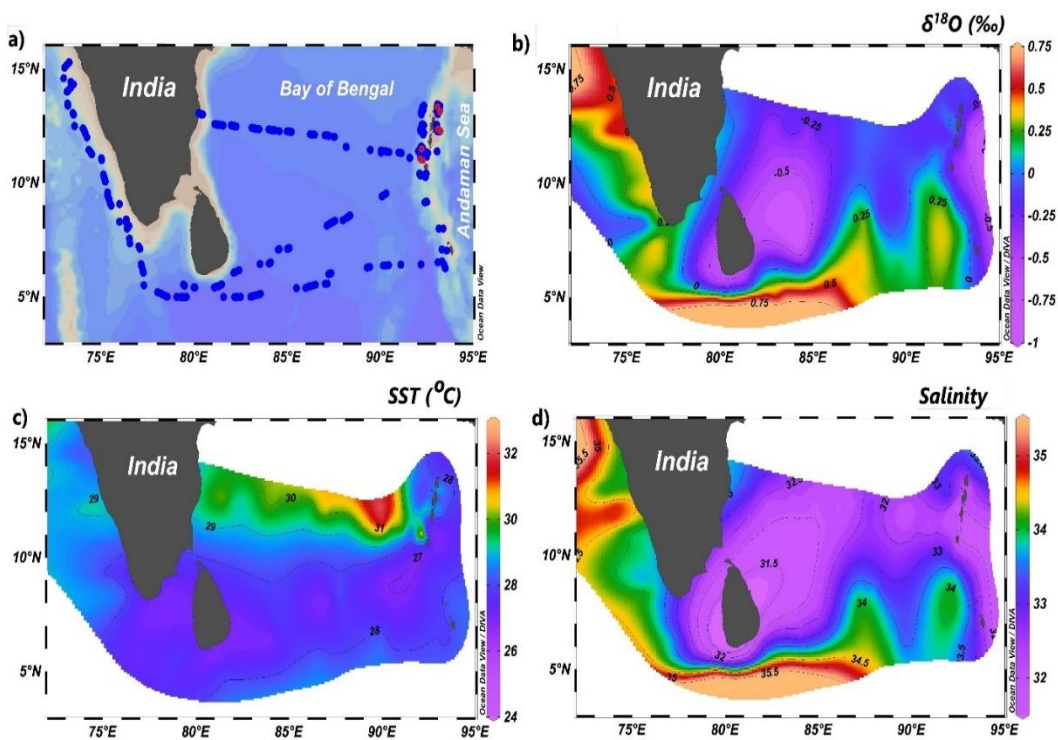


Figure 3.1: Spatial distribution of a) sampling locations (red dots; subsurface water sampling locations of the Andaman Islands), b) $\delta^{18}\text{O}$, c) sea surface temperature and d) salinity of surface seawater samples (total samples $n = 315$) collected in the northern Indian Ocean during April 2016 and December 2016 - January 2017, excluding the subsurface water samples from the Andaman Sea.

A strong correlation between $\delta^{18}\text{O}$ and S [$\delta^{18}\text{O} = 0.26 (\pm 0.01) \times S - 8.55 (\pm 0.22)$; $R^2 = 0.83$; $p < 0.05$; Figure 3.2a], and significant anti-correlation between $\delta^{18}\text{O}$ and $d\text{-excess}$ ($R^2 = 0.27$; $p < 0.05$; Figure 3.2b) were observed in the northern Indian Ocean. Values of slope and intercept for $\delta^{18}\text{O}$ – S relation observed in our study were in the range reported from the previous studies (Achyuthan et al., 2013; Singh et al., 2010). A relatively weaker, but still significant correlation between $\delta^{18}\text{O}$ and δD was observed in the northern Indian Ocean [$\delta\text{D} = 3.71 (\pm 0.40) \times \delta^{18}\text{O} + 2.19 (\pm 0.11)$; $R^2 = 0.22$, $p < 0.05$; figure not shown]. Slope of the observed $\delta^{18}\text{O}$ – δD relation is less than that observed for the global surface ocean water ($\delta\text{D} = 7.37 \times \delta^{18}\text{O} - 0.72$; $R^2 = 0.97$, $n = 244$; (Rohling, 2007; Schmidt et al., 1999) and global meteoric water line [GMWL; $\delta\text{D} = 8.17 (\pm 0.17) \times \delta^{18}\text{O} - 11.27 (\pm 0.5)$; Craig, 1961]. This lower slope is inferred as due

to either evaporation or mixing with highly saline waters of different origins or both (Craig and Gordon, 1965b; Deshpande et al., 2013; Gat, 1996; Rohling, 2007).

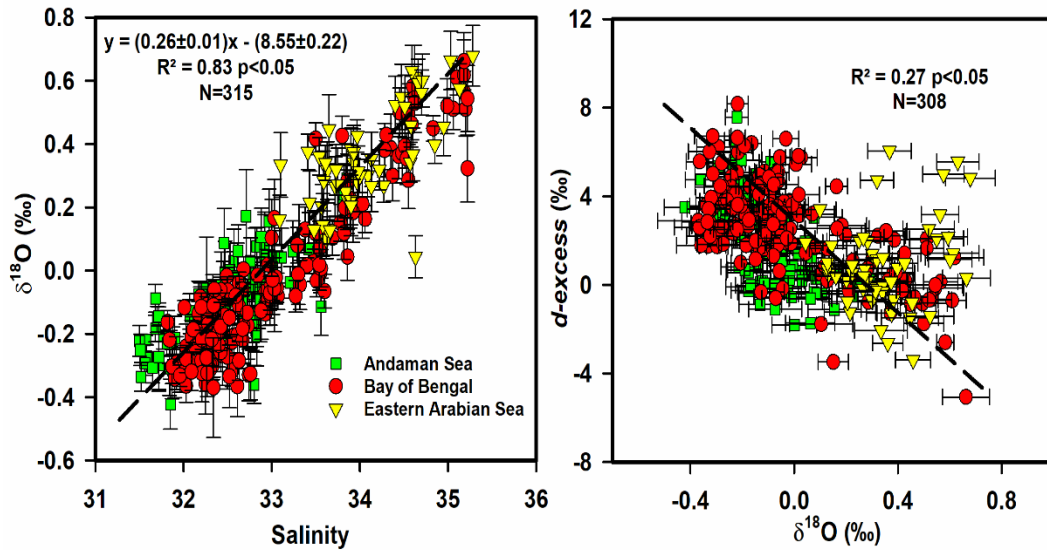


Figure 3.2: a) $\delta^{18}\text{O}$ –S relation and b) d -excess– $\delta^{18}\text{O}$ relation surface water samples ($n = 315$; excluding subsurface samples in the Andaman Sea) collected in the northern Indian Ocean during April-2016 and December 2016 - January 2017. Error bars represent $\pm 1\sigma$ (standard deviation) for a sample measured six times in IRMS.

Observed inverse relation of d -excess with $\delta^{18}\text{O}$ and lower slope of the δD – $\delta^{18}\text{O}$ relation together showed that kinetic fractionation influences these relationships in BoB surface water (Masson-Delmotte et al., 2008). The mean d -excess value for all the samples but subsurface water samples was ~ 2.16 (± 2.20 ‰). Based on d -excess and S values, we observed that 67% of the samples having $S < 33.5$ were associated with higher d -excess values, i.e., ~ 3.85 ‰ (± 1.36 ‰), which could be attributed to the continental runoff mixing (d -excess ~ 10 ‰). 73% of the water samples with $S > 33.5$ were associated with the lower d -excess values, i.e., ~ 0.34 ‰ (± 0.93 ‰), which suggested the mixing of oceanic water (d -excess ~ 0 ‰). Samples with $S > 33.5$ were mostly confined to the southern BoB, as this region (far away from the coastal region) may not be influenced by continental runoff (Seo et al., 2009; Vinayachandran et al., 1999). The d -excess– $\delta^{18}\text{O}$ relation again showed the higher d -excess values are

associated with lower $\delta^{18}\text{O}$, which supported the influence of continental mixing (*d-excess* > 2 ‰; Figure 3.2b) in the coastal region.

3.2.2. Variation in $\delta^{18}\text{O}$, δD and salinity during spring

$\delta^{18}\text{O}$ and S varied from -0.36 ‰ to 0.16 ‰ and 31.5 to 34.06, respectively, during spring (April 2016) in the BoB along the cruise track (Figure 3.3a, b, d). Compared with the surroundings along the cruise track, higher SST was observed over the central BoB and southern Andaman Sea (Figure 3.3c). Low $\delta^{18}\text{O}$ (-0.31‰ to -0.05‰) and corresponding low S (31.5 to 32.33) values were observed in the Andaman Sea, while high values of these parameters were observed in the eastern coast of India (off Chennai; Figure 3.3b, d). Low $\delta^{18}\text{O}$ and associated low S in the surface water off the Andaman Sea and the central BoB (~82°E - 86°E) might be due to the inputs of freshwater through the rivers of Myanmar (Irrawaddy and Salween) from preceding winter monsoon (Figure 3.3b, 3d). Significantly strong $\delta^{18}\text{O}$ -S relation [$\delta^{18}\text{O} = 0.14 (\pm 0.01) \times S - 4.58 (\pm 0.48)$; $R^2 = 0.43$, $p < 0.05$; Figure 3.4a] was observed in BoB.

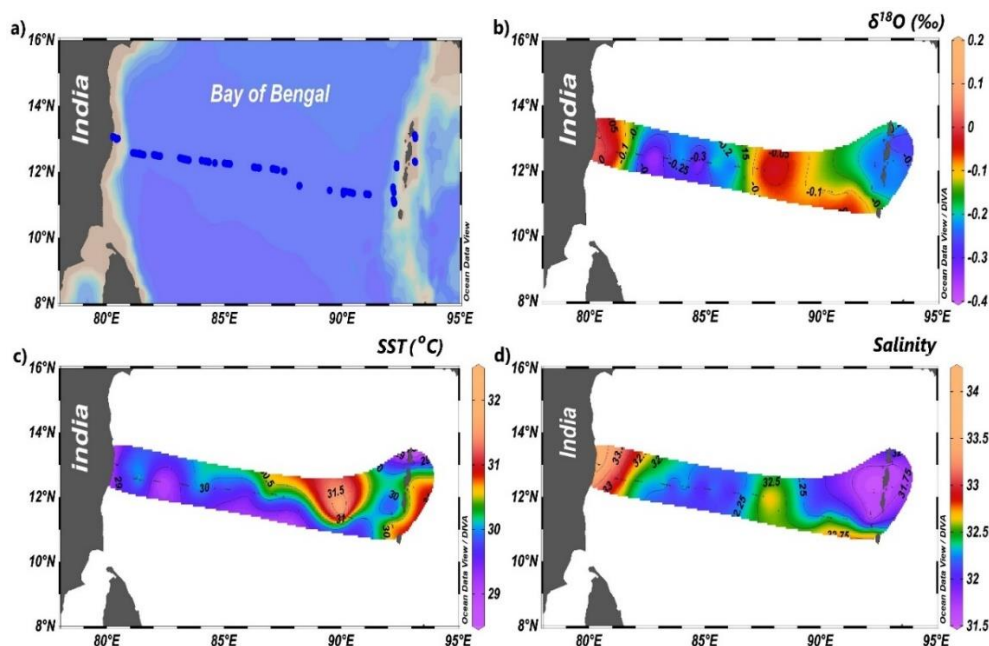


Figure 3.3: Spatial distribution of a) sampling locations, b) $\delta^{18}\text{O}$, c) Sea surface temperature, and d) Salinity of surface seawater samples (total samples $n = 112$) in BoB for spring (April-2016) excluding the subsurface samples in the Andaman Sea.

This study area, which covers the sampling from coastal to open ocean, is affected by different processes such as river runoff, precipitation, boundary currents (EICC; Chapter-1), and wind-driven mixing. The observed $\delta^{18}\text{O}$ -S relation should be a result of all these processes. Similar $\delta^{18}\text{O}$ and S values in the surface water from coastal to open BoB have been observed earlier (Delaygue et al., 2001; Singh et al., 2010). The lower slope in $\delta^{18}\text{O}$ -S relation during spring could be interpreted as the dominant effect of evaporation over all other processes (Singh et al., 2014). However, even when P+R dominates over E, lower slope of $\delta^{18}\text{O}$ -S relation for surface water samples during summer monsoon was reported previously in the same region (north of $\sim 10^\circ\text{N}$), with $\delta^{18}\text{O} = 0.14 (\pm 0.01) \times S - 4.7 (\pm 0.4)$; $R^2 = 0.6$; $p < 0.05$ (Achyuthan et al., 2013). The observed δD - $\delta^{18}\text{O}$ relation during this period was $\delta\text{D} = 8.75 (\pm 1.30) \times \delta^{18}\text{O} + 4.15 (\pm 0.25)$; $R^2 = 0.30$, $p < 0.05$ (Figure 3.4b). The δD - $\delta^{18}\text{O}$ relation for these water samples with a lower intercept than that of the GMWL inferred dominance of evaporation during this period (Rohling, 2007). However, the observed higher slope of the δD - $\delta^{18}\text{O}$ relation than that observed for the Himalayan river waters $7.14 (\pm 0.21)$ and Peninsular $5.31 (\pm 0.35)$ river waters (Achyuthan et al., 2013) inferred that our sampled region was influenced by precipitation in addition to run-off.

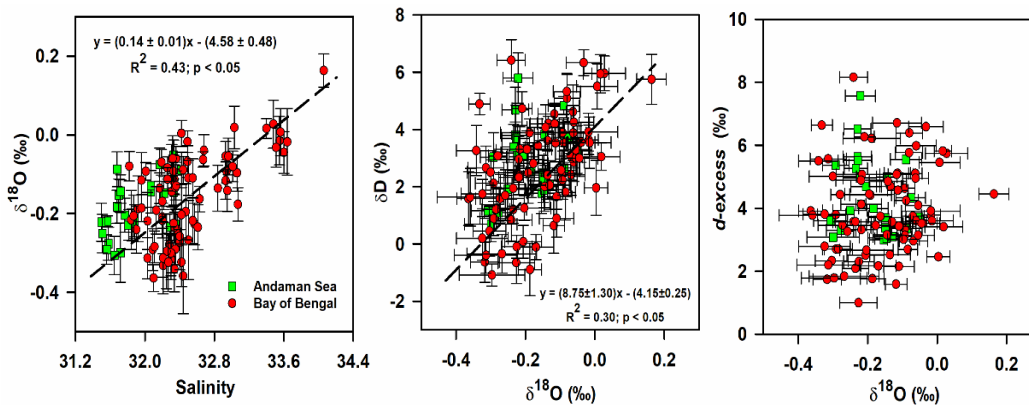


Figure 3.4: a) $\delta^{18}\text{O}$ -S relation, b) δD - $\delta^{18}\text{O}$ relation, and c) d -excess- $\delta^{18}\text{O}$ relation for sea surface water samples collected during spring ($n = 112$; April-2016) excluding the subsurface samples in the Andaman Sea.

3.2.3. $\delta^{18}\text{O}$, δD and salinity variation during winter

The surface water sample collection during winter (December-2016 to February-2017) was extended to SEAS (Figure 3.5a). SEAS is influenced by the west Indian coastal current (WICC; Schott and McCreary Jr, 2001), which brings the low saline water from BoB to the eastern Arabian Sea during winter. The intrusion of BoB's water modulates the oxygen isotopic variation and S in the surface water in SEAS. The observed $\delta^{18}\text{O}$ and S in BoB during the winter were ranged -0.42 ‰ to 0.68 ‰ and 31.52 to 35.2, respectively, with low values near coastal locations (Figure 3.5b, d). High SST (> 28.5 °C) was observed in the southern BoB and the SEAS (Figure 3.5c). Low $\delta^{18}\text{O}$ and low S in BoB could be due to the influx from the Peninsular and Himalayan Rivers through EICC (Lambs et al., 2005; Warriar et al., 2010). Significantly stronger $\delta^{18}\text{O}$ –S relation was observed during this period [$\delta^{18}\text{O} = 0.28 (\pm 0.01) \times S - 9.10 (\pm 0.30)$; $R^2 = 0.83$, $p < 0.05$; $n = 203$; Figure 3.6a] than that during the spring (Figure 4a). Higher slope 0.28 (± 0.01) and lower intercept -9.10 (± 0.30) of the $\delta^{18}\text{O}$ –S relation compared to the spring [slope = 0.14 (± 0.01) and intercept = -4.58 (± 0.48) respectively] implied the influence of freshwater/runoff on the $\delta^{18}\text{O}$ –S relation during winter (Singh et al., 2010). The higher slope, which is associated with ^{18}O depleted overflow, could be due to the 'amount effect' (Araguás-Araguás et al., 1998b; Dansgaard, 1964; Yadava and Ramesh, 2005).

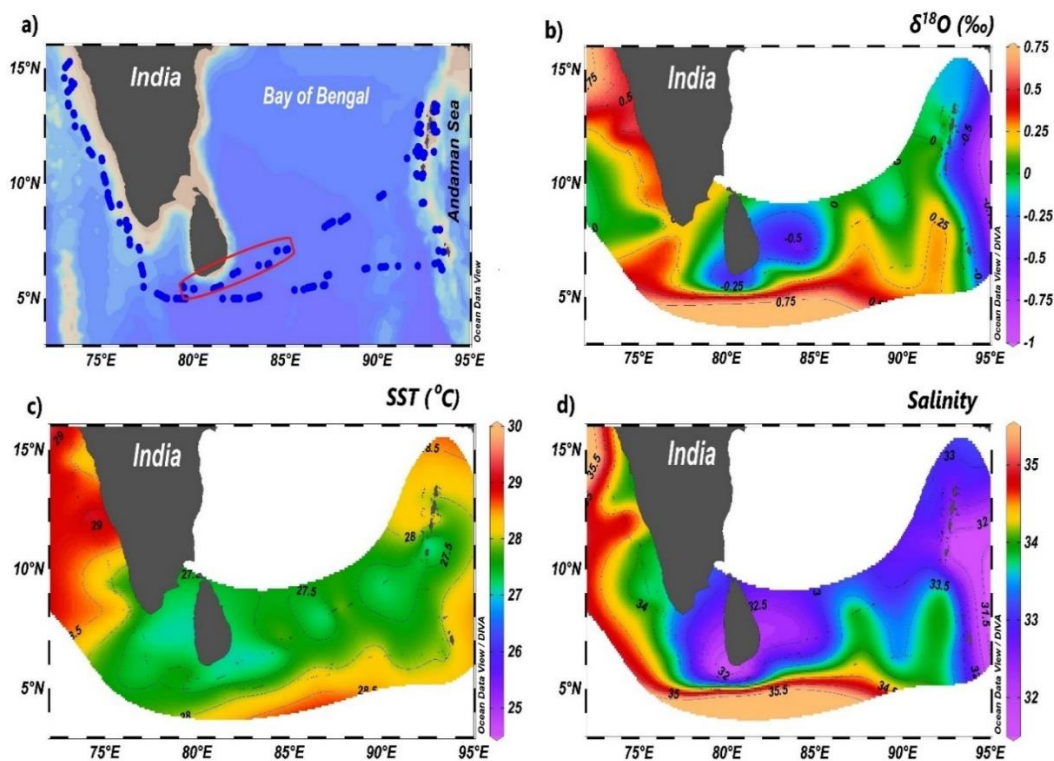


Figure 3.5: Spatial distribution of **a)** sampling locations (red box shows “Vardah” cyclone-affected region), **b)** $\delta^{18}\text{O}$, **c)** sea surface temperature and **d)** salinity of sea surface water samples (total samples $n = 203$) in the northern Indian Ocean for winter (during December-2016 to February-2017).

Singh et al, (2014) observed a temporal change in $\delta^{18}\text{O}$ – S relation with a substantial increase (decrease) in the slope (intercept) than the previous estimates (Delaygue et al., 2001; Singh et al., 2010), which has been attributed to the debouch of increase in Himalayan glaciers melt in the Bay. We observed significantly strong $\delta^{18}\text{O}$ – S relation in BoB with $\delta^{18}\text{O} = 0.32 (\pm 0.01) \times S - 10.6 (\pm 0.4)$, $R^2 = 0.91$, $p < 0.01$ (data not shown). Our data showed a higher slope (0.32 ± 0.01) and decreased intercept (-10.6 ± 0.4) than that reported by Singh et al., (2014), which might be due to an additional melt of Himalayan glaciers during 2006-2017.

Severe cyclonic storms associated with heavy rains, which frequently occur in BoB (Singh et al., 2000), can also modify the $\delta^{18}\text{O}$ – S relation. “Vardah” was a severe cyclone, which occurred during mid-December 2016. During Vardah, heavy to very heavy rainfall was recorded over southeastern India (i.e., Tamil Nadu, Pondicherry,

and southern Andhra Pradesh). Water samples collected during the cruise SS-355-leg-I (mid-December 2016) off southern Sri Lanka (marked by red box Figure 3.5a) fall in the Vardah cyclonic affected region. Negative $\delta^{18}\text{O}$ and lower S values in this region might be due to the rain associated with Vardah. This cyclonic effect (low $\delta^{18}\text{O}$ and low S values) was not recorded in the samples collected during mid-January 2017 in the same locations (samples south of red box; Figure 3.5a). However, for a better understanding of the cyclone effect on the $\delta^{18}\text{O}$ composition of seawater, extensive water sampling during pre- and post-cyclone is required.

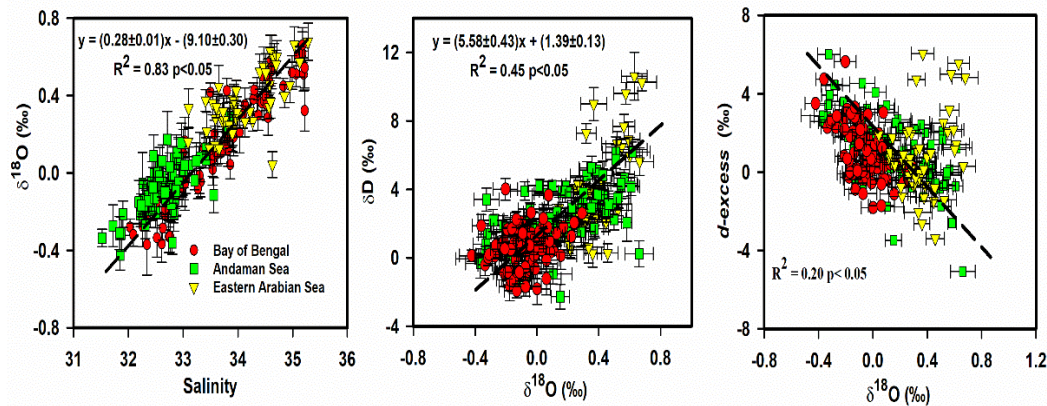


Figure 3.6: a) $\delta^{18}\text{O}$ –S relation, b) δD – $\delta^{18}\text{O}$, and c) *d-excess*– $\delta^{18}\text{O}$ relation for samples ($n = 203$) collected in the northern Indian Ocean during winter.

The δD – $\delta^{18}\text{O}$ relation for the samples collected in BoB showed a significant correlation: $\delta\text{D} = 5.58 (\pm 0.43) \times \delta^{18}\text{O} + 1.39 (\pm 0.13)$; $R^2 = 0.45$; $p < 0.05$ (Figure 3.6b). The δD – $\delta^{18}\text{O}$ relation for these water samples was associated with a lower intercept than the GMWL, which can be inferred as the domination of evaporation. The slope of the δD – $\delta^{18}\text{O}$ relation was similar to the slopes of that in the Peninsular rivers [5.31 (± 0.35); particularly southern rivers like Pennar, Cauvery and Krishna; (Achyuthan et al., 2013)]. Samples from the southernmost locations, which were collected during January 2017 (Figure 3.5a), showed that $\delta\text{D} = 7.18 (\pm 0.99) \times \delta^{18}\text{O} + 0.86 (\pm 0.37)$ ($R^2 = 0.36$; $p < 0.05$; not shown), where the slope is similar to that for Himalayan rivers [7.14 (± 0.21)]. The lower *d-excess* (evaporation during non-equilibrium conditions leads to negative values; Dansgaard, 1964) association with higher $\delta^{18}\text{O}$ (evaporation

makes residue seawater enriched in ^{18}O ; Figure 3.6c) inferred that the kinetic fractionation influence these relations in BoB waters during evaporation in winter (Kumar and Prasad, 1996).

3.2.4. Vertical distribution of $\delta^{18}\text{O}$ and salinity

It is important to understand deep-sea circulation as it plays a vital role in the earth's climate. A direct measure of deep-sea circulation is difficult due to its slow motion as compared to the surface ocean circulation (Sverdrup et al., 1942). Based on θ -S profiles, the existence of Persian Sea Gulf Water mass (PSGW; at ~200 – 500 m) and the Red Sea Water (RSW; at 500 – 1000 m) masses have been identified in BoB (Jain et al., 2017; Rochford, 1964; Varadachari et al., 1968b). Besides, one study observed the PSGW (200 – 400 m) and RSW (400 – 900 m) in the Andaman Sea (Raju et al., 1981). However, there is no other recent evidence of distinct water masses (such as PSGW and RSW) in the Andaman Sea, which suggests the need to revisit the Andaman Sea and further investigation of these water masses signatures. Surface water samples (0 – 20 m) from the Andaman Sea witnessed $S < 32.5$, which could be attributed to the influx of freshwater runoff from the Indian and Myanmar rivers through BoB (Figure 3.7b). At deeper water depths (~200 m), S increased up to 35.02 (Figure 3.7b). Due to the confinement of sampling locations to the coastal region and limited sampling depths (Figure 3.7a), distinct water masses were not observed at deeper depths. However, a steep increase of density with depth might be related to the presence of PSGW (Based on the previous study, inferences). The high salinity (34.8 – 35.02) water at a depth 200 – 500 m with low temperature (10 – 13 °C) and σ_θ (26.3 – 26.9 kg m^{-3}) was observed, which has a characteristic of the PSGW (Prasad et al., 2001, Figure 3.7d).

$\delta^{18}\text{O}$ varied from -0.27 to 0.18 at 0 – 200 m off the Andaman Islands (Figure 3.7c). $\delta^{18}\text{O}$ variation of subsurface water samples showed a gradual enrichment over a depth ranged > 10-100 m in all the profiles (Figure 3.7b). In all the subsurface water samples, a depletion in $\delta^{18}\text{O}$ was observed at ~20 m depth except for station-2 (S-2) and station-3 (S-3) (Figure 3.7c). Strong $\delta^{18}\text{O}$ - S relation for all subsurface water samples was

observed ($R^2 = 0.84$; $p < 0.01$; red dashed line; Figure 3.7e), with slope = $0.13 (\pm 0.01)$ and intercept = $-4.21 (\pm 0.28)$; where the slope and intercept are comparable to the slope and intercept of BoB surface water samples from this study (Figure 3.4a) and previous study (Singh et al., 2010). At S-1 and S-3, $\delta^{18}\text{O}$ peaked at 50 m depth, with enrichment of $\sim 0.36 \text{ ‰}$ and $\sim 0.27 \text{ ‰}$ compared to surface values, respectively. Whereas, a gradual increase in $\delta^{18}\text{O}$ values was observed until 100 m depth at the rest of the stations. Maximum enrichment of $\sim 0.44 \text{ ‰}$ (difference in $\delta^{18}\text{O}$ at 100 m and the surface) was observed at S-5. We divided $\delta^{18}\text{O}$ profiles into two zones: zone-1 (0 – 50 m depth; mixed depth) and zone-2 (50 – 200 m).

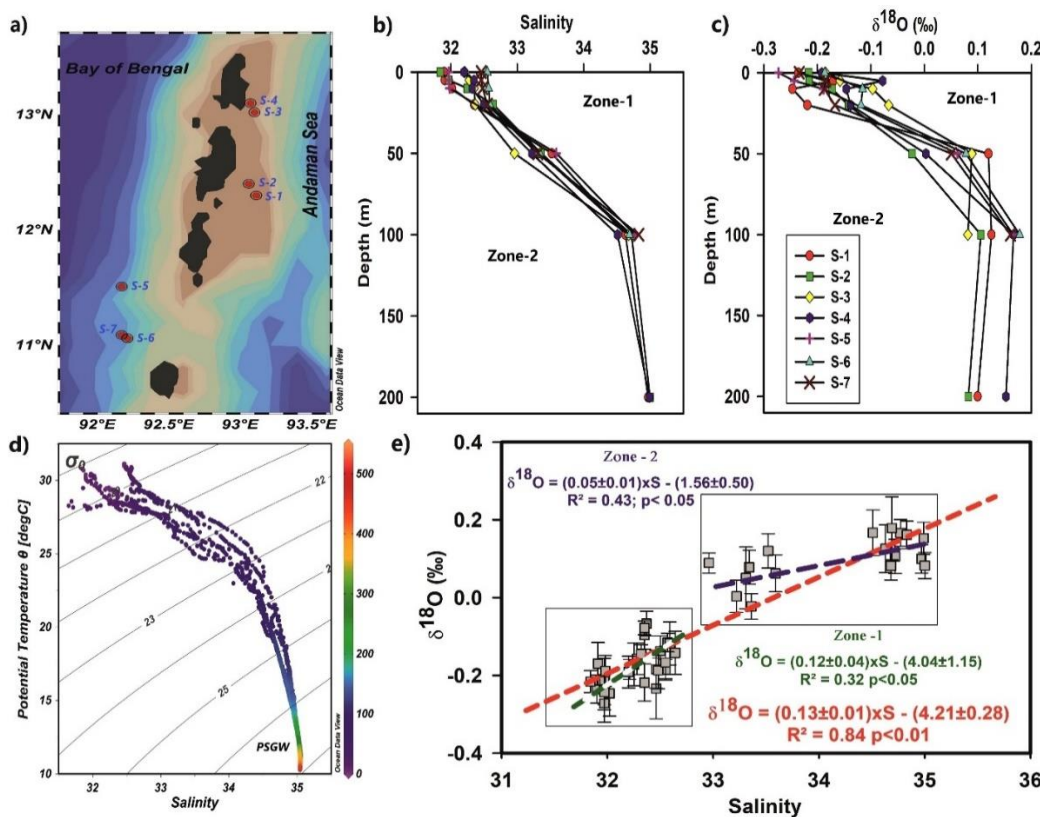


Figure 3.7: a) Sampling location for subsurface water samples (~ 200 m depth) collected off Andaman Island. b) Salinity profile, c) $\delta^{18}\text{O}$ profile, d) θ -S diagram Persian Gulf water mass (PSGW) water masses (200-500 m), and e) $\delta^{18}\text{O}$ -S relations for all the subsurface water samples (red dashed line), for zone- 1 (0-50 m) water samples (green dashed line; inside square box) and for zone- 2 (50-200 m) water samples (blue dashed line; inside rectangle box).

The $\delta^{18}\text{O}$ -S relation for the zone-1 witnessed a slope of $0.12 (\pm 0.04)$ and intercept $-4.04 (\pm 1.15)$ [$R^2 = 0.32$; $p < 0.05$; green dashed line; Figure 3.7e], which were similar

(based on Student's t-test) to that observed in BoB surface water samples in this study (Figure 3.4a) and a previous study (Singh et al., 2010). In zone-2, $\delta^{18}\text{O}$ -S relation has a slope 0.05 (± 0.01) and intercept -1.56 (± 0.5) [$R^2 = 0.43$; $p < 0.05$; blue dashed line; Figure 3.7e]. The observed lower slope and higher intercept for the deeper zone (zone-2) water as compared to mixed depth (zone-1) could be due to the presence of different masses at different zones. The $\delta^{18}\text{O}$ -S relation in the zone-2 might be characterized for PSGW (as of now, no other water masses have been identified). However, there is a need for $\delta^{18}\text{O}$ and S measurements from much deeper and spatially distributed surface waters in the Andaman Sea to characterize $\delta^{18}\text{O}$ -S for different masses.

3.3. The Arabian Seawater samples

The Arabian Sea (AS) is affected by the intense rainfall (direct precipitation) and wind-induced subsurface water mixing over the northern and western AS (Baars et al., 1995; Bauer et al., 1991; Kumar and Prasad, 1996; Lighthill, 1969; Madhupratap et al., 1996a; Schanze et al., 2010). During summer monsoon these wind-induced upper ocean mixing, causing the vertical movement of subsurface water to the surface, brings high nutrient, low-temperature water, which enhances the productivity over the western AS and during winter convecting mixing is prominent over the northern AS (Schott and McCreary Jr, 2001; Goes et al., 2005; Madhupratap et al., 1996). Geographically, both the AS and the BoB located in similar latitudes but associated with different physical and chemical characteristics. The Evaporation (E) dominates over Precipitation (P), and Runoff (R) in the AS (negative P+R-E salinity budget), causing higher salinity water in the AS than in the BoB (Rao and Sivakumar, 2003; Sengupta et al., 2006). In addition to these surface water dynamics (wind-induced mixing, runoff, precipitation, and surface currents) in the AS, water masses formation due to higher evaporation than precipitation and runoff, causes significant changes in density difference, and lead to the formation of different water masses with higher density. Different water masses have been identified in the AS with characteristic ranges in temperature, salinity, and density (discusses in detail in Chapter-1). However, water mass formation is not found in the BoB due to stronger river runoff induced

stratification (Prasad et al., 2001; Schott and McCreary Jr, 2001a; Shetye et al., 1994; Wyrski, 1973).

To understand the surface and subsurface water dynamics and variability of $\delta^{18}\text{O}$ and δD composition with depth in the AS, water samples were collected all along the cruise track during April 2017. A total of 82 depth specific (~ 2 m up to 1000 m water depth) water samples were collected using CTD rosette from 13 stations (red dots), and 21 surface water samples were collected using bucket thermometer instrument (black triangles; Figure 3.8). Temperature and salinity of the collected water samples were measured on-board, whereas the isotopic composition was measured at PRL, Ahmedabad (detail description is explained in detail in Chapter-2).

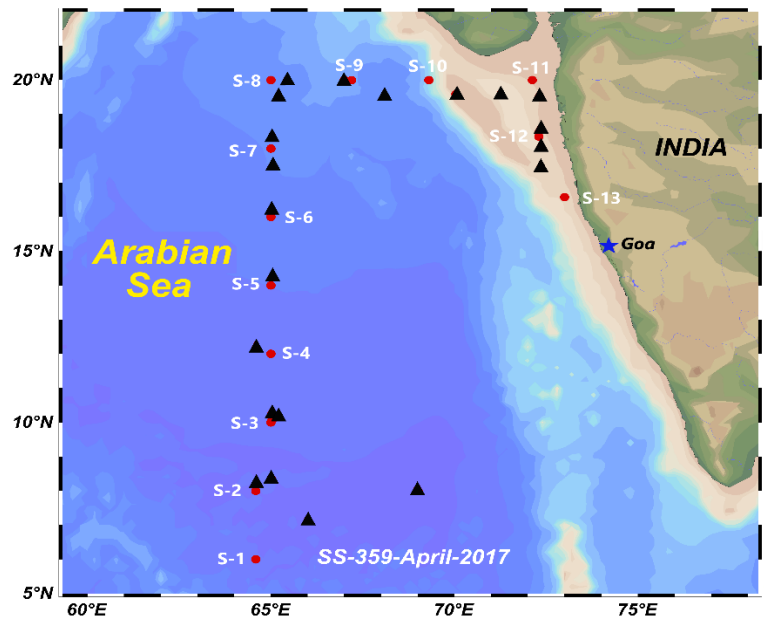


Figure 3.8: Water sample collection locations during SS-359 during April-2017. Red dots show the depth specific water samples collection location using CTD (S-1 to S-13), and black triangles show the surface water samples collection location using a bucket thermometer instrument.

3.3.1. Spatial Distribution

Significant spatial variability of salinity, temperature, δD , and $\delta^{18}\text{O}$ of surface seawater samples was observed over the AS during pre-monsoon (Figure 3.9). Surface water samples salinity and temperature varied from 34.3 – 36.82 and 27.6 to 32.8 °C

respectively (Figure 3.9a, b), whereas the δD and $\delta^{18}O$ values ranged from 1.88 to 9.00 ‰ and 0.08 to 1.10 ‰, respectively (Figure 3.9c, d). Warm and low saline water was observed over the southern AS, whereas relatively colder and high saline water was observed over the northern AS. The northern AS was ~ 2 °C colder than the southern AS, this cold and high saline water might be the traces of preceding winter monsoon induced convective mixing over the northern AS (Figure 3.9a, b; Madhupratap et al., 1996). Northwest Indian coastal waters were associated with high saline and higher temperature (Figure 3.9). Lower δD values over the southern ocean and higher values over the northern Indian Ocean were observed (Figure 3.9c). The spatial distribution of $\delta^{18}O$ of surface water samples shows that the southern AS associated with low $\delta^{18}O$ and lower S, whereas the central to northern AS was associated with higher $\delta^{18}O$ values (Figure 3.9d). The low δD , $\delta^{18}O$, and lower salinity waters over southern AS show the remnant of BoB water that transported through surface currents (winter monsoon current; WMC; discussed in Chapter-1) during preceding winter monsoon. Previous studies have also observed the lower δD and $\delta^{18}O$ over the BoB during winter (Achyuthan et al., 2013; Deshpande et al., 2013; Singh et al., 2000). The northwest Indian coastal water associated with relatively higher salinity and $\delta^{18}O$ than the southern AS (Fig. 3.9d).

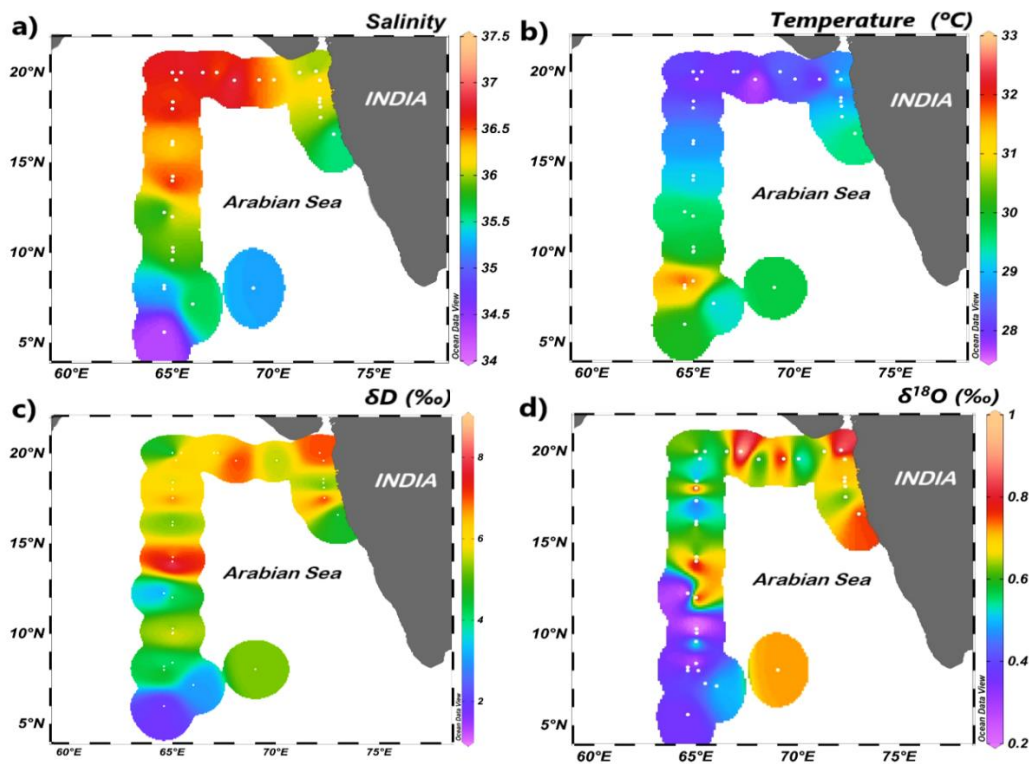


Figure 3.9: Spatial variability of a) Salinity b) temperature c) δD d) $\delta^{18}O$ of surface seawater samples over the AS.

3.3.2. Vertical profile of $\delta^{18}O$, δD , Salinity, and Temperature

Significant variations in the salinity in spatial (horizontal direction at deeper depths) and in the vertical direction along the cruise track were observed over the AS (Figure 3.10 a, b). Higher salinity values were seen from south to northward direction with lower values at the south, and higher in the north. Similar gradients were also observed in the deeper waters but relatively lower changes (horizontal difference) than at the surface (Figure 3.10). These salinity values were consistent with the lower density (contours) water body at the southern AS (Figure 3.10 b). Seawater temperature not varied significantly at the surface as like salinity. However, a significant variation in temperature was observed in the vertical profile with a maximum value of 30.22 °C at the surface, and the minimum at deeper depth 7.12 °C was observed (Figure 3.10 c). The depth (thickness) of higher seawater temperature water body at surface was deeper in the southern AS and shallower at northern AS. The thermocline depth (depth at

which temperature gradient is steepest; ~ 20 °C isotherm) varied all along the cruise track with shallower in the northern AS and at deeper depth in the southern AS (Figure 3.10 c). This vertical variation in the thermocline (20 °C isotherm) depth shows the winter mixing process over the northern AS.

Both $\delta^{18}\text{O}$ and δD varied significantly in spatially (horizontal direction at deeper levels) as well as in the vertical profile (Figure 3.10 d, e). Lower $\delta^{18}\text{O}$ at southern AS and higher $\delta^{18}\text{O}$ over the central to northern AS were observed with overall value ranges from 0.36-1.07 ‰. Lower $\delta^{18}\text{O}$ was seen over the southern and northern AS with a slight increase in $\delta^{18}\text{O}$ in central AS at subsurface water levels (250 – 800 m; Figure 3.10 d). The lowest values of $\delta^{18}\text{O}$ were found at deeper levels (~ 1000 m), and consistent along the north-south direction with very slight variation. A similar variation for the δD with relatively higher values at the surface and with significant vertical variability in δD was observed (Figure 3.10 e). The subsurface water samples were associated with lower δD values than at surface but higher than deeper values (1000 m depth). At S-8, higher δD values were found with increasing depth (a peak values in subsurface water at ~ 400 to 700 m depth).

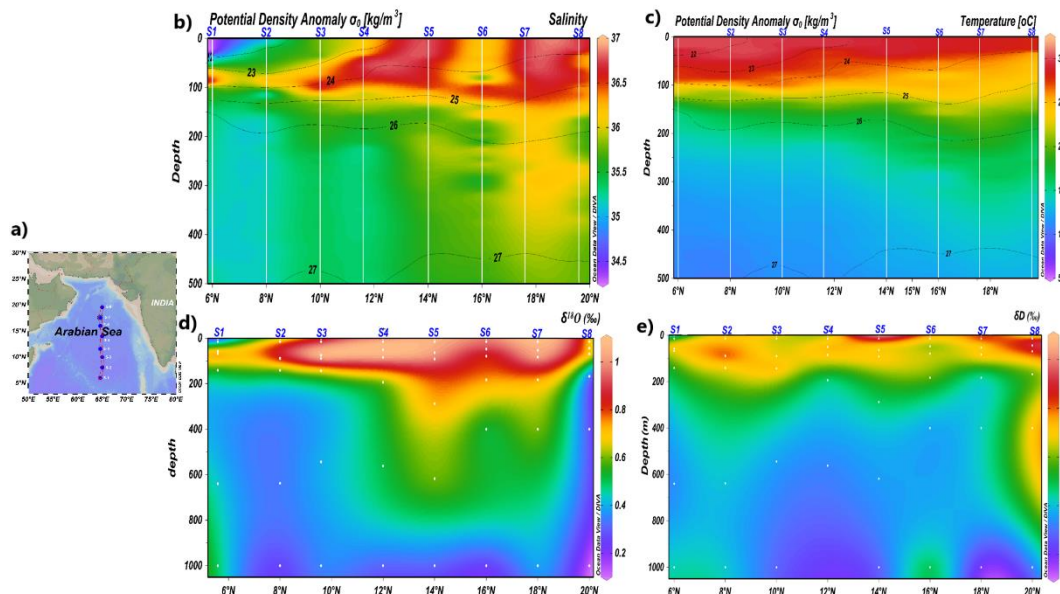


Figure 3.10: Section plots for water samples collected a) sample location, b) salinity, c) temperature d) $\delta^{18}\text{O}$, e) δD . Density contours (black lines) were shown in (a) and (b), Station locations are represented by S-1 to S-8.

The surface water $\delta^{18}\text{O}$, δD , S, and temperature variability were directly related to the upper ocean dynamics and influenced by various processes (such as river runoff, different water bodies mixing, direct precipitation, and evaporation). However, these processes were almost negligible at subsurface and deeper depths. Variations in the subsurface to deeper levels represent the deep-water dynamics (such as vertical mixing, water masses movement), which affects the $\delta^{18}\text{O}$, δD composition of deeper water (Figure 3.11).

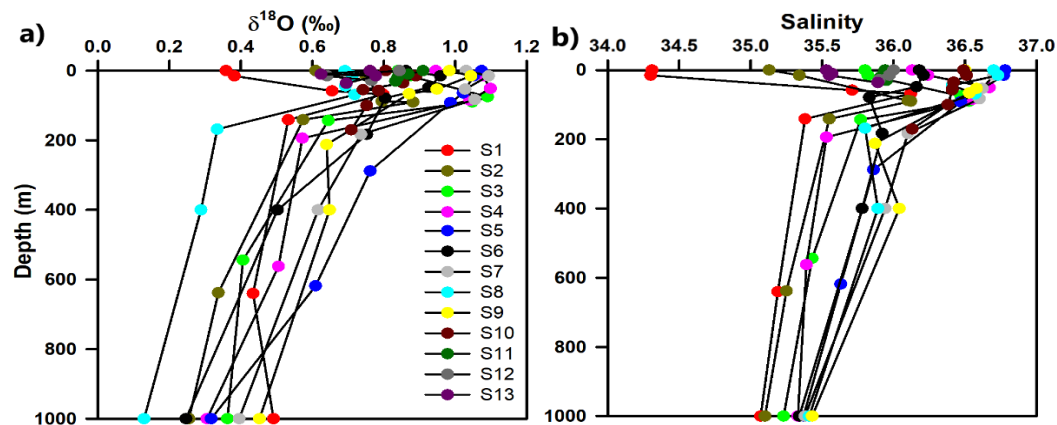


Figure 3.11: Vertical variation of a) $\delta^{18}\text{O}$ and b) S profile over the sampling station.

A significant relations $\delta^{18}\text{O}$ –S and $\delta^{18}\text{O}$ – δD of seawater were observed for all the samples together (from the surface to the deeper water; Figure 3.12). Lowest $\delta^{18}\text{O}$ values were associated with relatively lower salinity deeper waters. The $\delta^{18}\text{O}$ –S showed a linear relationship with slope of $0.35 (\pm 0.03)$ and intercept $-11.84 (\pm 1.12)$ with $r = 0.79$; $p < 0.05$ (Figure 3.12a). Similarly, $\delta^{18}\text{O}$ – δD were associated with slope $5.71 (\pm 0.80)$ and intercept = $0.66 (\pm 0.61)$ with $r = 0.64$; $p < 0.64$ (Figure 3.12b). However, for the surface samples (excluding subsurface and deep water samples), no significant relation was observed.

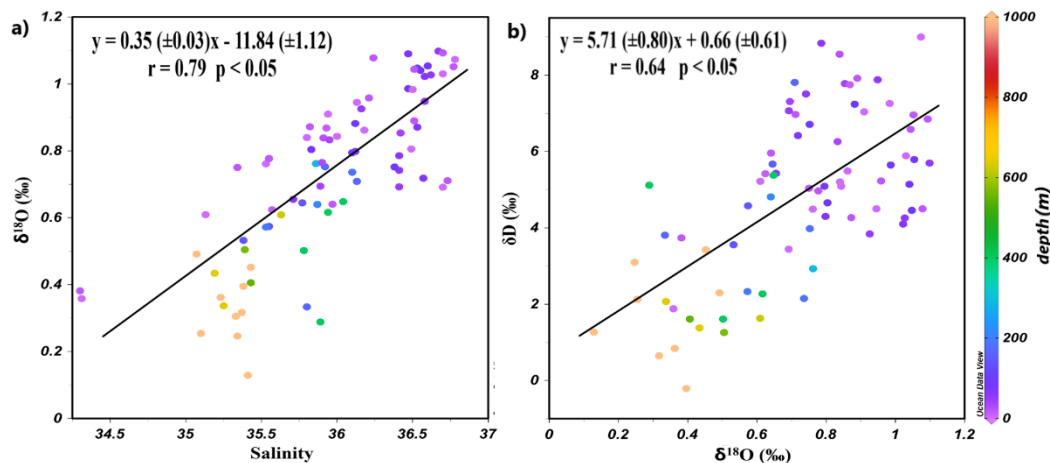


Figure 3.12: a) $\delta^{18}\text{O}$ –S and b) δD – $\delta^{18}\text{O}$ relation for the water samples collected using CTD at a specific depth location. Color represents the water depth for water samples.

3.3.3. Water masses over the Arabian Sea

Significant variations in S and potential temperature (θ) were observed with S varying from 34.1 to 36.7, and potential temperature (θ) ranging from 7.12 to 30.22 °C. Based on the θ –S data from CTD rosette and depth specific water samples, we have identified four different water masses in the AS: namely Bay of Bengal Water mass (BoBW), Arabian Sea High Saline Water mass (ASHSW), Persian Gulf Water mass (PGW) and the Red Sea Water mass (RSW; Figure 3.13a, b). These water masses were identified based on the defined ranges of potential temperature, salinity, and corresponding water density by Prasad et al. (2001) (Discussed in detail in Chapter-1).

The CTD derived and depth specific water sample derived θ –S diagrams show that the ASHSW mass is confined to the shallow water depth, and associated with high salinity, low density with higher temperature values. In our θ –S diagram over the southern AS, low salinity surface water was observed, and it is identified as the BoBW mass (remnants of preceding winter monsoon transported BoB water). The East India Coastal Current (EICC boundary current), followed by the WMC transports low salinity water from the northern BoB to the AS during the winter monsoon (strong transport) followed by the early pre-monsoon (weaker transport; Wyrтки, 1973; Schott

and McCreary Jr, 2001). The Significant variation in the θ -S curve at a water depth of 400 – 600 m was identified as the PGW mass followed by traces of the RSW mass at 850 – 1000 m. For understanding the $\delta^{18}\text{O}$ variation with water masses, another parameter $\delta^{18}\text{O}$ of water was replaced by the water depth in the θ -S diagram (color bar; Figure 3.13c). It shows that the ASHSW mass was associated with higher and RSW mass with relatively lower $\delta^{18}\text{O}$ values (Figure 3.13c).

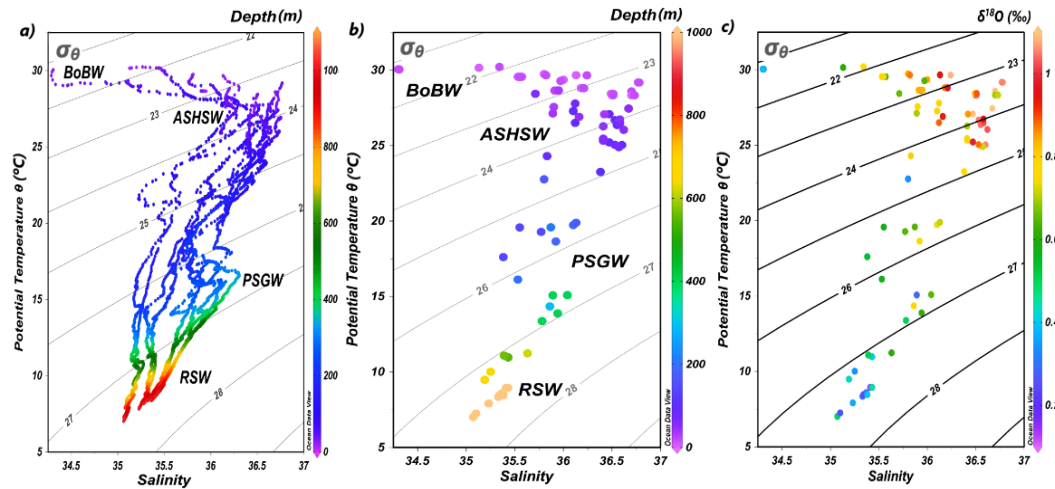


Figure 3.13: Potential temperature and Salinity along with density diagram for water mass identification. **a)** CTD rosette data, **b)** water sample collected at specific depths derived data, **c)** $\delta^{18}\text{O}$ of water sample instead of depth in the z-axis.

3.3.4. $\delta^{18}\text{O}$ -S relation in different Water Masses

To understand the variability of $\delta^{18}\text{O}$, δD , and S of seawater with depth due to various deep-water dynamics, the entire water column was divided into three zones. These zones were selected based on the observed major dominant water masses with specific water depth ranges. The Zone-I represents the water column bounded by the region between 0-250 m water depths and associated with ASHSW mass. The $\delta^{18}\text{O}$ and S range from 0.33 – 1.09 ‰ and 34.3 – 36.78, respectively. Significant relation is observed for $\delta^{18}\text{O}$ -S with slope = 0.27 (± 0.03) and intercept = -8.84 (± 1.20), $r = 0.75$; $p < 0.05$ (Figure 3.14a). However, after removing the influence of BoBW mass at southern AS, no significant change was seen in the $\delta^{18}\text{O}$ -S relation [slope = 0.29

(± 0.05), intercept = $-9.51 (\pm 1.67)$] which might be due to limited points from BoBW mass (southernmost samples only two data points).

The Zone-II represents a region between 250-650 m water depths and associated with PGW mass. The $\delta^{18}\text{O}$ and S range from 0.29-0.76 ‰ and 35.19 – 36.04, respectively. Significant relation is observed between $\delta^{18}\text{O}$ and S with slope = $0.35 (\pm 0.09)$ and intercept = $-11.99 (\pm 3.39)$, $r = 0.81$; $p < 0.05$ (Figure 3.14b).

The Zone-III represent the depth below 650 m up to 1000 m; however, the water samples are collected from ~ 1000 m depth only, so it is considered as 1000 m level. At this depth (~ 1000 m), RSW mass is observed. The $\delta^{18}\text{O}$ and S range from 0.13 – 0.49 and 35.07- 35.43, respectively. However, an insignificant negative correlation between $\delta^{18}\text{O}$ -S was observed (Figure 3.14c).

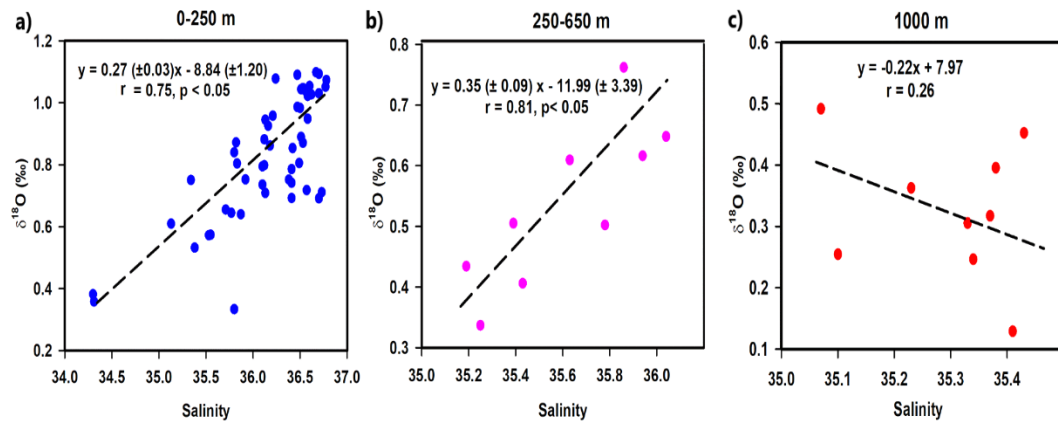


Figure 3.14: $\delta^{18}\text{O}$ - S relation for a) Zone-I (0-250 m; ASHSW), b) Zone-II (250-650 m; PGSW), and c) Zone-III (1000 m; RSW).

3.4. Conclusion

1. New data set on $\delta^{18}\text{O}$, δD and S of surface water samples from the northern Indian Ocean showed significant variations in their relationship. $\delta^{18}\text{O}$ -S relation with higher slope and lower intercept during winter was due to the intrusion of freshwater in BoB.

The $\delta^{18}\text{O}$ – δD relation showed seasonal variation due to the influence of the Himalayan and Peninsular river systems on it. *d-excess*-S relation along with

corresponding $\delta^{18}\text{O}$ values inferred that the 67% of total water samples with $S < 33.5$ and ~73% of total water samples with $S > 33.5$ were influenced by the continental runoff and open ocean water mixing, respectively. Significantly stronger $\delta^{18}\text{O} - \delta\text{D}$ and *d-excess*- $\delta^{18}\text{O}$ relation in BoB inferred that the kinetic fractionation dominated more during winter than in spring.

Low $\delta^{18}\text{O}$ with lower $S (< 32.5)$ over the surface Andaman Sea is due to the freshwater influx from Indian and Myanmar rivers in this region. Subsurface $\delta^{18}\text{O}$ composition off the Andaman Islands suggested gradual enrichment in $\delta^{18}\text{O}$ values with depth. $\delta^{18}\text{O}-S$ relation in the upper layer (0-50 m) waters in the Andaman Sea was similar to BoB surface waters. The preliminary analysis shows statistically different $\delta^{18}\text{O}-S$ relation in deeper water (50-200 m) than for shallow water (0-50 m) that could be a characteristic of water mass dynamics.

2. For the southern Arabian Sea, water samples show lower $\delta^{18}\text{O}$, δD , and S than the northern Arabian Sea, this might be the contribution from winter monsoon transported BoB water. Relatively cooler and higher salinity values over the northern Arabian Sea might be the winter convection remnant of the preceding winter monsoon. Four different water masses were identified with significant variations in $\delta^{18}\text{O}$ and δD composition. Deeper waters are associated with the lower $\delta^{18}\text{O}$ and δD than the surface waters. Our sub-divisional analysis of water column in three zones based on the observed water masses at different water depths shows different $\delta^{18}\text{O}-S$ relation. The stronger positive relations for Zone-I and Zone-II and weaker negative relation for Zone-III are observed.

Chapter-4
***Paleoceanography and paleoclimatology of
the northern Indian Ocean***

Paleoceanography and Paleoclimate of the northern Indian Ocean

The Indian summer monsoon is associated with widespread rainfall over the entire Indian subcontinent, whereas winter monsoon contributes to a significant amount of rain, limited to the southern Indian peninsula. During extreme rainfall events (which have characteristic depleted oxygen isotopic composition: $\delta^{18}\text{O}$) associated with high runoff into the Indian Ocean through the various river, channels are observed and cause significant change in the $\delta^{18}\text{O}$ of the surface ocean (Discussed in details in Chapter-3). Subsequently, these changes are recorded and remain preserved in the Indian Ocean, which can be retrieved back from various archives (bulk sediment, coral reefs, foraminifera species, diatoms); this makes the northern Indian Ocean a big reservoir for understanding past monsoon variability. The northern Indian Ocean (comprises of the Arabian Sea: AS, Bay of Bengal: BoB and the Andaman Sea); though these water bodies are located in the same latitudinal region, because of different influencing processes, they have diverse characteristic isotopic compositions (details in Chapter-

1). This makes each of these basins (AS, BoB, and the Andaman Sea) a unique reservoir to understand monsoon-induced changes in the oceanic conditions.

Based on a variety of established proxies, large amount of work has been already carried out in the Indian Ocean to reconstruct the past monsoon; however, most of the studies are confined to the eastern AS. Very few studies are reported from the BoB, the Andaman Sea and the western AS (details in Chapter-1). In this chapter, results from the study made on three different deep sea-sediment cores from the northern Indian Ocean is presented. Previously published well-dated high-resolution records from sediment cores have been used for verifying coherence and spatial variability of monsoon over the northern Indian Ocean during last ~70 ka.

4.1. The Eastern Arabian Sea: $\delta^{18}\text{O}$ variability and its implication for ISM variability for the last ~ 25 ka

Stable oxygen isotopic composition ($\delta^{18}\text{O}$) of foraminifera from the sediments of the northern Indian Ocean were used earlier to decipher past changes in the intensity of the South Asian Monsoon. (Duplessy, 1982) based on a study involving several sediment cores, showed that the summer monsoon rain was reduced significantly during the Last Glacial Maximum (LGM): $\delta^{18}\text{O}$ of LGM planktonic foraminifera were relatively higher, resulting from reduced freshwater discharge from the major monsoon fed Indian rivers. Likewise, (Sarkar et al., 1990) showed that the winter monsoon rains were intensified during LGM by analyzing four different species of planktonic foraminifera from a sediment core from the Eastern Arabian Sea. These prompted further studies on the high resolution $\delta^{18}\text{O}$ in planktonic foraminifera preserved in marine sediment cores from the locations of rapid sedimentation, both from the Western (Sirocko et al., 1991; Parton et al., 2015) and the Eastern Arabian Sea (e.g., Tiwari et al. 2010); and from the northern (e.g. Kudrass 2001) and the southern Bay of Bengal (Raza et al., 2014b; Raza and Ahmad, 2013). Variation in the rates of sedimentation over the eastern Arabian Sea for last ~20 ka (Narayana et al., 2009) and paleo-productivity from the equatorial Indian Ocean (Beaufort, 1996) have also been studied. Except for the early work of Duplessy (1982), inferences from most

subsequent studies were based on single-core collected at different locations, and most lacked modern calibration for the interpretation of planktonic foraminiferal $\delta^{18}\text{O}$. For instance, Sarkar et al. (2000) used limited data as an approximate calibration to show that the Eastern Arabian Sea responded to the summer monsoon runoff from the Western Ghats of peninsular India. They inferred that the summer monsoon rains steadily increased during the Holocene.

In contrast to the previous studies from the eastern Arabian Sea, (Gupta et al., 2003) surmised that during the Holocene, monsoon winds had significantly *weakened* over the Western Arabian Sea, based on the abundance counts of *G. bulloides*. *G. bulloides* is a planktonic species that lives in eutrophic, high nutrient-rich, and is a low-temperature habitat species. It is believed to be the upwelling indicator species as during upwelling the high nutrient-rich, low-temperature water from subsurface brought to surface make the surface water favorable for the *G. bulloides* growth. However, there was no modern calibration of this proxy, other than the assumption that upwelling is related to the square of the wind strength (Overpeck et al., 1996). This result, bolstered by subsequent reports of speleothem $\delta^{18}\text{O}$ records from Oman (located in the western limit of the South Asian Monsoon;(Fleitmann et al., 2003) and China (East Asian Monsoon, Wang et al. 2005), led to the general acceptance of the weakening summer monsoon trend during the Holocene, in spite of the evidence to the contrary: Kudrass et al. (2001) showed that the monsoon runoff into the BoB had steadily increased from 21 ka (LGM) to ~4ka (see also Sarkar et al., 2000). Tiwari et al. (2010) attempted to reconcile these contrasting findings by suggesting that increased upwelling in the Western Arabian Sea might have suppressed carbonate productivity by favouring silicate productivity, a suggestion yet to be tested (Ramesh et al. 2010).

Three recent developments make it necessary to revisit the reconstructed monsoon variability during the past ~25 ka. First, (Singh et al., 2010) showed that both the slope and intercept of the salinity- $\delta^{18}\text{O}$ relation in the northern Indian Ocean are sensitive to monsoon runoff; the slope (intercept) is higher (lower) during years of enhanced (reduced) runoff. Second, a new, high resolution spatiotemporal $\delta^{18}\text{O}$ data set of 631

seawater samples has become available (Figure 4.1) for testing the assumptions based on which down-core $\delta^{18}\text{O}$ variations were interpreted (Deshpande et al., 2013), *viz.*, the variation in the $\delta^{18}\text{O}$ and salinity of the Eastern Arabian Sea surface is dominantly governed by the summer monsoon runoff from the Western Ghats. Third, an increasing number of sediment cores have been analyzed during the past decade from the Eastern Arabian Sea alone, and high-resolution planktonic foraminifera $\delta^{18}\text{O}$ variations have been reported.

4.2. $\delta^{18}\text{O}$ of seawater variability over the Arabian Sea

4.2.1. The modern salinity- $\delta^{18}\text{O}$ relationship in the Eastern Arabian Sea

The dynamics of the AS and the BoB have been widely studied (Han et al., 2001; Rao and Sivakumar, 2003; Schott and McCreary Jr, 2001b; Wyrcki, 1973). During summer (June to September), the eastward flowing summer monsoon current carries the high salinity water from the AS to the BoB (Kumar and Prasad, 1999b; Vinayachandran et al., 1999). During the summer monsoon, the BoB receives freshwater both from direct rains and runoff from the Ganga-Brahmaputra Rivers. This low salinity water is transported from the BoB to the south-eastern AS during winter (October to February) by the winter monsoon current (WMC) driven by the dry north-easterly winds. The West India Coastal Currents (WICC) carries this low saline water from the south-eastern AS to the northern AS. During the winter monsoon, high precipitation occurs over south-eastern India (the southern states of Tamil Nadu and southeast coastal Andhra Pradesh), while rainfall at this time is quite low over Kerala compared to the summer monsoon. The winter monsoon runoff debouches into the adjacent coastal BoB through the peninsular rivers. As expected, this runoff is also transported to the AS by the WMC.

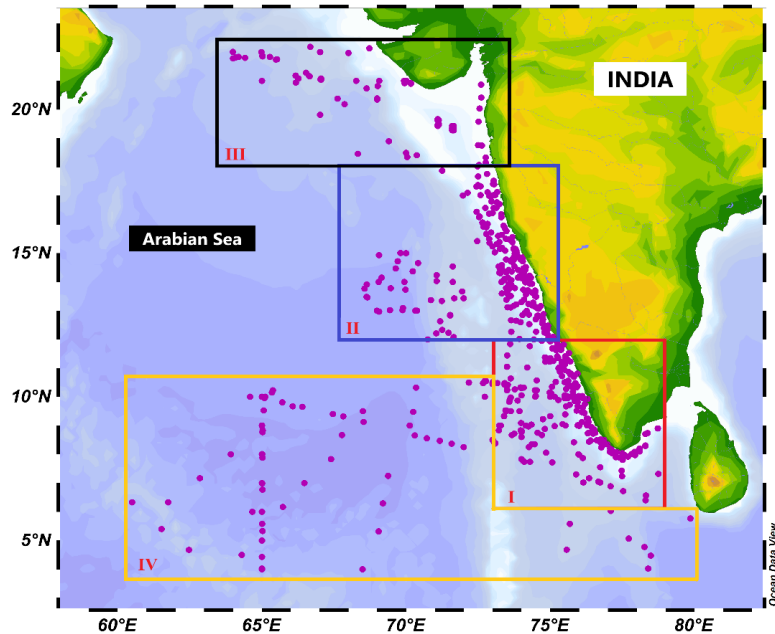


Figure 4.1: Seawater sampling locations in the Eastern Arabian Sea (Deshpande et al., 2013), sub-divided into four regions: **I** 6 °N-12 °N, **II** 12 °N-18 °N, **III** 18 °N-22 °N, and **IV** 4 °N-10 °N/60 °E-80 °E.

Here, we investigate the salinity- $\delta^{18}\text{O}$ relation in the Eastern AS, dividing the later into four major regions (Figure 4.1), three of which fall under the influence of the WICC, and one under the influence of the WMC.

For seawater samples from the region I (6°N-12°N), salinity- $\delta^{18}\text{O}$ relations are shown in Figure 4.2a & b, during monsoon (Jun-Sept), post-monsoon (Oct-Feb), respectively. A significant correlation ($P < 0.05$) between the two is only seen for the post-monsoon (Figure 4.2b). During the southwest monsoon, although the adjoining state of Kerala receives high monsoon rainfall (~2000 mm. Lekshmy et al. 2015), this runoff does not seem to improve the S- $\delta^{18}\text{O}$ correlation. However, during the post-monsoon period (winter season over the Indian sub-continent), low salinity- $\delta^{18}\text{O}$ water from the Bay of Bengal is brought to the southern AS by the winter monsoon current, which appears to improve the correlation significantly.

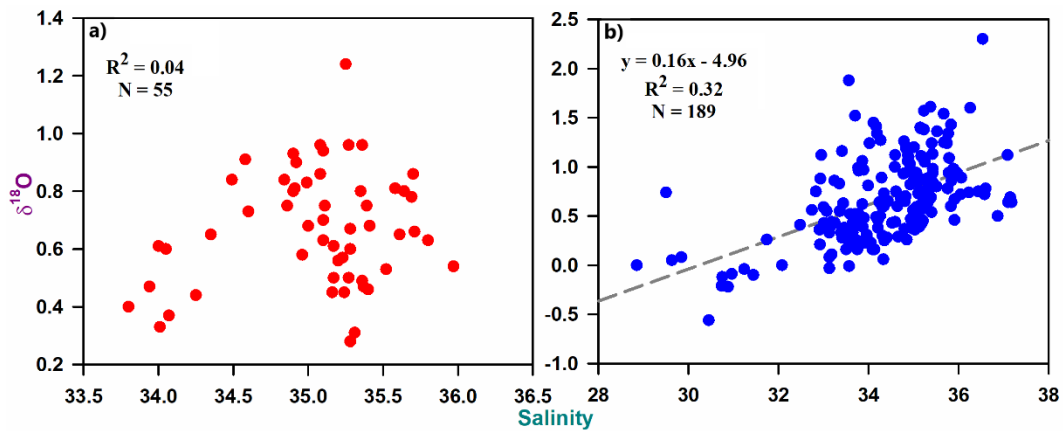


Figure 4.2: $\delta^{18}\text{O}$ – S relation for samples from the region I (6°N - 12°N) **a)** during the summer monsoon (Jun-Sep) insignificant correlation, **b)** post-monsoon (Oct-Feb), correlation is significant at $p < 0.05$.

North of region I, *i.e.*, in region II (12°N - 18°N , Figure 4.1), during both the summer and winter monsoons, significant correlations are observed between salinity and $\delta^{18}\text{O}$ (Figure 4.3a & b). The statistically significant correlation during the monsoon represents the effect of high precipitation (~ 4000 mm, Sarkar et al., 2000) over the Mangalore region of the Western Ghats, which runs off into the Eastern AS.

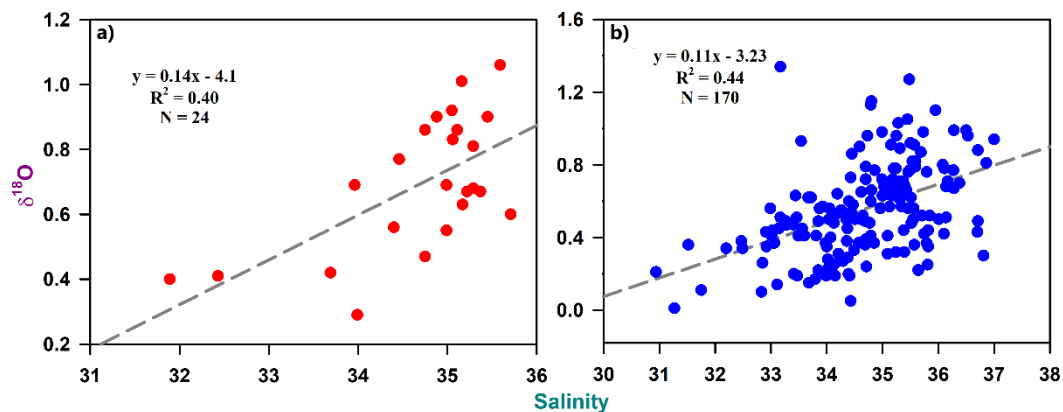


Figure 4.3: Salinity and $\delta^{18}\text{O}$ relations for samples from the region II (12°N - 18°N) during **(a)** summer monsoon (Jun-Sep) and **(b)** post-monsoon (Oct-Feb). Correlations are significant at $p < 0.05$.

In the extreme north-eastern AS, *i.e.*, region III (18°N - 22°N ; Figure 4.1), the samples collected are limited to pre and post-monsoon with few data for the summer monsoon.

The salinity- $\delta^{18}\text{O}$ plot of these data shows a scatter (Figure 4.4). This is because the effect of WICC in this northern region III is not as strong as in the southern regions I and II.

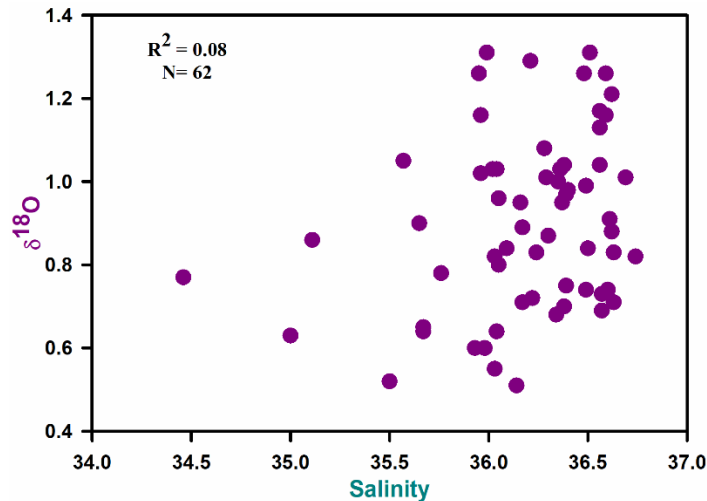


Figure 4.4: Salinity and $\delta^{18}\text{O}$ relations for samples from the region III (18°N - 22°N).

In summary, except for region II that receives copious summer monsoon runoff from the Western Ghats, the summer monsoon runoff from the subcontinent to the Bay of Bengal, propelled by winter monsoon winds towards the AS appears to be the dominant control on the modern salinity - $\delta^{18}\text{O}$ relation in the surface eastern the AS.

Seawater samples from the region IV near the equatorial AS (4°N - 10°N ; Figure 4.1), exhibit a very poor correlation (scatter) between salinity and $\delta^{18}\text{O}$ (Figure 4.5a) during the summer monsoon, whereas during the post-monsoon (winter) the most significant correlation is observed (Figure 4.5b). During this period, low salinity/ $\delta^{18}\text{O}$ water is transported from the Bay of Bengal to the south of the AS, it divides into two branches south of Sri Lanka, one branch moves towards the north of the AS through the WICC and the other, continues to flow westward as a winter monsoon current (WMC; Wyrcki, 1973). The latter appears to cause a high correlation between salinity and $\delta^{18}\text{O}$ over this region during winter, while during summer, poor correlation results from lack of direct overhead precipitation/monsoon runoff to this region.

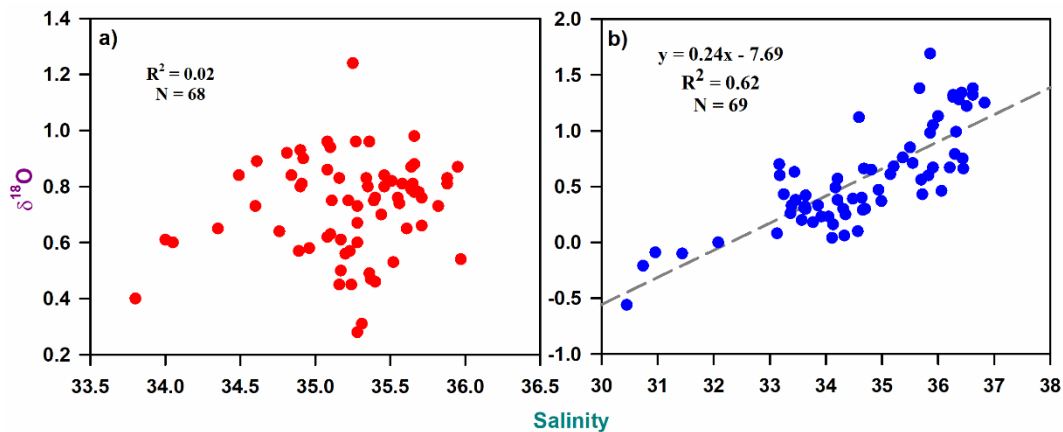


Figure 4.5: The relation between salinity and $\delta^{18}\text{O}$ for samples from region IV (4°N - $10^\circ\text{N}/79^\circ\text{E}$ - 65°E) during **a)** the summer monsoon, insignificant correlation, and **b)** the post-monsoon, significant correlation ($p < 0.05$).

4.2.2. Rainfall-Intercept-Slope relation

The slopes and intercepts of salinity and $\delta^{18}\text{O}$ relationships were obtained for monthly data from Oct-Feb and plotted (Figure 4.6) against the rainfall over southeastern India (data source: <ftp://www.tropmet.res.in/pub/data/rain/iitm-regionrf.txt>). The significant increase is observed in the slopes and decreases in the intercepts of the salinity- $\delta^{18}\text{O}$ relation in regions I& II (left panels of Figure 4.6) and IV (right panels of Figure 4.6), though the data length is limited to a few years. ^{18}O - depleted runoff could also result from the ‘amount effect’: higher rainfall is associated with lower $\delta^{18}\text{O}$ (Araguás-Araguás and Froehlich, 1998; Dansgaard, 1964; Yadava and Ramesh, 2005). Thus the stronger winter monsoon rainfall over southeast India, which is relatively more depleted in ^{18}O (Lekshmy et al., 2015; Srivastava et al., 2015), could also increase the slope and decrease the intercept.

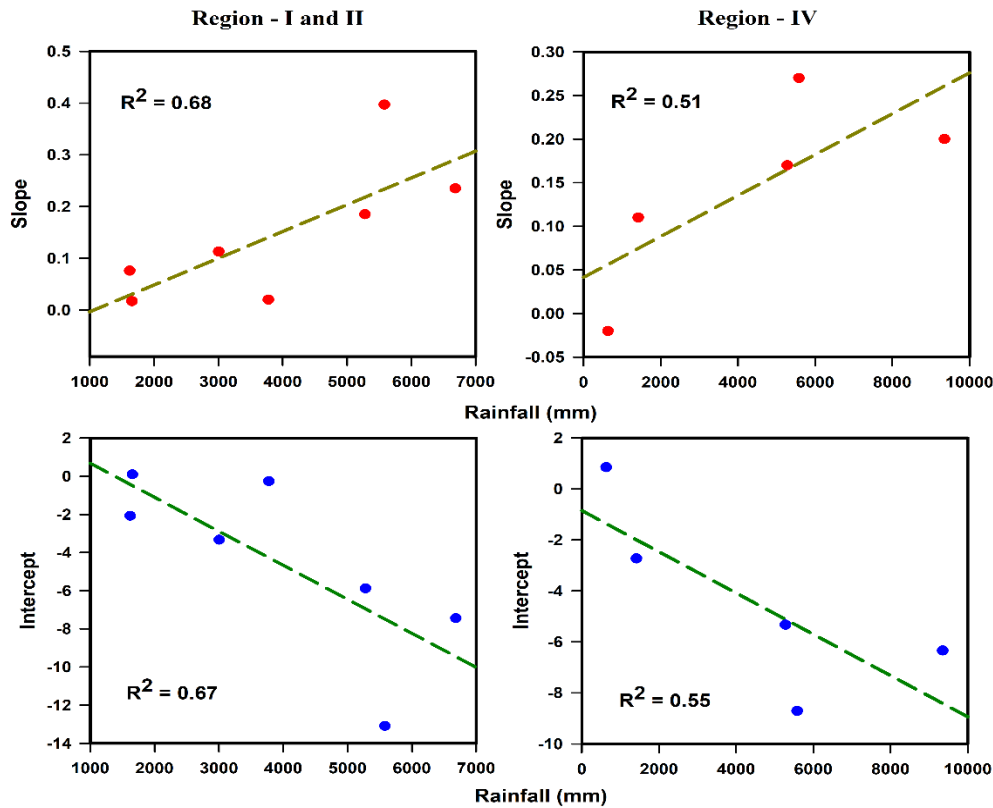


Figure 4.6: Slopes (top) and intercepts (bottom) of the $\delta^{18}\text{O}$ -salinity relations of various data sets are plotted against the corresponding monthly rainfall over southeast India, which is a rough measure of river discharge, left: for regions I and II (6°N - 18°N), right: for region IV (4°N - $10^\circ\text{N}/79^\circ\text{E}$ - 60°E), robust regression was done using MATLAB.

4.2.3. Sediment core studies from the Arabian Sea

Table. 4.1 summarizes the references wherein past variations in the SST, $\delta^{18}\text{O}$ of seawater, and salinity has been reconstructed from different sediment cores from the Eastern AS. The interpretation of planktonic foraminiferal $\delta^{18}\text{O}$ is mostly based on a combination of SST, monsoon runoff, and the global ice-volume effect. Govil and Naidu (2010) claim that the eastern AS surface was $\sim 4^\circ\text{C}$ cooler than the present during the LGM and that there was $\sim 2^\circ\text{C}$ increase from the LGM to the present. Anand et al. (2008) found that during the interstadial periods, the Eastern AS received a higher flux of low salinity water.

For a total of 22 sediment cores, high resolution planktonic foraminiferal $\delta^{18}\text{O}$ have been reported (Table. 4.1) for the four regions of the Eastern AS demarcated in Figure 4.8.

Table 4.1: Sediment cores from the Eastern Arabian Sea that have yielded $\delta^{18}\text{O}$ data on planktonic foraminifera discussed in the text. References 1-6 from region 6 °N-12 °N, 7-10 from 12 °N-18 °N (off the coast of Western Ghats), 11 from the region 18 °N-20 °N, 12-15 from 4 °N-10 °N (Winter Monsoon Current region).

Core sample	Latitude	Longitude	Water depth (m)	Species
SK148/4 ^a	8°12' N	75°54' E	1420	<i>G. ruber</i>
AAS62/2 ^b	11°3' N	74°37' E	800	<i>G. ruber</i>
MD77194 ^c	10°28' N	75°14' E	1222	<i>G. ruber</i>
AAS62/1 ^d	11°3' N	74°37' E	800	<i>G. ruber</i>
SK237-GC04 ^e	10°58' N	74°6' E	1245	<i>G. ruber</i>
GC-5 ^f	10°23' N	75°34' E	280	<i>G. ruber</i>
AAS9/21 ^g	14°3' N	72°39' E	1807	<i>G. ruber</i>
SK-117-GC8 ^h	15°29' N	72°51' E	2500	<i>G. sacculifer</i>
3104G ⁱ	12°55' N	71°45' E	1680	<i>G. sacculifer</i> , <i>G. menardii</i>
3268G5 ⁱ	12°40' N	74°07' E	600	<i>G. sacculifer</i>
SK-17 ^j	15°15' N	72°58' E	840	<i>G. ruber</i>
SL-1 ^k	19°N	65.4	3167	<i>G. ruber</i>
SS3827G ^l	3°42' N	75°54' E	3118	<i>G. ruber</i> , <i>G. sacculifer</i> , <i>G. menardii</i> ,
SK-20-185 ^m	10°N	71°5' E	2523	<i>G. ruber</i> , <i>G. sacculifer</i> , <i>G. menardii</i>
SK-129/CR05 ⁿ	9°21' N	71°59' E	2300	<i>G. ruber</i>
MD900963 ^o	5°03' N	73°53' E	2446	<i>G. ruber</i>
SK-128A-30 ^p	15° 02' N	71°41' E	2000	<i>G. ruber</i>
SK-128A-31 ^p	13°16' N	71° E	2400	
26KL ^q	15°30' N	68°45' E	3776	<i>G. ruber</i>
36KL ^q	17°04' N	69°02' E	2055	
GC-3 ^r	14°36' N	72°86' E	335-355	<i>G. ruber</i> , <i>G. sacculifer</i>
GC-6 ^r	9°15' N	75°78' E		

^a Rao et al., 2010; ^b Rao et al., 2008; ^c Cayre and Bard, 1999; ^d Kessarkar et al., 2013; ^e Saraswat et al., 2013; ^f Thamban et al., 2001; ^g Govil and Naidu, 2010; ^h Banakar et al., 2010; ⁱ Sarkar et al., 2000; ^j Singh et al., 2006; ^k Guptha et al., 2005; ^l Tiwari et al., 2005; ^m Sarkar et al., 1990; ⁿ Pattan et al., 2005; ^o Rostek et al., 1993; ^p Prabhu et al., 2004; ^q Dahl and Oppo, 2006; ^r Thamban et al., 2001.

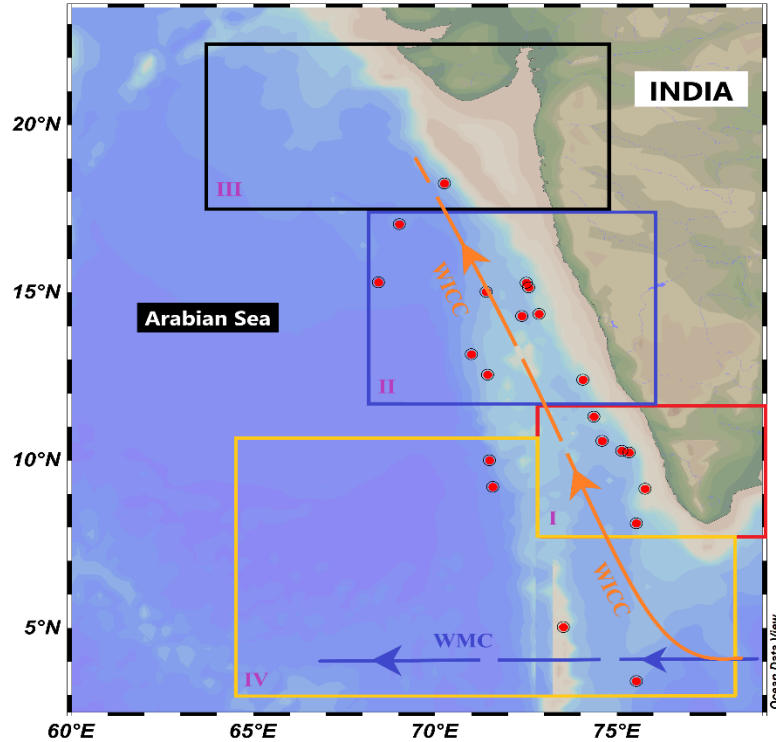


Figure 4.8: Locations of sediment samples from the eastern Arabian Sea studied in this work (see Table 1 for details).

The abundance of the most commonly used foraminifera species (*G. ruber*) in these cores is known to peak during the summer monsoon (Curry et al., 1992). Therefore, it is expected that the sediment core will predominantly record the signals of summer monsoon precipitation. We, however, note that Curry et al. (1992) presented sediment trap data only for two years for the AS. Even the easternmost trap is located west of 70°E (15°30'N and 68°45' E), outside the region of influence of the Winter Monsoon Current (Figure 4.9, Map).

Figure 4.9a shows the abundances of *G. ruber*, in 1986, there is a broad peak covering the period of June to September, but there are some smaller peaks on either side, showing that though the peak abundance is in August, it grows from May (data for 1987) to December (data for 1986). The data are too limited to assume that the oxygen isotope ratio of *G. ruber* near this location reflects entirely of only during summer

monsoon conditions. Oxygen isotope ratios of a minimal number of samples were also presented by Curry et al. (1992). In 1986, the maximum depletion was seen for October 1986 samples (triangles in Figure 4.9b), not during the peak monsoon.

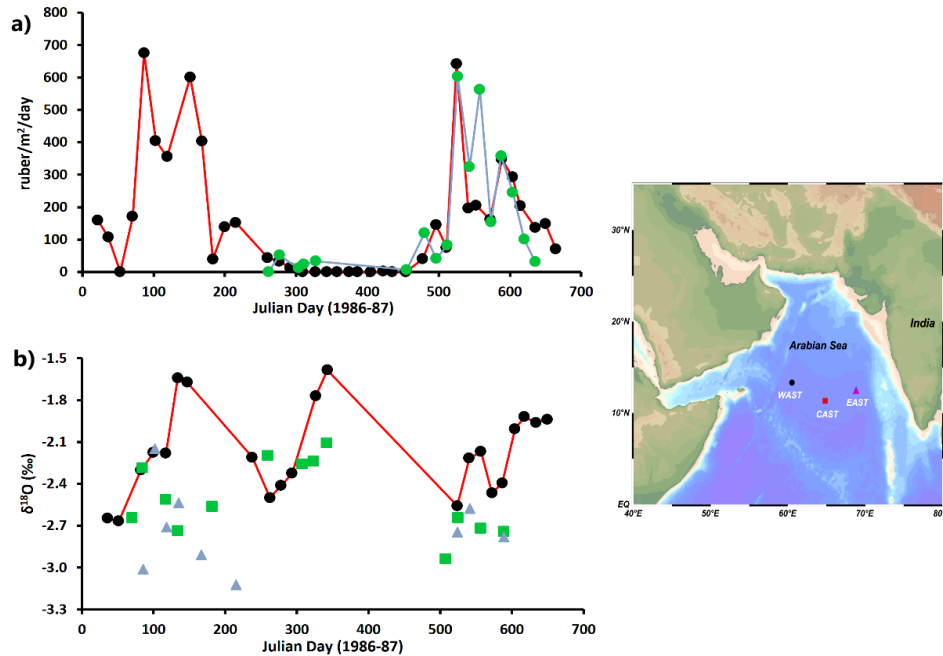


Figure 4.9. A sediment trap data from the central Arabian Sea **a)** abundance variation of *G. ruber* **b)** $\delta^{18}\text{O}$ variation of *G. ruber*. (Curry et al., 1992). EAST: Eastern Arabian Sea Trap [triangle], CAST: Central Arabian Sea Trap [square], WAST: Western Arabian Sea Trap [dot].

It is known that the planktonic $\delta^{18}\text{O}$ is a function of temperature, as well as the $\delta^{18}\text{O}$ of seawater ($\delta^{18}\text{O}_{\text{sw}}$). Thus, it is crucial to deconvolve these influences prior to interpreting foraminiferal $\delta^{18}\text{O}$ as $\delta^{18}\text{O}_{\text{sw}}$ alone. Using Mg/Ca record presented by Saraswat et al. (2013) for the AS, we corrected for the temperature effect on foraminiferal $\delta^{18}\text{O}$.

Figure 4.10 shows data from six sediment cores from the region I (6°N-12°N). During 25 to 17 ka, the monsoon was weaker, as indicated by ^{18}O enrichment in planktonic foraminifera, after correcting for lower temperatures and the global ice volume change, as discussed by the references on the top of each plot. However, none of these records show an increasing $\delta^{18}\text{O}$ trend during the Holocene. If anything, there is a decreasing trend in two of these records (Rao et al., 2010 & Thamban et al., 2001), indicating that

during most of the Holocene, region-I continued to receive more and more low salinity water from the Bay of Bengal through the WICC.

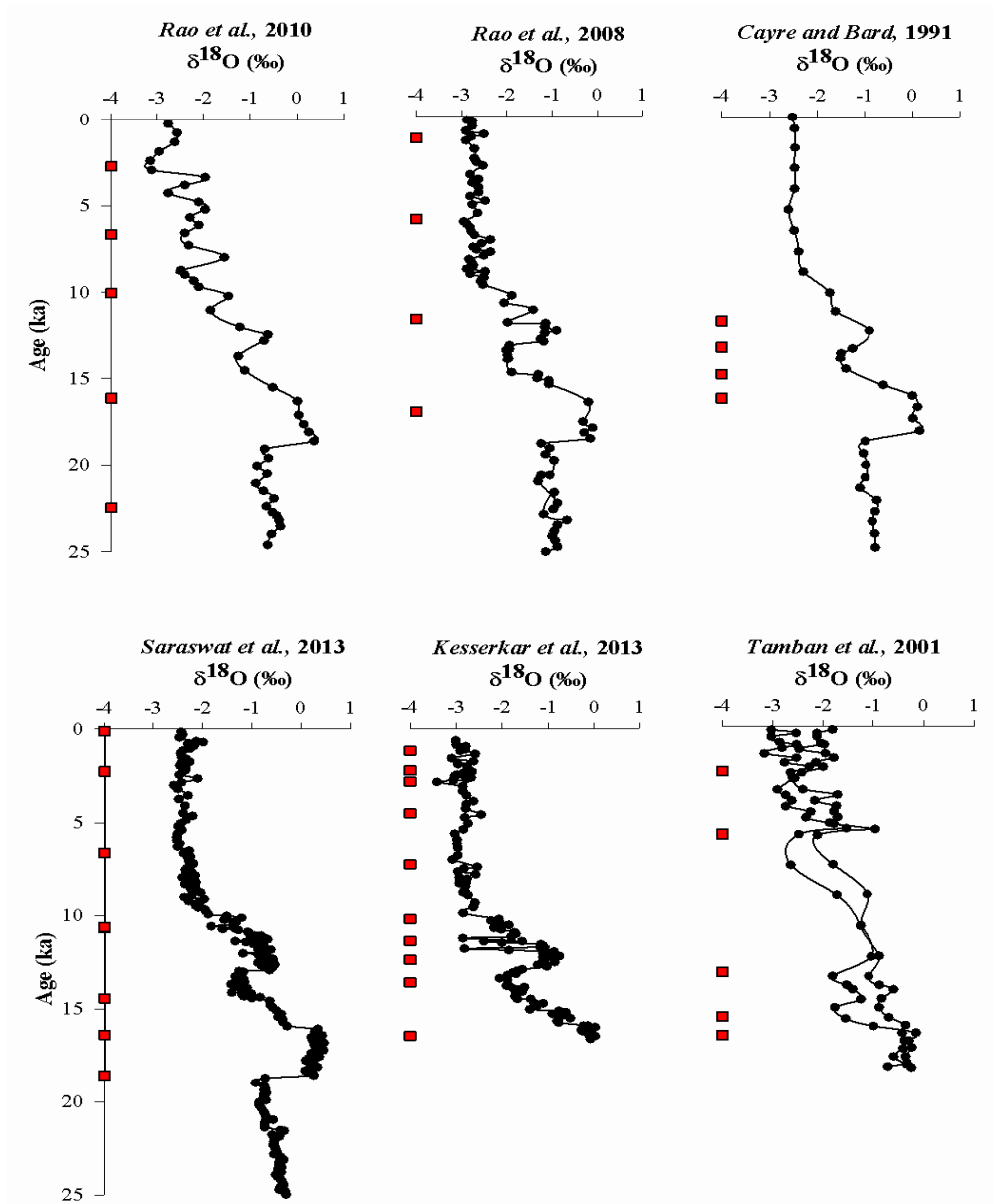


Figure 4.10: $\delta^{18}\text{O}$ records of *G. ruber* (●) and *G. sacculifer* (◆) from various sediment cores from the region I (6°N - 12°N) in the Eastern Arabian Sea. Red squares on the age axes indicate radiocarbon dating horizons.

Figure 4.11 depicts data from five sediment cores from region-II (12°N - 18°N) of the Eastern AS and one core available from region-III (18°N - 20°N). The inference made for the region-I is reconfirmed here: again, from 25 to 17 ka, the summer monsoon was

weaker. Data from Guptha et al., (2005) and Govil and Naidu (2010) clearly support the increasing summer monsoon trend in the Holocene earlier reported by Sarkar et al. (2000).

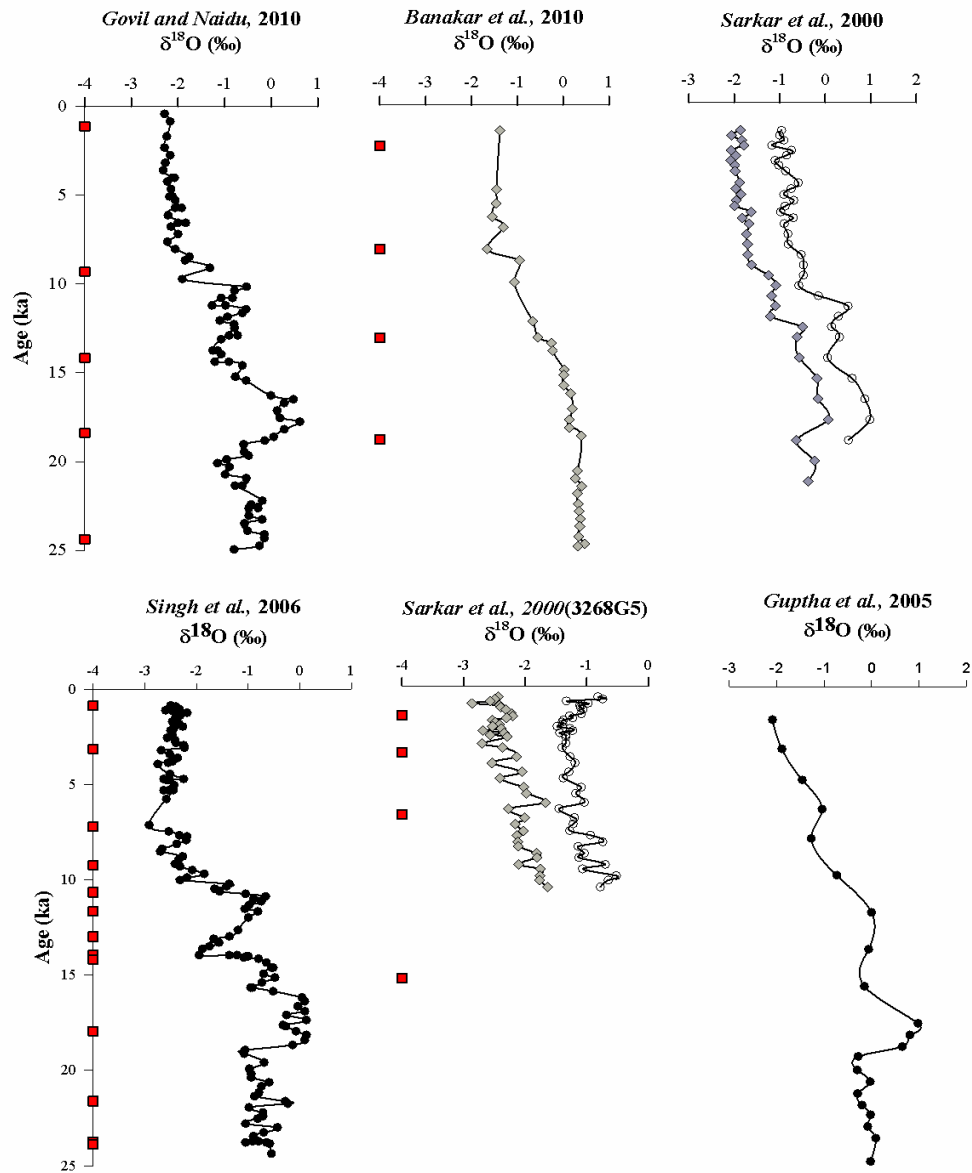


Figure 4.11: δ¹⁸O records of *G. ruber* (●), *G. sacculifer* (◆), and *G. menardii* (o) from various sediment cores from the region II (12°N-18°N) in the Arabian Sea. The bottom right plot refers to sediment core from the region III (18°N-20°N) of the Eastern Arabian Sea. Red squares on the age axes indicate radiocarbon dating horizons.

Four sediment cores were identified from the region-IV (4°N-10°N), where the effect of the winter monsoon current is observed, and the corresponding data are shown in Figure 4.12. These data again reconfirm the strengthening of the summer monsoon trend during the Holocene (Sarkar et al., 1990; Pattan et al., 2005; Tiwari et al., 2005). Further coarse resolution data from some additional cores with poorer chronologies from the Eastern AS (Figure 4.13) indicate that there was no reduction in the monsoon intensity during the Holocene, as found by Fleitmann et al. (2003) in an Omani speleothem. It can also be argued that these records might simply reflect the strength of the WICC and WMC, *i.e.*, decreased volume transport in these currents, in addition to the monsoonal runoff variability into the Bay of Bengal. But to a large extent, the monsoon winds and precipitation over India are correlated (Tiwari et al., 2006), and they are likely to have co-varied in the past. This needs to be tested in the future by comparing paleo-records of wind and run-off proxies in the Bay of Bengal.

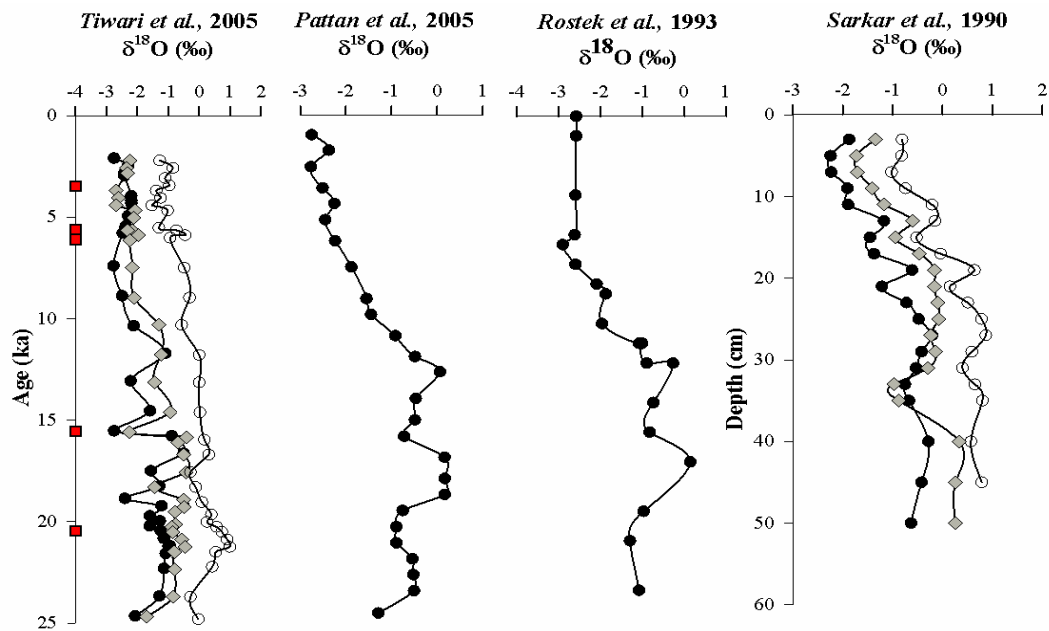


Figure 4.12: $\delta^{18}\text{O}$ records of *G. ruber* (●), *G. sacculifer* (◆) and *G. menardii* (○) from various sediment cores from the Region IV (4°N-10°N) in the Eastern Arabian Sea. Red squares on the age axes indicate radiocarbon dating horizons.

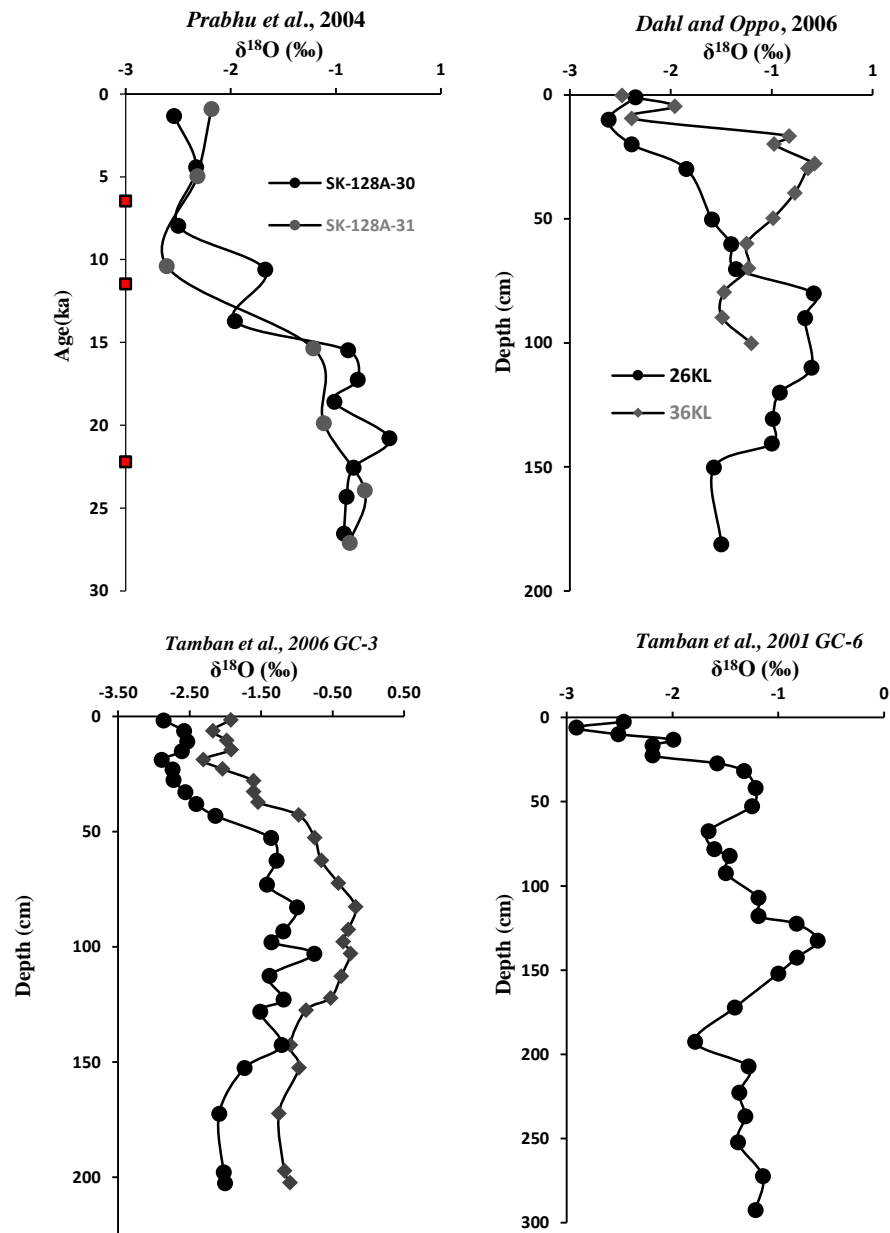


Figure 4.13: Coarse-resolution $\delta^{18}\text{O}$ records of *G. ruber* (●), *G. sacculifer* (◆), and *G. menardii* (○) from some additional sediment cores from the Eastern Arabian Sea, with less chronological control. Red squares on the age axes indicate radiocarbon dating horizons.

4.3. Southern Arabian Sea

Southern Arabian Sea (north of the equator and off Kanyakumari) is a region where the maximum influence of the AS and the BoB water mixing occurs. The influence of the AS and BoB water masses transportation during the different seasons through East

India Coastal Current (EICC) and WICC is prominently observed at this location. These currents transported the freshwater (low saline) from the northern BoB to the northern and western AS during winter and reversed its direction during summer and transport high saline water to the BoB (Wyrski 1973; Shetye et al. 1991). This shows that the southern AS is more strongly influenced by the monsoon-driven freshwater runoff (during summer) to the BoB through various river channels and later transported by the boundary currents during winter.

To understand the past monsoon induced variability over the southern AS, a ~6 m long deep-sea sediment core SK-151-A/3 was retrieved from off Tuticorin from a water depth of ~ 400 m (discussed in detail in Chapter-2, Figure 2.5). Accelerator Mass Spectrometer (AMS) ¹⁴C radiocarbon ages were estimated for mixed planktonic foraminifera assemblages (*Globigerinoides ruber*, *Globigerinoides sacculifer*, *Globorotalia menardii* and *Orbulina universa*).

The age-depth model indicates that the core SK-151-A/3 provides a continuous record of the last ~ 45 – 18 ka (Figure 4.14). The AMS ¹⁴C dates and calibrated ages are given in Table 4.2. The sedimentation rate varies with depth and distance of the land to the basin, which was controlled by the strength of the monsoon and resultant changes in the fluvial system. Changes in the sedimentation rate give preliminary clues about the past variation in the fluvial erosion input, aeolian dust, and marine productivity (Prins et al., 2000).

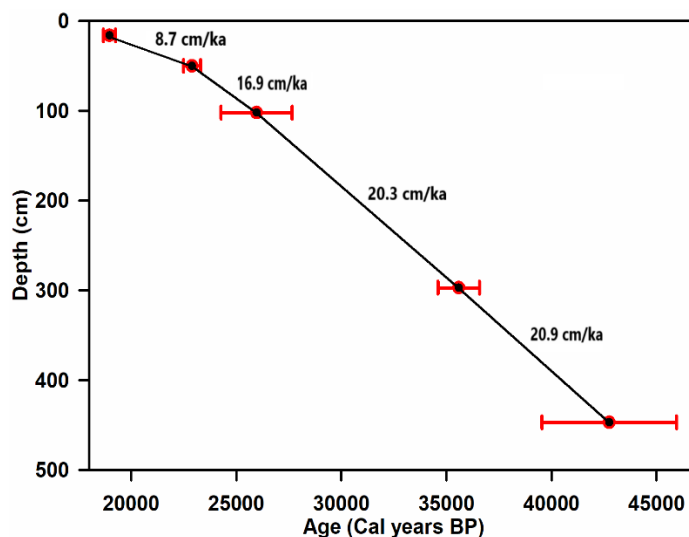


Figure 4.14: Age-depth model of a sediment core from southern AS (SK-151-A/3). Slopes represent the sedimentation rates. The black dots (ages) represent the calibrated ^{14}C AMS ages, and the error bar represents the ranges in ages (for calibrated ages).

Table 4.2: AMS ^{14}C dates and calibrated ages of Sediment core SK-151-A/3.

S. No	Sample	Depth (cm)	Radiocarbon Age (years BP)	Error	Calibrated Age range (1σ)
1.	PRL - 3408	16	16,151	252	18,677 - 19,252
2.	PRL - 3410	50	19,457	354	22,489 - 23,299
3.	PRL - 3412	102	22,311	1651	24,270 - 27,665
4.	PRL - 3416	297	32,144	933	34,597 - 36,574
5.	PRL - 3418	447	39,344	3460	39,547 - 45,946

The subsamples were analyzed for $\delta^{18}\text{O}$ of two planktonic species (*G. ruber* and *G. menardii*) and one benthic species (*Uvigerina peregrina*). The planktonic foraminifera species viz. *G. ruber* and *G. menardii* are present in the surface ocean throughout the year (Anand et al., 2008; Gupta et al., 1997). The planktonic species *G. ruber* lives in the mixed layer, at a mean depth of ~0-25m (MLD; Fairbanks et al. 1980, 1982; Anand et al. 2008) and the thermocline depth species *G. menardii*, at a depth of 100-150 m (TD; Fairbanks et al. 1980).

4.3.1. ISM variability for the last ~ 45 ka

The $\delta^{18}\text{O}$ of *G. ruber* varied from $\sim -0.6\text{‰}$ to -2.00‰ , and *G. menardii* ranged from 0.77‰ to -1.24‰ during the last $\sim 45 - 18\text{ ka}$ (Figure 4.15). The isotopic composition of *G. ruber* and *G. menardii* shows that the ocean environment was varied significantly but still suitable for their habitation during the last $\sim 45\text{ ka}$ (i.e., more negative $\delta^{18}\text{O}$ for shallow-dwelling species, *ruber* and less negative for the deeper dwelling species, *menardii*). However, during the periods of weaker monsoon, the relative difference of *G. ruber* and *G. menardii* changes. Based on the last $\sim 45\text{ ka}$ record of $\delta^{18}\text{O}$ of planktonic foraminifera (*G. ruber*), four intense active monsoon periods were observed; these have relatively lower $\delta^{18}\text{O}$ values (Figure 4.15). Three weak monsoon periods were observed with high $\delta^{18}\text{O}$ values, close to $\sim 0.7\text{‰}$ (Figure 4.15). These strong and weaker monsoon periods were also recorded by the deep-dwelling planktonic species *G. menardii*. Two episodes of intense monsoon periods, followed by a gradual decrease in the monsoon strength during $38-32\text{ ka}$ and $28-22\text{ ka}$, were observed (Figure 4.15). Stronger monsoon during late LGM was observed at $\sim 19-18\text{ ka}$. Previous studies (Sarkar et al. 1990); have shown that during LGM winter, the monsoon was more active than the summer monsoon. As this region is influenced by both winter and summer monsoons, these depleted levels during LGM might represent signatures of the stronger winter monsoon (Figure 4.15).

In addition to the long term variability in monsoon, possibly induced by the global glacials and interglacials (Caley et al., 2011; Clemens et al., 2010; Zhisheng et al., 2011), significant variation within these were observed (Bond et al., 1993; Dansgaard et al., 1982; Heinrich, 1988). Abrupt shifts in the global climate were observed during $\sim 100 - 10\text{ ka}$, but not witnessed such events during the Holocene (Ganopolski and Rahmstorf, 2001; Heinrich, 1988). These short period, global scale abrupt climate events, were recorded in most of the high-resolution terrestrial and marine proxy records, possibly affected the Indian monsoon significantly (Burns et al., 2003; Deplazes et al., 2014, 2013; Dutt et al., 2015; Kathayat et al., 2016; Kudrass, 2001; Schulz et al., 1998; Shakun et al., 2007).

Our study on sediment core provides a continuous high-resolution record for the LGM to ~45 ka, covering the Marine Isotopic Stage-3 (MIS-3) and late MIS-2 (Figure 4.15). MIS-3 (~ 57 to 29 ka) was a warm period, and MIS-2 (~ 29 to 14 ka; LGM) was a cold period. Within MIS-3, global short term intense warm and cold periods were observed. These global cold (warm) events were associated with weaker (stronger) monsoon over the Indian subcontinent (Deplazes et al., 2014; Kudrass, 2001). These cold and warm events during the MIS-3 and MIS-2 were identified as Heinrich Events (HE) and Dansgaard-Oeschger (DO) events, respectively (Dansgaard et al., 1982; Heinrich, 1988; Stocker, 1999).

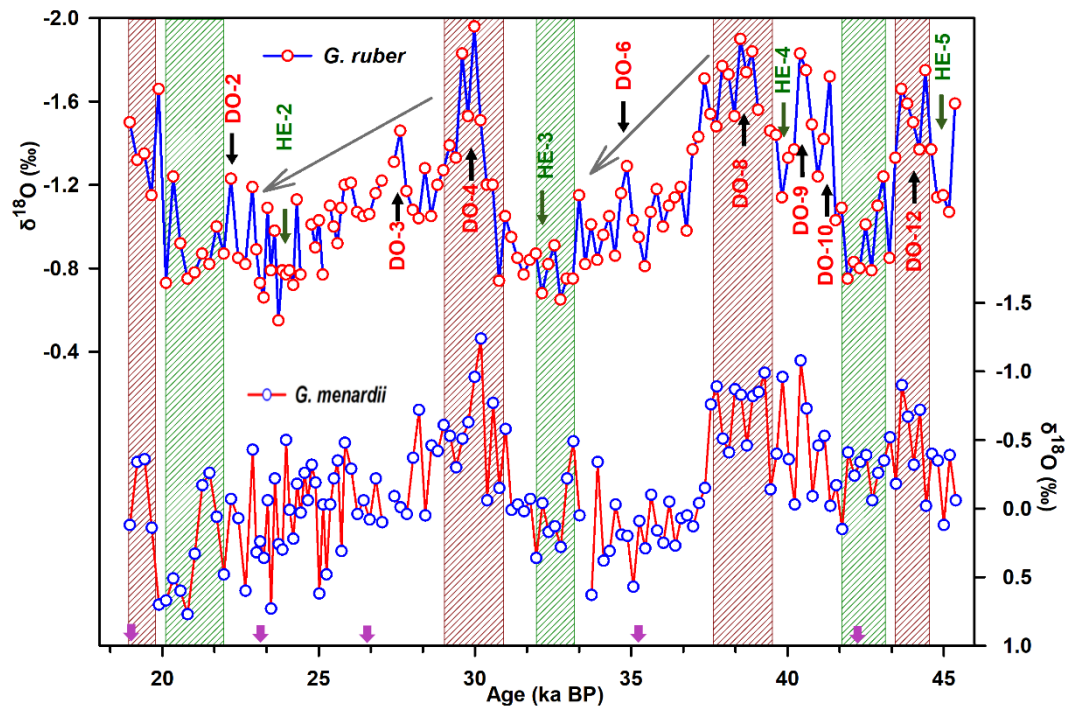


Figure 4.15: Down core $\delta^{18}\text{O}$ variability of planktonic foraminifera species (*G. ruber*: blue curve and *G. menardii*: red curve; DO: Dansgaard-Oeschger Events; HE: Heinrich Events) of sediment core SK-151-A/3 from the southern Arabian Sea. Dark red vertical shades represent active monsoon, and dark green vertical shades represent weaker monsoon periods, purple arrows at the bottom shows the layers where radiocarbon ^{14}C AMS ages were estimated.

Previous studies have shown weakened monsoon conditions over the northern Indian subcontinent during Heinrich events and DO events (Deplazes et al., 2014, 2013; Kathayat et al., 2016; Kudrass, 2001). Our sedimentary $\delta^{18}\text{O}$ record also shows

significant variation in $\delta^{18}\text{O}$ of planktonic foraminifera in response to these short term abrupt global climate events. Relatively stronger monsoon periods were associated with the warm DO events, and the weaker monsoon periods were with the cold Heinrich Events. Abrupt events of monsoon co-relatable with the four Heinrich events (HE-2, HE-3, HE-4, and HE-5) and eight Dansgaard-Oeschger events (DO-2, DO-3, DO-4, DO-6, DO-8, DO-9, DO-10, and DO-12) were observed in our record (Figure 4.14). Significantly changes in $\delta^{18}\text{O}$ of *G. ruber* during these DO events were observed except for DO-2, where variation is small than other events. All were associated with higher $\delta^{18}\text{O}$ values infers weaker monsoon. Similar to *G. ruber*, $\delta^{18}\text{O}$ variability of subsurface species *G. menardii* also followed similar patterns during these abrupt events. The difference between $\delta^{18}\text{O}$ of *G. menardii* and *G. ruber* species was less during the cold Heinrich events, and more during the warm DO events. This suggests that wind-induced mixing was vigorous during cold and was weak during warm events, possibly due to variations in the stratification.

A significant variation in the $\delta^{18}\text{O}$ of benthic species was observed for the last ~ 45-18 ka. $\delta^{18}\text{O}$ variation of benthic foraminifera represents cold and warmer periods and mostly associated with glacial and interglacial changes (Lisiecki and Raymo, 2005; Prell and Kutzbach, 1987; Shackleton, 1969). The benthic species (*Uvigerina peregrine*) $\delta^{18}\text{O}$ ranges from ~ 2.76 to 1.76 ‰ for the last ~45 ka (Figure 4.16). Two extreme cold events (dark red vertical shades) and two very warm events (green vertical shades) were observed during the last ~ 45-18 ka. These intense cold and warm periods were associated with weak and strong monsoon conditions.

The $\delta^{13}\text{C}$ of benthic foraminifera varied from -0.01 to -1.32 ‰ for the last ~ 45 to 18 ka (Figure 4.16). It varied opposite to the $\delta^{18}\text{O}$ variation, with trends of low value in the warm events and higher values during the cold events. Two extreme high-value events, during ~ 29 to 27 ka and ~ 42- 41 ka, were observed in $\delta^{13}\text{C}$ data of the benthic foraminifera. Lowest values in the data were observed during ~36-30 ka; however, during this period, significant changes in the $\delta^{18}\text{O}$ were not found (Figure 4.16).

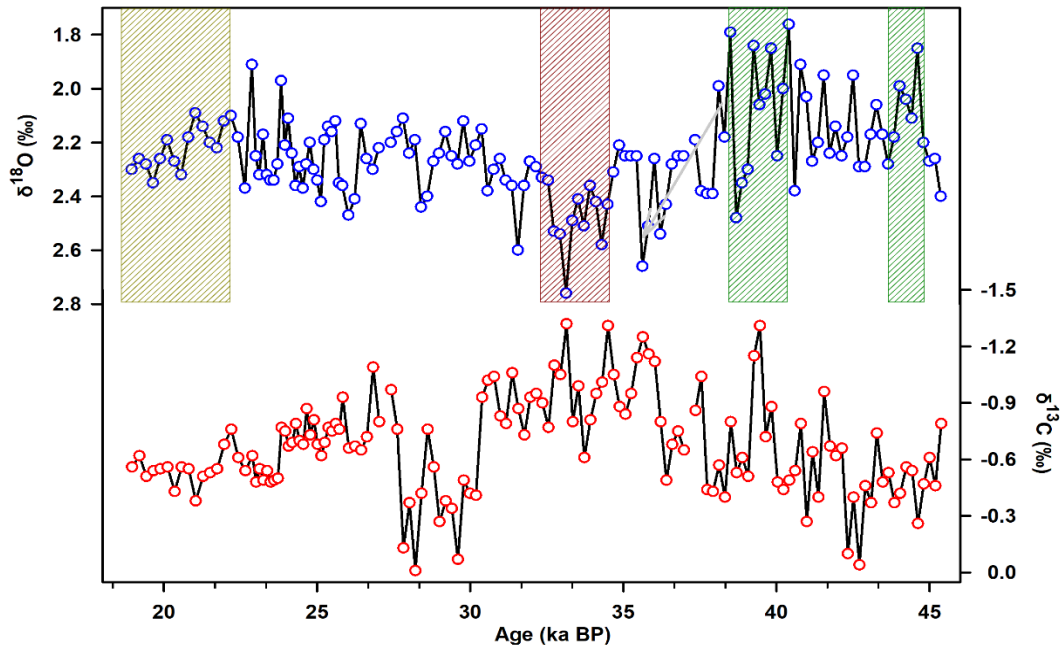


Figure 4.16: Downcore variability of $\delta^{18}\text{O}$ (blue curve) and $\delta^{13}\text{C}$ (red curve) of benthic foraminifera (*Uvigerina peregrina*). Patches are used to discuss extreme variations.

4.4. The Bay of Bengal

The BoB is an ideal place to understand the variability in the monsoon fed riverine input during the past. It is dominated by high riverine input, and direct precipitation than evaporation makes BoB a well stratified and low saline water body. The salinity increases from north to southern BoB (as moves away from the freshwater source regions). Very few studies have attempted to monsoon reconstruction from BoB (based on $\delta^{18}\text{O}$ -foraminifera), and showed that during the Last Glacial Maximum Indian summer monsoon was weaker (Cullen, 1981; Duplessy, 1982; Kudrass, 2001; Rashid et al., 2007; Raza et al., 2014b) and winter monsoon was stronger (Sarkar et al., 1990). During LGM, the temperature was lower by 2-3 °C (Rashid et al., 2007), and salinity was higher by 1-2 (psu) than the present values (Cullen, 1981; Kudrass, 2001).

The surface biological productivity high over the BoB due to the monsoon induced surface dynamics but yet remains significantly lower than that observed in the AS. The high influx of freshwater riverine input makes the BoB a well-stratified water body which restricts the wind-induced vertical mixing (Gomes et al., 2000; Madhupratap et

al., 1996b; Prasanna Kumar et al., 2002). Previous studies have shown, high productivity and downward particle flux were observed during the summer monsoon (Guptha et al., 1997). Small scale oceanic eddies play an essential role in increasing the productivity in BoB, by supplying a significant amount of nutrients in the photic zone through upward pumping of nutrient-rich subsurface water (S. P. Kumar et al., 2007; Prasanna Kumar et al., 2004b; Vidya and Kumar, 2013; Vinayachandran and Mathew, 2003). During the periods of reduction in freshwater influx, direct precipitation, and during stronger winter monsoon season; the surface water becomes relatively denser, which initiates the vertical mixing, and hence, the stratification over the BoB is disturbed. Cold and dry winter monsoon winds increase the evaporation and cause the surface water to cool further, which enhances convective mixing in the BoB. This seasonal variation of convective mixing might be prolonged and become stronger during the cold and weak monsoon periods, such as glacial periods (e.g., LGM), and affects the productivity over the BoB.

During the high surface productivity, organic carbon in the marine system plays an important role by consuming a significant amount of atmospheric carbon dioxide (CO₂), and their preservation in the sediments causes long term sink for CO₂ (Wollast and Billen, 1981). Due to high biological productivity and elevated sedimentation rates, continental margins are the hot spots for most of the carbon burial in the oceans (e.g., Premuzic et al. 1982; Smith and Mackenzie 1987; de Haas et al. 2002). The stable isotopic composition of organic carbon ($\delta^{13}\text{C}_{\text{org}}$) variations can help to understand the sources for total organic carbon during different climatic conditions (glacial and interglacial periods). The C4 plants have $\delta^{13}\text{C}$ values higher than -20 ‰ whereas for C3 plants less than -20 ‰.

Nitrogen is a critical nutrient in marine ecosystems and limits the growth of marine life over most of the oceans (Falkowski, 1997). Measurements of nitrogen isotope ratios ($\delta^{15}\text{N}$) in marine sediments provide a unique way of understanding the past and present marine nitrogen cycle and its relationship to climate change with time. $\delta^{15}\text{N}$ compositions of sedimentary organic matter potentially reflect biological processes in

water columns, such as denitrification (Altabet et al., 1995; Ganeshram et al., 1995), nitrogen fixation (Haug et al., 1998), and the degree of nitrate utilization by algae (Altabet and Francois, 1994; Holmes et al., 1996; Robinson et al., 2004). However, alteration may occur (through various ways or processes; e.g., diagenesis) before the signal of $\delta^{15}\text{N}$ of exported production is buried. As compared with the AS, the BoB is under-represented in paleoclimate and paleoceanographic perspective. In terms of paleoproductivity, no significant results have been reported so far, except Pattan et al. (2013).

A ~ 4.85 m long sediment core (SK-336-GC-I) was retrieved from the western BoB for understanding paleo-productivity variability. The age-depth model shows SK-336-GC-I gives a continuous record for last ~16ka (Figure 4.17). The AMS ^{14}C ages and calibrated ages are given in Table 4.3. The age model indicates that the core SK-336-GC-I provides a continuous record of the last ~ 16 ka. A significant variation in the sedimentation rate was observed, as shown by changes in the slope (Figure 4.17).

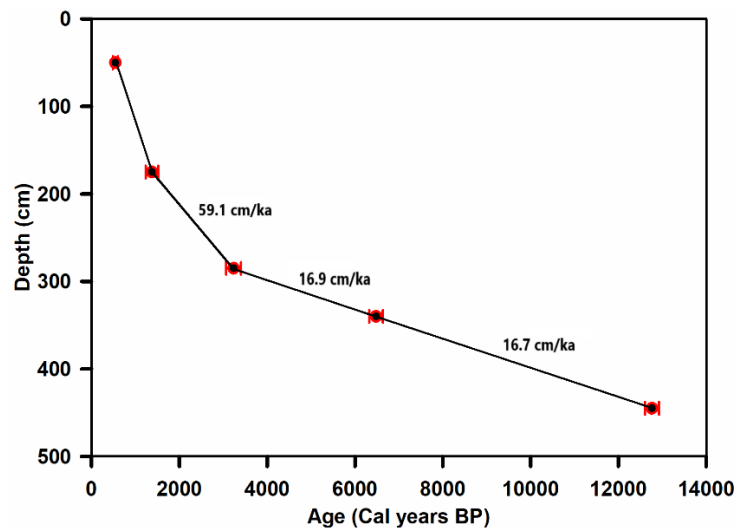


Figure 4.17: Age-depth model of a sediment core from western BoB (SK-336-GC-I). Slopes represent the sedimentation rates. The black dots (ages) represent the calibrated ^{14}C AMS ages, and the error bar represents the ranges in age (for calibrated ages).

Table 4.3: AMS ^{14}C dates and calibrated ages of Sediment core SK-336-GC-I.

S. No	Sample	Depth (cm)	Radiocarbon Age (years BP)	Error	Calibrated Age range (1 σ)
1.	PRL - 3403	50	523	118	430 - 541
2.	PRL - 3404	175	2,318	126	1,234 - 1,518
3.	PRL - 3405	285	3,900	123	3,065 - 3,407
4.	PRL - 3406	340	6,571	132	6,324 - 6,637
5.	PRL - 3407	445	11,781	155	12,606 - 12,927

4.4.1. Paleoproductivity variability for last ~16 ka

The 4.85 m long sediment core (SK-336-GC-I) provides continuous records of the last ~16 ka, and samples were analyzed for $\delta^{15}\text{N}$, $\delta^{13}\text{C}_{\text{org}}$, and N & C_{org} (wt. %). The $\delta^{13}\text{C}_{\text{org}}$ values ranged from -24.19 to -15.14 ‰ during the last ~16 ka, with maximum depletion was observed during ~6 ka (Figure 4.18a). However, a strong reduction (a spike) was observed with value -24.19 ‰ in the recent sediment. During the early deglacial to early Holocene (~16 – 8 ka), a depleting $\delta^{13}\text{C}_{\text{org}}$ trend was observed, followed by an increasing trend until present (~8ka – present). During Holocene, $\delta^{13}\text{C}_{\text{org}}$ was observed as ~ -20.5 ‰ (Figure 4.18a). The $\delta^{13}\text{C}_{\text{org}}$ data was associated with depleted values during Holocene (average value < -20 ‰) and during deglacial periods (16-11 ka) associated with higher values (> -20 ‰), which show the C4 plants contributed significantly during the deglacial period (Figure4.18a). Similar variations with higher values during the cold events: (MIS 2 - 4) observed in the sediment core records from the AS, BoB, and Andaman Sea (Fontugne and Duplessy, 1986).

Overall, $\delta^{15}\text{N}$ of bulk sediment varied from 3.76 - 6.88 ‰ with maximum enrichment during early deglacial and present, whereas the maximum depletion was observed around the mid-Holocene (~ 4 - 5 ka; Figure 4.18b). An increasing trend in $\delta^{15}\text{N}$ of the bulk sediment was observed between the mid-Holocene to the present. During the early Holocene, $\delta^{15}\text{N}$ was ~ 5 ‰, which is higher than the mid-Holocene but lower than the early deglacial and recent sediments. Significant variability, with an overall decreasing trend, was observed during ~16 – 8 ka. $\delta^{15}\text{N}$ having high values during the deglacial and then becomes low during the early to mid-Holocene (~8 – 4 ka); might be due to decrease in the productivity and denitrification (e.g., Altabet et al. 2002) owing to the

enhanced stratification induced by variation in the monsoon intensity during early to mid-Holocene over the BoB (Figure 4.18b).

Significant variations in the C_{org} (wt %) and N (wt %) were observed during the last ~16 ka (Figure 4.18c, d). The C_{org} (%) and N (%) values varied from 1.26 to 3.23 (%) and 0.06 to 0.15 (wt %), respectively. A spike in higher C_{org} value (~ 3.23%) was observed in the recent sediment during the mid-Holocene and late deglacial period (excluding the spiked value), and minimum values were observed during the early deglacial and the present sediment samples (Figure 4.18c). During the early Holocene, the mean C_{org} was ~1.8 %, which was less than the mid-Holocene and late deglacial but higher than the early deglacial and the present sediment samples. During early to late deglacial, an increasing C_{org} was observed with lower values during the early Holocene (~8 - 10 ka) followed by an increasing and then decreasing trend in C_{org} values during (~8 – 4 ka) and (~4 ka - present), respectively. Similar to the C_{org} (wt %), N (wt %) values also show an overall increasing trend during deglacial to early Holocene and decreasing trend during early Holocene to present samples (Figure 4.18d). During the early Holocene, the mean N (~ 0.12 %) was relatively higher than the present and the early deglacial sediment samples. The range of C_{org} (wt %) values observed at our study site is similar to the values estimated in the eastern and central BoB (Fontugne and Duplessy, 1986), and western BoB (Krishna et al., 2013; Phillips et al., 2014). C_{org} composition can be influenced by productivity as well as by the terrestrial organic carbon fluxes (Burdige, 2005) and by the rate of decomposition (Canfield, 1994; Versteegh and Zonneveld, 2002). A higher sedimentation rate can also influence C_{org} content since it may suppress oxygen exposure required for the decomposition (Müller and Suess, 1979).

Large fluctuations in the record of C/N ratios were observed during the last ~16 ka; with an overall decreasing trend during deglacial and increasing trend during the Holocene (Figure 4.18e). C/N ratios ranged from 12.65 - 22.75, with an average value of ~ 17.75 during the last ~ 16 ka. The lowest C/N ratios were observed during the early Holocene (Figure 4.18e).

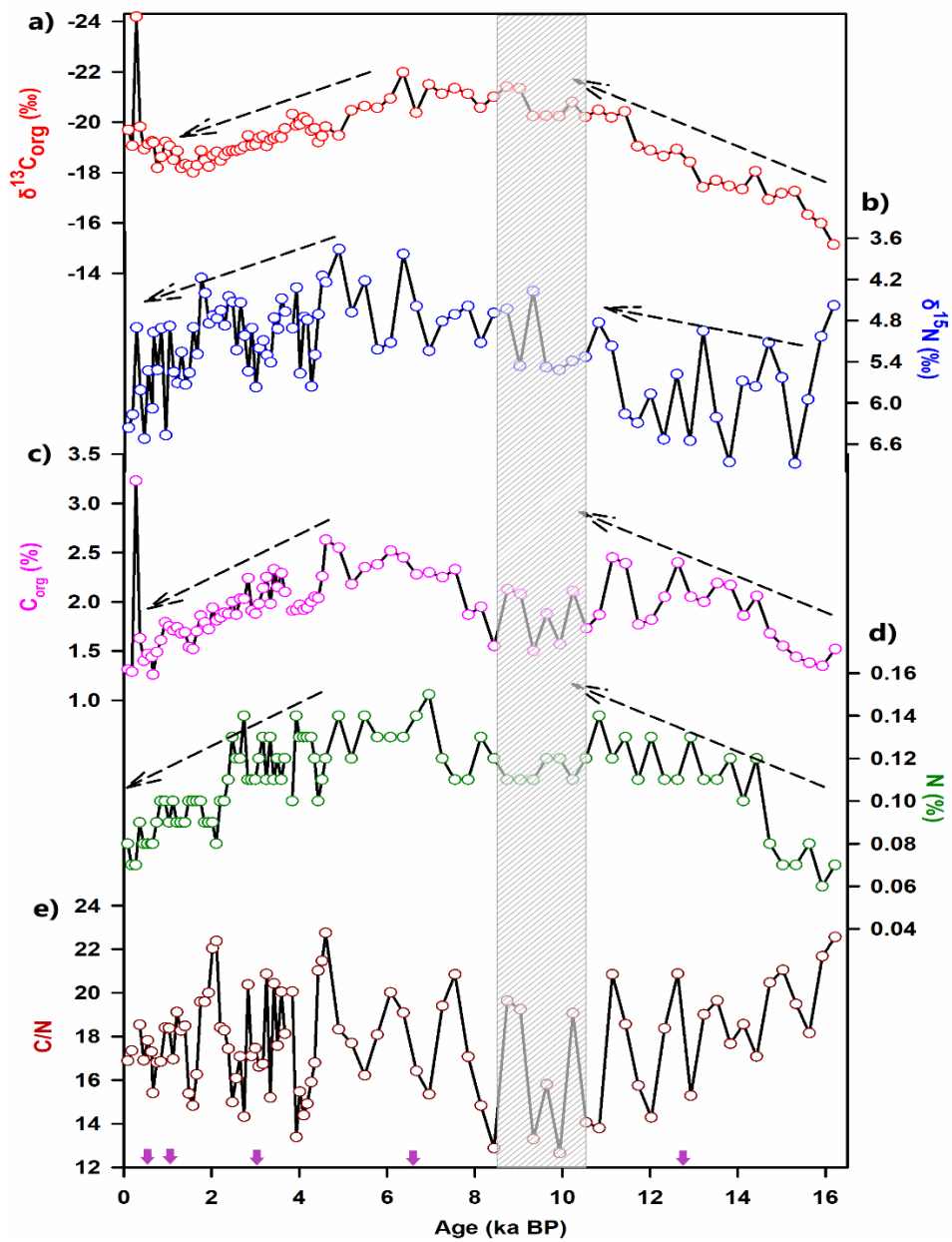


Figure 4.18: Downcore variation of **a)** $\delta^{13}\text{C}_{\text{org}}$ **b)** $\delta^{15}\text{N}$ **c)** C_{org} (wt %) **d)** N (wt %) and **e)** C/N ratio of bulk sediment of SK-336-GC-I core from the western Bay of Bengal. Purple arrows at the bottom (x-axis) show the layers where radiocarbon ^{14}C AMS ages were estimated.

Considerable variation in the regional productivity over ocean during different climatic conditions (such as glacial and interglacial periods), with some regions experiencing

an increase of productivity during warmer periods (Pedersen, 1983; Schrader, 1992), and in other regions during cold periods were observed (Kumar et al., 1993; Otto et al., 1995). Our data shows relatively higher productivity conditions during the deglacial than during the Holocene (increasing C_{org} and $\delta^{15}N$ trends). During the early deglacial period, a weak summer monsoon and relatively stronger northeast monsoon might result in a favorable condition (less-stratified water column, evaporative cooling induced density convective mixing) for increased productivity than those during the Holocene.

The overall variations in the bulk sediment $\delta^{13}C_{org}$ and C/N ratios from the BoB show a mixed influence of terrestrial and marine input during the deglacial to the late Holocene (16 ka to present). It triggers the need for additional analysis of multiple geochemical proxies for a clear and better understanding of terrestrial and marine sources of the organic matter.

4.5. The Andaman Sea

The Indian Summer Monsoon is a primary source of freshwater to all major river systems of India, Bangladesh, Pakistan, and Myanmar. As all these rivers finally debouch into the Indian Ocean and make it a potential region for studying the variations in the freshwater discharges (river runoff/direct precipitation) which is primarily modulated by the ISM (Milliman and Meade, 1983; Mohanty et al., 2008; Rashid et al., 2007). The BoB and the Andaman Sea (Colin et al., 1999, 1998) in the north-eastern Indian Ocean gets a significant supply of freshwater during summer monsoon through the rivers like Ganga, Meghna, Brahmaputra, Irrawaddy and Salween (Subramanian, 1996, 1993). These river systems makes the northern BoB always fresher than the southern BoB with a salinity gradient of ~ 0.2 per degree latitude (Sijinkumar et al., 2016) and this low saline water later is transported to the other basins through the boundary currents (Schott and McCreary Jr, 2001b; Vinayachandran and Kurian, 2008; Wyrтки, 1973).

The previous planktonic foraminiferal $\delta^{18}\text{O}$ based studies from the Indian Ocean showed weaker ISM (Duplessy, 1982; Kudrass 2001) and stronger winter monsoon than the present during the LGM (Sarkar et al., 1990). Based on upwelling indices such as the abundance of planktonic foraminiferal species (*e.g.*, *Globigerina bulloides*) and variability in eolian inputs, the strength, and timing of the past monsoon winds were inferred from sediment records of the western AS (Gupta et al., 2003; Singh et al., 2016). Paleo-monsoon reconstruction studies based on sediment cores from the Andaman Sea (Ahmad et al., 2000; Colin et al., 1999, 1998; Naqvi et al., 1994; Rashid et al., 2007) have reported glacial-interglacial variations in the surface water characteristics of Andaman Sea (Ahmad et al., 2000, 2008). Fossil records from the Andaman Sea showed variation in the productivity, maximum abundance, and excellent preservation of pteropods during the stadial periods (Sijinkumar et al., 2015, 2010b). Based on the paired Mg/Ca and $\delta^{18}\text{O}$ data on the planktonic foraminifer shells, Rashid et al. (2007) showed rapid changes in climate during the last deglaciation and Holocene including substantial changes in the Indian Ocean monsoon system. Sijinkumar et al. (2016) showed that the Andaman Sea was relatively fresher in comparison to BoB surface waters during LGM probably due to the semi-enclosed nature of the Andaman Basin.

While there are a good number of studies aimed at reconstructing the paleo-monsoon from the foraminiferal $\delta^{18}\text{O}$ records from the Andaman Sea, very few studies tried to examine the relative differences of $\delta^{18}\text{O}$ between the species dwelling within the Mixed Layer Depth (MLD; *G. ruber* and *G. sacculifer*; Fairbanks et al., 1980, 1982; Anand et al., 2008) and the Thermocline Depth (TD; *G. menardii*), which can give clues to the past changes in the upper ocean stratification (*e.g.*, Singh et al., 2016). Therefore, here I discuss new results on $\delta^{18}\text{O}$ of *G. sacculifer* (MLD species) and *G. menardii* (TD species; Fairbanks et al., 1980) from a core SK-234-60 from the Andaman Sea (Figure 4.19). The two planktonic species from different habitat depths were used to examine the freshwater-induced stratification in the Andaman Sea, and its variation with related to paleo-monsoon intensity.

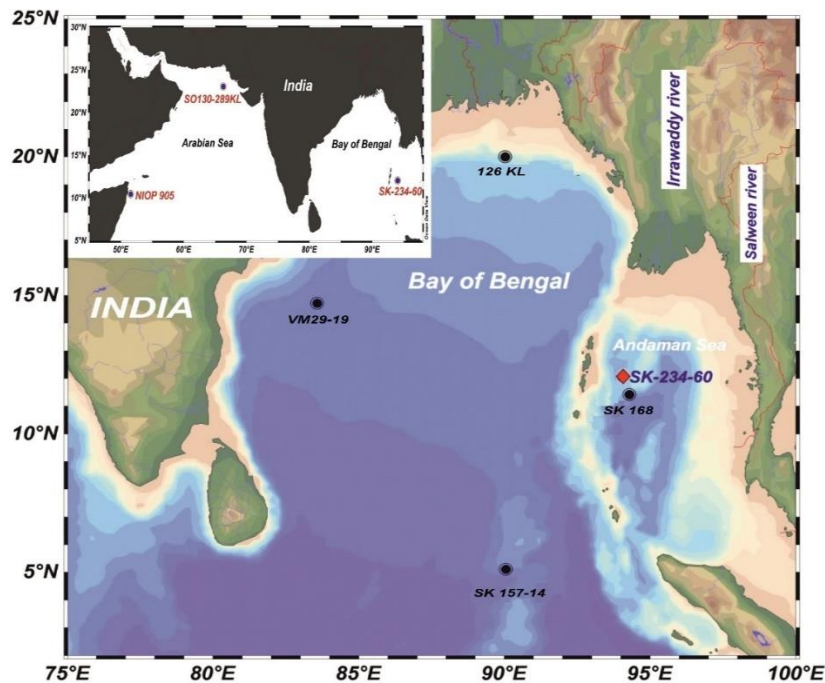


Figure 4.19: Location of the sediment core SK-234-60 (filled diamond; red) used in this study, also shown are cores from the Bay of Bengal (126 KL: Kudrass et al., 2001; VM 29-19: Rashid et al., 2011; SK 157-14: Raza et al., 2014) and the Andaman Sea (SK 168: Sijinkumar et al. 2011) studied earlier. GRIP ice core (Grootes and Stuiver 1997) NIOP-905 (Western Arabian Sea, Jung, et al. 2009) and SO130-289KL (the northeastern Arabian Sea, Deplazes, et al., 2013) are also used in this study (shown in inset).

4.5.1. $\delta^{18}\text{O}$ variability for last ~66 ka

The $\delta^{18}\text{O}$ of *G. ruber* varied from $\sim -0.32\text{‰}$ to -3.12‰ , *G. sacculifer* from $\sim -0.57\text{‰}$ to -2.81‰ while *G. menardii* ranged from -0.56‰ to -1.31‰ during the last ~66 ka (Figure 4.20). These isotopic compositions of *G. ruber*, *G. sacculifer*, and *G. menardii* show that the relatively different habitats were maintained through time, except during times of reduced monsoon runoff, when this difference decreased.

Planktonic foraminiferal $\delta^{18}\text{O}$ variation is a function of temperature and $\delta^{18}\text{O}$ of seawater ($\delta^{18}\text{O}_{\text{sw}}$). Thus, it is important to remove the temperature effect influences to interpreting planktonic $\delta^{18}\text{O}$ as $\delta^{18}\text{O}_{\text{sw}}$ alone. Using the Mg/Ca record for the last ~54 ka presented by the Gebregiorgis et al. (2016), temperature effect on the *G. ruber* and *G. sacculifer* $\delta^{18}\text{O}$ variation has been corrected. The earlier (~66-54 ka) part of the $\delta^{18}\text{O}$ data is corrected by assuming that change in the temperature during that period was less than 1°C , so 0.1‰ correction to the $\delta^{18}\text{O}$ of both *G. ruber* and *G. sacculifer* were

applied. After correcting for the temperature effect, the paleo-monsoon variation over the Andaman Sea is inferred based on the $\delta^{18}\text{O}$ of *G. ruber* (Figure 4.18). The $\delta^{18}\text{O}$ of *G. ruber* varied from -1.4‰ to -2.6‰ during MIS-3 (~57-24 ka; Figure 4.20). The $\delta^{18}\text{O}$ of these species remained constant during ~58-42 ka; thereafter a sudden depletion in the $\delta^{18}\text{O}$ of *G. sacculifer* followed by gradual enrichment till late MIS-3 (42-25 ka) is seen, whereas *G. menardii* shows a gradual depletion trend from 42-25 ka (Figure 4.20). During ~58 ka, another cold event was observed, with a $\delta^{18}\text{O}$ value of ~ -1.2‰ for *G. ruber*, which is less depleted than during the LGM (~ -0.3‰).

4.5.2. Paleomonsoon reconstruction

A) $\delta^{18}\text{O}$ variation during the LGM to Holocene:

The ^{18}O enrichment (relative to the early Holocene) during the LGM in *G. menardii* was the lowest, followed by *G. sacculifer* (respectively ~1.1‰ and ~1.6‰) and *G. ruber* (~1.8‰, indicating that the $\delta^{18}\text{O}$ values mainly responded to the surface water ^{18}O depletion due to monsoon runoff variation). This enrichment bolsters the earlier observation of Duplessy (1982) of a relatively weaker ISM during the LGM and higher evaporation due to increased dry and cool winter monsoon along with the global ice volume change (Sarkar et al., 1990). The mean observed changes in the $\delta^{18}\text{O}$ of *G. ruber* during LGM to early Holocene was ~ -1.85‰ (Figure 4.20). This variation may be contributed by the global ice volume effect (~1.1‰; (Fairbanks and Matthews, 1978; Schrag et al., 1996), and the remaining ~0.75‰ by the local changes (E-P/freshwater runoff induced salinity). Kudrass et al. (2001) showed that the salinity was 2 (psu) higher than that at present from the northern BoB during the LGM, whereas Cullen et al. (1981) showed that it was about 1 (psu) higher for the same time period. This study shows that the remaining ~ 0.75‰ change is contributed by increased salinity by 2 (psu) due to a strong excess of evaporation over precipitation, (i.e., positive E-P; Duplessy, 1982; Sarkar et al., 1990). An increased ISM strength, i.e., systemically depleted ^{18}O composition of *G. ruber* observed during the transition period of LGM to the Holocene corroborates earlier studies, that reported a significant increase in the summer

monsoon (Kudrass et al., 2001; Rashid et al., 2007; Govil and Naidu, 2011). However, the present core is unable to record clearly the short duration cold event Younger Dryas (YD) due to the coarse resolution of the record (Figure 4.18). According to Sonzogni et al. (1998) and Rashid et al. (2007), during the Holocene SST variation was insignificant, and the observed $\delta^{18}\text{O}$ variation was mainly controlled by the salinity changes due to fluctuations in the river influx to the Andaman Sea.

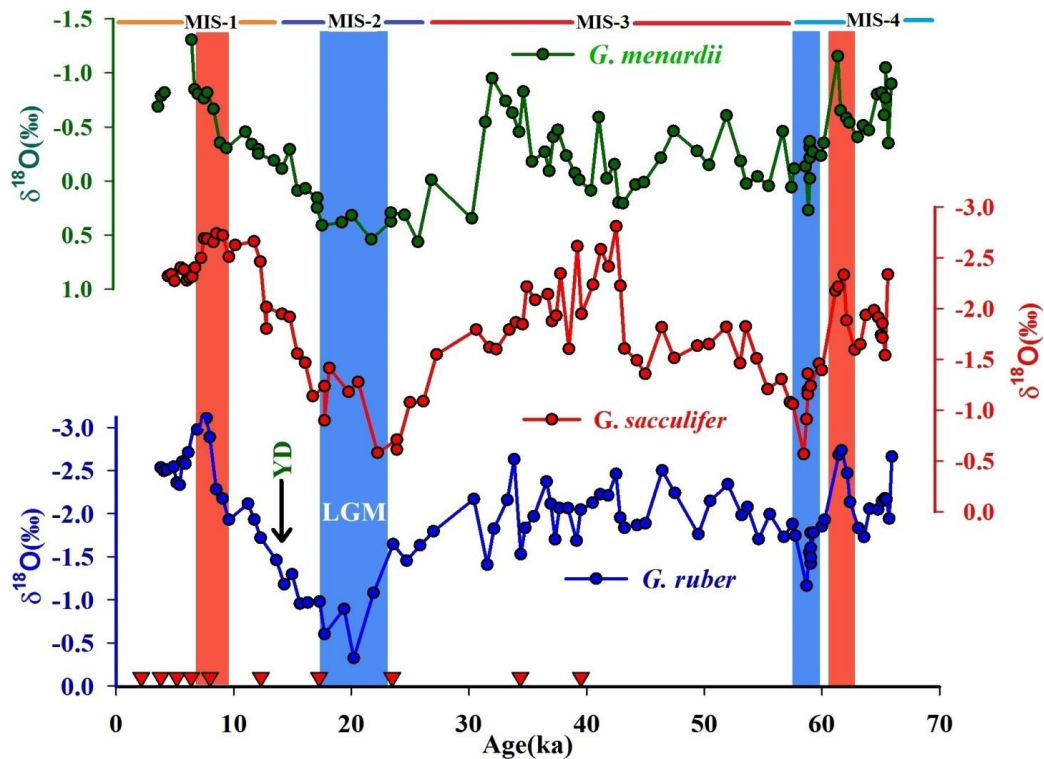


Figure 4.20: Downcore $\delta^{18}\text{O}$ data of SK-234-60 for *G. ruber*, *G. sacculifer* (mixed layer dwelling species), and *G. menardii* (thermocline dwelling species) from the 250–355 μm size fractions. AMS ^{14}C -dated depths are marked by red inverted triangles (Ages were obtained from AMS laboratory, Arizona, USA; Awasthi et al., 2014). Marine Isotopic Stages (MIS) are represented by the lines at the top of the plot. Blue vertical shades represent the weaker monsoon, and red vertical shades represent the stronger monsoon periods.

The mixed layer dwelling species *G. ruber* is very temperature sensitive (Sadekov et al., 2009); this shows that $\delta^{18}\text{O}$ variation of *G. ruber* during the Holocene was more dominantly controlled by the river runoff to the Andaman Sea (Bolton et al., 2013; Mohtadi et al., 2014). An abrupt decrease in the monsoon strength was observed during

early mid-Holocene (~7-4.5 ka; Figure 4.20). This led to the steep depletion in the ^{18}O variation trend of planktonic foraminifera from the late LGM to the early Holocene shows the increase in ISM and a consequent large freshwater influx to the Andaman Sea. The isotopic compositions of the other two planktonic foraminiferal species *G. sacculifer* and *G. menardii* also show similar variations (Figure 4.18).

B) $\delta^{18}\text{O}$ variation during Marine Isotopic Stages-3 (MIS-3):

The relatively enriched (depleted) average $\delta^{18}\text{O}$ of planktonic species *G. ruber* during MIS-3 than the early Holocene (LGM) shows weaker (stronger) ISM during MIS-3 relative to the early Holocene (LGM). Previous work by (Govil and Naidu, 2010) based on the $\delta^{18}\text{O}_w$ shown that the monsoon-driven precipitation was stronger in MIS-3 than the LGM and weaker than at present. During MIS-3, the average $\delta^{18}\text{O}$ of *G. ruber* remained more or less constant, followed with enrichment of $\delta^{18}\text{O}$ during the late MIS-3, represent the weakening of ISM and positive E-P during late MIS-3 (Figure 4.20). Whereas significant change in the $\delta^{18}\text{O}$ of *G. sacculifer* and *G. menardii* is observed within the MIS-3, a sudden depletion in the $\delta^{18}\text{O}$ of *G. sacculifer* from early to mid-MIS-3 followed by steep enrichment whereas, the $\delta^{18}\text{O}$ of *G. menardii* shows a weaker enhancement followed by the steep enrichment trends indicating relatively stronger monsoon during early to mid-MIS-3 followed by the weaker monsoon than during late MIS-3. Another strong ^{18}O depletion of planktonic foraminifera species was observed at ~62 ka (late MIS-4) shows intensified monsoon activity other than during the early Holocene (Figure 4.20).

4.5.3. Freshwater induced paleo-ocean stratification

The stratification in the BoB and the Andaman Sea is mainly controlled by the freshwater runoff from the monsoon-driven rivers and the direct precipitation (Chamarthi et al. 2008; Silva et al. 2017). The relative difference of $\delta^{18}\text{O}$ of *G. menardii* (TD) and the *G. sacculifer* (MLD; $\delta^{18}\text{O}_{men} - \delta^{18}\text{O}_{sac}$) indicates the degree of surface

(upper ocean) stratification (Singh et al., 2016). Direct precipitation/river (low salinity water) runoff due to stronger monsoon strengthens the upper ocean stratification, and weaker runoff periods disturb the stratification. The mean difference in $\delta^{18}\text{O}$ between *G. ruber* and *G. sacculifer* is -0.14 ± 0.42 and is not considered here as it is rather insignificant considering analytical errors. The difference between *G. menardii* and *G. sacculifer* is 1.48 ± 0.46 and is considered to decipher the upper ocean stratification. In the present study, three strong upper ocean stratification events (blue vertical shades) and three weak stratifications (red arrows) periods have been observed during the last ~66 ka (Figure 4.21). A significant lower difference in $(\delta^{18}\text{O}_{men} - \delta^{18}\text{O}_{sac})$ during the LGM (Figure 4.21) shows weaker stratification due to the reduced runoff of freshwater as a result of the weaker southwest monsoon (Duplessy et al., 1982) and stronger winter monsoon than at present (Sarkar et al., 1990). The situation might have increased the wind-driven mixing by lowering TD in the Andaman Sea. The significantly higher difference in $(\delta^{18}\text{O}_{men} - \delta^{18}\text{O}_{sac})$ during the early Holocene indicates the stronger stratification by increased freshwater runoff, which reduces the wind-driven mixing, followed by the weaker stratification towards mid-Holocene.

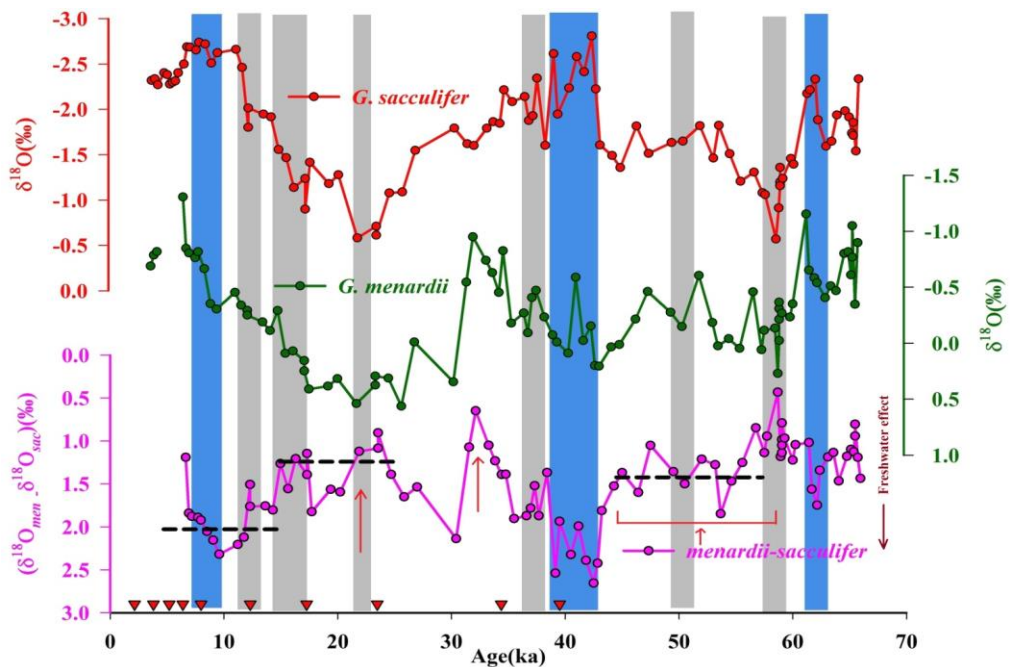


Figure 4.21: $\delta^{18}\text{O}$ of *G. sacculifer*, *G. menardii*, and $(\delta^{18}\text{O}_{men} - \delta^{18}\text{O}_{sac})$ for the last ~66 ka from

sediment core SK-234-60. Blue vertical shades represent periods of stronger upper ocean stratification; red arrows represent weaker stratification events; grey vertical shades represent weak stratification during Heinrich events. AMS ^{14}C - dated depths are marked by red triangles. Horizontal dashed lines show the average values for different time intervals discussed in the text.

Previous studies from the Andaman Sea have shown that during the early Holocene monsoon was stronger than the present and the thermocline was deeper, followed by shoaling of thermocline depth from the early to mid-Holocene, with a sharp increase in ΔT_{MLD-TD} (temperature difference between MLD and TD species) with decreasing monsoon strength (Sarkar et al., 1990; Gebregiorgis et al., 2016). Based on the ΔT_{MLD-TD} variations, Gebregiorgis et al. (2016) have shown that the thermocline was shallower during the YD and LGM. The observed average stratification strength (horizontal dashed lines) during the early to mid-MIS-3 (~43-60 ka) is relatively stronger than LGM but weaker than early Holocene, indicating the stronger monsoon activity. Another strong stratification was observed during mid to late MIS-3 (~43-39 ka), which is much stronger than the early Holocene stratification, representing the stronger monsoon event, whereas in the $\delta^{18}\text{O}$ of *G. ruber* such monsoon activity is not observed. During the Heinrich events, i.e., short timescale North Atlantic cold events (Heinrich 1988; Bond et al., 1993), the monsoon was weaker (Deplazes et al., 2014). These weaker monsoon events are also observed in the core SK-234-60, with relative lower ($\delta^{18}\text{O}_{men} - \delta^{18}\text{O}_{sac}$), shows the weaker stratification during these events (Figure 4.21; grey vertical bars) due to reduced monsoon runoff.

4.5.4. Comparison of results from Sediment Cores from the Indian Ocean

Previously published $\delta^{18}\text{O}$ of planktonic foraminifera species from well-dated sediment cores of the Indian Ocean (Kudrass et al., 2001; Rashid et al., 2011; Sijinkumar et al., 2011; Raza et al., 2014; Figure 4.19) and GISP $\delta^{18}\text{O}$ (ice core) compared with the present sediment core SK-234-60 record (Figure 4.22a, b). The major climatic events, including Heinrich events (LGM, H-1, 2, 4, 5 and 6, YD; cold events), have been observed in all the cores, which indicates that the climate of different regions of the world is quite connected (Figure 4.22a). The monsoon was weaker during all these cold

events resulting in weak stratification. The $\delta^{18}\text{O}$ variations of planktonic species match well with summer insolation variation at 30°N . The documented changes in SK-234-60 are coherent with observed $\delta^{18}\text{O}$ variations in the sediment cores from the AS and the BoB (Figure 4.22a, b). This implies that the past variation in the Indian Ocean currents system was well preserved and recorded by all the cores. The abrupt weakening of ISM during the mid-Holocene ($\sim 7\text{-}4\text{ ka}$) in $\delta^{18}\text{O}$ of SK-234-60 was also observed in the KL-126 record from the northern BoB. The relatively lower decreasing slope in the KL-126 compared to SK-234-60 is due to a large number of rivers debouching into the northern BoB, whereas Irrawaddy and Salween are the only two river systems contributing freshwater to the Andaman Sea (Ahmad et al., 2000). Steady $\delta^{18}\text{O}$ variations with an overall small enrichment trend with large fluctuations during the MIS-3 ($\sim 57\text{-}25\text{ ka}$) are observed in all the sediment cores from the Indian Ocean (Figure 4.22b).

The $\delta^{18}\text{O}$ values of *G. ruber* of the present study SK-234-60 during the early Holocene is more negative than the southern BoB core (Raza et al., 2014); but less negative in comparison with the northern and western BoB cores (Figure 4.22b) (Kudrass et al., 2001; Rashid et al., 2011). These spatial variations of $\delta^{18}\text{O}$ show that the surface seawater of the Andaman Sea was depleted ^{18}O during early Holocene than southern BoB surface water but enriched than the northern BoB surface water, which might be due to the relative difference in the freshwater discharge to the respective locations. The increase in the monsoon strength from late LGM to early Holocene with maximum ^{18}O depletion during the $\sim 8\text{ ka}$ has been recorded by all cores and confirmed by cores from the eastern AS (Banakar et al., 2010 and references cited). Except for the southern BoB, the rest of the core locations show a weakening of ISM during the mid-Holocene.

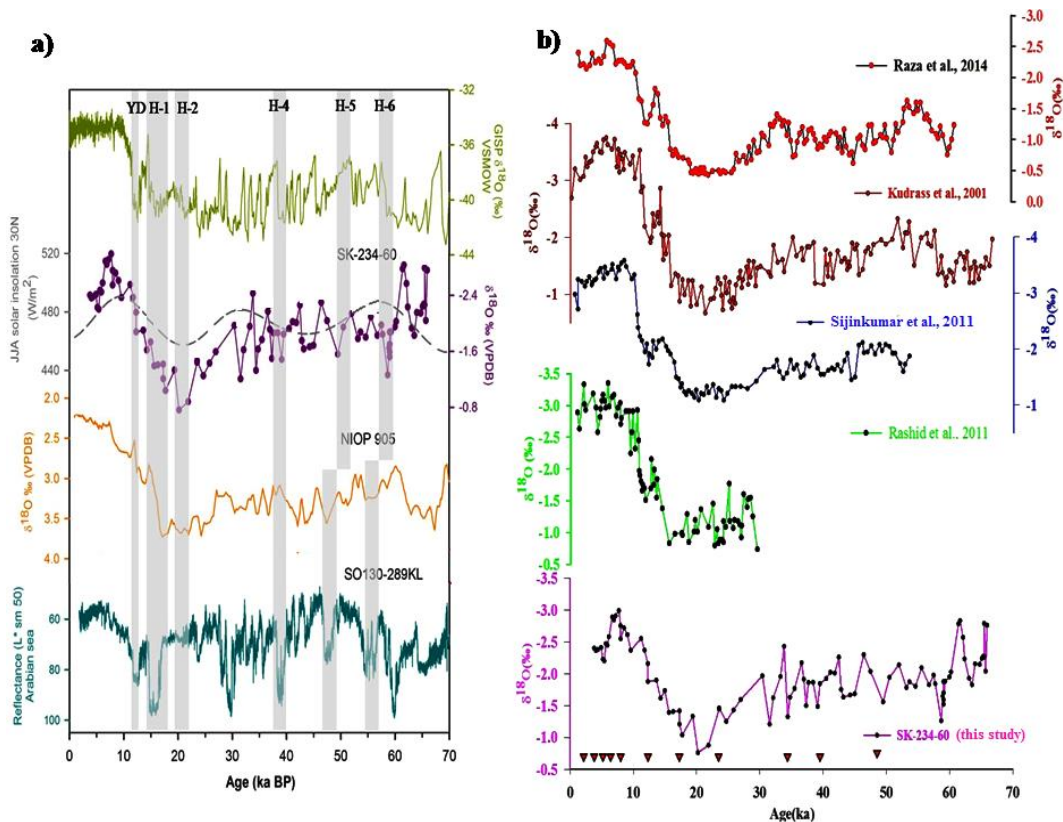


Figure 4.22: **a)** Comparison of the $\delta^{18}\text{O}$ time series of the Andaman Sea sediment core SK-234-60 (present study) with $\delta^{18}\text{O}$ values of GRIP ice core (Green, Grootes and Stuiver., 1997), the insolation at 30°N (dashed gray line); the $\delta^{18}\text{O}$ record of the planktic foraminifera *N. dutertrei* from the Arabian Sea core NIOP-905 (Yellow, Jung et al., 2009) and the reflectance data from the Arabian Sea sediment core SO130-289KL, (dark green, Deplazes et al., 2013). The grey vertical bands represent ice calving events in the North-Atlantic known as Heinrich events and are shown from H-1 to H-6, the colder stadial YD. **b)** Comparison of data from the Bay of Bengal (Kudrass et al., 2001; Rashid et al., 2011), the Andaman Sea (Sijinkumar et al., 2011) and from the southern Bay of Bengal (Raza et al., 2014) sediment cores with the present study.

4.6. Conclusion

a) A fresh data set of seawater $\delta^{18}\text{O}$ and salinity shows, except for the central coastal Eastern Arabian Sea (which is influenced strongly by the summer monsoon runoff from the Western Ghats of India during summer monsoon), there is a strong effect of winter monsoon and West India coastal currents on the seawater $\delta^{18}\text{O}$ -S relation. A compilation of recent high resolution foraminiferal $\delta^{18}\text{O}$ data from 22 sediment cores from the Eastern Arabian Sea appears to dispel the idea that the south Asian Summer monsoon has steadily

declined during the Holocene. Speleothem $\delta^{18}\text{O}$ data from central India (core monsoon region) and planktonic foraminiferal $\delta^{18}\text{O}$ of several sediment cores from the Eastern Arabian Sea do indicate that the summer monsoon steadily strengthened during the Holocene.

- b)** Based on $\delta^{18}\text{O}$ of planktonic foraminifera from the southern Arabian Sea for the last ~ 45 ka record, four intense active monsoon periods were observed with lower $\delta^{18}\text{O}$ values. However, another active monsoon was observed during ~42 – 41 ka. Three weaker monsoon periods were observed with higher $\delta^{18}\text{O}$ values, with ~ 0.7 ‰ enrichment. Similar strong and weak monsoon periods were reproduced by the deep-dwelling planktonic species *G. menardii*. Significant variation in the $\delta^{18}\text{O}$ values of *G. ruber* in response to abrupt short term climate events were observed, with warm Dansgaard-Oeschger events associated with stronger monsoon and cold Heinrich Events were associated with the weaker monsoon. Benthic $\delta^{18}\text{O}$ variability shows two extreme cold and two warm events during the last ~ 45-18 ka, associated with the weaker and stronger monsoon, respectively. The $\delta^{13}\text{C}$ of benthic foraminifera varied opposite to $\delta^{18}\text{O}$ variation with lower value trend in the warm events and higher trend during cold events. Two extreme higher value events were observed in $\delta^{13}\text{C}$ of benthic foraminifera during ~ 29 to 27 ka and ~ 42-41 ka. Extreme lower values were observed during ~36-30 ka and a lower peak during ~49 ka; however, during these periods, significant changes in the $\delta^{18}\text{O}$ were not observed.
- c)** Significant variation in $\delta^{15}\text{N}$, $\delta^{13}\text{C}_{\text{org}}$, and N & C_{org} (wt %) of bulk sediment from the BoB are observed for the last ~ 16 ka. These variations show that for the last ~ 16 ka, productivity over the western BoB was changed significantly. Sediment core record shows that during the early to late deglacial period, $\delta^{13}\text{C}_{\text{org}}$ was higher than -20 ‰ infers the C4 plants contributed significantly. Relatively stronger productivity was observed during deglacial than during Holocene (increasing C_{org} and $\delta^{15}\text{N}$ trends); due to variation in the upper ocean stratification. During the early deglacial period, a weaker southwest monsoon

and relatively stronger northeast monsoon might result in favorable conditions (less-stratified water column, evaporative cooling induced density convective mixing) for relatively stronger productivity than during Holocene. The overall variation of bulk sediment $\delta^{13}\text{C}_{\text{org}}$ and C/N ratios from the BoB show a mixed influence of terrestrial and marine input during the deglacial to late Holocene (~ 16 ka to present).

- d)* Based on the records of $\delta^{18}\text{O}$ variations in the three different planktonic foraminiferal species from the Andaman Sea, an abrupt decrease in the monsoon runoff during the mid-Holocene (7-4.5 ka) is inferred. During MIS-3, summer monsoon was relatively weaker than MIS-1 and stronger than MIS-2. Based on the $\delta^{18}\text{O}$ difference of foraminiferal of MLD dwelling and TD dwelling species, distinct weaker and stronger freshwater induced upper ocean stratification events were observed. Strong stratification is observed during the early Holocene, mid-MIS-3, and at ~62 ka due to an increased freshwater influx from Irrawaddy, Salween river systems, and direct precipitation over the Andaman Sea whereas weak stratification is observed during the LGM and late MIS-3. Freshwater induced stratification was stronger during the early to mid-MIS-3 than that during LGM, but weaker than that during early Holocene. Weaker monsoon strength was observed during the Heinrich events associated with weaker stratification. The compilation of different sediment cores from the BoB and the Andaman Sea shows that during early Holocene, the $\delta^{18}\text{O}$ of surface seawater in the Andaman Sea was depleted than that from southern BoB, but enriched from northern and western BoB core records.

Chapter-5

***ISM variabilities and teleconnections with
the Global processes: understanding from
instrumental and paleoclimate data***

ISM variabilities and teleconnections with the global processes

Indian Summer Monsoon (ISM) plays a key role in the climate of southeast Asia. It contributes 80% of the annual rainfall over central Indian plains (Bollasina, 2014; Jain and Kumar, 2012; Mooley and Parthasarathy, 1984). The average ISM rainfall over India (1901 – 2013) is about 900 ± 90 mm, where below or above one standard deviation (~10%) signifies drought and flood conditions (Saikranthi et al., 2017). It has been observed that apart from the long term (Glacial and interglacial periods) and short term (cold and warm periods such as Heinrich and Dansgaard–Oeschger, Younger Dryas events) global climate events, the climatological average rainfall over India varies at intra-annual to intra-seasonal timescales (Ashok et al., 2007; Gadgil, 2003; Wang et al., 2003). These high-frequency fluctuations in the ISM have been identified to be associated with coupled global ocean-atmospheric processes.

The geographical coverage of the Indian subcontinent is large enough to observe the spatial variability in rainfall patterns during the same season, which has large heterogeneity, and hence considering it as a single entity is not appropriate. El Niño–Southern Oscillation (ENSO), plays an important role in modulating the ISM strength (Kumar et al., 1999; Maity and Kumar, 2006; Mishra et al., 2012; Turner et al., 2005).

Influence of El-Niño (a positive sea surface temperature anomaly: SST anomaly over the central Pacific Ocean) on ISM have been studied widely (Ashok et al., 2004, 2001; Ashok and Saji, 2007; Kumar et al., 1999; Navarra et al., 1999; Sarkar et al., 2004; Sikka, 1980; Walker, n.d.). ENSO has a profound impact on weather and climate at global scales (Cai et al., 2011; Collins et al., 2010; Deser et al., 2010; Trenberth, 1997; Wallace et al., 1998). Besides, other coupled processes such as Indian Ocean Dipole, Madden Julian Oscillation, Pacific Decadal Oscillation are known to affect ISM (explained in Chapter-1).

The oxygen isotope of rainfall ($\delta^{18}\text{O}_{\text{rain}}$) is used as a proxy for rainfall reconstruction (Burns et al., 2002; Craig, 1961; Dansgaard, 1964). A decrease in $\delta^{18}\text{O}$ is inferred as the strengthening of rainfall (amount effect; Dansgaard 1964). There is scarcity in the availability of long term and spatially well-distributed $\delta^{18}\text{O}_{\text{rain}}$ observations over the Indian subcontinent, and most studies were restricted to regional scales. Past-rainfall variation has been studied based on the $\delta^{18}\text{O}$ of different continental/marine proxies (such as tree rings, cave deposits, corals, and deep-sea sediment cores) over tropical regions (Explained in Chapter-1). Speleothem (calcium carbonate cave deposits) is a continental proxy for the reconstruction of ISM. The high-resolution (annual layer formation) cave deposit records and tree ring chronology records from different regions of the Indian subcontinent were used to identify the drought and heavy rainfall periods (Cook et al., 2010; Sinha et al., 2011b, 2007).

Very few studies using the rainfall and $\delta^{18}\text{O}_{\text{rain}}$ variability have focused on ENSO influence on the spatial and temporal variability of rainfall over Indian subcontinent (Midhun and Ramesh, 2016; Myers et al. 2015). ENSO is believed to affect ISM: most of the severe droughts in India were associated with active ENSO periods. Given the heterogeneity in rainfall patterns over India, in this work, I revisited the ENSO influence on ISM to understand the spatial and temporal patterns of instrumental rainfall record and model-simulated $\delta^{18}\text{O}_{\text{rain}}$ during ENSO events and their implications for paleoclimate reconstruction.

5.1. Study Area and Multi-data Analysis

In this study, the monthly and seasonal rainfall variations over the Indian subcontinent regions bounded by 74.5 – 86.5°E, 16.5 – 26.5°N (Central Indian region, CI; also known as core monsoon region) and 92.5 – 110°E, 22.5 – 25.5°N (Northeast Indian region, includes Bangladesh, Myanmar, and other adjacent regions; NEI) were studied during El- Niño periods. HadISST derived SST anomaly over Niño3.4 index region used as an El-Niño indicator. The Homogeneous Indian Monthly Rainfall Data (rain gauges data), Global Precipitation Climatology Project (GPCP) satellite remote sensing derived data, and isoGSM model simulated $\delta^{18}\text{O}_{\text{rain}}$ and rainfall data used for spatial and temporal rainfall analysis. In addition, two high resolution (annual growth) cave deposit speleothem records from Jhumar cave (CI record) and Wah Shikar Cave (NEI record) were studied for past spatial variability in ISM over Indian subcontinent in response to ENSO. Detailed information on the data is given in Chapter-2.

5.2. Climatological rainfall pattern

5.2.1. Monthly rainfall variation

With the north-southward movement of ITCZ, the spatial patterns of rainfall over the Indian subcontinent at a monthly scale varies spatially and temporally. Knowledge on the variability of rainfall in response to ENSO will help to identify the deviation of normal rainfall regions while forecasting during the ENSO episodes. The spatial correlation patterns of the climatological monthly average rainfall and SST anomaly over the Niño3.4 index (ENSO indicator) for 1979-2013 shows significant variability in the rainfall pattern distribution at the regional scales (Figure 5.1). During February-September, rainfall over central to southern peninsular India was negatively correlated with ENSO, whereas during January, October, and November most of the Indian regions were associated with a positive relation. Eastern India and most parts of Myanmar and the Bangladesh regions were associated with strong positive correlation during February, March, July, October, November, and December with weak positive correlation during September.

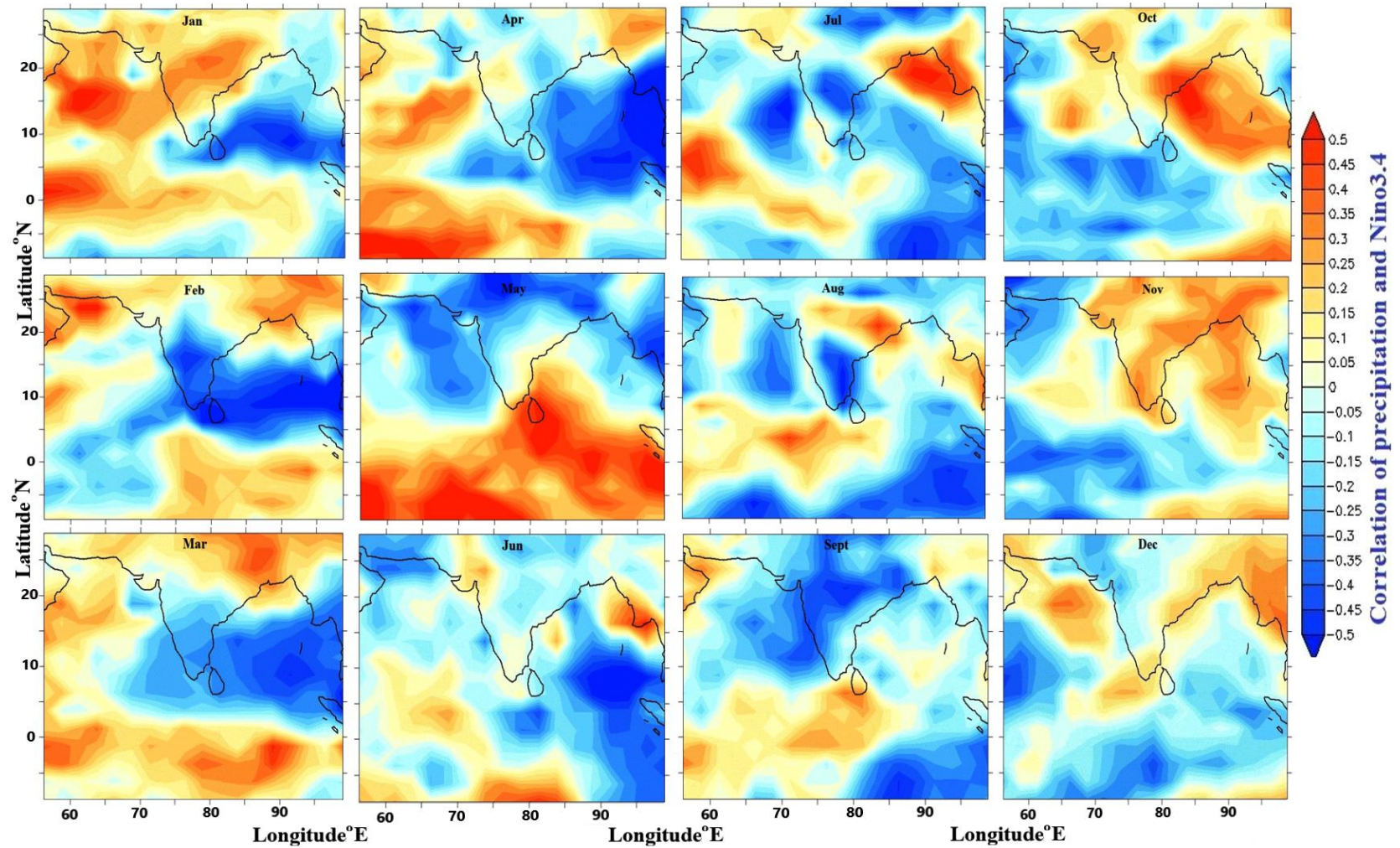


Figure 5.1: Spatial correlation coefficient patterns for rainfall and SST anomaly (for Niño3.4 region) over the Indian subcontinent and adjoining oceans at monthly timescales for 1979 – 2013. The correlation regions bounded by $r > |0.3|$ are significant at $p < 0.05$.

These positive and negative correlations with SST anomaly over the Niño3.4 region (ENSO indicator) showed regions with above and below the normal rainfall, respectively. These significant positive (negative) spatial correlations of rainfall and Niño3.4 show the active (weak) rainfall condition during corresponding El-Niño months. A positive correlation between rainfall and ENSO during July to November over the Andaman Islands (and nearby ocean) and negative correlation during the remaining months (Figure 5.1) were observed. These spatial correlation patterns suggest that during the El-Niño (La-Niña) periods, the Andaman Islands landmass may get an above normal (weaker) rainfall than the rest of months. However, rainfall variability at monthly timescales over the Indian subcontinent is not merely the ENSO effect, and there are other local and shorter time scale processes (examples Madden Julian Oscillation), which can also affect the rainfall patterns at monthly timescales. Previous studies have shown that the active/break monsoon periods in the rainfall over the Indian subcontinent at regional scales are associated with the migration of convecting clouds associated with the MJO (Joseph et al., 2009). Despite various other processes which can affect rainfall patterns, significant spatial correlations of climatological monthly mean rainfall and corresponding climatological monthly mean ENSO were observed.

5.2.2. Seasonal rainfall variation

The seasonal variations of rainfall amount are controlled by the variability in wind strength, direction, and associated moisture content, with maximum rainfall during the summer monsoon (June, July, August, and September: JJAS). During winter monsoon (December, January, and February: DJF), most southeastern peninsular India (Tamil Nadu, Pondicherry, and some parts of Kerala) gets the maximum rainfall (discussed more details in Chapter-1). During the El-Niño periods, seasonal rainfall varied spatially (Figure 5.2 and Figure 5.3). Spatial correlation patterns of rainfall and ENSO showed a significantly strong negative correlation over the southeastern Indian subcontinent (during DJF), which infers winter monsoon rainfall over these regions are below normal (Figure 5.2a). During normal rainfall conditions, JJAS analysis showed

maximum rainfall over the Western Ghats, CI, and NEI, but during El-Niño events, significant changes in these rainfall patterns were observed with a dipole variation (exact opposite rainfall condition over CI and NEI Figure 5.2b). During the El-Niño events, the rainfall over the Western Ghats and CI reduced (negative correlation), and the amount of rainfall over NEI (includes Myanmar and southern Bangladesh) remained around the climatological mean or above (positive correlation; Figure 5.3). However, Saikranthi et al. (2017) have shown that the rainfall systems are distinctly different during the El-Niño and La-Niña events, which were associated with variation in the Walker circulation branches over India and adjoining Oceans.

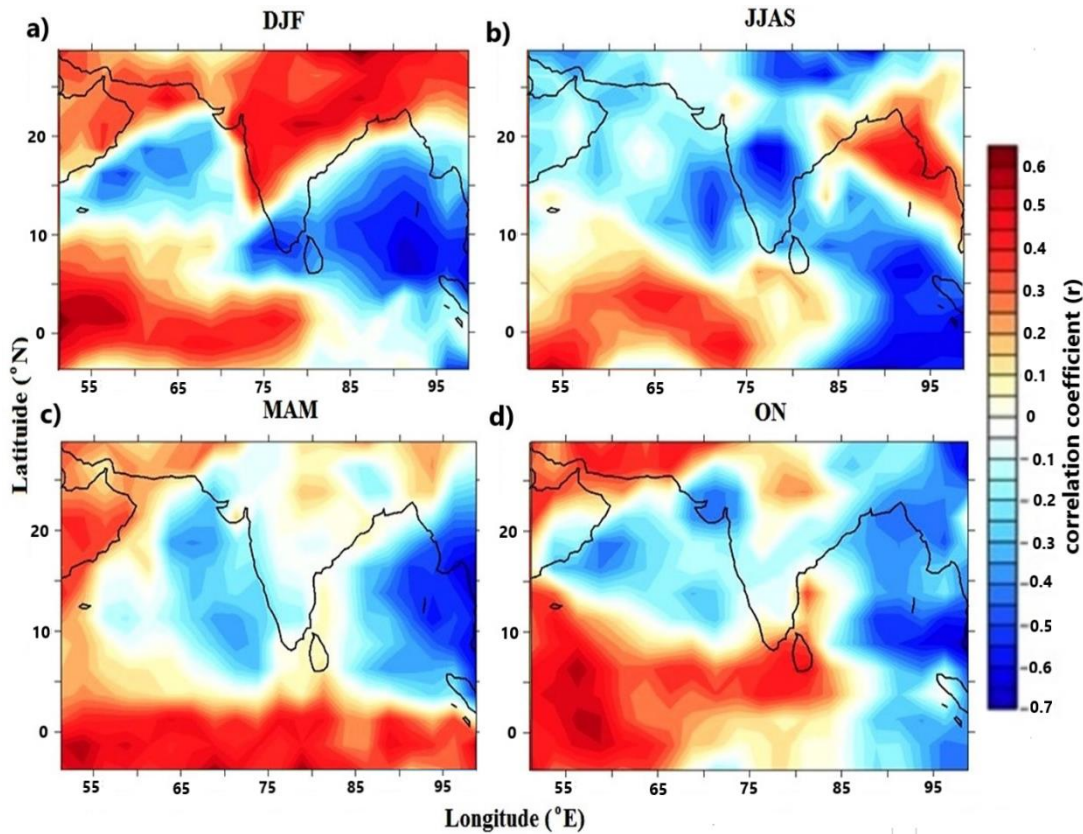


Figure 5.2: Seasonal variation of spatial correlation patterns of rainfall and Niño 3.4 index over the Indian subcontinent and adjoining oceans during 1979-2013 **a)** winter (DJF) **b)** summer (JJAS) **c)** pre-monsoon (MAM) and **d)** post-monsoon (ON). The regions with correlations coefficients $|r| > \pm 0.3$ bounded by are significant at $p < 0.05$.

During neutral ENSO conditions, some parts of northern India get rain due to western disturbances pre-monsoon (MAM). While during ON, eastern coastal India gets rain as a result of the cyclonic activity over the Bay of Bengal. A spatial weaker correlation of rainfall pattern showed reduced rainfall conditions during MAM and ON (Figure 5.2c, d), which might be due to weakening of cyclonic activity over the Arabian Sea and Bay of Bengal. Previous studies have shown the reduced tropical cyclone activity during the El-Niño periods (Felton et al., 2013; Mahala et al., 2015; Mohapatra et al., 2015). The low-level anti-cyclonic vorticity inhibits convection and low tropical cyclonic heat potential over the Bay of Bengal, which provides negative feedback for cyclone during El-Niño (Girishkumar and Ravichandran, 2012b). The weak negative correlation of ENSO events with rainfall for ON shows the reduced tropical cyclones induced rainfall conditions (Figure 5.2d). The spatial correlation analysis at seasonal scale shows that during ENSO events, a below-normal rainfall (weak spatial distribution of rain systems) over most parts of the Indian subcontinent was observed except over few regions of northern and NEI (Figure 5.2). CI and NEI receive below and above normal rainfall, respectively, during moderate to strong ENSO events during JJAS (Figure 5.3). Weak but significant negative correlation showed reduced cyclone activities during MAM and ON. Reduced rainfall conditions during winter monsoon during DJF, needs to be studied in details and reconfirm it.

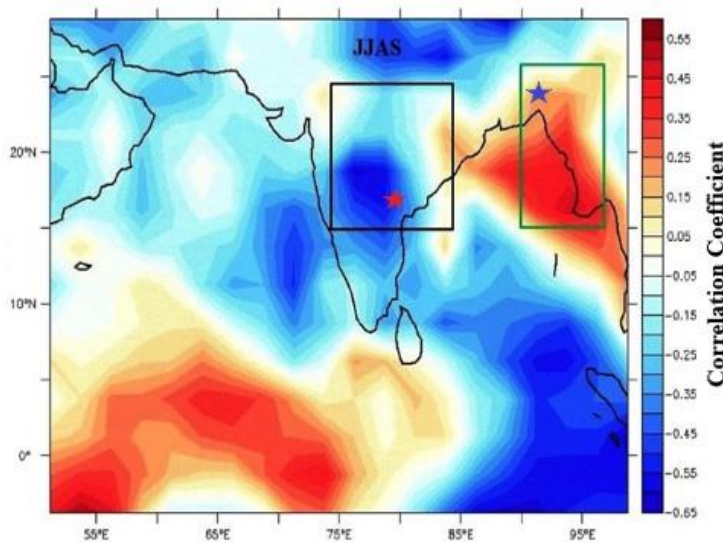


Figure 5.3: Spatial correlation coefficient pattern for JJAS rainfall and SST anomaly (for Nino3.4 region) over Indian and adjoining oceans for the period 1979 – 2013. The regions bounded by $r > |0.35|$ are significant at $p < 0.05$. The black and green boxes are the CI and NEI study regions for rainfall pattern variability. Star symbols represent speleothem samples records (red: Jhumar cave; blue: Shikar cave) used in the present study.

5.3. isoGSM model derived rainfall variation

The spatial distribution of isoGSM derived rainfall over the Indian subcontinent reproduces the observed variability with some limitations (Midhun and Ramesh, 2016). However, similar negative rainfall variabilities with ENSO episodes were observed in the model simulations over CI, but the model was unable to reproduce the stronger rainfall events over the NEI. The GPCP and IMD derived rainfall amount showed a strong negative (positive) correlation over the CI (NEI) region with ENSO events with $r = -0.57$ (0.65) [$n = 14$; for GPCP] and 0.51 (0.73) [$n = 12$; for IMD merged data] at $p < 0.05$ respectively (Figure 5.4; n = number of identified El-Niño events during 1960-2013). Here I considered the El-Niño events with SST anomaly > 0.5 °C over the Nino3.4 region, where this threshold temperature anomaly represents moderate to strong events (Araghinejad and Meidani, 2013; Iizumi et al., 2014; Kiem and Franks, 2001). However, the isoGSM model derived rainfall showed a weak correlation over CI ($r = 0.01$) and NEI ($r = 0.15$) by considering all the El-Niño events from 1979 – 2009 (total identified number of El-Niño years: $n = 11$). This weak correlation over CI

was improved by excluding the 1997/98 El-Niño event to $r = -0.56$; $p < 0.05$ ($n = 10$; Figure 5.4). The correlation did not improve over the NEI by removing this 1997/98 El-Niño event.

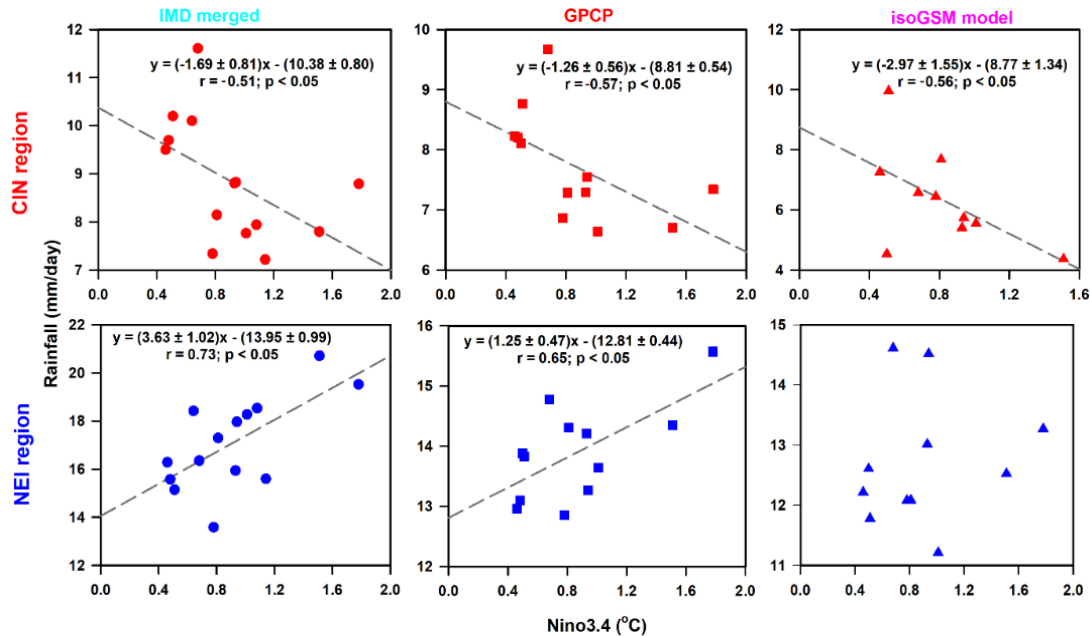


Figure 5.4: Scatter plots of El-Niño events with SST anomaly ($> 0.5^{\circ}\text{C}$) over Nino3.4 region and corresponding rainfall amount over CIN (upper row: red color) and NEI (lower row: blue color) for different datasets (IMD: dots; GPCP: squares and isoGSM model: triangle).

5.4. ISM variation over CI during 1965 – 2013

The rainfall variation over CI was studied for the last ~50 years (1965 – 2013). Earlier studies have shown that the ISM declined during 1901-2012 due to the warming of the western tropical Indian Ocean (Roxy et al., 2015). On the contrary, Jin and Wang (2017) have shown that ISM strengthened from 2002-2013/14, which was inferred as the restoration of land-sea temperature gradient improvement. The time series analysis of mean JJAS rainfall (ISM) for CI along with El-Niño variation was re-analyzed (black box, Figure 5.3). A significant correlation was observed between the rainfall (IMD merged and GPCP derived) and Nino3.4. The trends remained insignificant for both CI and NEI regions for the entire rainfall data together for 1965-2013 (~50 years). In the recent decade (during 2002-2013), the variability of rainfall variation over CI

(NEI) has shown a strengthening signature (weakening), which was concurred with the decrease in the El-Niño strength with $r = -0.59$ ($p < 0.05$; Figure 5.5a, b). It infers that the variability in the El-Niño strength caused the revival of ISM over CI during 2002-2013. Other strengthening events of ISM rainfall were observed and concurred with the weakening of El-Niño strength during 1965-1975 (Figure 5.5A; $r = -0.69$ at $p < 0.05$). During 1976-1997, relatively weaker but significant ($r = -0.25$) decreasing trend of ISM was observed even with co-occurrence of strongest El-Niño events. This weaker decreasing ISM trend is inferred to the high number of the strong El-Niño and the La-Niña episodes associated with 1976-1997, which might have suppressed the overall inverse trend with strong ENSO events (Figure 5.5a). Similar results were observed for the NEI for the period 2002 – 2013 (significantly weaker monsoon; $r = 0.59$; $p < 0.05$), but insignificant trends were observed during 1965 – 1997 (Figure 5.5b). The observed improvement in the land-sea temperature gradient was inferred to the global warming hiatus (Jin and Wang, 2017), i.e., slow down or pause in the increase of global mean temperature (GMT). However, Hu and Fedorov (2017) have shown that global warming hiatus was rather related to the declining of El-Niño strength (Medhaug et al., 2017; Su et al., 2017). Revisiting the time series analysis of GMT and Nino3.4 index for the last ~50 years (1965-2013) showed that the short-time pauses in GMT (global warming hiatus) were repeated several times in the past and were associated with the weakening trends in the SST anomaly over the CP (Nino3.4 region; Figure 5.6). During 1960 – 1975, another global warming hiatus like the situation was observed and associated with the weakening of ENSO strength and increased ISM (Figure 5.6; Figure 5.5a). This analysis further reconfirms that global warming hiatus is a temporary pause and linked with the long term pause or weakening of ENSO strength. This concludes that the long term strengthening or weakening of ISM trends are controlled by the variation in land-sea temperature gradients along with the long term changes in the ENSO strength, which again controls the GMT fluctuation rates.

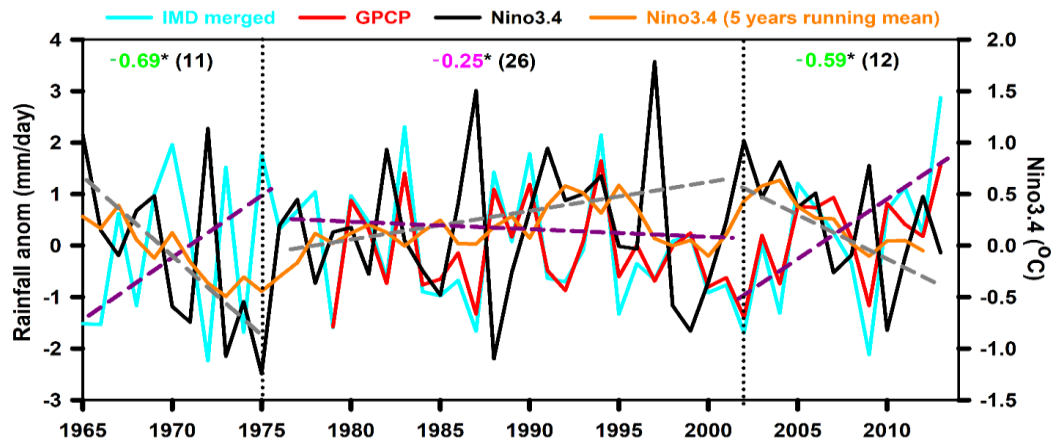


Figure 5.5a: Time series analysis of JJAS average rainfall variation over CI for the last ~50 years (1965 – 2013) using IMD merged (green), and GPCP (red) data are overlapping with the Nino3.4 index (JJAS average; black and five years moving average; orange). The vertical dotted lines represent three periods of strong (green) and weaker (pink) monsoon (explained in the text), and corresponding correlation coefficients are shown within the plot, * represents the significant at $p < 0.05$, values within brackets represent the number of years.

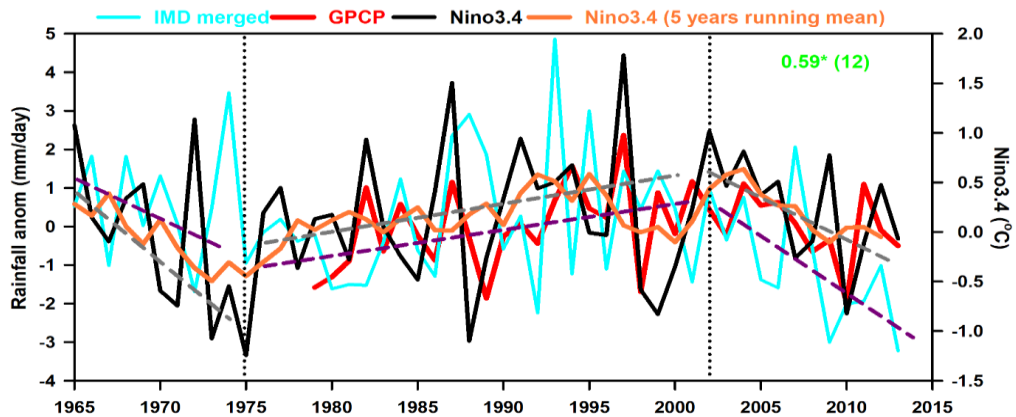


Figure 5.5b: Time series analysis of JJAS average rainfall variation over NEI for the last ~50 yrs (1965-2013) using IMD (cyan) and GPCP (red) data overlapping with the Nino3.4 index (JJAS average; black colored and orange: five years running moving average). The trends are the significance level at $p < 0.05$ for 2002-2013. The correlation between the Nino3.4 index and rainfall (GPCP data) in the plot for 2002-2013 (green; the number of years in the bracket).

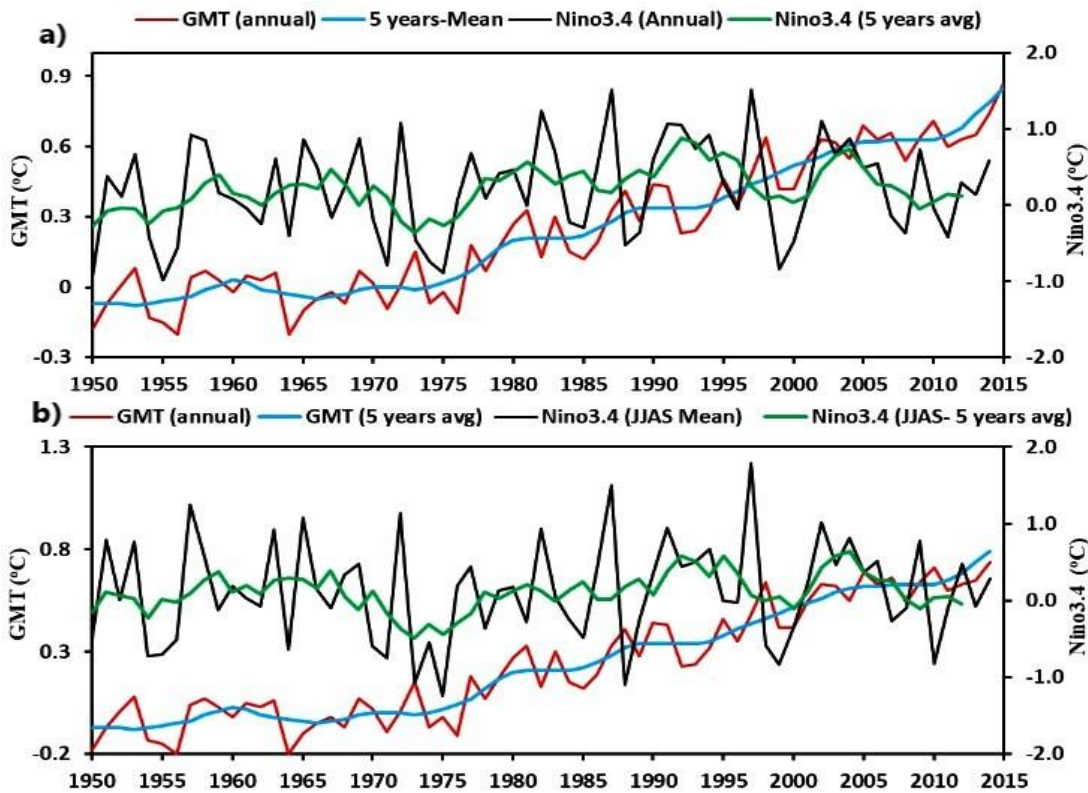


Figure 5.6: Time series analysis of Global Mean Temperature (GMT) annual (red-colored) and 5 years moving average (blue colored) **a)** average Nino3.4 SST anomaly (annual: black; green: 5 years moving average), **b)** average Nino3.4 SST anomaly (JJAS average: black; green: 5years moving average).

5.5. The isoGSM model derived $\delta^{18}\text{O}_{\text{rain}}$ variation

The spatial patterns of $\delta^{18}\text{O}_{\text{rain}}$ during El-Niño events can help for a better understanding of present and past (proxy-based) rainfall conditions over the Indian subcontinent during these global events. The spatial distribution of isotope-enabled GCM simulations (isoGSM model) derived $\delta^{18}\text{O}_{\text{rain}}$ during moderate to intense El-Niño periods were associated with higher values of $\delta^{18}\text{O}_{\text{rain}}$ over the CI (a decrease in the rainfall conditions; Figure 5.7). The positive IOD events are associated with relatively higher rainfall over the Indian subcontinent (Gadgil, 2003; Kripalani and Kumar, 2004; P. Kumar et al., 2007) and were observed to be linked with lower $\delta^{18}\text{O}_{\text{rain}}$. However, when both strong El-Niño and positive IOD like conditions co-occur, isoGSM model simulations of $\delta^{18}\text{O}_{\text{rain}}$ spatial patterns were unable to distinguish these effects

remarkably (Figure 5.7; 1997, a strong El-Niño and positive IOD period linked with above-normal rainfall over Indian subcontinent). These analyses showed that the isoGSM model could identify the effects of ENSO and IOD phenomenon on $\delta^{18}\text{O}_{\text{rain}}$, based on their strength and time of occurrence.

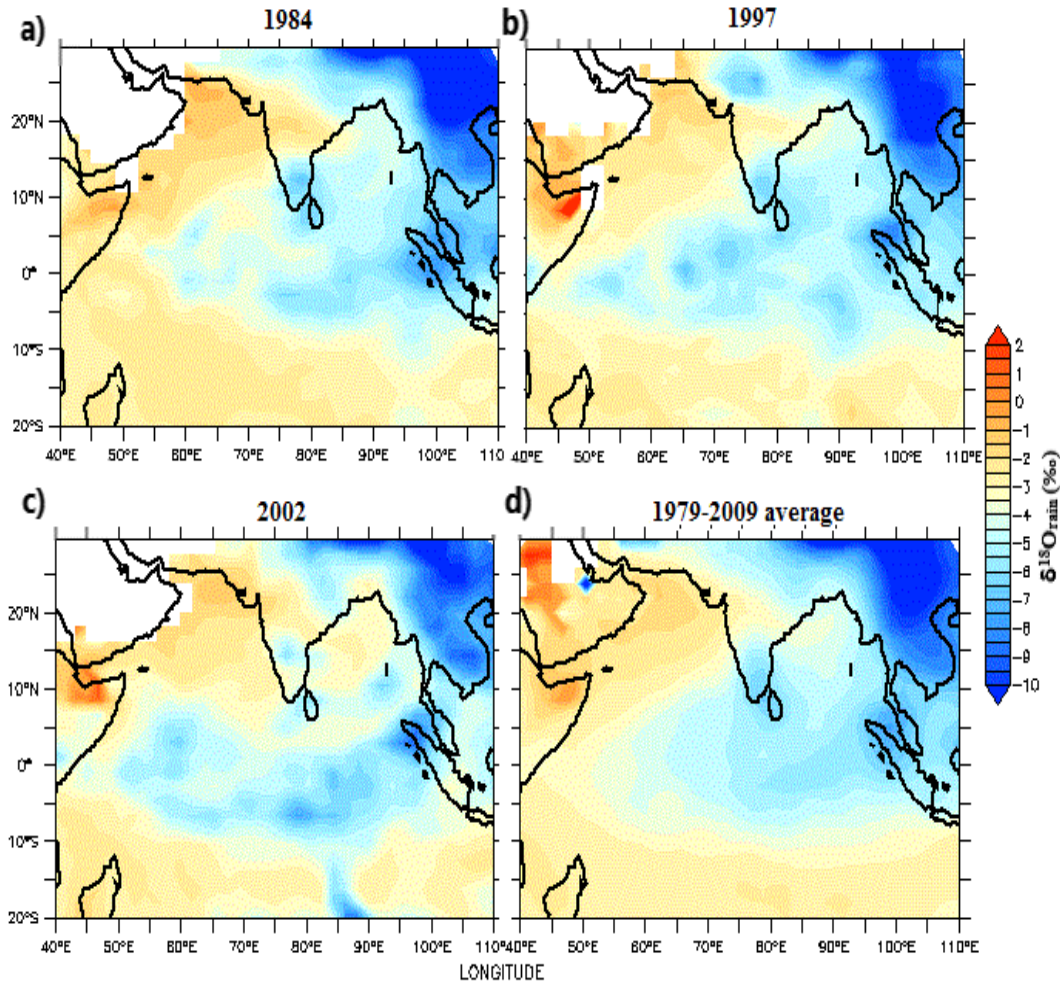


Figure 5.7: The spatial distribution of the JJAS $\delta^{18}\text{O}_{\text{rain}}$ (‰) from the isoGSM model over the Indian subcontinent during different strengths of El-Niño years **a)** 1984, **b)** 1997 (strong El-Niño and positive IOD events occurred concurrently), **c)** 2002, **d)** 1979 to 2009 average. Positive values represent low rainfall, and negative values represent high rainfall regions.

The scatter plots for the $\delta^{18}\text{O}_{\text{rain}}$ (isoGSM derived), and ENSO episodes (when SST anomaly $> +0.5$ °C) showed a significant strong positive correlation and associated with higher $\delta^{18}\text{O}_{\text{rain}}$ values over CI ($r = 0.48$; $p < 0.05$; Figure 5.8a). This positive correlation infers that the rainfall was weaker over the CI, causing $\delta^{18}\text{O}_{\text{rain}}$ values to

increase due to amount effect (evaporation; Rozanski et al. 1993; Gat 1996; Clark and Fritz 2013). However, both the spatial and scatter plots for $\delta^{18}\text{O}_{\text{rain}}$ (isoGSM derived) were unable to reproduce stronger/above-normal rainfall conditions over the NEI during the same El-Niño (Figure 5.7; Figure 5.8b).

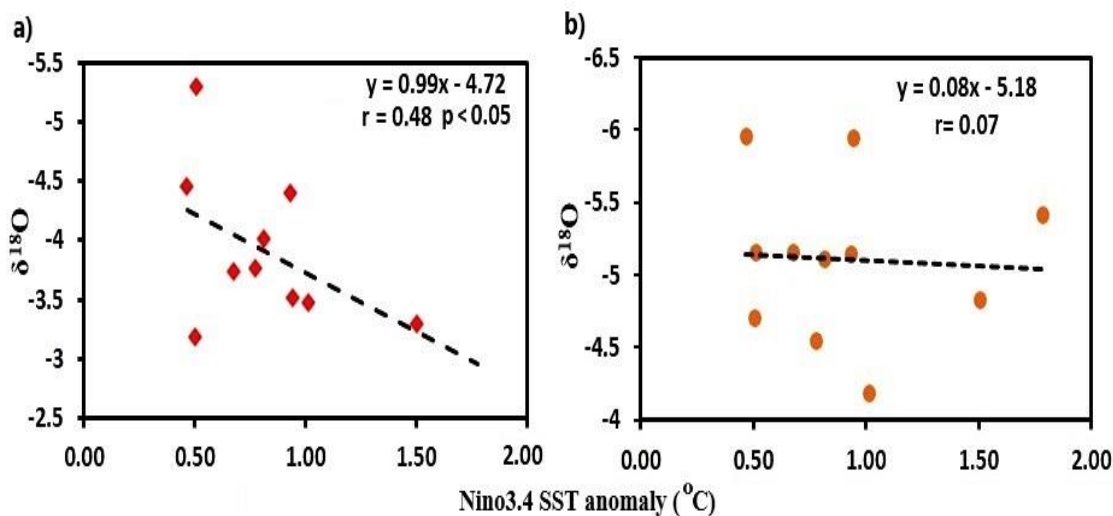


Figure 5.8: Scatter plot for El-Niño events with SST anomaly ($> 0.5^{\circ}\text{C}$) over the Nino3.4 region and corresponding $\delta^{18}\text{O}_{\text{rain}}$ (isoGSM model-derived) over **a)** CI and **b)** NEI during 1979-2009.

The spatial correlation of $\delta^{18}\text{O}_{\text{rain}}$ (isoGSM derived) of CI with global rainfall (isoGSM and GPCP derived) showed significant positive correlations ($r \geq 0.3$; $p < 0.05$) over the CP region (Nino3.4; Figure 5.9a, b). These relations might improve by removing the effect of IOD and Pacific Decadal Oscillation on $\delta^{18}\text{O}_{\text{rain}}$. These spatial correlation patterns again reconfirm the negative El-Niño effect on rainfall distribution over the Indian subcontinent. The positive correlation of $\delta^{18}\text{O}_{\text{rain}}$ of CI with rainfall over CP (represent El-Niño condition) infers that as rainfall over CP increasing, the $\delta^{18}\text{O}_{\text{rain}}$ of CI values increases, which represents the weaker rainfall conditions (Figure 5.9a, b). The rainfall (isoGSM and GPCP derived) over the NEI was positively related to the $\delta^{18}\text{O}_{\text{rain}}$ of CI, which indirectly represents the stronger NEI rainfall conditions during weaker and stronger rainfall over CI and CP respectively (Figure 5.9a, b). Similarly, a positive correlation between the $\delta^{18}\text{O}_{\text{rain}}$ of CI and global SST data was observed over

CP, represent increasing $\delta^{18}\text{O}_{\text{rain}}$ of CI values are associated with higher SST anomaly over CP (El-Niño events; Figure 5.9c).

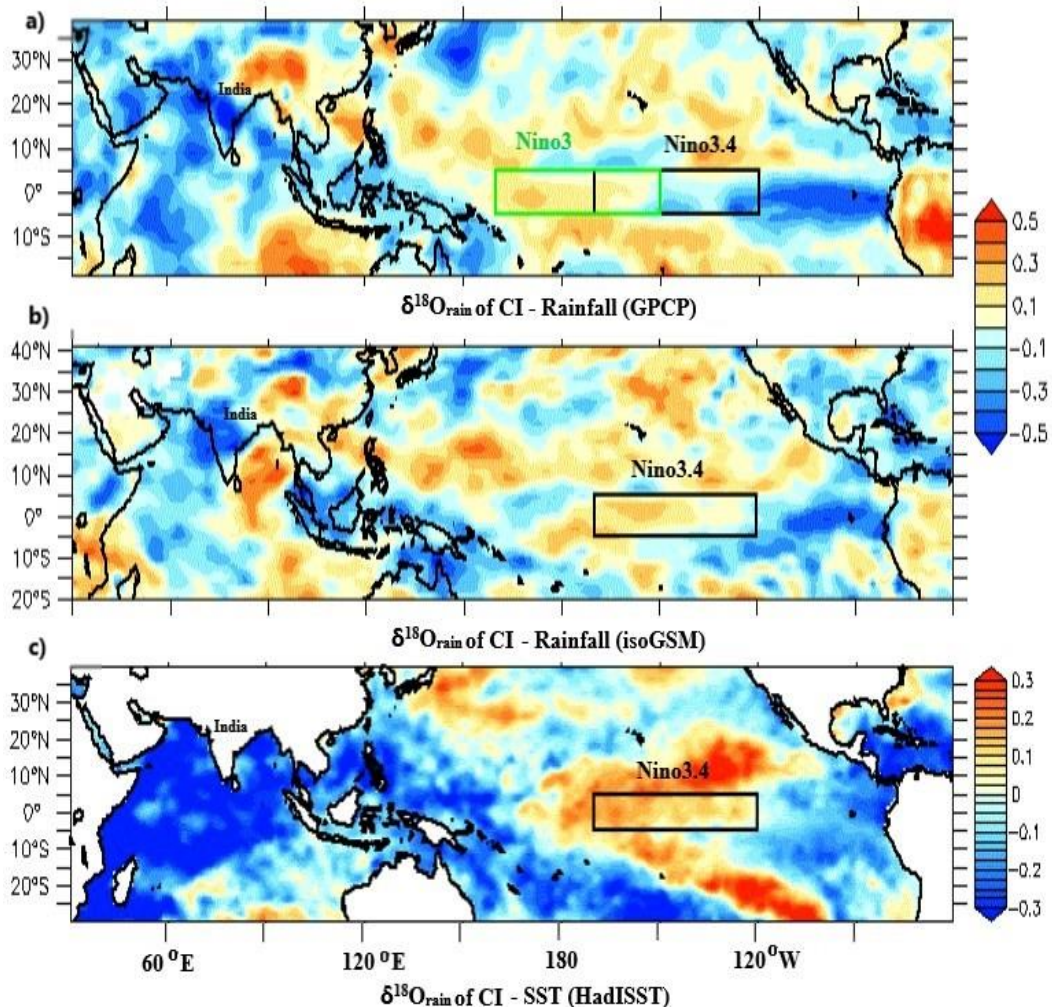


Figure 5.9: Spatial correlation coefficient patterns for $\delta^{18}\text{O}_{\text{rain}}$ of CI (isoGSM derived) with a) GPCP derived rainfall b) isoGSM derived rainfall c) SST anomaly during the period 1979 – 2009. The black box represents the Nino3.4 region and green box Nino3 region.

5.6. Observations in the paleoclimate data

Previous speleothem proxy-based studies have discussed the variation of rainfall in different climatic conditions. Most of these deposits recorded the major short term global climatic events (its effect on Indian monsoon) such as Heinrich events (weaker monsoon), Younger Dryas (weaker monsoon), Bølling Allerød (stronger monsoon) events (Band et al., 2018; Fleitmann et al., 2003; Gautam et al., 2019; Sinha et al.,

2011a; Tiwari et al., 2011; Yadava and Ramesh, 2005). The $\delta^{18}\text{O}$ variation of cave deposits reflects the variation in the rainfall amount over the cave location (Berkelhammer et al., 2010; Sinha et al., 2007; Yadava and Ramesh, 2005). We have reanalyzed the $\delta^{18}\text{O}$ variation of Jhumar and Shikar cave speleothems records from the CI and NEI respectively for the last ~50 years (1960-2008) and corresponding ENSO variability. Both these two cave speleothem records analysis show that the CI (NEI) cave record positively (negatively) correlated with the El-Niño events. It infers that when the SST anomaly over Nino3.4 increases, the $\delta^{18}\text{O}$ record of Jhumar cave deposit shows an increase in the $\delta^{18}\text{O}$ values, which infers the decreasing rainfall conditions over CI. Significant trends were observed in both cave deposits, with an overall strong decreasing ISM strength was observed during 1960-1988, and intense, increasing ISM strength for the periods 1988-2008 over CI region (Figure 5.10a; dark pink dashed trend lines). Similarly, an increasing and decreasing summer monsoon rainfall were observed over the NEI for the same period, respectively (Figure 5.10b). The increasing rainfall (a depleting $\delta^{18}\text{O}$ trend) during the 2002 – 2008 in the Jhumar cave record (CI) and a decreasing trend in the Shikar cave record (NEI) were observed. This dipole nature rainfall variability over CI and NEI during 2002-2008 (even only six years record available) reproduces the inferences based on instrumental data (Figure 5.5a).

In addition to these intervals, the high-resolution speleothem records of CI and NEI showed the decadal variations of low rainfall (pink; negative correlation trend) and the high rainfall (cyan; positive correlation trend) episodes (Figure 5.10: vertical dotted line regions). During 1962 – 1975 & 1988 – 2013, stronger (weaker) and 1975 – 1988 weaker (stronger) monsoon conditions over the CI (NEI) were observed (Figure 5.10a, marked with vertical dotted lines). All these short-time changes (decadal events) in the monsoon strengthening trends are significant at $p < 0.05$ and marked with cyan (strong) and pink (weak) rainfall conditions (Figure 5.10). These short-term changes in monsoon strength were also observed in the instrumental data (Figure 5.5A). It reconfirms that the signatures of the negative (positive) relation of rainfall with ENSO over CI (NEI) and such signals are adeptly recorded by these high-resolution cave

deposits. The strongest El-Niño 1997/98 period was associated with the above-normal rainfall over the Indian subcontinent, which is associated with relatively lower $\delta^{18}\text{O}$ (strong rainfall) in these cave records.

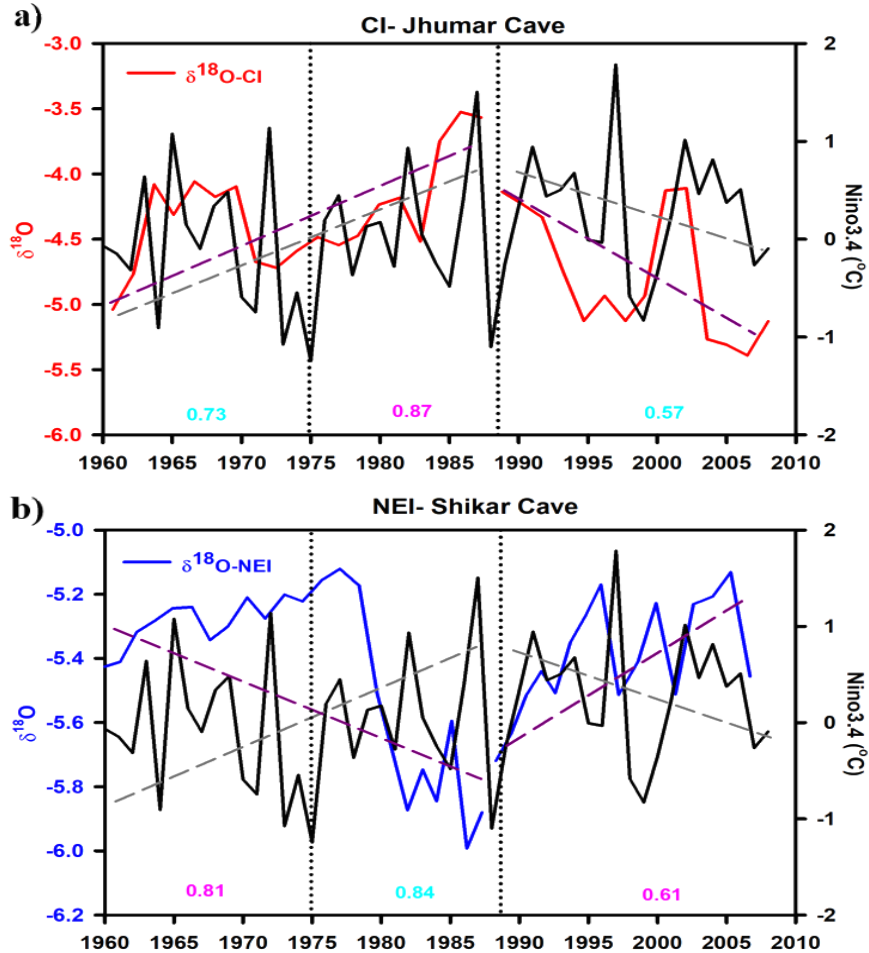


Figure 5.10: Time series analysis of Nino3.4 SST anomaly (black) and $\delta^{18}\text{O}$ of speleothem cave deposit records from **a)** CI-Jhumar cave deposit record (red) **b)** NEI-Shikar cave deposit record (blue); grey and dark pink dashed line shows the trends in Nino3.4 index and $\delta^{18}\text{O}$ variations (significant at $p < 0.05$) for the last ~50 years data. The vertical dotted lines represent three periods of strong (cyan) and weaker (pink) monsoon (explained in the text) over the CI and NEI cave records, and all correlations are significant at $p < 0.05$.

Based on these new calibrations of instrumental and proxy data for last ~ 50 years, we showed that the observed decreasing (increasing) $\delta^{18}\text{O}_{\text{calcite}}$ of Jhumar (Shikar) cave record during 1625 – 1715 might represent the long term pause in the El-Niño events or stronger La-Niña like condition were continued and lead to causing stronger (weaker) rainfall over the CI (NEI; Figure 5.11b, c). However, further analysis is highly

recommended for the confirmation of long term pause in El-Niño (or stronger La-Niña) events during 1625-1715.

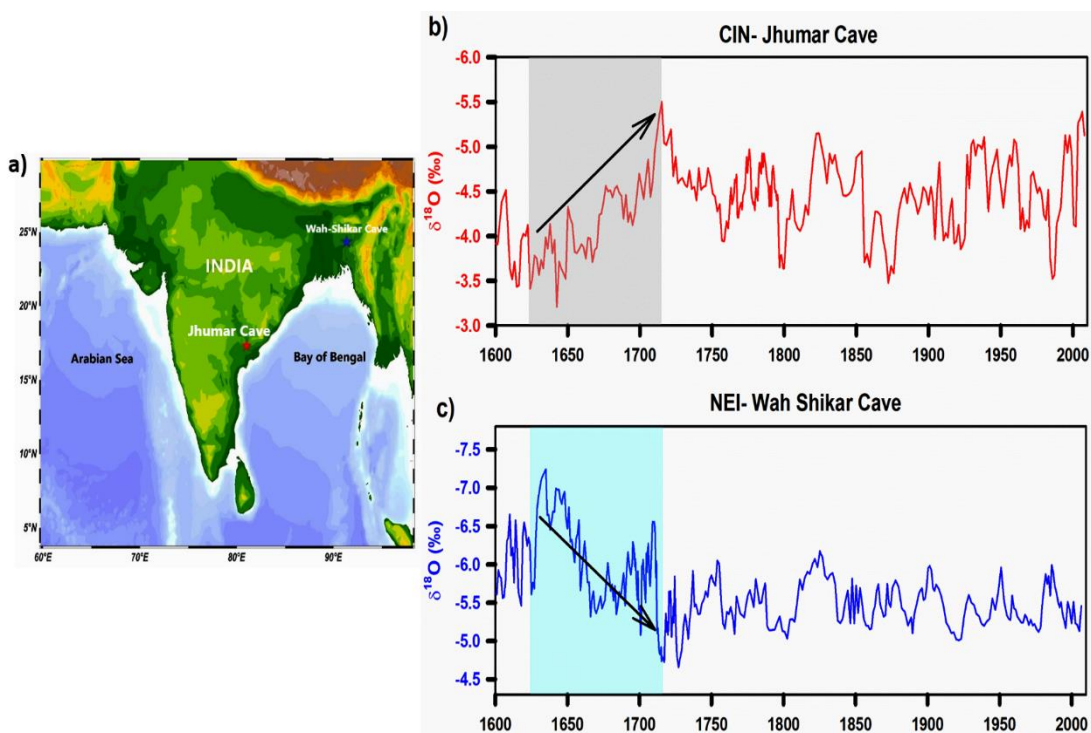


Figure 5.11: a) Cave location from CIN (filled star; red) and NEI (filled star; blue), b) $\delta^{18}\text{O}$ variation of speleothem sample from CIN Jhumar Cave, c) $\delta^{18}\text{O}$ variation record of speleothem sample from NEI-Wah Shikar Cave. Grey and blue shaded regions show the long-term stronger and weaker monsoon periods, respectively.

5.7. Conclusion

The spatiotemporal patterns of rainfall over India and the adjoining Indian Ocean regions at monthly to seasonal time scales in response to the ENSO were studied. A variable spatial-correlation between rainfall over India and SST anomaly over the Nino3.4 region is observed at monthly time scales. A strong negative and positive correlation over CI and NEI, respectively, with moderate to strong El-Niño events, were observed during the summer monsoon (JJAS). Our results suggest that the strong El-Niño events cause relatively weaker summer monsoon rainfall over CI and significantly stronger/above normal rainfall over the NEI during the same event. $\delta^{18}\text{O}_{\text{rain}}$ (model-derived) over CI and corresponding moderate to strong El-Niño events showed a positive correlation, which mimics the observations. These analyses infer that

the long term trends in the ISM strength are controlled by the long term variation of ENSO strength. The paleoclimate proxy records from the CI and NEI cave deposits showed similar patterns in response to moderate to intense El-Niño periods from 1965 – 2010. Both observational and proxy records showed short term decadal variation in the ISM concurred with El-Niño. High-resolution speleothem records from CI and NEI showed an absence of long term El-Niño or stronger La-Niña like conditions during 1625 – 1715, which were associated with stronger (weaker) rainfall over CI (NEI).

Chapter-6
Summary and Scope for Future Work

Chapter-6

This thesis work attempted to understand the dynamics of modern seawater stable isotopic composition ($\delta^{18}\text{O}$, δD) and its controlling processes. Based on modern seawater calibration, stable isotopic compositions of the northern Indian Ocean, upper ocean dynamics, and monsoon variations during last ~70 ka were studied. In addition to the monsoon reconstruction based on deep-sea sediment cores, Indian monsoon variability in response to the coupled ocean-atmospheric processes were studied. The major findings are summarized below:

6.1. Dynamics of $\delta^{18}\text{O}$ and δD in the Northern Indian Ocean

6.1.1. Surface seawater samples

- New data set on $\delta^{18}\text{O}$, δD , and Salinity (S) of surface water samples from the northern Indian Ocean showed significant variations in their relationship.
- Variable $\delta^{18}\text{O}$ –S relation for the surface water samples over the Bay of Bengal (BoB) were observed; with a higher slope and lower intercept during winter than those during summer monsoon period. However, no significant $\delta^{18}\text{O}$ -S

relation for surface water samples during pre-monsoon was observed over the Arabian Sea (AS).

- A strong influence of winter monsoon and the West India coastal currents that transports the monsoon runoff from the BoB to the AS during winter, on the seawater $\delta^{18}\text{O}$ -S relation over the eastern and northern equatorial AS was observed.
- The $\delta^{18}\text{O}$ - δD relation showed seasonal variations due to the influence of the Himalayan and Peninsular river systems on it.
- *d-excess*-S relation along with corresponding $\delta^{18}\text{O}$ values inferred that 67% of total water samples with $S < 33.5$ and ~73% of total water samples with $S > 33.5$ were influenced by the continental runoff and open ocean water mixing, respectively.
- $\delta^{18}\text{O}$ - δD and *d-excess*- $\delta^{18}\text{O}$ relations in the BoB surface water samples infer that the kinetic fractionation dominated more during winter than in spring.
- Lower salinity (< 32.5) and associated lower $\delta^{18}\text{O}$ of surface water samples shows the freshwater influx from the BoB water and Myanmar rivers in the Andaman Sea.
- Pre-monsoon surface water samples over the AS were associated with higher $\delta^{18}\text{O}$, δD , and S values except for the southern AS samples, which might be remnant of the transported BoB water during preceding winter.

6.1.2. Subsurface seawater samples:

- Subsurface $\delta^{18}\text{O}$ composition off the Andaman Islands suggests a gradual enrichment in the $\delta^{18}\text{O}$ values with depth during spring-2016. $\delta^{18}\text{O}$ -S relation in the upper layer (0-50 m) waters in the Andaman Sea was similar to BoB surface waters.
- Significant variation in the $\delta^{18}\text{O}$ -S relation for deep waters (200-500 m depth) in the Andaman Sea was observed. The preliminary analysis shows statistically different $\delta^{18}\text{O}$ -S relation in deeper water (50-200 m) than for shallow water (0-50 m) could be a characteristic of water mass dynamics.

- Significant variation in the $\delta^{18}\text{O}$, δD , S, and temperature was observed at the surface to the deeper (~ 1000 m depth) ocean in the AS during April-2017.
- Significant variation in the thermocline depth was observed with deeper in the southern AS and shallower in the northern AS.
- Our sub-divisional analysis of water column in three zones (based on the observed water masses at different water depths) over the AS shows different $\delta^{18}\text{O}$ -S relation: with stronger positive relation for Zone-I (0-250 m) and Zone-II (250-650 m) and weaker negative relation for Zone-III (~1000 m).

6.2. Paleoceanography of Indian Ocean and Monsoon reconstruction

6.2.2. The Arabian Sea sediment cores:

- A compilation of recent high resolution foraminiferal $\delta^{18}\text{O}$ data from 22 sediment cores from the Eastern Arabian Sea appears to dispel the idea that the south Asian Summer monsoon has steadily declined during the Holocene.
- Based on the last ~ 45 ka record of $\delta^{18}\text{O}$ of planktonic foraminifera (*G. ruber*) from the southern AS, four intense active monsoon periods were observed with lower $\delta^{18}\text{O}$ values. However, another active monsoon was seen during ~ 42 – 41 ka.
- Three weaker monsoon periods were observed with higher $\delta^{18}\text{O}$ values ~ 0.7 ‰. Similar active and weaker monsoon periods were reproduced by the deep-dwelling planktonic species *G. menardii*.
- Significant variation in the $\delta^{18}\text{O}$ values of *G. ruber* in response to abrupt short term climate events were observed: with warm Dansgaard-Oeschger events associated with the relatively stronger monsoon and cold Heinrich Events associated with the weaker monsoon.
- Based on the benthic $\delta^{18}\text{O}$ variability, two extreme colder events and two warmer events were observed for the last ~ 45-18 ka. These cold and warm periods were associated with the weaker and stronger monsoon over the Indian subcontinent (a reduced runoff condition; *G. ruber* $\delta^{18}\text{O}$ data).

- The $\delta^{13}\text{C}$ of benthic foraminifera varied opposite to the $\delta^{18}\text{O}$ variation and associated with depleting trend during the warm periods and enrichment trend during the cold periods.
- Two extreme higher $\delta^{13}\text{C}$ value events were observed in benthic foraminifera during ~29 to 27 ka and ~ 42- 41 ka. Extreme lower values were observed during ~36-30 ka, and higher during ~49 ka; however, during these periods, significant changes in the $\delta^{18}\text{O}$ were not found.

6.2.2. *The Bay of Bengal sediment core:*

- Significant variation in the $\delta^{15}\text{N}$, $\delta^{13}\text{C}_{\text{org}}$, and N & C_{org} (wt %) of the bulk sediment samples of a deep-sea sediment core from the western BoB for last ~ 16 ka were observed.
- $\delta^{15}\text{N}$, $\delta^{13}\text{C}_{\text{org}}$, and N & C_{org} (wt %) variability show that for the last ~ 16 ka, productivity over the western BoB varied significantly.
- Sediment core data shows that during the early to late deglacial period, $\delta^{13}\text{C}_{\text{org}}$ was less than -20 ‰, which shows that C4 plants contributed significantly.
- Relatively higher productivity conditions during deglacial than during Holocene (increasing C_{org} and $\delta^{15}\text{N}$ trends) is observed due to variation in the upper ocean stratification.
- The overall variation of bulk sediment $\delta^{13}\text{C}_{\text{org}}$ and C/N ratios from the BoB shows a mixed influence of terrestrial and marine input during the deglacial to late Holocene (~ 16 ka to present).

6.2.3. *The Andaman Sea sediment core:*

- Based on the records of $\delta^{18}\text{O}$ variations in the three different planktonic foraminiferal species, an abrupt decrease in the ISM during the mid-Holocene (7-4.5 ka) was observed.
- During MIS-3, summer monsoon was relatively weaker than MIS-1 and stronger than MIS-2.

- Based on the $\delta^{18}\text{O}$ difference between the shallow dwelling and deep-dwelling species, distinct weaker and stronger freshwater induced upper ocean stratification events were observed.
- Stable stratification was observed during the early Holocene, mid-MIS-3, and at ~62 ka, due to an increased freshwater influx from Irrawaddy, Salween river systems, and direct precipitation over the Andaman Sea whereas weak stratification was observed during the LGM and late MIS-3.
- Freshwater induced stratification was stronger during the early to mid-MIS-3 than that during LGM, but weaker than that during early Holocene.
- Weaker monsoon conditions were observed during the Heinrich events associated with weaker stratification.
- Compilation of different sediment cores from BoB and the Andaman Sea shows that during early Holocene, the $\delta^{18}\text{O}$ of surface seawater in the Andaman Sea was depleted than that from southern BoB but enriched from northern and western BoB core records.

6.3. Indian Monsoon Variability in response to the coupled processes

- Significant variation in the spatiotemporal patterns of rainfall in response to the ENSO was observed over India and the adjoining Indian Ocean regions at monthly to seasonal time scales.
- A variable spatial-correlation between rainfall over India and SST anomaly over the Niño3.4 region (ENSO) is observed at monthly time scales. A strong negative and positive correlation over CI and NEI, respectively, with El-Niño events during the summer monsoon (JJAS), is observed.
- Our results suggest that the strong El-Niño events cause relatively weaker summer monsoon rainfall over CI and significantly stronger/above normal rainfall over the NEI during the same event.
- Isotope enabled model-derived $\delta^{18}\text{O}$ of rain over CI is positively correlated with moderate to strong El-Niño events.
- The spatial and temporal analysis of instrumental and GCM model derived rainfall (and associated $\delta^{18}\text{O}$) analyses infer that the long term trends in the

Indian summer monsoon strength are controlled by the long term variation of ENSO strengths.

- Paleoclimate proxy records (cave deposits) from the CI and NEI showed similar patterns in response to moderate to intense El-Niño events during the last ~ 50 years data (1965 – 2010).
- High-resolution speleothem records are able to show the ENSO induced changes in the rainfall over CI and NEI.
- Both instrumental and paleoclimate proxy records showed a decadal variability in the ISM concurred with variation in the El-Niño strengths.
- High-resolution speleothem records from CI an NEI showed an absence of long term El-Niño or stronger La-Niña like conditions during 1625 – 1715 AD, which were associated with stronger (weaker) rainfall conditions over CI (NEI).

6.4. Scope for Future Work:

The major part of this thesis work has been able to address the broad objectives decided during inception; however, following new questions and issues were envisaged during the progress of this thesis work which seems to have very good potential for future research:

1. Variation in the $\delta^{18}\text{O}$ of rainfall in response to ENSO was studied over the Indian subcontinent. However, our analysis shows a weaker but significant variation over western India and the southern Indian peninsula. This needs to be studied in detail.
2. Variation in the $\delta^{18}\text{O}$ of rainfall in response to the Indian Ocean Dipole, Pacific Decadal Oscillation, and other global short and long term processes are needed for a better understanding of monsoon variability and paleoclimate reconstruction.
3. $\delta^{15}\text{N}$ and $\delta^{13}\text{C}_{\text{org}}$ in bulk material of the BoB sediment core show significant variation in the past-productivity. However, it is still under-represented, and

hence more sediment core should be studied for paleoproductivity, possibly including some other trace elements as well, apart from the stable isotopes.

4. Seasonal variations in the vertical depth profile of $\delta^{18}\text{O}$ -S relation need a better understanding of identifying characteristics of water masses in the Arabian Sea.
5. Stable isotopic ($\delta^{18}\text{O}$, δD) compositions of surface and sub-surface seawater samples over the BoB during pre and post-cyclone for better estimation of their influences.
6. A large number of spatially well-distributed surface seawater sampling from the Andaman Sea is required. This is for identifying spatial and seasonal variations in the $\delta^{18}\text{O}$, δD compositions, and characterizing the $\delta^{18}\text{O}$ -S relationship and controlling processes.
7. Vertical water sampling (high-resolution depth specific water sampling) and their $\delta^{18}\text{O}$, δD compositions from the Andaman Sea seem to be necessary for understanding mixing of different water masses and their dynamics.
8. With the advancement of new techniques (laser-based mass analyser) in high-resolution (~minutes) measurement of isotopic composition of the ambient atmospheric moisture, influence of various atmospheric processes (short to long time scale) may be studied; at terrestrial sites, a long-term such studies can highlight ENSO effects on the atmospheric hydro-dynamics.

References:

- Achyuthan, H., Deshpande, R., Rao, M., Kumar, B., Nallathambi, T., Kumar, K.S., Ramesh, R., Ramachandran, P., Maurya, A., Gupta, S., 2013. Stable isotopes and salinity in the surface waters of the Bay of Bengal: implications for water dynamics and palaeoclimate. *Mar. Chem.* 149, 51–62.
- Adkins, J.F., McIntyre, K., Schrag, D.P., 2002. The salinity, temperature, and $\delta^{18}\text{O}$ of the glacial deep ocean. *Science* 298, 1769–1773.
- Aggarwal, P.K., Alduchov, O.A., Froehlich, K.O., Araguas-Araguas, L.J., Sturchio, N.C., Kurita, N., 2012. Stable isotopes in global precipitation: A unified interpretation based on atmospheric moisture residence time. *Geophys. Res. Lett.* 39.
- Ahmad, S., Anil Babu, G., Padmakumari, V., Dayal, A., Sukhija, B., Nagabhushanam, P., 2005. Sr, Nd isotopic evidence of terrigenous flux variations in the Bay of Bengal: Implications of monsoons during the last ~ 34,000 years. *Geophys. Res. Lett.* 32.
- Ahmad, S., Patil, D., Rao, P., Nath, B., Rao, B., Rajagopalan, G., 2000. Glacial-interglacial changes in the surface water characteristics of the Andaman Sea: Evidence from stable isotopic ratios of planktonic foraminifera. *J. Earth Syst. Sci.* 109, 153.
- Ahmad, S.M., Babu, G.A., Padmakumari, V.M., Raza, W., 2008. Surface and deep water changes in the northeast Indian Ocean during the last 60 ka inferred from carbon and oxygen isotopes of planktonic and benthic foraminifera. *Palaeogeogr. Palaeoclimatol. Palaeoecol.* 262, 182–188.
- Ali, S., Hathorne, E.C., Frank, M., Gebregiorgis, D., Statterger, K., Stumpf, R., Kutterolf, S., Johnson, J.E., Giosan, L., 2015. South Asian monsoon history over the past 60 kyr recorded by radiogenic isotopes and clay mineral assemblages in the Andaman Sea. *Geochem. Geophys. Geosystems* 16, 505–521.
- Altabet, M.A., Francois, R., 1994. Sedimentary nitrogen isotopic ratio as a recorder for surface ocean nitrate utilization. *Glob. Biogeochem. Cycles* 8, 103–116.
- Altabet, M.A., Francois, R., Murray, D.W., Prell, W.L., 1995. Climate-related variations in denitrification in the Arabian Sea from sediment $^{15}\text{N}/^{14}\text{N}$ ratios. *Nature* 373, 506.
- Altabet, M.A., Higginson, M.J., Murray, D.W., 2002. The effect of millennial-scale changes in Arabian Sea denitrification on atmospheric CO_2 . *Nature* 415, 159.

- Anand, P., Kroon, D., Singh, A.D., Ganeshram, R.S., Ganssen, G., Elderfield, H., 2008. Coupled sea surface temperature-seawater $\delta^{18}\text{O}$ reconstructions in the Arabian Sea at the millennial scale for the last 35 ka. *Paleoceanography* 23, 1–8. <https://doi.org/10.1029/2007PA001564>
- Araghinejad, S., Meidani, E., 2013. A review of climate signals as predictors of long-term hydro-climatic variability, in: *Climate Variability-Regional and Thematic Patterns*. InTech.
- Araguás-Araguás, L., Froehlich, K., 1998. Stable isotope composition of precipitation over southeast Asia. *J. Geophys. Res.* 103, 28721–28742. <https://doi.org/10.1029/98JD02582>
- Araguás-Araguás, L., Froehlich, K., Rozanski, K., 1998a. Stable isotope composition of precipitation over southeast Asia. *J. Geophys. Res. Atmospheres* 103, 28721–28742.
- Araguás-Araguás, L., Froehlich, K., Rozanski, K., 1998b. Stable isotope composition of precipitation over southeast Asia. *J. Geophys. Res. Atmospheres* 103, 28721–28742.
- Arnold, J.R., Libby, W.F., 1949. Age determinations by radiocarbon content: checks with samples of known age. *Science* 110, 678–680.
- Ashok, K., Behera, S.K., Rao, S.A., Weng, H., Yamagata, T., 2007. El Niño Modoki and its possible teleconnection. *J. Geophys. Res. Oceans* 112.
- Ashok, K., Chan, W., Motoi, T., Yamagata, T., 2004. Decadal variability of the Indian Ocean dipole. *Geophys. Res. Lett.* 31.
- Ashok, K., Guan, Z., Yamagata, T., 2001. Impact of the Indian Ocean dipole on the relationship between the Indian monsoon rainfall and ENSO. *Geophys. Res. Lett.* 28, 4499–4502.
- Ashok, K., Saji, N., 2007. On the impacts of ENSO and Indian Ocean dipole events on sub-regional Indian summer monsoon rainfall. *Nat. Hazards* 42, 273–285.
- As-syakur, A.R., Adnyana, I.W.S., Mahendra, M.S., Arthana, I.W., Merit, I.N., Kasa, I.W., Ekayanti, N.W., Nuarsa, I.W., Sunarta, I.N., 2014. Observation of spatial patterns on the rainfall response to ENSO and IOD over Indonesia using TRMM Multisatellite Precipitation Analysis (TMPA). *Int. J. Climatol.* 34, 3825–3839. <https://doi.org/10.1002/joc.3939>
- Baars, M.A., Schalk, P.H., Veldhuis, M.J., 1995. Seasonal fluctuations in plankton biomass and productivity in the ecosystems of the Somali Current, Gulf of Aden and southern Red Sea. Presented at the Status and future of large marine

ecosystems of the Indian Ocean. A report of the International Symposium and Workshop, IUCN-The World Conservation Union Gland, Switzerland, pp. 53–73.

- Baertschi, P., 1976. Absolute $\delta^{18}\text{O}$ content of standard mean ocean water. *Earth Planet. Sci. Lett.* 31, 341–344.
- Banakar, V.K., Mahesh, B.S., Burr, G., Chodankar, A.R., 2010. Climatology of the Eastern Arabian Sea during the last glacial cycle reconstructed from paired measurement of foraminiferal $\delta^{18}\text{O}$ and Mg/Ca. *Quat. Res.* 73, 535–540. <https://doi.org/10.1016/j.yqres.2010.02.002>
- Band, S., Yadava, M., Lone, M.A., Shen, C.-C., Sree, K., Ramesh, R., 2018. High-resolution mid-Holocene Indian Summer Monsoon recorded in a stalagmite from the Kotumsar Cave, Central India. *Quat. Int.* 479, 19–24.
- Bauer, S., Hitchcock, G.L., Olson, D.B., 1991. Influence of monsoonally-forced Ekman dynamics upon surface layer depth and plankton biomass distribution in the Arabian Sea. *Deep Sea Res. Part Oceanogr. Res. Pap.* 38, 531–553.
- Bé, A.W., Hutson, W.H., 1977. Ecology of planktonic foraminifera and biogeographic patterns of life and fossil assemblages in the Indian Ocean. *Micropaleontology* 369–414.
- Beaufort, L., 1996. Dynamics of the monsoon in the equatorial Indian Ocean over the last 260,000 years. *Quat. Int.* 31, 13–18. [https://doi.org/10.1016/1040-6182\(95\)00017-D](https://doi.org/10.1016/1040-6182(95)00017-D)
- Benway, H.M., Mix, A.C., 2004. Oxygen isotopes, upper-ocean salinity, and precipitation sources in the eastern tropical Pacific. *Earth Planet. Sci. Lett.* 224, 493–507.
- Berger, W.H., Parker, F.L., 1970. Diversity of planktonic foraminifera in deep-sea sediments. *Science* 168, 1345–1347.
- Berkelhammer, M., Sinha, A., Mudelsee, M., Cheng, H., Edwards, R.L., Cannariato, K., 2010. Persistent multidecadal power of the Indian Summer Monsoon. *Earth Planet. Sci. Lett.* 290, 166–172.
- Bhushan, R., Yadava, M., Shah, M.S., Raj, H., 2019. Performance of a new 1MV AMS facility (AURiS) at PRL, Ahmedabad, India. *Nucl. Instrum. Methods Phys. Res. Sect. B Beam Interact. Mater. At.* 439, 76–79.
- Bigg, G.R., Rohling, E.J., 2000. An oxygen isotope data set for marine waters. *J. Geophys. Res. Oceans* 105, 8527–8535.

- Black, D.E., Abahazi, M.A., Thunell, R.C., Kaplan, A., Tappa, E.J., Peterson, L.C., 2007. An 8-century tropical Atlantic SST record from the Cariaco Basin: Baseline variability, twentieth-century warming, and Atlantic hurricane frequency. *Paleoceanography* 22.
- Bollasina, M.A., 2014. Hydrology: Probing the monsoon pulse. *Nat. Clim. Change* 4, 422.
- Bolton, C.T., Chang, L., Clemens, S.C., Kodama, K., Ikehara, M., Medina-Elizalde, M., Paterson, G.A., Roberts, A.P., Rohling, E.J., Yamamoto, Y., 2013. A 500,000 year record of Indian summer monsoon dynamics recorded by eastern equatorial Indian Ocean upper water-column structure. *Quat. Sci. Rev.* 77, 167–180.
- Bond, G., Broecker, W., Johnsen, S., McManus, J., Labeyrie, L., Jouzel, J., Bonani, G., 1993. Correlations between climate records from North Atlantic sediments and Greenland ice. *Nature* 365, 143.
- Breitenbach, S.F., Adkins, J.F., Meyer, H., Marwan, N., Kumar, K.K., Haug, G.H., 2010. Strong influence of water vapor source dynamics on stable isotopes in precipitation observed in Southern Meghalaya, NE India. *Earth Planet. Sci. Lett.* 292, 212–220.
- Broecker, W., Peng, T., 1982. *Tracers in the Sea*, Lamont-Doherty Geological Observatory Press, Palisades, N.
- Broecker, W.S., Maier-Reimer, E., 1992. The influence of air and sea exchange on the carbon isotope distribution in the sea. *Glob. Biogeochem. Cycles* 6, 315–320.
- Burdige, D.J., 2005. Burial of terrestrial organic matter in marine sediments: A re-assessment. *Glob. Biogeochem. Cycles* 19.
- Burns, S.J., Fleitmann, D., Matter, A., Kramers, J., Al-Subbary, A.A., 2003. Indian Ocean climate and an absolute chronology over Dansgaard/Oeschger events 9 to 13. *Science* 301, 1365–1367.
- Burns, S.J., Fleitmann, D., Mudelsee, M., Neff, U., Matter, A., Mangini, A., 2002. A 780-year annually resolved record of Indian Ocean monsoon precipitation from a speleothem from south Oman. *J. Geophys. Res. Atmospheres* 107.
- Byrne, M.P., O’gorman, P.A., 2013. Land–ocean warming contrast over a wide range of climates: Convective quasi-equilibrium theory and idealized simulations. *J. Clim.* 26, 4000–4016.

- Cai, W., Van Rensch, P., Cowan, T., Hendon, H.H., 2011. Teleconnection pathways of ENSO and the IOD and the mechanisms for impacts on Australian rainfall. *J. Clim.* 24, 3910–3923.
- Caley, T., Malaizé, B., Revel, M., Ducassou, E., Wainer, K., Ibrahim, M., Shoaib, D., Migeon, S., Marieu, V., 2011. Orbital timing of the Indian, East Asian and African boreal monsoons and the concept of a ‘global monsoon.’ *Quat. Sci. Rev.* 30, 3705–3715.
- Canfield, D.E., 1994. Factors influencing organic carbon preservation in marine sediments. *Chem. Geol.* 114, 315–329.
- Cappa, C.D., Hendricks, M.B., DePaolo, D.J., Cohen, R.C., 2003. Isotopic fractionation of water during evaporation. *J. Geophys. Res. Atmospheres* 108.
- Chakraborty, S., Sinha, N., Chattopadhyay, R., Sengupta, S., Mohan, P., Datye, A., 2016. Atmospheric controls on the precipitation isotopes over the Andaman Islands, Bay of Bengal. *Sci. Rep.* 6, 19555.
- Chamarthi, S., Ram, P.S., Josyula, L., 2008. Effect of river discharge on Bay of Bengal circulation. *Mar. Geod.* 31, 160–168.
- Chand, R., Singh, C., 2015. Movements of western disturbance and associated cloud convection. *J Ind Geophys Union* 19, 62–70.
- Chatterjee, A., Shankar, D., McCreary, J., Vinayachandran, P., Mukherjee, A., 2017. Dynamics of Andaman Sea circulation and its role in connecting the equatorial Indian Ocean to the Bay of Bengal. *J. Geophys. Res. Oceans* 122, 3200–3218.
- Clark, I.D., Fritz, P., 2013. *Environmental isotopes in hydrogeology*. CRC press.
- Clemens, S.C., Prell, W.L., Sun, Y., 2010. Orbital-scale timing and mechanisms driving Late Pleistocene Indo-Asian summer monsoons: Reinterpreting cave speleothem $\delta^{18}O$. *Paleoceanography* 25, 1–19. <https://doi.org/10.1029/2010PA001926>
- Colin, C., Kissel, C., Blamart, D., Turpin, L., 1998. Magnetic properties of sediments in the Bay of Bengal and the Andaman Sea: impact of rapid North Atlantic Ocean climatic events on the strength of the Indian monsoon. *Earth Planet. Sci. Lett.* 160, 623–635.
- Colin, C., Turpin, L., Bertaux, J., Desprairies, A., Kissel, C., 1999. Erosional history of the Himalayan and Burman ranges during the last two glacial–interglacial cycles. *Earth Planet. Sci. Lett.* 171, 647–660.

- Collins, M., An, S.-I., Cai, W., Ganachaud, A., Guilyardi, E., Jin, F.-F., Jochum, M., Lengaigne, M., Power, S., Timmermann, A., 2010. The impact of global warming on the tropical Pacific Ocean and El Niño. *Nat. Geosci.* 3, 391.
- Cook, E.R., Anchukaitis, K.J., Buckley, B.M., D'Arrigo, R.D., Jacoby, G.C., Wright, W.E., 2010. Asian monsoon failure and megadrought during the last millennium. *Science* 328, 486–489.
- Craig, H., 1961. Isotopic variations in meteoric waters. *Science* 133, 1702–1703.
- Craig, H., 1957. Isotopic standards for carbon and oxygen and correction factors for mass-spectrometric analysis of carbon dioxide. *Geochim. Cosmochim. Acta* 12, 133–149.
- Craig, H., Gordon, L.I., 1965a. Deuterium and oxygen 18 variations in the ocean and the marine atmosphere.
- Craig, H., Gordon, L.I., 1965b. Deuterium and oxygen 18 variations in the ocean and the marine atmosphere.
- Criss, R.E., 1999. Principles of stable isotope distribution. Oxford University Press on Demand.
- Cullen, J.L., 1981. Microfossil evidence for changing salinity patterns in the Bay of Bengal over the last 20 000 years. *Palaeogeogr. Palaeoclimatol. Palaeoecol.* 35, 315–356.
- Cullen, J.L., Prell, W.L., 1984. Planktonic foraminifera of the northern Indian Ocean: distribution and preservation in surface sediments. *Mar. Micropaleontol.* 9, 1–52.
- Curry, W., Ostermann, D., Guptha, M., Ittekkot, V., 1992. Foraminiferal production and monsoonal upwelling in the Arabian Sea: evidence from sediment traps. *Geol. Soc. Lond. Spec. Publ.* 64, 93–106.
- Da Silva, R., Mazumdar, A., Mapder, T., Peketi, A., Joshi, R., Shaji, A., Mahalakshmi, P., Sawant, B., Naik, B., Carvalho, M., 2017. Salinity stratification controlled productivity variation over 300 ky in the Bay of Bengal. *Sci. Rep.* 7, 14439.
- Dansgaard, W., 1964. Stable isotopes in precipitation. *Tellus* 16, 436–468.
- Dansgaard, W., Clausen, H., Gundestrup, N., Hammer, C., Johnsen, S., Kristinsdottir, P., Reeh, N., 1982. A new Greenland deep ice core. *Science* 218, 1273–1277.
- de Haas, H., van Weering, T.C., de Stigter, H., 2002. Organic carbon in shelf seas: sinks or sources, processes and products. *Cont. Shelf Res.* 22, 691–717.

- Delaygue, G., Bard, E., Rollion, C., Jouzel, J., Stiévenard, M., Duplessy, J., Ganssen, G., 2001. Oxygen isotope/salinity relationship in the northern Indian Ocean. *J. Geophys. Res. Oceans* 106, 4565–4574.
- Deplazes, G., Lückge, A., Peterson, L.C., Timmermann, A., Hamann, Y., Hughen, K.A., Röhl, U., Laj, C., Cane, M.A., Sigman, D.M., 2013. Links between tropical rainfall and North Atlantic climate during the last glacial period. *Nat. Geosci.* 6, 213.
- Deplazes, G., Lückge, A., Stuut, J.W., Pätzold, J., Kuhlmann, H., Husson, D., Fant, M., Haug, G.H., 2014. Weakening and strengthening of the Indian monsoon during Heinrich events and Dansgaard-Oeschger oscillations. *Paleoceanography* 29, 99–114.
- Deser, C., Alexander, M.A., Xie, S.-P., Phillips, A.S., 2010. Sea surface temperature variability: Patterns and mechanisms. *Annu. Rev. Mar. Sci.* 2, 115–143.
- Deshpande, R., Muraleedharan, P., Singh, R.L., Kumar, B., Rao, M.S., Dave, M., Sivakumar, K., Gupta, S., 2013. Spatio-temporal distributions of $\delta^{18}\text{O}$, δD and salinity in the Arabian Sea: Identifying processes and controls. *Mar. Chem.* 157, 144–161.
- Duplessy, J.C., 1982. Glacial to interglacial contrasts in the northern Indian Ocean. *Nature* 295, 494–498.
- Duplessy, J.C., Lalou, C., Vinot, A.C., 1970. Differential isotopic fractionation in benthic foraminifera and paleotemperatures reassessed. *Science* 168, 250–251.
- Dutt, S., Gupta, A.K., Clemens, S.C., Cheng, H., Singh, R.K., Kathayat, G., Edwards, R.L., 2015. Abrupt changes in Indian summer monsoon strength during 33,800 to 5500 years BP. *Geophys. Res. Lett.* 42, 5526–5532.
- Dwivedi, S., Uma, R., Kumar, T.L., Narayanan, M., Pokhrel, S., Kripalani, R., 2019. New spatial and temporal indices of Indian summer monsoon rainfall. *Theor. Appl. Climatol.* 135, 979–990.
- Emery, W., 2001. Water types and water masses. *Encycl. Ocean Sci.* 6, 3179–3187.
- Emiliani, C., 1955. Pleistocene temperatures. *J. Geol.* 63, 538–578.
- Epstein, S., Mayeda, T., 1953. Variation of O^{18} content of waters from natural sources. *Geochim. Cosmochim. Acta* 4, 213–224.
- Erez, J., Luz, B., 1983. Experimental paleotemperature equation for planktonic foraminifera. *Geochim. Cosmochim. Acta* 47, 1025–1031.

- Fairbanks, R., Matthews, R., 1978. The oxygen isotope stratigraphy of the Pleistocene reef tracts of Barbados, West Indies. *Quat. Res.* 10, 181–196.
- Fairbanks, R.G., 1989. A 17,000-year glacio-eustatic sea level record: influence of glacial melting rates on the Younger Dryas event and deep-ocean circulation. *Nature* 342, 637.
- Fairbanks, R.G., Sverdlow, M., Free, R., Wiebe, P.H., Bé, A.W., 1982. Vertical distribution and isotopic fractionation of living planktonic foraminifera from the Panama Basin. *Nature* 298, 841.
- Fairbanks, R.G., WIEBE, P.H., Bé, A.W., 1980. Vertical distribution and isotopic composition of living planktonic foraminifera in the western North Atlantic. *Science* 207, 61–63.
- Fairchild, I.J., Frisia, S., Borsato, A., Tooth, A.F., 2006. Speleothems.
- Falkowski, P.G., 1997. Evolution of the nitrogen cycle and its influence on the biological sequestration of CO₂ in the ocean. *Nature* 387, 272.
- Faure, G., 1977. Principles of isotope geology.
- Felton, C.S., Subrahmanyam, B., Murty, V., 2013. ENSO-modulated cyclogenesis over the Bay of Bengal. *J. Clim.* 26, 9806–9818.
- Fleitmann, D., Burns, S.J., Mudelsee, M., Neff, U., Kramers, J., Mangini, A., Matter, A., 2003. Holocene forcing of the Indian monsoon recorded in a stalagmite from southern Oman. *Science* 300, 1737–1739.
- Fontugne, M.R., Duplessy, J.-C., 1986. Variations of the monsoon regime during the upper Quaternary: evidence from carbon isotopic record of organic matter in North Indian Ocean sediment cores. *Palaeogeogr. Palaeoclimatol. Palaeoecol.* 56, 69–88.
- Gadgil, R., Viegas, A., Thulasimala, D., 2015. Foraminifera: Indicators of past environment; Key to future: A review.
- Gadgil, S., 2007. The Indian Monsoon. *Resonance* 12, 4–20.
- Gadgil, S., 2003. The Indian monsoon and its variability. *Annu. Rev. Earth Planet. Sci.* 31, 429–467.
- Gadgil, Sulochana, Gadgil, Siddhartha, 2006. The Indian monsoon, GDP and agriculture. *Econ. Polit. Wkly.* 41, 4887–4895.

- Galvin, J., 2008. The weather and climate of the tropics: Part 6–Monsoons. *Weather* 63, 129–137.
- Ganeshram, R.S., Pedersen, T.F., Calvert, S.E., Murray, J.W., 1995. Large changes in oceanic nutrient inventories from glacial to interglacial periods. *Nature* 376, 755.
- Ganopolski, A., Rahmstorf, S., 2001. Rapid changes of glacial climate simulated in a coupled climate model. *Nature* 409, 153.
- Gat, J.R., 1996. Oxygen and hydrogen isotopes in the hydrologic cycle. *Annu. Rev. Earth Planet. Sci.* 24, 225–262.
- Gat, J.R., Gonfiantini, R., 1981. Stable isotope hydrology. Deuterium and oxygen-18 in the water cycle.
- Gautam, P., Narayana, A., Band, S., Yadava, M., Ramesh, R., Wu, C.-C., Shen, C.-C., 2019. High-resolution reconstruction of Indian summer monsoon during the Bølling-Allerød from a central Indian stalagmite. *Palaeogeogr. Palaeoclimatol. Palaeoecol.* 514, 567–576.
- Gebregiorgis, D., Hathorne, E.C., Sijinkumar, A., Nath, B.N., Nürnberg, D., Frank, M., 2016. South Asian summer monsoon variability during the last ~ 54 kys inferred from surface water salinity and river runoff proxies. *Quat. Sci. Rev.* 138, 6–15.
- Ghosh, S., Vittal, H., Sharma, T., Karmakar, S., Kasiviswanathan, K., Dhanesh, Y., Sudheer, K., Gunthe, S., 2016. Indian summer monsoon rainfall: implications of contrasting trends in the spatial variability of means and extremes. *PloS One* 11, e0158670.
- Gibson, R., Atkinson, R., 2003. Oxygen minimum zone benthos: adaptation and community response to hypoxia. *Ocean. Mar. Biol Annu Rev* 41, 1–45.
- Girishkumar, M., Ravichandran, M., 2012a. The influences of ENSO on tropical cyclone activity in the Bay of Bengal during October–December. *J. Geophys. Res. Oceans* 117.
- Girishkumar, M., Ravichandran, M., 2012b. The influences of ENSO on tropical cyclone activity in the Bay of Bengal during October–December. *J. Geophys. Res. Oceans* 117, 1–13.
- Goes, J.I., Thoppil, P.G., do R Gomes, H., Fasullo, J.T., 2005. Warming of the Eurasian landmass is making the Arabian Sea more productive. *Science* 308, 545–547.

- Gomes, H.R., Goes, J.I., Saino, T., 2000. Influence of physical processes and freshwater discharge on the seasonality of phytoplankton regime in the Bay of Bengal. *Cont. Shelf Res.* 20, 313–330.
- Govil, P., Naidu, P.D., 2010. Evaporation-precipitation changes in the eastern Arabian Sea for the last 68 ka: Implications on monsoon variability. *Paleoceanography* 25.
- Grootes, P., Stuiver, M., 1997. Oxygen 18/16 variability in Greenland snow and ice with 10– 3-to 105-year time resolution. *J. Geophys. Res. Oceans* 102, 26455–26470.
- Guhathakurta, P., Rajeevan, M., 2008. Trends in the rainfall pattern over India. *Int. J. Climatol. J. R. Meteorol. Soc.* 28, 1453–1469.
- Gupta, A.K., Anderson, D.M., Overpeck, J.T., 2003. Abrupt changes in the Asian southwest monsoon during the Holocene and their links to the North Atlantic Ocean. *Nature* 421, 354.
- Guptha, M., Curry, W., Ittekkot, V., Muralinath, A., 1997. Seasonal variation in the flux of planktic Foraminifera; sediment trap results from the Bay of Bengal, northern Indian Ocean. *J. Foraminifer. Res.* 27, 5–19.
- Hagemann, R., Nief, G., Roth, E., 1970. Absolute isotopic scale for deuterium analysis of natural waters. Absolute D/H ratio for SMOW 1. *Tellus* 22, 712–715.
- Han, W., McCreary Jr, J.P., Kohler, K.E., 2001. Influence of precipitation minus evaporation and Bay of Bengal rivers on dynamics, thermodynamics, and mixed layer physics in the upper Indian Ocean. *J. Geophys. Res. Oceans* 106, 6895–6916.
- Heinrich, H., 1988. Origin and consequences of cyclic ice rafting in the northeast Atlantic Ocean during the past 130,000 years. *Quat. Res.* 29, 142–152.
- Helland-Hansen, B., 1916. *Nogen hydrografiske metoder*. Scand Naturforsker Mote Kristiana Oslo.
- Hemleben, C., Spindler, M., Anderson, O.R., 2012. *Modern planktonic foraminifera*. Springer Science & Business Media.
- Henrichs, S.M., 1992. Early diagenesis of organic matter in marine sediments: progress and perplexity. *Mar. Chem.* 39, 119–149.
- Hillaire-Marcel, C., Ravelo, A., 2007. The use of Oxygen and Carbon isotopes of Foraminifera in Paleoclimatology. *Dev. Mar. Geol. Proxies Late Cenozoic Paleoclimatogr.* Burlingt. Elsevier Sci.

- Holmes, R.M., Jones, J.B., Fisher, S.G., Grimm, N.B., 1996. Denitrification in a nitrogen-limited stream ecosystem. *Biogeochemistry* 33, 125–146.
- Horii, T., Ueki, I., Hanawa, K., 2012. Breakdown of ENSO predictors in the 2000s: Decadal changes of recharge/discharge-SST phase relation and atmospheric intraseasonal forcing. *Geophys. Res. Lett.* 39, 1–5.
- Howarth, R.W., 1988. Nutrient limitation of net primary production in marine ecosystems. *Annu. Rev. Ecol. Syst.* 19, 89–110.
- Howarth, R.W., Marino, R., 2006. Nitrogen as the limiting nutrient for eutrophication in coastal marine ecosystems: evolving views over three decades. *Limnol. Oceanogr.* 51, 364–376.
- Hu, S., Fedorov, A.V., 2017. The extreme El Niño of 2015–2016 and the end of global warming hiatus. *Geophys. Res. Lett.* 44, 3816–3824.
- Hua, Q., 2009. Radiocarbon: a chronological tool for the recent past. *Quat. Geochronol.* 4, 378–390.
- Iizumi, T., Luo, J.-J., Challinor, A.J., Sakurai, G., Yokozawa, M., Sakuma, H., Brown, M.E., Yamagata, T., 2014. Impacts of El Niño Southern Oscillation on the global yields of major crops. *Nat. Commun.* 5, 3712.
- Ishikawa, S., Oda, M., 2007. Reconstruction of Indian monsoon variability over the past 230,000 years: Planktic foraminiferal evidence from the NW Arabian Sea open-ocean upwelling area. *Mar. Micropaleontol.* 63, 143–154.
- Jain, S.K., Kumar, V., 2012. Trend analysis of rainfall and temperature data for India. *Curr. Sci.* 102, 37–49.
- Jain, V., Shankar, D., Vinayachandran, P., Kankonkar, A., Chatterjee, A., Amol, P., Almeida, A., Michael, G., Mukherjee, A., Chatterjee, M., 2017. Evidence for the existence of Persian Gulf water and Red Sea water in the Bay of Bengal. *Clim. Dyn.* 48, 3207–3226.
- Jin, L., Chen, F., Ganopolski, A., Claussen, M., 2007. Response of East Asian climate to Dansgaard/Oeschger and Heinrich events in a coupled model of intermediate complexity. *J. Geophys. Res. Atmospheres* 112.
- Jin, Q., Wang, C., 2017. A revival of Indian summer monsoon rainfall since 2002. *Nat. Clim. Change* 7, 587–594.
- Joseph, S., Sahai, A., Goswami, B., 2009. Eastward propagating MJO during boreal summer and Indian monsoon droughts. *Clim. Dyn.* 32, 1139–1153.

- Ju, J., Slingo, J., 1995. The Asian summer monsoon and ENSO. *Q. J. R. Meteorol. Soc.* 121, 1133–1168.
- Jung, S.J., Kroon, D., Ganssen, G., Peeters, F., Ganeshram, R., 2009. Enhanced Arabian Sea intermediate water flow during glacial North Atlantic cold phases. *Earth Planet. Sci. Lett.* 280, 220–228.
- Kalnay, E., Kanamitsu, M., Kistler, R., Collins, W., Deaven, D., Gandin, L., Iredell, M., Saha, S., White, G., Woollen, J., Zhu, Y., Chelliah, M., Ebisuzaki, W., Higgins, W., Janowiak, J., Mo, K.C., Ropelewski, C., Wang, J., Leetmaa, A., Reynolds, R., Jenne, R., Joseph, D., 1996. The NCEP/NCAR 40-year reanalysis project. *Bull. Am. Meteorol. Soc.* 77, 437–471.
- Karim, A., Veizer, J., 2002. Water balance of the Indus River Basin and moisture source in the Karakoram and western Himalayas: Implications from hydrogen and oxygen isotopes in river water. *J. Geophys. Res. Atmospheres* 107, ACH-9.
- Kathayat, G., Cheng, H., Sinha, A., Spötl, C., Edwards, R.L., Zhang, H., Li, X., Yi, L., Ning, Y., Cai, Y., 2016. Indian monsoon variability on millennial-orbital timescales. *Sci. Rep.* 6, 24374.
- Kawamura, R., Uemura, K., Suppiah, R., 2005. On the recent change of the Indian summer monsoon-ENSO relationship. *SOLA* 1, 201–204.
- Kessarkar, P.M., Purnachandra Rao, V., Naqvi, S., Karapurkar, S.G., 2013. Variation in the Indian summer monsoon intensity during the Bølling-Ållerød and Holocene. *Paleoceanography* 28, 413–425.
- Kiem, A.S., Franks, S.W., 2001. On the identification of ENSO-induced rainfall and runoff variability: a comparison of methods and indices. *Hydrol. Sci. J.* 46, 715–727.
- Kishtawal, C., Pal, P., Narayanan, M., 1991. Water vapour periodicities over Indian Ocean during contrasting monsoons from NOAA satellite data. *Proc. Indian Acad. Sci.-Earth Planet. Sci.* 100, 341–359.
- Kothawale, D., Rajeevan, M., 2017. Monthly, seasonal and annual rainfall time series for all-India, homogeneous regions and meteorological subdivisions: 1871–2016. *Pune Indian Inst. Trop. Meteorol.* RR138.
- Kotthoff, U., Groeneveld, J., Ash, J., Fanget, A.-S., Krupinski, N.Q., Peyron, O., Stepanova, A., Warnock, J., Van Helmond, N.A., Passey, B.H., 2017. Reconstructing Holocene temperature and salinity variations in the western Baltic Sea region: a multi-proxy comparison from the Little Belt (IODP Expedition 347, Site M0059). *Biogeosciences* 14, 5607–5632.

- Kripalani, R., Kumar, P., 2004. Northeast monsoon rainfall variability over south peninsular India vis-à-vis the Indian Ocean dipole mode. *Int. J. Climatol.* 24, 1267–1282.
- Krishna Kumar, K., Rupa Kumar, K., Ashrit, R., Deshpande, N., Hansen, J.W., 2004. Climate impacts on Indian agriculture. *Int. J. Climatol. J. R. Meteorol. Soc.* 24, 1375–1393.
- Krishna, M., Naidu, S., Subbaiah, C.V., Sarma, V., Reddy, N., 2013. Distribution and sources of organic matter in surface sediments of the eastern continental margin of India. *J. Geophys. Res. Biogeosciences* 118, 1484–1494.
- Krishnamurthy, V., Ajayamohan, R., 2010. Composite structure of monsoon low pressure systems and its relation to Indian rainfall. *J. Clim.* 23, 4285–4305.
- Krishnamurthy, V., Kinter, J.L., 2003. The Indian monsoon and its relation to global climate variability, in: *Global Climate*. Springer, pp. 186–236.
- Krishnamurthy, V., Kirtman, B.P., 2003. Variability of the Indian Ocean: Relation to monsoon and ENSO. *Q. J. R. Meteorol. Soc. J. Atmospheric Sci. Appl. Meteorol. Phys. Oceanogr.* 129, 1623–1646.
- Krishnan, R., Mujumdar, M., Vaidya, V., Ramesh, K., Satyan, V., 2003. The abnormal Indian summer monsoon of 2000. *J. Clim.* 16, 1177–1194.
- Kudrass, H.R., 2001. Modulation and amplification of climatic changes in the Northern Hemisphere by the Indian summer monsoon during the past 80 k . y . 63–66.
- Kumar, K.K., Rajagopalan, B., Cane, M.A., 1999. On the weakening relationship between the Indian monsoon and ENSO. *Science* 284, 2156–2159.
- Kumar, K.K., Rajagopalan, B., Hoerling, M., Bates, G., Cane, M., 2006. Unraveling the mystery of Indian monsoon failure during El Niño. *Science* 314, 115–119.
- Kumar, K.N., Rajeevan, M., Pai, D., Srivastava, A., Preethi, B., 2013. On the observed variability of monsoon droughts over India. *Weather Clim. Extrem.* 1, 42–50.
- Kumar, N., Gwiazda, R., Anderson, R., Froelich, P., 1993. $^{231}\text{Pa}/^{230}\text{Th}$ ratios in sediments as a proxy for past changes in Southern Ocean productivity. *Nature* 362, 45.
- Kumar, P., Kumar, K.R., Rajeevan, M., Sahai, A., 2007. On the recent strengthening of the relationship between ENSO and northeast monsoon rainfall over South Asia. *Clim. Dyn.* 28, 649–660.

- Kumar, S.P., Nuncio, M., Ramaiah, N., Sardesai, S., Narvekar, J., Fernandes, V., Paul, J.T., 2007. Eddy-mediated biological productivity in the Bay of Bengal during fall and spring intermonsoons. *Deep Sea Res. Part Oceanogr. Res. Pap.* 54, 1619–1640.
- Kumar, S.P., Prasad, T., 1999a. Formation and spreading of Arabian Sea high-salinity water mass. *J. Geophys. Res. Oceans* 104, 1455–1464.
- Kumar, S.P., Prasad, T., 1999b. Formation and spreading of Arabian Sea high-salinity water mass. *J. Geophys. Res. Oceans* 104, 1455–1464.
- Kumar, S.P., Prasad, T., 1996. Winter cooling in the northern Arabian Sea. *Curr. Sci.* 834–841.
- Lambs, L., Balakrishna, K., Brunet, F., Probst, J.-L., 2005. Oxygen and hydrogen isotopic composition of major Indian rivers: a first global assessment. *Hydrol. Process.* 19, 3345–3355.
- Lawrence, R.J., Gedzelman, D.S., 1996. Low stable isotope ratios of tropical cyclone rains. *Geophys. Res. Lett.* 23, 527–530.
- LeGrande, A.N., Schmidt, G.A., 2006. Global gridded data set of the oxygen isotopic composition in seawater. *Geophys. Res. Lett.* 33.
- Lekshmy, P., Midhun, M., Ramesh, R., 2015. Spatial variation of amount effect over peninsular India and Sri Lanka: Role of seasonality. *Geophys. Res. Lett.* 42, 5500–5507.
- Libby, W.F., Anderson, E.C., Arnold, J.R., 1949. Age determination by radiocarbon content: world-wide assay of natural radiocarbon. *Sci. N. Y. NY* 109, 227–228.
- Lighthill, M.J., 1969. Dynamic response of the Indian Ocean to onset of the southwest monsoon. *Philos. Trans. R. Soc. Lond. Ser. Math. Phys. Sci.* 265, 45–92.
- Lisiecki, L.E., Raymo, M.E., 2005. A Pliocene-Pleistocene stack of 57 globally distributed benthic $\delta^{18}\text{O}$ records. *Paleoceanography* 20.
- Madhupratap, M., Kumar, S.P., Bhattathiri, P., Kumar, M.D., Raghukumar, S., Nair, K., Ramaiah, N., 1996a. Mechanism of the biological response to winter cooling in the northeastern Arabian Sea. *Nature* 384, 549.
- Madhupratap, M., Kumar, S.P., Bhattathiri, P., Kumar, M.D., Raghukumar, S., Nair, K., Ramaiah, N., 1996b. Mechanism of the biological response to winter cooling in the northeastern Arabian Sea. *Nature* 384, 549.

- Mahala, B.K., Nayak, B.K., Mohanty, P.K., 2015. Impacts of ENSO and IOD on tropical cyclone activity in the Bay of Bengal. *Nat. Hazards* 75, 1105–1125.
- Maity, R., Kumar, D.N., 2006. Bayesian dynamic modeling for monthly Indian summer monsoon rainfall using El Nino–Southern Oscillation (ENSO) and Equatorial Indian Ocean Oscillation (EQUINOO). *J. Geophys. Res. Atmospheres* 111, 1–12.
- Mallya, G., Mishra, V., Niyogi, D., Tripathi, S., Govindaraju, R.S., 2016. Trends and variability of droughts over the Indian monsoon region. *Weather Clim. Extrem.* 12, 43–68.
- Masson-Delmotte, V., Hou, S., Ekaykin, A., Jouzel, J., Aristarain, A., Bernardo, R., Bromwich, D., Cattani, O., Delmotte, M., Falourd, S., 2008. A review of Antarctic surface snow isotopic composition: Observations, atmospheric circulation, and isotopic modeling. *J. Clim.* 21, 3359–3387.
- McConnell, M.C., Thunell, R.C., Lorenzoni, L., Astor, Y., Wright, J.D., Fairbanks, R., 2009. Seasonal variability in the salinity and oxygen isotopic composition of seawater from the Cariaco Basin, Venezuela: Implications for paleosalinity reconstructions. *Geochem. Geophys. Geosystems* 10.
- McCreary Jr, J.P., Kohler, K.E., Hood, R.R., Olson, D.B., 1996. A four-component ecosystem model of biological activity in the Arabian Sea. *Prog. Oceanogr.* 37, 193–240.
- McGee, D., Moreno-Chamarro, E., Green, B., Marshall, J., Galbraith, E., Bradtmiller, L., 2018. Hemispherically asymmetric trade wind changes as signatures of past ITCZ shifts. *Quat. Sci. Rev.* 180, 214–228.
- Medhaug, I., Stolpe, M.B., Fischer, E.M., Knutti, R., 2017. Reconciling controversies about the ‘global warming hiatus.’ *Nature* 545, 41–47.
- Merlivat, L., 1978. Molecular diffusivities of H₂¹⁶O, HD¹⁶O, and H₂¹⁸O in gases. *J. Chem. Phys.* 69, 2864–2871.
- Merlivat, L., Jouzel, J., 1979. Global climatic interpretation of the deuterium-oxygen 18 relationship for precipitation. *J. Geophys. Res. Oceans* 84, 5029–5033.
- Midhun, M., Ramesh, R., 2016. Validation of δ¹⁸O as a proxy for past monsoon rain by multi-GCM simulations. *Clim. Dyn.* 46, 1371–1385.
- Milliman, J.D., Meade, R.H., 1983. World-wide delivery of river sediment to the oceans. *J. Geol.* 91, 1–21.

- Mishra, V., Smoliak, B.V., Lettenmaier, D.P., Wallace, J.M., 2012. A prominent pattern of year-to-year variability in Indian Summer Monsoon Rainfall. *Proc. Natl. Acad. Sci.* 109, 7213–7217.
- Mohanty, P., Pradhan, Y., Nayak, S., Panda, U., Mohapatra, G., 2008. Sediment Dispersion in the Bay of Bengal, in: *Monitoring and Modelling Lakes and Coastal Environments*. Springer, pp. 50–78.
- Mohapatra, M., Geetha, B., Balachandran, S., Rathore, L., 2015. On the tropical cyclone activity and associated environmental features over north Indian Ocean in the context of climate change. *J. Clim. Change* 1, 1–26.
- Mohtadi, M., Prange, M., Oppo, D.W., De Pol-Holz, R., Merkel, U., Zhang, X., Steinke, S., Lückge, A., 2014. North Atlantic forcing of tropical Indian Ocean climate. *Nature* 509, 76.
- Mooley, D., Parthasarathy, B., 1984. Fluctuations in all-India summer monsoon rainfall during 1871–1978. *Clim. Change* 6, 287–301.
- Mooley, D., Shukla, J., 1989. Main features of the westward-moving low pressure systems which form over the Indian region during the summer monsoon season and their relation to the monsoon rainfall. *Mausam* 40, 137–152.
- Müller, P.J., Suess, E., 1979. Productivity, sedimentation rate, and sedimentary organic matter in the oceans—I. Organic carbon preservation. *Deep Sea Res. Part Oceanogr. Res. Pap.* 26, 1347–1362.
- Munz, P.M., Siccha, M., Lückge, A., Böll, A., Kucera, M., Schulz, H., 2015. Decadal-resolution record of winter monsoon intensity over the last two millennia from planktic foraminiferal assemblages in the northeastern Arabian Sea. *The Holocene* 25, 1756–1771.
- Murray, J.W., 2006. *Ecology and applications of benthic foraminifera*. Cambridge University Press.
- Murtugudde, R., Annamalai, H., 2004. Role of the Indian Ocean in regional climate variability. *Geophys Monogr* 147, 213–246.
- Myers, C.G., Oster, J.L., Sharp, W.D., Bennartz, R., Kelley, N.P., Covey, A.K., Breitenbach, S.F., 2015. Northeast Indian stalagmite records Pacific decadal climate change: Implications for moisture transport and drought in India. *Geophys. Res. Lett.* 42, 4124–4132.
- Naidu, P.D., Babu, C.P., Rao, C.M., 1992. The upwelling record in the sediments of the western continental margin of India. *Deep Sea Res. Part Oceanogr. Res. Pap.* 39, 715–723.

- Naqvi, W.A., Charles, C.D., Fairbanks, R.G., 1994. Carbon and oxygen isotopic records of benthic foraminifera from the Northeast Indian Ocean: implications on glacial-interglacial atmospheric CO₂ changes. *Earth Planet. Sci. Lett.* 121, 99–110.
- Navarra, A., Ward, M., Miyakoda, K., 1999. Tropical-wide teleconnection and oscillation. I: Teleconnection indices and type I/type II states. *Q. J. R. Meteorol. Soc.* 125, 2909–2935.
- Nieuwenhuize, J., Maas, Y.E., Middelburg, J.J., 1994. Rapid analysis of organic carbon and nitrogen in particulate materials. *Mar. Chem.* 45, 217–224.
- Noone, D., 2012. Pairing measurements of the water vapor isotope ratio with humidity to deduce atmospheric moistening and dehydration in the tropical midtroposphere. *J. Clim.* 25, 4476–4494.
- O'HARE, G., 1997. The Indian Monsoon Part 1: The Wind System. *Geogr. J. Geogr. Assoc.* 82, 218.
- O'Neil, J.R., Clayton, R.N., Mayeda, T.K., 1969. Oxygen isotope fractionation in divalent metal carbonates. *J. Chem. Phys.* 51, 5547–5558.
- Otto, J., Hermelin, R., Shimmield, G.B., 1995. Impact of productivity events on the benthic foraminiferal fauna in the Arabian Sea over the last 150,000 years. *Paleoceanography* 10, 85–116.
- Parthasarathy, B., Kumar, K.R., Munot, A., 1993. Homogeneous Indian monsoon rainfall: variability and prediction. *Proc. Indian Acad. Sci.-Earth Planet. Sci.* 102, 121–155.
- Parthasarathy, B., Munot, A., Kothawale, D., 1994. All-India monthly and seasonal rainfall series: 1871–1993. *Theor. Appl. Climatol.* 49, 217–224.
- Parton, A., White, T.S., Parker, A.G., Breeze, P.S., Jennings, R., Groucutt, H.S., Petraglia, M.D., 2015. Orbital-scale climate variability in Arabia as a potential motor for human dispersals. *Quat. Int.* 382, 82–97. <https://doi.org/10.1016/j.quaint.2015.01.005>
- Patnaik, R., Gupta, A.K., Naidu, P.D., Yadav, R., Bhattacharyya, A., Kumar, M., 2012. Indian monsoon variability at different time scales: marine and terrestrial proxy records.
- Pattan, J., Mir, I.A., Parthiban, G., Karapurkar, S.G., Matta, V., Naidu, P., Naqvi, S., 2013. Coupling between suboxic condition in sediments of the western Bay of Bengal and southwest monsoon intensification: a geochemical study. *Chem. Geol.* 343, 55–66.

- Pausata, F.S., Battisti, D.S., Nisancioglu, K.H., Bitz, C.M., 2011. Chinese stalagmite $\delta^{18}\text{O}$ controlled by changes in the Indian monsoon during a simulated Heinrich event. *Nat. Geosci.* 4, 474.
- Pearson, P.N., 2012. Oxygen Isotopes in Foraminifera: Overview and Historical Review $\text{R} = 18\text{O} / 16\text{O}$. *Paleontol. Soc. Pap.* 18, 1–38.
- Pedersen, T.F., 1983. Increased productivity in the eastern equatorial Pacific during the last glacial maximum (19,000 to 14,000 yr BP). *Geology* 11, 16–19.
- Petrucci, R.H., Herring, F.G., Bissonnette, C., Madura, J.D., 2017. General chemistry: principles and modern applications. Pearson.
- Phillips, S.C., Johnson, J.E., Giosan, L., Rose, K., 2014. Monsoon-influenced variation in productivity and lithogenic sediment flux since 110 ka in the offshore Mahanadi Basin, northern Bay of Bengal. *Mar. Pet. Geol.* 58, 502–525.
- Pisharoty, P., Desai, B., 1956. Western disturbances and Indian weather. *Indian J Meteorol Geophys* 7, 333–338.
- Potts, P.J., 2012. A handbook of silicate rock analysis. Springer Science & Business Media.
- Prasad, T., 1997. Annual and seasonal mean buoyancy fluxes for the tropical Indian Ocean. *Curr. Sci.* 667–674.
- Prasad, T., Ikeda, M., Kumar, S.P., 2001. Seasonal spreading of the Persian Gulf Water mass in the Arabian Sea. *J. Geophys. Res. Oceans* 106, 17059–17071.
- Prasanna Kumar, S., Muraleedharan, P., Prasad, T., Gauns, M., Ramaiah, N., De Souza, S., Sardesai, S., Madhupratap, M., 2002. Why is the Bay of Bengal less productive during summer monsoon compared to the Arabian Sea? *Geophys. Res. Lett.* 29, 88–1.
- Prasanna Kumar, S., Narvekar, J., Kumar, A., Shaji, C., Anand, P., Sabu, P., Rijomon, G., Josia, J., Jayaraj, K., Radhika, A., 2004a. Intrusion of the Bay of Bengal water into the Arabian Sea during winter monsoon and associated chemical and biological response. *Geophys. Res. Lett.* 31.
- Prasanna Kumar, S., Nuncio, M., Narvekar, J., Kumar, A., Sardesai, de S., De Souza, S., Gauns, M., Ramaiah, N., Madhupratap, M., 2004b. Are eddies nature's trigger to enhance biological productivity in the Bay of Bengal? *Geophys. Res. Lett.* 31.
- Prasanna, V., 2014. Impact of monsoon rainfall on the total foodgrain yield over India. *J. Earth Syst. Sci.* 123, 1129–1145.

- Prell, W., 1981. Faunal and isotopic indices of monsoonal upwelling: Western Arabian Sea. *Oceanol. Acta* 4, 91–98.
- Prell, W.L., Kutzbach, J.E., 1987. Monsoon variability over the past 150,000 years. *J. Geophys. Res.* 92, 8411–8425. <https://doi.org/10.1029/JD092iD07p08411>
- Premuzic, E.T., Benkovitz, C.M., Gaffney, J.S., Walsh, J.J., 1982. The nature and distribution of organic matter in the surface sediments of world oceans and seas. *Org. Geochem.* 4, 63–77.
- Prins, M., Postma, G., Weltje, G.J., 2000. Controls on terrigenous sediment supply to the Arabian Sea during the late Quaternary: the Makran continental slope. *Mar. Geol.* 169, 351–371.
- Rajeevan, M., Bhate, J., Kale, J., Lal, B., 2006. High resolution daily gridded rainfall data for the Indian region: Analysis of break and active monsoon spells. *Curr. Sci.* 296–306.
- Rajeevan, M., Gadgil, S., Bhate, J., 2010. Active and break spells of the Indian summer monsoon. *J. Earth Syst. Sci.* 119, 229–247.
- Rajeevan, M., Pai, D., 2007. On the El Niño-Indian monsoon predictive relationships. *Geophys. Res. Lett.* 34, 1–4.
- Rajeevan, M., Unnikrishnan, C., Bhate, J., Niranjana Kumar, K., Sreekala, P., 2012. Northeast monsoon over India: variability and prediction. *Meteorol. Appl.* 19, 226–236.
- Raju, D., Gouveia, A., Murty, C., 1981. Some physical characteristics of Andaman Sea waters during winter.
- Ramesh, R., Sarin, M., 1992. Stable isotope study of the Ganga (Ganges) river system. *J. Hydrol.* 139, 49–62.
- Ramesh, R., Tiwari, M., Chakraborty, S., Managave, S., Yadava, M., Sinha, D., 2010. Retrieval of south Asian monsoon variation during the Holocene from natural climate archives. *Curr. Sci.* 99, 1770–1786.
- Rao, G.V., Schaub Jr, W.R., Puetz, J., 1981. Evaporation and precipitation over the Arabian Sea during several monsoon seasons. *Mon. Weather Rev.* 109, 364–370.
- Rao, P., Mohanty, U., Ramesh, K., 2005. The evolution and retreat features of the summer monsoon over India. *Meteorol. Appl.* 12, 241–255.

- Rao, R., Sivakumar, R., 2003. Seasonal variability of sea surface salinity and salt budget of the mixed layer of the north Indian Ocean. *J. Geophys. Res. Oceans* 108.
- Rashid, H., England, E., Thompson, L., Polyak, L., 2011. Late glacial to Holocene Indian summer monsoon variability based upon sediment. *Terr. Atmosphere Ocean Sci.* 22, 215–228. [https://doi.org/10.3319/TAO.2010.09.17.02\(TibXS\)1](https://doi.org/10.3319/TAO.2010.09.17.02(TibXS)1).
- Rashid, H., Flower, B.P., Poore, R.Z., Quinn, T.M., 2007. A ~25 ka Indian Ocean monsoon variability record from the Andaman Sea. *Quat. Sci. Rev.* 26, 2586–2597. <https://doi.org/10.1016/j.quascirev.2007.07.002>
- Rashid, H., Gurlan, A.T., Marche, B., Sheppard, K., Khélifi, N., 2019. Changes in Indian Summer Monsoon Using Neodymium (Nd) Isotopes in the Andaman Sea During the Last 24,000 years. *Earth Syst. Environ.* 1–13.
- Ratnam, J.V., Behera, S.K., Masumoto, Y., Takahashi, K., Yamagata, T., 2010. Pacific Ocean origin for the 2009 Indian summer monsoon failure. *Geophys. Res. Lett.* 37, 1–6.
- Ravelo, A., Fairbanks, R., 1995. Carbon isotopic fractionation in multiple species of planktonic foraminifera from core-tops in the tropical Atlantic. *Oceanogr. Lit. Rev.* 10, 854.
- Rayner, N., Parker, D.E., Horton, E., Folland, C., Alexander, L., Rowell, D., Kent, E., Kaplan, A., 2003. Global analyses of sea surface temperature, sea ice, and night marine air temperature since the late nineteenth century. *J. Geophys. Res. Atmospheres* 108, 1–37.
- Raza, T., Ahmad, S.M., 2013. Surface and deep water variations in the northeast Indian Ocean during 34-6 ka BP: Evidence from carbon and oxygen isotopes of fossil foraminifera. *Quat. Int.* 298, 37–44. <https://doi.org/10.1016/j.quaint.2012.05.005>
- Raza, T., Ahmad, S.M., Sahoo, M., Banerjee, B., Bal, I., Dash, S., Suseela, G., Mukherjee, I., 2014a. Hydrographic changes in the southern Bay of Bengal during the last ~65,000 y inferred from carbon and oxygen isotopes of foraminiferal fossil shells. *Quat. Int.* 333, 77–85. <https://doi.org/10.1016/j.quaint.2014.02.010>
- Raza, T., Ahmad, S.M., Sahoo, M., Banerjee, B., Bal, I., Dash, S., Suseela, G., Mukherjee, I., 2014b. Hydrographic changes in the southern Bay of Bengal during the last ~65,000 y inferred from carbon and oxygen isotopes of foraminiferal fossil shells. *Quat. Int.* 333, 77–85. <https://doi.org/10.1016/j.quaint.2014.02.010>

- Raza, T., Ahmad, S.M., Steinke, S., Raza, W., Lone, M.A., Beja, S.K., Suseela, G., 2017. Glacial to Holocene changes in sea surface temperature and seawater $\delta^{18}\text{O}$ in the northern Indian Ocean. *Palaeogeogr. Palaeoclimatol. Palaeoecol.* 485, 697–705.
- Robinson, R.A.J., Bird, M., Oo, N.W., Hoey, T., Aye, M.M., Higgitt, D., Swe, A., Tun, T., Win, S.L., 2007. The Irrawaddy river sediment flux to the Indian Ocean: the original nineteenth-century data revisited. *J. Geol.* 115, 629–640.
- Robinson, R.S., Brunelle, B.G., Sigman, D.M., 2004. Revisiting nutrient utilization in the glacial Antarctic: Evidence from a new method for diatom-bound N isotopic analysis. *Paleoceanography* 19.
- Rochford, D., 1964. Salinity maxima in the upper 1000 metres of the north Indian Ocean. *Mar. Freshw. Res.* 15, 1–24.
- Rodolfo, K.S., 1969. Sediments of the Andaman basin, northeastern Indian Ocean. *Mar. Geol.* 7, 371–402.
- Rohling, E.J., 2007. Progress in paleosalinity: Overview and presentation of a new approach. *Paleoceanography* 22.
- Roxy, M.K., Ritika, K., Terray, P., Murtugudde, R., Ashok, K., Goswami, B., 2015. Drying of Indian subcontinent by rapid Indian Ocean warming and a weakening land-sea thermal gradient. *Nat. Commun.* 6, 1–5.
- Rozanski, K., Araguás-Araguás, L., Gonfiantini, R., 1993. Isotopic patterns in modern global precipitation. *Clim. Change Cont. Isot. Rec.* 1–36.
- Rozanski, K., Araguas-Araguas, L., Gonfiantini, R., 1992. Relation between long-term trends of oxygen-18 isotope composition of precipitation and climate. *Science* 258, 981–985.
- Rozanski, K., Sonntag, C., 1982. Vertical distribution of deuterium in atmospheric water vapour. *Tellus* 34, 135–141.
- Sadekov, A., Eggins, S.M., De Deckker, P., Ninnemann, U., Kuhnt, W., Bassinot, F., 2009. Surface and subsurface seawater temperature reconstruction using Mg/Ca microanalysis of planktonic foraminifera *Globigerinoides ruber*, *Globigerinoides sacculifer*, and *Pulleniatina obliquiloculata*. *Paleoceanography* 24.
- Sahoo, B., Bhaskaran, P.K., 2016. Assessment on historical cyclone tracks in the Bay of Bengal, east coast of India. *Int. J. Climatol.* 36, 95–109.

- Saikranthi, K., Radhakrishna, B., Satheesh, S., Rao, T.N., 2017. Spatial variation of different rain systems during El Niño and La Niña periods over India and adjoining ocean. *Clim. Dyn.* 50, 3671–3685.
- Saraswat, R., 2015. Non-destructive foraminiferal paleoclimatic proxies: A brief insight.
- Saraswat, R., Lea, D.W., Nigam, R., Mackensen, A., Naik, D.K., 2013. Deglaciation in the tropical Indian Ocean driven by interplay between the regional monsoon and global teleconnections. *Earth Planet. Sci. Lett.* 375, 166–175. <https://doi.org/10.1016/j.epsl.2013.05.022>
- Saraswat, R., Naik, D.K., Nigam, R., Gaur, A.S., 2016. Timing, cause and consequences of mid-Holocene climate transition in the Arabian Sea. *Quat. Res.* 86, 162–169.
- Sarkar, A., Ramesh, R., Bhattacharya, S., Rajagopalan, G., 1990. Oxygen isotope evidence for a stronger winter monsoon current during the last glaciation. *Nature* 343, 549.
- Sarkar, A., Ramesh, R., Somayajulu, B.L.K., Agnihotri, R., Jull, A.J.T., Burr, O.S., 2000. High resolution Holocene monsoon record from the eastern Arabian Sea. *Earth Planet. Sci. Lett.* 177, 209–218. [https://doi.org/10.1016/S0012-821X\(00\)00053-4](https://doi.org/10.1016/S0012-821X(00)00053-4)
- Sarkar, S., Singh, R.P., Kafatos, M., 2004. Further evidences for the weakening relationship of Indian rainfall and ENSO over India. *Geophys. Res. Lett.* 31, 1–4.
- Schanze, J.J., Schmitt, R.W., Yu, L., 2010. The global oceanic freshwater cycle: A state-of-the-art quantification. *J. Mar. Res.* 68, 569–595.
- Schmidt, G., 1999. Global seawater oxygen-18 database. [Httpdata Giss Nasa Govo18data.](http://data.giss.nasa.gov/o18data/)
- Schott, F.A., McCreary Jr, J.P., 2001a. The monsoon circulation of the Indian Ocean. *Prog. Oceanogr.* 51, 1–123.
- Schott, F.A., McCreary Jr, J.P., 2001b. The monsoon circulation of the Indian Ocean. *Prog. Oceanogr.* 51, 1–123.
- Schrader, H., 1992. Coastal upwelling and atmospheric CO₂ changes over the last 400,000 years: Peru. *Mar. Geol.* 107, 239–248.

- Schrag, D.P., Hampt, G., Murray, D.W., 1996. Pore fluid constraints on the temperature and oxygen isotopic composition of the glacial ocean. *Science* 272, 1930–1932.
- Schulz, H., von Rad, U., Erlenkeuser, H., 1998. Correlation between Arabian Sea and Greenland climate oscillations of the past 110,000 years. *Nature* 393, 54.
- Sengupta, D., Bharath Raj, G., Shenoi, S., 2006. Surface freshwater from Bay of Bengal runoff and Indonesian throughflow in the tropical Indian Ocean. *Geophys. Res. Lett.* 33.
- Sengupta, S., Parekh, A., Chakraborty, S., Ravi Kumar, K., Bose, T., 2013. Vertical variation of oxygen isotope in Bay of Bengal and its relationships with water masses. *J. Geophys. Res. Oceans* 118, 6411–6424.
- Seo, H., Xie, S.-P., Murtugudde, R., Jochum, M., Miller, A.J., 2009. Seasonal effects of Indian Ocean freshwater forcing in a regional coupled model. *J. Clim.* 22, 6577–6596.
- Sessions, A.L., Burgoyne, T.W., Hayes, J.M., 2001. Determination of the H3 factor in hydrogen isotope ratio monitoring mass spectrometry. *Anal. Chem.* 73, 200–207.
- Shackleton, N., 1967. Oxygen isotope analyses and Pleistocene temperatures re-assessed. *Nature* 215, 15.
- Shackleton, N.J., 1969. The last interglacial in the marine and terrestrial records. *Proc. R. Soc. Lond. B Biol. Sci.* 174, 135–154.
- Shakun, J.D., Burns, S.J., Fleitmann, D., Kramers, J., Matter, A., Al-Subary, A., 2007. A high-resolution, absolute-dated deglacial speleothem record of Indian Ocean climate from Socotra Island, Yemen. *Earth Planet. Sci. Lett.* 259, 442–456.
- Shetye, S., Gouveia, A., Shenoi, S., 1994. Circulation and water masses of the Arabian Sea. *Proc. Indian Acad. Sci.-Earth Planet. Sci.* 103, 107–123.
- Shetye, S., Shenoi, S., Gouveia, A., Michael, G., Sundar, D., Nampoothiri, G., 1991. Wind-driven coastal upwelling along the western boundary of the Bay of Bengal during the southwest monsoon. *Cont. Shelf Res.* 11, 1397–1408.
- Sijinkumar, A., Nath, B.N., Possnert, G., Aldahan, A., 2011. Pulleniatina Minimum Events in the Andaman Sea (NE Indian Ocean): Implications for winter monsoon and thermocline changes. *Mar. Micropaleontol.* 81, 88–94.
- Sijinkumar, A.V., Clemens, S., Nath, B.N., Prell, W., Benshila, R., Lengaigne, M., 2016. $\delta^{18}\text{O}$ and salinity variability from the Last Glacial Maximum to Recent

in the Bay of Bengal and Andaman Sea. *Quat. Sci. Rev.* 135, 79–91.
<https://doi.org/10.1016/j.quascirev.2016.01.022>

Sijinkumar, A.V., Nath, B.N., Guptha, M.V., Ahmad, S.M., Rao, B.R., 2015. Timing and preservation mechanism of deglacial pteropod spike from the Andaman Sea, northeastern Indian Ocean. *Boreas* 44, 432–444.

Sijinkumar, A.V., Nath, B.N., Guptha, M.V.S., 2010a. Late Quaternary record of pteropod preservation from the Andaman Sea. *Mar. Geol.* 275, 221–229.
<https://doi.org/10.1016/j.margeo.2010.06.003>

Sijinkumar, A.V., Nath, B.N., Guptha, M.V.S., 2010b. Late Quaternary record of pteropod preservation from the Andaman Sea. *Mar. Geol.* 275, 221–229.
<https://doi.org/10.1016/j.margeo.2010.06.003>

Sikka, D., 1980. Some aspects of the large scale fluctuations of summer monsoon rainfall over India in relation to fluctuations in the planetary and regional scale circulation parameters. *Proc. Indian Acad. Sci.-Earth Planet. Sci.* 89, 179–195.

Sikka, D., 1978. Some aspects of the life history, structure and movement of monsoon depressions, in: *Monsoon Dynamics*. Springer, pp. 1501–1529.

Silva, R., Mazumdar, A., Mapder, T., Peketi, A., Joshi, R., Shaji, A., Mahalakshmi, P., Sawant, B., Naik, B., Carvalho, M., 2017. Salinity stratification controlled productivity variation over 300 ky in the Bay of Bengal. *Sci. Rep.* 7, 14439.

Singh, a D., Kroon, D., Ganeshram, R.S., 2006. Millennial scale variations in productivity and OMZ intensity in the Eastern Arabian Sea. *J. Geol. Soc. India* 68, 369–377.

Singh, A., Jani, R., Ramesh, R., 2010. Spatiotemporal variations of the $\delta^{18}\text{O}$ –salinity relation in the northern Indian Ocean. *Deep Sea Res. Part Oceanogr. Res. Pap.* 57, 1422–1431.

Singh, A., Mohiuddin, A., Ramesh, R., Raghav, S., 2014. Estimating the Loss of Himalayan Glaciers under Global Warming Using the $\delta^{18}\text{O}$ –Salinity Relation in the Bay of Bengal. *Environ. Sci. Technol. Lett.* 1, 249–253.

SINGH, A.D., 2016. Indian Contributions to Marine Micropaleontology (2010-2015). *Proc. Indian Natl. Sci. Acad.* 82, 663–673.

Singh, A.K., Tiwari, M., Srivastava, A., Sinha, D.K., Ramesh, R., 2016. Wind Strength Variability in the Western Arabian Sea since the Last Glacial Maximum: Southwest vs. Northeast Monsoon Modes. *J. Clim. Change* 2, 57–70.

- Singh, M., Bhatla, R., 2019. Modulation of active-break spell of Indian summer monsoon by Madden Julian Oscillation. *J. Earth Syst. Sci.* 128, 70.
- Singh, O., Khan, T.A., Rahman, M.S., 2000. Changes in the frequency of tropical cyclones over the North Indian Ocean. *Meteorol. Atmospheric Phys.* 75, 11–20.
- Sinha, A., Berkelhammer, M., Stott, L., Mudelsee, M., Cheng, H., Biswas, J., 2011a. The leading mode of Indian Summer Monsoon precipitation variability during the last millennium. *Geophys. Res. Lett.* 38.
- Sinha, A., Cannariato, K.G., Stott, L.D., Cheng, H., Edwards, R.L., Yadava, M.G., Ramesh, R., Singh, I.B., 2007. A 900-year (600 to 1500 AD) record of the Indian summer monsoon precipitation from the core monsoon zone of India. *Geophys. Res. Lett.* 34.
- Sinha, A., Stott, L., Berkelhammer, M., Cheng, H., Edwards, R.L., Buckley, B., Aldenderfer, M., Mudelsee, M., 2011b. A global context for megadroughts in monsoon Asia during the past millennium. *Quat. Sci. Rev.* 30, 47–62.
- Sirocko, F., Sarnthein, M., Lange, H., Erlenkeuser, H., 1991. Atmospheric summer circulation and coastal upwelling in the Arabian Sea during the Holocene and the last glaciation. *Quat. Res.* 36, 72–93. [https://doi.org/10.1016/0033-5894\(91\)90018-Z](https://doi.org/10.1016/0033-5894(91)90018-Z)
- Smerdon, J.E., 2017. What was Earth's climate like before we were measuring it? *Significance* 14, 24–29.
- Smith, S., Mackenzie, F., 1987. The ocean as a net heterotrophic system: implications from the carbon biogeochemical cycle. *Glob. Biogeochem. Cycles* 1, 187–198.
- Smith, S.L., Codispoti, L., 1980. Southwest monsoon of 1979: chemical and biological response of Somali coastal waters. *Science* 209, 597–600.
- Somayajulu, B., Rengarajan, R., Jani, R., 2002. Geochemical cycling in the Hooghly estuary, India. *Mar. Chem.* 79, 171–183.
- Sonntag, C., Münnich, K., Jacob, H., Rozanski, K., 1983. Variations of deuterium and oxygen-18 in continental precipitation and groundwater, and their causes, in: *Variations in the Global Water Budget*. Springer, pp. 107–124.
- Srivastava, R., Ramesh, R., Gandhi, N., Jani, R.A., Singh, A.K., 2015. Monsoon onset signal in the stable oxygen and hydrogen isotope ratios of monsoon vapor. *Atmos. Environ.* 108, 117–124. <https://doi.org/10.1016/j.atmosenv.2015.02.062>

- Srivastava, R., Ramesh, R., Prakash, S., Anilkumar, N., Sudhakar, M., 2007. Oxygen isotope and salinity variations in the Indian sector of the Southern Ocean. *Geophys. Res. Lett.* 34.
- Stocker, T., 1999. Abrupt climate changes: from the past to the future—a review. *Int. J. Earth Sci.* 88, 365–374.
- Stuiver, M., Reimer, P., Reimer, R., 2017. CALIB 7.1 [WWW program] at <http://calib.org>. Last Accessed 8–24.
- Su, J., Zhang, R., Wang, H., 2017. Consecutive record-breaking high temperatures marked the handover from hiatus to accelerated warming. *Sci. Rep.* 7, 1–9.
- Subramanian, V., 1996. The sediment load of Indian rivers—an update. *IAHS Publ.-Ser. Proc. Rep.-Intern Assoc Hydrol. Sci.* 236, 183–190.
- Subramanian, V., 1993. Sediment load of Indian rivers. *Curr. Sci.* 928–930.
- Sulochana, G., Francis, P., 2016. El Nino and the Indian rainfall in June. *Curr. Sci.* 110, 1010–1022.
- Sverdrup, H.U., Johnson, M.W., Fleming, R.H., 1942. *The Oceans: Their physics, chemistry, and general biology*. Prentice-Hall New York.
- Tarback, E.J., Lutgens, F.K., 1979. *The atmosphere: an introduction to meteorology*. Prentice Hall.
- Tiwari, M., Nagoji, S.S., Anilkumar, N., Rajan, S., 2015. Oxygen isotope distribution at shallow to intermediate depths across different fronts of the Southern Ocean: Signatures of a warm-core eddy. *Deep Sea Res. Part II Top. Stud. Oceanogr.* 118, 170–176.
- Tiwari, M., Nagoji, S.S., Kartik, T., Drishya, G., Parvathy, R., Rajan, S., 2013. Oxygen isotope–salinity relationships of discrete oceanic regions from India to Antarctica vis-à-vis surface hydrological processes. *J. Mar. Syst.* 113, 88–93.
- Tiwari, M., Ramesh, R., Bhushan, R., Sheshshayee, M.S., Somayajulu, B.L.K., Jull, A.J.T., Burr, G.S., 2010. Did the Indo-Asian summer monsoon decrease during the Holocene following insolation? *J. Quat. Sci.* 25, 1179–1188. <https://doi.org/10.1002/jqs.1398>
- Tiwari, M., Ramesh, R., Yadava, M., Somayajulu, B., Jull, A.T., Burr, G., 2006. Is there a persistent control of monsoon winds by precipitation during the late Holocene? *Geochem. Geophys. Geosystems* 7.

- Tiwari, M., Singh, A.K., Ramesh, R., 2011. High-resolution monsoon records since Last Glacial Maximum: a comparison of marine and terrestrial paleoarchives from South Asia. *J. Geol. Res.* 2011, 1–12.
- Trenberth, K.E., 1997. The definition of el nino. *Bull. Am. Meteorol. Soc.* 78, 2771–2777.
- Turner, A., Inness, P., Slingo, J., 2005. The role of the basic state in the ENSO–monsoon relationship and implications for predictability. *Q. J. R. Meteorol. Soc. J. Atmospheric Sci. Appl. Meteorol. Phys. Oceanogr.* 131, 781–804.
- Urey, H.C., 1947. The thermodynamic properties of isotopic substances. *J. Chem. Soc. Resumed* 562–581.
- Varadachari, V., Murty, C., Reddy, C.G., 1968a. Salinity maxima associated with some sub-surface water masses in the upper layers of the Bay of Bengal. *B Natl Inst Sci India.*
- Varadachari, V., Murty, C., Reddy, C.G., 1968b. Salinity maxima associated with some sub-surface water masses in the upper layers of the Bay of Bengal. *B Natl Inst Sci India.*
- Verma, K., Bharti, S., Singh, A., 2018. Late Glacial–Holocene record of benthic foraminiferal morphogroups from the eastern Arabian Sea OMZ: Paleoenvironmental implications. *J. Earth Syst. Sci.* 127, 21.
- Versteegh, G.J., Zonneveld, K.A., 2002. Use of selective degradation to separate preservation from productivity. *Geology* 30, 615–618.
- Vidya, P., Kumar, S.P., 2013. Role of mesoscale eddies on the variability of biogenic flux in the northern and central Bay of Bengal. *J. Geophys. Res. Oceans* 118, 5760–5771.
- Vinayachandran, P., Kurian, J., 2008. Modeling Indian Ocean circulation: Bay of Bengal fresh plume and Arabian Sea mini warm pool. Presented at the Proceedings of the 12th Asian Congress of Fluid Mechanics, Citeseer, pp. 18–21.
- Vinayachandran, P., Masumoto, Y., Mikawa, T., Yamagata, T., 1999. Intrusion of the southwest monsoon current into the Bay of Bengal. *J. Geophys. Res. Oceans* 104, 11077–11085.
- Vinayachandran, P., Mathew, S., 2003. Phytoplankton bloom in the Bay of Bengal during the northeast monsoon and its intensification by cyclones. *Geophys. Res. Lett.* 30.

- Vitousek, P.M., Howarth, R.W., 1991. Nitrogen limitation on land and in the sea: how can it occur? *Biogeochemistry* 13, 87–115.
- Walker, G., n.d. Y EW Bliss, 1932. *World Weather V Men Roy Meteor Soc* 4, 53–84.
- Wallace, J., Rasmusson, E., Mitchell, T., Kousky, V., Sarachik, E., Storch, H. von, 1998. On the structure and evolution of ENSO-related climate variability in the tropical Pacific: Lessons from TOGA. *J. Geophys. Res. Oceans* 103, 14241–14259.
- Wang, B., Ding, Q., Fu, X., Kang, I., Jin, K., Shukla, J., Doblas-Reyes, F., 2005a. Fundamental challenge in simulation and prediction of summer monsoon rainfall. *Geophys. Res. Lett.* 32.
- Wang, B., Ding, Q., Fu, X., Kang, I., Jin, K., Shukla, J., Doblas-Reyes, F., 2005b. Fundamental challenge in simulation and prediction of summer monsoon rainfall. *Geophys. Res. Lett.* 32.
- Wang, B., Liu, J., Kim, H.-J., Webster, P.J., Yim, S.-Y., 2012. Recent change of the global monsoon precipitation (1979–2008). *Clim. Dyn.* 39, 1123–1135.
- Wang, B., Wu, R., Li, T., 2003. Atmosphere–warm ocean interaction and its impacts on Asian–Australian monsoon variation. *J. Clim.* 16, 1195–1211.
- Wang, B., Xiang, B., Li, J., Webster, P.J., Rajeevan, M.N., Liu, J., Ha, K.-J., 2015. Rethinking Indian monsoon rainfall prediction in the context of recent global warming. *Nat. Commun.* 6.
- Warrier, C.U., Babu, M.P., Manjula, P., Velayudhan, K., Hameed, A.S., Vasu, K., 2010. Isotopic characterization of dual monsoon precipitation—evidence from Kerala, India. *Curr. Sci.* 1487–1495.
- Wassenaar, L., Terzer-Wassmuth, S., Douence, C., Araguas-Araguas, L., Aggarwal, P., Coplen, T.B., 2018. Seeking excellence: An evaluation of 235 international laboratories conducting water isotope analyses by isotope-ratio and laser-absorption spectrometry. *Rapid Commun. Mass Spectrom.* 32, 393–406.
- Wollast, R., Billen, G., 1981. In, *Flux of Organic Carbon by Rivers to the Ocean. Presented at the Conference*, pp. 331–359.
- Wyrtki, K., 1973. Physical oceanography of the Indian Ocean, in: *The Biology of the Indian Ocean*. Springer, pp. 18–36.
- Yadava, M., Ramesh, R., 2005. Monsoon reconstruction from radiocarbon dated tropical Indian speleothems. *The Holocene* 15, 48–59.

- Yadava, M., Ramesh, R., 1999. Speleothems—useful proxies for past monsoon rainfall.
- Yang, H., Johnson, K.R., Griffiths, M.L., Yoshimura, K., 2016. Interannual controls on oxygen isotope variability in Asian monsoon precipitation and implications for paleoclimate reconstructions. *J. Geophys. Res. Atmospheres* 121, 8410–8428. <https://doi.org/10.1002/2015JD024683>
- Yonge, C.J., Goldenberg, L., Krouse, H.R., 1989. An isotope study of water bodies along a traverse of southwestern Canada. *J. Hydrol.* 106, 245–255.
- Yoshimura, K., Kanamitsu, M., Noone, D., Oki, T., 2008. Historical isotope simulation using reanalysis atmospheric data. *J. Geophys. Res. Atmospheres* 113, 1–15.
- Zachos, J., Pagani, M., Sloan, L., Thomas, E., Billups, K., 2001. Trends, rhythms, and aberrations in global climate 65 Ma to present. *Science* 292, 686–693.
- Zhang, J., 1985. Living planktonic foraminifera from the eastern Arabian Sea. *Deep Sea Res. Part Oceanogr. Res. Pap.* 32, 789–798.
- Zhisheng, A., Clemens, S.C., Shen, J., Qiang, X., Jin, Z., Sun, Y., Prell, W.L., Luo, J., Wang, S., Xu, H., 2011. Glacial-interglacial Indian summer monsoon dynamics. *Science* 333, 719–723.
- Zika, J.D., Skliris, N., Nurser, A.G., Josey, S.A., Mudryk, L., Laliberté, F., Marsh, R., 2015. Maintenance and broadening of the ocean’s salinity distribution by the water cycle. *J. Clim.* 28, 9550–9560.